

https://dspace.org/

Friction and wear of selected metal-ceramic and polycrystalline diamond sliding couples

Damm, Oliver Frank Rudolf August

1995
http://hdl.handle.net/10539/22163

Downloaded from a DSpace repository. https://dspace.org/

Figure 4.5: SEM micrograph showing the typical microstructure of Ce-TZP ceramic.. 80

Figure 4.6: Variation of apparent contact pressure as a function of sliding distance for AISI 440C steel sliding on (a) ground and (b) polished alumina. 85

Figure 4.7: Typical friction coefficient traces obtained under a load of 50 N for (a) polished Sialon and (b) polished Si_3N_4. 87

Figure 4.8: Friction trace obtained for AISI 440C sliding against polished Si_3N_4 under a load of 80 N. Note absence of oscillations and high coefficient of friction88

Figure 4.9: Summary of stabilized friction coefficients obtained for the various sliding couples: (a) for ground ceramic surfaces and (b) polished surfaces. 91

Figure 4.10: Typical wear depth traces for (a) ground and (b) polished alumina (dry sliding, 50 N load). 96

Figure 4.11: Total wear depth (a) and stabilized wear rate (b) for sliding couples involving ground ceramic surfaces. 98

Figure 4.12: Total wear depth (a) and stabilized wear rates (b) for sliding couples involving polished ceramic surfaces. 99

Figure 4.13: General appearance of wear scars on (a) ground and (b) polished alumina (load 50 N, magnification 50 x). 103

Figure 4.14: SEM micrographs of wear scars generated on ground alumina surfaces: (a) 20N load, centre of scar; (b) 20 N load, edge of scar; (c) 50 N load, centre of scar; and (d) 50 N load, edge of scar. 104

Figure 4.15: SEM micrographs of wear scars generated on polished alumina: (a) 20 N load, centre of scar; (b) 20 N load, edge of scar; (c) 50 N load, centre of scar; and (d) 50 N load, edge of scar. 105

Figure 4.16: Original appearance of (a) ground and (b) polished alumina surfaces prior to tribological testing. 106

Figure 4.17: EDS spectra obtained from (a) ground alumina, 20 N load; (b) ground alumina, 50 N load; (c) polished alumina, 20 N load; and (d) polished alumina, 50 N load, confirming that transfer layers on these surfaces originated from the steel ball. 108

Figure 4.18: General appearance of wear scars on (a) ground and (b) polished PSZ (applied load 50 N, magnification 8x). 111

Figure 2.15: Schematic summary of friction versus mean contact pressure for various styli sliding on the (001) face of a diamond. Soft ∥ implies sliding in the <100> direction parallel to the polish lines, soft ⊥ implies sliding in the <010> direction orthogonal to the polish lines and hard refers to sliding in the <110> direction. 47

Figure 2.16: Sliding experiment on (100) surface of diamond as a function of temperature: (a) in the presence of water and (b) liquid paraffin. 48

Figure 2.17: Friction on (100) surface as a function of the number of traversals on the same track. 49

Figure 3.1: General view of the reciprocating tribometer (a); and close-up views of the scotch yoke drive system (b) and the specimen stage assembly (c). 56

Figure 3.1 (cont.) 57

Figure 3.2: Flushing of the specimen contact using water recirculating facility. 60

Figure 3.3: Typical screen display prior to starting a test. During a test, the acquired friction and wear data is displayed graphically and numerically in the centre window. 62

Figure 3.4: Y-t recorder traces of two low-speed tests run to validate the form of the friction force signal. 67

Figure 3.5: Overall view of the vibration analysis equipment (a) and close-up view of the accelerometers (b). 68

Figure 3.6: Typical static calibration curve for friction force transducer system. 71

Figure 3.7: Typical friction curve obtained from a dynamic calibration run compared to the friction coefficient specified for the commercial Optimol SRV reciprocating sliding test rig. 73

Figure 4.1: Optical micrograph of a sectioned AISI 440C stainless steel ball, 100x magnification. 77

Figure 4.2: SEM micrograph showing typical microstructure of an alumina disc. . . . 78

Figure 4.3: SEM micrograph showing the typical structure of the Mg-PSZ ceramic. . 79

Figure 4.4: SEM micrograph showing the typical microstructure of 3Y-TZP ceramic. 79

LIST OF FIGURES

Page

Figure 2.1: Variation of coefficient of friction with normal load for a 60° diamond cone sliding on a silicon carbide single crystal. 9

Figure 2.2: Formation of Hertzian cone cracks (a) under a static indenter and (b) during sliding. 12

Figure 2.3: Influence of grain size on volumetric wear resistance of alumina and zirconia during (a) unidirectional and (b) reciprocating sliding contact. 14

Figure 2.4: Transitions in wear coefficient, K, of the total sliding system for self-mated Si-SiC under unlubricated sliding. 19

Figure 2.5: Humidity- and stroke length-dependent wear transitions for self-mated MgO-PSZ under unlubricated fretting. 19

Figure 2.6: Phase-change induced wear transitions in MgO-PSZ as a function of sliding speed and ambient temperature. 20

Figure 2.7: Wear transitions in Si_3N_4 induced by tribooxidation. 20

Figure 2.8: Alumina wear map under dry sliding conditions, determined using a step loading test procedure. 22

Figure 2.9: Wear maps for the self-mated dry sliding of silicon nitride. 22

Figure 2.10: Different types of transfer film formed by ceramic sliding couples. 25

Figure 2.11: (a) Pressure-velocity wear map for steel pairs in unidirectional, unlubricated sliding; and (b) temperature map for similar steel pairs sliding under similar conditions. 34

Figure 2.12: Load-velocity experimental friction maps 36

Figure 2.13: Load-velocity experimental wear maps 37

Figure 2.14: Wear rates (a) and friction curves (b) for stainless steel sliding against ceramics and itself under 10 N load and 0,1 m/s velocity in water. Transfer layer formation (i.e. negative mass loss) on the ceramic discs is represented by shadowed columns in (a). The friction curves represent 2500 m of sliding and the shadowed areas represent their amplitudes. 41

5. POLYCRYSTALLINE DIAMOND (PCD) SLIDING COUPLES 142
5.1 Introduction 142
5.2 Test Equipment and Methodology 143
5.2.1 Test equipment 143
5.2.2 Experimental materials and methodology 144
5.3 Unlubricated Sliding Behaviour 146
5.3.1 Run-in characteristics 146
5.3.2 Specimen geometry effects 149
5.3.3 Influence of load and load carrying capacity (LCC) 150
5.3.4 Surface effects and tribofilm formation 155
5.3.5 Influence of drilling fluid constituents 173
5.3.6 Influence of temperature 181
5.4 Water-Lubricated Sliding Behaviour 182
5.4.1 Run-in characteristics 182
5.4.2 Influence of load and load carrying capacity (LCC) 187
5.4.3 Surface effects and tribofilm formation 191
5.5 Commercial Implications 202
5.6 Summary 202

6. CONCLUSIONS 205
6.1 General 205
6.2 Metal-Ceramic Sliding Couples 206
6.3 Polycrystalline Diamond Sliding Couples 207
6.4 Hydro-Power Mining Systems 209
6.5 PCD Thrust Bearings 210

REFERENCES 211

APPENDIX A: Reciprocating sliding tribometer design drawings

APPENDIX B: Friction coefficient curves for metal-ceramic sliding couples

3.3 Computer Software Development 59
3.3.1 Menu structure 61
3.3.2 Sub-menus 61
3.3.3 Data acquisition and storage 64
3.4 Commissioning of Tribometer 66
3.4.1 Data acquisition system 66
3.4.2 Vibration analysis 67
3.4.3 Static and dynamic calibration 70
3.5 Summary 72

4. METAL-CERAMIC SLIDING COUPLES 74
4.1 Introduction 74
4.1.1 Materials selection 74
4.1.2 Test environment 77
4.2 Experimental Details 77
4.2.1 Materials 77
4.2.2 Tribological Test Conditions and Procedures 82
4.2.3 Analytical techniques 85
4.3 Friction and Wear Results 86
4.3.1 General friction behaviour 86
4.3.2 Friction coefficient results 90
4.3.3 Wear results 94
4.4 Wear Scar Development and Tribofilm Formation 102
4.4.1 Alumina 102
4.4.2 Zirconia ceramics 110
4.4.3 Silicon-based ceramics 125
4.5 Influence of Water Chemistry 132
4.5.1 Introduction 132
4.5.2 Results and discussion 133
4.6 Summary 140

CONTENTS

Page

1. INTRODUCTION 1
   1.1 The Hydro-Power Concept 1
   1.2 Borehole Drilling in the Oil Industry 2
   1.3 Thesis Organization 4

2. LITERATURE REVIEW 5
   2.1 Introduction 5
   2.2 Basic Concepts in Ceramic Friction and Wear 8
      2.2.1 Sliding friction 8
      2.2.2 Fracture and wear 10
      2.2.3 Friction and wear transitions 17
      2.2.4 Surface film formation and environmental effects 23
   2.3 Metal-Ceramic Sliding Systems 30
      2.3.1 Introduction 30
      2.3.2 Friction and Wear 31
      2.3.3 Surface film formation and environmental effects 38
   2.4 Synthetic Diamond Materials 42
      2.4.1 Introduction 42
      2.4.2 PCD: Synthesis and properties 44
      2.4.3 Friction of diamond 45
      2.4.4 Wear of diamond 50

3. DEVELOPMENT OF HIGH-SPEED RECIPROCATING TRIBOMETER 54
   3.1 Introduction 54
   3.2 Specifications and Design 54

ACKNOWLEDGEMENTS

1. Professor M N James and Dr G G Garrett, my supervisors at the University of the Witwatersrand, for their guidance, patience and understanding.
2. Dr G J Wright, my Programme Manager at the CSIR, for his support and unfailing encouragement and for leading by example.
3. My colleagues who provided invaluable advice and assistance, particularly Mr A Jurriaanse, who conducted much of the tribotesting on diamond materials, as well as Mr K Tank and Dr N J Pipkin of De Beers DRL.
4. Messrs. Wynand Louw and Martin van Staden for conducting the XPS analyses and assisting in their interpretation.
5. The Research Organization of the Chamber of Mines of South Africa (COMRO), for sponsoring much of the work on ceramics and permission to publish the results in this thesis.
6. The De Beers Diamond Research Laboratory (DRL) and the CSIR for sponsoring the work on diamond, supply of test materials and permitting the results to be used in this thesis. It recorded that the opinions expressed in this work do not necessarily reflect the opinions of De Beers.
7. My parents for years of support and encouragement.

DEDICATION

In memory of my father, Hans-Georg Jürgen Damm

and

to my wife, Sharon, and children Lauren and Jürgen, for their love and support, and for putting up with many lonely weekends and evenings during the preparation of this thesis.

surface, where it is bound in a complex tribofilm containing Si, Co, and W. Strong chemical interaction occurs between Si and Co, and there was some analytical evidence for a complex Si-Co-O compound in the tribofilm. Such effects do not appear to occur under water-lubricated conditions, probably as a result of the combined effects of lower temperatures, reduced adhesion and material transfer, and the fact that much debris is swept out of the contact zone by the water.

The formation of Co and Si-rich tribofilms was explained in terms of a thermally activated mechanism whereby the relevant binder phase migrates to the surface of the PCD compact under the influence of frictional heating. While further studies are required to confirm and describe the mechanistic details, indications are that differential thermal expansion between the binder phase and the surrounding, rigid diamond network cannot account completely for the effect. It appears that the migration is sustained by a diffusion mechanism, which probably involves the diffusion of vacancies into the PCD compact. The precise nature of the driving force for the migration remains uncertain, but it is possible that a significant part is provided by the binder phase undergoing chemical reactions (oxidation) at the sliding surface. Loose wear debris generated from the binder phase played a contributory rôle in tribofilm formation, by becoming compacted on the sliding surfaces.

Drilling fluid constituents bentonite, silica, and barite have a beneficial effect on the friction coefficient and LCC of self-mated Syndite. This is related to the removal of deleterious Co-rich tribofilms by these materials, through a complex mechanism involving both mechanical abrasion and chemical interactions. The addition of haematite must be avoided since it results in rapid seizure of self-mated Syndite and severe surface damage. This was most likely caused by graphitization and structural degradation of the diamond surfaces, which is known to be promoted by the presence of catalyst (or solvent) materials such as cobalt and iron.

The friction coefficient of self-mated Syndite in dry sliding increased with increasing temperature, reaching an apparent maximum between 60 °C and 100 °C. Beyond this point, both parameters decreased to an apparent minimum at ~160 °C. These effects were explained in terms of the influence of temperature on the rate of binder phase migration and tribofilm formation, as well as on the mechanical properties of the tribofilms.

ABSTRACT

This thesis describes a study of the friction and wear characteristics of a range of oxide and silicon-based ceramics sliding against AISI 440C stainless steel, as well as various sliding combinations of two types of De Beers polycrystalline diamond (PCD), namely Syndite and Syndax. To facilitate the former work, a high-speed reciprocating sliding test machine with computerized data acquisition and control was developed.

It was confirmed that under water-lubricated sliding, the oxide ceramics (alumina, PSZ, 3Y-TZP, and Ce-TZP) showed higher friction coefficients and wear rates than the silicon-based ceramics (Sialon and silicon nitride). This was related to different levels of adhesion and the formation of metallic transfer films. For the zirconia ceramics, increased transformation toughening was associated with increased surface fracture damage and metallic film formation. In general, the metallic transfer films were beneficial, protecting the underlying ceramic and dominating the friction and wear behaviour. The superior performance of the silicon-based ceramics was related to the formation of lubricious tribofilms containing silicon oxides and hydroxides.

Experiments with synthetic mine water as lubricant demonstrated that the presence of significant amounts of chloride and sulphate in the water generally reduced friction and wear. This was tentatively explained in terms of reduced adhesion and the promotion of iron oxide and hydroxide formation. It is suggested that the influence of sulphate may be more important in this regard than that of chloride.

The tribological behaviour of self-mated Syndite PCD sliding couples is dominated by the formation of Co-rich tribofilms, which are associated with increased friction coefficients and reduced load carrying capacity (LCC). Syndax, which employs silicon as the binder phase, shows lower friction coefficients and higher LCC under both dry and water-lubricated sliding conditions. Mixed Syndax/Syndite couples show superior performance to self-mated Syndite under dry sliding conditions, but no improvements in the presence of water. The former effect is related to the preferential removal of Co from the Syndite surface to the Syndax

DECLARATION

I declare that this thesis is my own, unaided work, except where due acknowledgement is given to others. It is being submitted for the Degree of Doctor of Philosophy in the University of the Witwatersrand, Johannesburg. It has not been submitted before for any degree or examination in any other University.

E. Gauw

21st day of December 1995

FRICTION AND WEAR OF SELECTED METAL - CERAMIC AND POLYCRYSTALLINE DIAMOND SLIDING COUPLES

Oliver Frank Rudolf August Damm

A thesis submitted to the Faculty of Engineering, University of the Witwatersrand, Johannesburg, in fulfilment of the requirements for the degree of Doctor of Philosophy.

Pretoria, 1995

CHAPTER 2

2. LITERATURE REVIEW

2.1 Introduction

Engineering ceramics mainly include compounds of C, N and O with Si and various metals, for example alumina (Al_2O_3), zirconia (ZrO_2), silicon carbide (SiC), silicon nitride (Si_3N_4), and silicon-aluminium oxynitride (SiAlON). The materials combine low density with good mechanical properties, such as high hardness, strength and stiffness up to high temperatures. Together with their excellent corrosion properties and oxidational stability, these characteristics make engineering ceramics very attractive for use in a wide range of agressive sliding applications where demanding mechanical, corrosive and thermal requirements exist [1]. Synthetic diamond materials exhibit many of the characteristics which distinguish engineering ceramics and are thus considered under the same category for the purpose of the present discussion.

Historically, intensive research efforts into the sliding friction and wear behaviour of ceramics were stimulated by industrial applications such as mechanical pump seal rings, cutting tools and components for internal combustion engines. In response to the requirements of aerospace development programmes, early research in the 1960's and 1970's focused on the elucidation of fundamental friction and wear mechanisms using single crystal ceramics, such as sapphire [2] and silicon carbide [3]. Together with fundamental studies on contact phenomena and fracture [4][5][6], this work provided the basis for much of the current understanding of ceramic tribology, as outlined by Buckley [7].

As ceramic materials technology developed further and industrial applications gained in importance during the 1970's and early 1980's, the research focus shifted towards the study of polycrystalline ceramics in mutual sliding contact and also began to consider metals in contact with ceramics in more detail. Although much of this work involved unlubricated sliding couples, the overriding importance of the environment and the formation of surface

1.3 Thesis Organization

A literature review was initially carried out to establish the level of existing knowledge concerning the tribological characteristics of metal-ceramic and PCD sliding couples (Chapter 2). A high-frequency reciprocating sliding tribometer with computerized data acquisition was developed to simulate the essential features of the motion of components in hydro-powered gold mining equipment (Chapter 3). This was subsequently used to study the friction and wear behaviour of various engineering ceramics sliding against AISI 440C stainless steel under both dry and water lubricated conditions (Chapter 4). A study of the tribological characteristics and operational performance limitations of various PCD sliding couples under both dry and water-lubricated conditions is described in Chapter 5. Finally, the results obtained from the work are summarized in Chapter 6, and conclusions drawn pertaining to the selection and development of improved sliding couples for use in hydro-powered stoping equipment as well as thrust bearings for down-hole drilling applications.

a thrust bearing is limited by the diameter of the outer bearing housing, which is similar to the diameter of the drill pipe, and the diameter of the bit drive shaft which is concentrically located in the bearing housing and connects the down-hole powerpack with the drill bit. Typically, this annular space is 18 mm wide with a pitch circle diameter of ~120 mm. In order to accommodate the high loads, traditional thrust bearings are thus made up of bearing stacks, which can comprise as many as 30 or 40 individual rotor/stator bearing sets. As a result, these bearing assemblies are up to 2,5 m long which, in turn, limits the radii which can be achieved in directional drilling. (In this drilling technique, the borehole is diverted from the vertical direction to access multiple oil fields from a single drill rig location, or to access oil deposits which could otherwise not be exploited).

Against this background, it was proposed to develop an improved thrust bearing which utilizes polycrystalline diamond (PCD) bearing faces. It was anticipated that the extreme hardness, wear resistance and low friction coefficients associated with diamond could provide the potential for reducing the overall length of the bearing, by making use of only two bearing face sets, and for improving the wear life of the assembly. Similar work has been carried out by Smith International, USA, and other organizations, but has been protected by a comprehensive patent portfolio. No information regarding the fundamental friction and wear characteristics of such bearings could be found in the open literature.

Initial development work conducted by the writer and co-workers showed that the performance of PCD thrust bearings appeared to be limited by erratic friction behaviour and unanticipated seizure of the bearing surfaces at high contact pressures, rather than by wear. A more fundamental study was thus initiated to examine the friction characteristics of various combinations of two PCD types under both dry and water-lubricated sliding conditions. The primary aim was to generate useful data concerning the operational limitations of these sliding couples, as well as to develop an understanding of the fundamental friction (and wear) mechanisms, to facilitate the selection and/or development of improved material couples for PCD thrust bearings.

programme of work was thus initiated by the Chamber of Mines Research Organization (COMRO) to study the friction and wear characteristics of AISI 440C - engineering ceramic sliding couples, with the aim of generating data and knowledge which could be applied in the design of improved reciprocating water-powered components.

1.2 Borehole Drilling in the Oil Industry

It is common practice in the drilling industry to pump large volumes of a water-based drilling fluid (or mud) down the drill pipe and through the drill bit to cool and lubricate the drill bit and flush the generated cuttings out of the borehole. Analogous to the hydro-power concept in gold mining, this has led to the development of down-hole powerpacks which make use of the stored energy in the drilling fluid to directly drive the drill bit. The two primary types are the Moineau positive displacement motor, which incorporates a helical shaft running in a rubber stator as the driving element, and the turbodrill, which comprises numerous rotor and stator turbine blade stages analogous to a gas turbine. Both motors are driven by the drilling fluid which is supplied at a typical rate of 3500 l/min.

The hydraulic and drilling loads are supported by a bearing pack which comprises a set of radial and bi-directional thrust bearings and is typically mounted between the drive unit and the drill bit at the bottom of the drill string. Due to the high flowrates and fairly agressive nature of the drilling fluid (which contains solids such as bentonite, barite and silica), it is usually impractical to seal these bearing units. Therefore, the bearing surfaces are generally lubricated with the drilling fluid, and this leads to rapid wear of the rubber/metal plain thrust bearings or the all-metal rolling element thrust bearings which are traditionally used. The typical lifetime of such a traditional thrust bearing set may vary between about 40 hours and 100 hours. Comparing this to the typical time required for retrieving the drill string from the borehole to replace the bearing (24 hours), the economic implications become clear.

Furthermore, the typical thrust loads which must be accommodated are of the order of 10 - 12 tonnes during drilling, while the superimposed shock loads can momentarily reach values in excess of three times this static load. The annular space which is available to accomodate

CHAPTER 1

1. INTRODUCTION

Mining is probably one of the most important industries worldwide, and particularly so in South Africa. Although the contribution of mining to the South African GDP has declined slightly over the past ten years, it remains an important contributor and an integral part of the economy.

The current trend for base mineral prices to remain static or decrease slightly has placed tremendous demands on the local and overseas mining industries to reduce unit production costs in order to preserve profitability. This has led to much research activity into improved mining methods and more efficient use of engineering materials in mining applications. Due to the arduous nature of these applications, the tribological characteristics of materials are of particular importance, and this aspect is addressed in the present work.

1.1 The Hydro-Power Concept

South African gold mines are among the deepest in the world and efficient cooling of the stope regions is critical to maintain an acceptable working environment. For this purpose, large amounts of chilled water are pumped down the mine shafts and into the stope regions. The hydro-power concept makes use of the potential energy stored in the vertical, chilled water column in the mine shaft to provide hydraulic power to stoping equipment, such as rock drills. This has important economic advantages over traditional pneumatic or hydraulic power sources. Other benefits include increased safety and compatibility with the existing mine infrastructure.

Initial research work showed that a serious performance-limiting factor in the development of high pressure, high frequency reciprocating components for water powered equipment like water hammers and rock drills, was severe sliding wear and stick-slip motion (i.e. high and variable friction coefficients) of the traditional AISI 440C stainless steel components. A

Table 4.12: XPS analysis results obtained on a polished Ce-TZP wear track after 6912 m of sliding under a load of 50 N. 124

Table 4.13: XPS analysis results obtained on a polished Ce-TZP wear track after 6912 m of sliding under a load of 50 N. 129

Table 4.14: XPS analysis results obtained on a polished Si_3N_4 wear track (6912 m of sliding, load 50 N). 131

Table 4.15: Comparison of steady-state coefficients of friction obtained in deionized water and Unisel synthetic mine water solution. 133

Table 4.16: Comparison of wear results obtained for alumina, Sialon and Si_3N_4 when lubricated with Unisel synthetic mine water and deionized water. 135

Table 4.17: Bond dissociation energies for selected silicon bonds 139

Table 5.1: Surface roughness values of the Syndite pin and disc run-in under a load of 490 N. 146

Table 5.2: XPS results obtained from a typical, thick tribofilm on a Syndite surface. 158

Table 5.3: XPS results obtained from a typical tribofilm on a Syndax surface after dry sliding against Syndite. 168

LIST OF TABLES

Page

Table 2.1: Ceramic wear data from literature 17
Table 2.2: Microhardness of tribofilms and lapped parent surfaces on several ceramics, along with bulk and contact temperatures (°C) 26
Table 2.3: Summary of previous work on the effect of water or increasing relative humidity for various ceramic sliding couples 28
Table 2.4: Some key properties of diamond compared to selected engineering ceramics. 42
Table 4.1: Material properties of the experimental ceramics 81
Table 4.2: Surface roughness values of ground and polished ceramic discs. 82
Table 4.3: Test matrix used for the friction and wear tests. 83
Table 4.4: Apparent contact pressure (MPa) for Sialon and Si_3N_4 under various loads. 89
Table 4.5: Stabilized friction coefficients for AISI 440C stainless steel sliding against the various ceramics. 90
Table 4.6: Summary of wear depth and steady-state wear rate results obtained for the various sliding couples. 97
Table 4.7: XPS analysis results obtained on polished alumina after 48 m of sliding under a load of 50 N. 109
Table 4.8: XPS analysis results obtained from a typical wear track on polished alumina after 6912 m of sliding under a load of 50 N. 109
Table 4.9: XPS analysis results obtained on polished alumina after 6912 m of sliding under a load of 50 N. 110
Table 4.10: XPS analysis results obtained on typical transfer layers generated on PSZ after 6912 m of sliding under a load of 50 N. 118
Table 4.11: XPS analysis results obtained on a polished 3Y-TZP wear track after 6912 m of sliding under a load of 50 N. 122

Figure 5.35: Load carrying capacity and friction behaviour of self-mated Syndite in water-lubricated sliding. 187

Figure 5.36: Load carrying capacity and friction behaviour of self-mated Syndax in water-lubricated sliding. 188

Figure 5.37: Load carrying capacity and friction behaviour of a Syndax (pin) / Syndite (disc) couple in water-lubricated sliding. 189

Figure 5.38: Load carrying capacity and friction behaviour of a Syndite (pin) / Syndax (disc) couple in water-lubricated sliding. 190

Figure 5.39: Optical micrographs of Co-rich tribofilm patches formed on Syndite during self-mated, water-lubricated sliding: (a) small patches; and (b) larger patches (500x mag.). 192

Figure 5.40: SEM micrograph of a typical Syndite surface produced in self-mated, water-lubricated sliding (a); and (b) EDS spectrum showing small amount of Co on the diamond surfaces. 193

Figure 5.41: Optical micrograph (a), 500x mag.; and (b) SEM micrograph of a typical Syndax surface produced in self-mated, water-lubricated sliding. 195

Figure 5.42: Optical micrograph (a), 500x mag.; and (b) SEM micrograph of the Syndite disc from the Syndax/Syndite water-lubricated sliding couple. 197

Figure 5.43: Optical micrograph (a), 500x mag.; and (b) SEM micrograph of the Syndax pin from the Syndax/Syndite water-lubricated sliding couple. 198

Figure 5.44: Optical micrograph (a), 500x; and (b) SEM micrograph of the Syndax disc from the Syndite/Syndax water-lubricated sliding couple. 200

Figure 5.45: Optical micrograph (a), 500x mag.; and (b) SEM micrograph of the Syndite pin from the Syndite/Syndax water-lubricated sliding couple. 201

Figure 5.21: Optical micrograph (a), 200x mag.; (b) SEM micrograph; and (c) EDS spectrum, showing the formation of Si and Co-rich tribofilms on the Syndax disc from the Syndite (pin) / Syndax (disc) dry sliding couple. 171

Figure 5.22: Optical micrograph (a), 200x mag.; and (b) SEM micrograph of the Syndite pin from the Syndite (pin) / Syndite (disc) dry sliding couple. 172

Figure 5.23: EDS spectra obtained from the Syndite pin: (a) inter-grain, binder phase region; and (b) typical polished diamond grain, showing absence of Co-rich tribofilms. 173

Figure 5.24: Surface appearance of Syndite after sliding in the presence of dry silica, showing abrasive grooving and fracture damage; 500x mag. 175

Figure 5.25: Influence of powdered silica on the friction behaviour of self-mated Syndite. 176

Figure 5.26: Influence of bentonite on the friction behaviour of self-mated Syndite. . 177

Figure 5.27: Influence of barite on the friction behaviour of self-mated Syndite. . . . 177

Figure 5.28: Influence of haematite on the friction behaviour of self-mated Syndite.. 178

Figure 5.29: Surface damage due to haematite in the sliding interface of self-mated Syndite; (a) 340x mag.; and (b) 140x mag. 179

Figure 5.30: Heavy deposits of Co-rich tribofilm, formed on Syndite during a polishing run after the test in the presence of haematite; (a) on pin, 500x; and (b) on disc, 340x mag. 180

Figure 5.31: Influence of temperature on the friction behaviour of self-mated Syndite sliding dry under a load of 574 N (contact pressure 9 MPa). 183

Figure 5.32: Influence of temperature on the friction behaviour of self-mated Syndite sliding dry under a load of 644 N (contact pressure 10,1 MPa). 184

Figure 5.33: Influence of temperature on the friction behaviour of self-mated Syndite sliding dry under a load of 960 N (contact pressure 15,1 MPa). 185

Figure 5.34: Influence of temperature on the friction behaviour of self-mated Syndite sliding dry under a load of 2980 N (contact pressure 46,8 MPa). 186

Figure 5.8: Load carrying capacity and friction behaviour of a Syndite (pin) / Syndax (disc) couple in dry sliding. 154

Figure 5.9: Well-developed tribofilms on (a) Syndite disc (140x mag.); and (b) Syndite pin (400x mag.). 156

Figure 5.10: Co-rich tribofilm on Syndite: (a) SEM micrograph; (b) EDS spectrum of tribofilm and (c) EDS spectrum of polished diamond grain without tribofilms. 157

Figure 5.11: Accumulation and compaction of Co-rich wear debris at the leading edge of a Syndite pin. 158

Figure 5.12: SEM micrographs of a worn Syndite surface: (a) area with Co-rich deposits and (b) similar area after cleaning with hydrochloric acid. 159

Figure 5.13: Typical appearance of Syndax disc from the self-mated Syndax couple under dry sliding: (a) optical micrograph (500x mag.); and (b) SEM micrograph. 161

Figure 5.14: Typical appearance of the Syndax pin from the self-mated Syndax couple under dry sliding: (a) optical micrograph (500x mag.); and (b) SEM micrograph. 162

Figure 5.15: EDS spectra obtained from polished diamond grains on (a) the Syndax disc and (b) the Syndax pin from the self-mated Sydax dry sliding couple. 163

Figure 5.16: Optical micrograph (a), 200x mag.; (b) SEM micrograph; and (c) EDS spectrum of the worn surface of the Syndite disc from the Syndax (pin) Syndite (disc) dry sliding couple. 164

Figure 5.17: SEM micrograph of the worn Syndite disc from the Syndax (pin) / Syndite (disc) dry sliding couple, showing accumulation of loose wear debris on the surface. 165

Figure 5.18: Optical micrograph (a), 200x mag.; and (b) SEM micrograph of Syndax pin from the Syndax (pin) Syndite (disc) dry sliding couple, showing extensive tribofilm formation. 165

Figure 5.18 (cont). 166

Figure 5.19: EDS spectrum of the tribofilm on the Syndax pin. 166

Figure 5.20: Co-Si binary phase diagram. 167

Figure 4.35: SEM micrographs showing polishing and filling of grinding grooves on a ground Sialon surface under a 50 N load; (a) general view and (b) centre of wear track. 128

Figure 4.36: EDS spectrum obtained from the wear scar shown in Figure 4.35. 128

Figure 4.37: SEM micrograph of a typical wear track generated on a polished Sialon surface under a load of 50 N. The EDS spectrum shows no significant metal transfer from the steel ball. 129

Figure 4.38: SEM micrographs of a wear track generated on a ground Si_3N_4 surface under a load of 50 N: (a) general view and (b) centre of track. 130

Figure 4.39: SEM micrograph of the original ground Si_3N_4 surface. 131

Figure 4.40: Typical friction trace obtained for AISI 440C sliding against alumina in Unisel solution under a load of 50 N. 133

Figure 4.41: Typical friction coefficient traces obtained for (a) Sialon and (b) Si_3N_4 sliding against AISI 440C in Unisel synthetic mine water solution. 134

Figure 4.42: Wear results for Al_2O_3, Sialon and Si_3N_4 sliding in deionized water and Unisel (WD = wear depth in mm, WR = wear rate in μm/m sliding). 135

Figure 5.1: Pin-on-disc (POD) tribometer used in the present work. 143

Figure 5.2: Optical micrographs of worn Syndax pin surfaces, showing abrasive grooving on the diamond particles and preferential wear and accumulation of loose debris at the inter-grain areas; (a) 200x and (b) 1000x magnification. . . 148

Figure 5.3: Influence of applied load on the friction force (top) and PCD temperature (bottom) for self-mated Syndax (untapered pin). 149

Figure 5.4: Load carrying capacity and friction behaviour of self-mated Syndite in dry sliding. 150

Figure 5.5: Influence of the presence of Co-rich tribofilms on the friction behaviour of self-mated Syndite. 151

Figure 5.6: Load carrying capacity and friction behaviour of self-mated Syndax in dry sliding. 152

Figure 5.7: Load carrying capacity and friction behaviour of a Syndax (pin) / Syndite (disc) couple in dry sliding. 153

Figure 4.19: General appearance of wear scars on (a) ground and (b) polished 3Y-TZP (applied load 50 N, magnification 8x). 112
Figure 4.20: General appearance of wear scars on (a) ground and (b) polished Ce-TZP (applied load 50 N, magnification 8x). 113
Figure 4.21: SEM micrograph showing polishing by plastic deformation on a typical ground PSZ surface. EDS spectrum shows lack of transferred material. 114
Figure 4.22: Preferential fracture damage at PSZ grain boundaries. 115
Figure 4.23: Typical example of a striated pit formed on the PSZ surfaces. 115
Figure 4.24: Grinding scratches filled with transferred material at the edge of a wear track on ground PSZ. 116
Figure 4.25: Typical examples of metallic transfer layers associated with areas of surface fracture on worn PSZ surfaces. 117
Figure 4.26: EDS spectra obtained from (a) transfer layer associated with fracture damage and (b) undamaged, polished area on worn PSZ ceramic. 117
Figure 4.27: Typical loose wear debris at the edges of the PSZ wear scars. 118
Figure 4.28: Typical fracture damage in the centre of 3Y-TZP wear scars. (Dark layer is a metallic transfer layer). 119
Figure 4.29: Fracture and transfer layer formation on polished 3Y-TZP under a 50 N load: (a) general view and (b) centre of wear track. 121
Figure 4.30: EDS spectrum obtained from the centre of the wear track shown in Figure 4.29. 121
Figure 4.31: Wear track generated on a polished Ce-TZP surface under a load of 50 N; (a) general view and (b) centre of track. 123
Figure 4.32: Wear track generated on a ground Ce-TZP surface under a load of 50 N; (a) general view and (b) centre of track. 124
Figure 4.33: Optical micrographs of wear tracks on (a) ground and (b) polished Sialon 101 (50 N load, 8x magnification). 126
Figure 4.34: Optical micrographs of wear tracks on (a) ground and (b) polished Si_3N_4 (50 N load, 8x magnification). 127

2.2.3 Friction and wear transitions

The current understanding of the wear of ceramics is inadequate for engineering design purposes [53]. One aspect of the problem is that investigators have used laboratory test conditions under which one particular wear mechanism dominated. It is now well known, however, that different wear mechanisms may operate simultaneously or sequentially, thus creating transitions as the experimental conditions change. Consequently, much of the data reported in the literature is not comparable. A recent review of the knowledge status on wear and lubrication of ceramics [54] demonstrated that of 300 collected papers, only 70 contained comparable wear information. Even among these, the scatter in data concerning material properties and wear is unacceptably high, as summarized in Table 2.1 by Hsu *et al* [55].

Table 2.1: Ceramic wear data from literature

	Al_2O_3		Si_3N_4		SiC		PSZ[1]	
	Mean	Range	Mean	Range	Mean	Range	Mean	Range
Fracture toughness, $MPa/m^{1/2}$	4	2-6	4,4	1,4-6	2,9	1,5-4	8	5-15
Hardness, GPa	16	11-22	16,3	13-17	25	13-34	12	10-14
Elastic Modulus, GPa	370	340-410	313	290-333	397	390-402	206	196-216
Density, g/cm^3	3,9	3,8-3,9	3,2	3,1-3,4	3,0	2,8-3,2	5,9	5,7-6,0
Wear Coefficients[2]								
Ambient	10^{-4}	10^{-6}-10^{-3}	10^{-4}	10^{-5}-10^{-4}	10^{-5}	10^{-6}-10^{-2}	10^{-4}	10^{-5}-10^{-4}
Humid air	10^{-7}	10^{-7}-10^{-6}	10^{-5}	10^{-6}-10^{-4}	N/A	N/A	10^{-6}	N/A
Lubricated[3]	10^{-5}	10^{-7}-10^{-3}	10^{-6}	N/A[4]	10^{-6}	N/A	10^{-7}	10^{-8}-10^{-6}

NOTES:
1. PSZ = Partially stabilized zirconia.
2. Dimensionless wear coefficient, K, as defined by in the Archard wear equation.
3. Lubricated denotes liquid lubricants were used, which may or may not lubricate.
4. N/A = insufficient data for reasonable value.

ceramics, leading to increased intergranular cracking. However, there is disagreement in the literature concerning the influence of this effect on wear rates. For example, Fischer *et al* [47] and Scott [48] found that the wear rates of toughened zirconias were significantly higher in water than in air. Conversely, a decrease in wear rate was recently observed by Stachowiak *et al* [49], despite an increase in small-scale surface fracture.

Third-body films which may be formed by tribochemical reaction, material transfer, or compaction of wear debris also exert a strong influence, to the point where wear can rarely be correlated directly with crack growth rates [16]. Lancaster [50] argued that improved wear models will need to be based not only on fracture mechanics, although fracture is clearly important in the generation of wear debris, but also need to take into account third-body formation and material microstructure. It would appear that such a model would have to be specific to particular materials, or at least to a material class, and that it may thus be impossible to develop a general model which will allow the accurate theoretical description and prediction of wear for most ceramic materials.

It is nevertheless useful for the following discussion to consider a simple model of wear, often referred to as the Archard wear equation, which relates the volume wear Q to the material surface hardness H, applied load F and sliding distance D:

$$Q = K \frac{FD}{H} \tag{2.4}$$

where K is the dimensionless wear coefficient, as defined by Rabinowicz [51][52]. Ceramic materials display a reasonably linear relationship between wear and sliding distance and load and therefore the wear coefficient is used by many investigators to report laboratory wear data. In some cases, the *dimensional* or *volumetric* wear coefficient is also used. It is defined as K/H with units $mm^3/N.m$ and represents the volume wear per unit sliding distance per unit applied load.

a transformation of the tetragonal to the monoclinic phase, analogous to the martensitic transformation observed in steels [34]. The fracture toughness of the ceramic is increased since the transformation absorbs a proportion of the driving energy of a propagating crack. Furthermore, the transformation is associated with a volume expansion of between 3 and 5 % which further retards crack propagation by generating compressive stresses at the crack tip. These microstructural toughening mechanisms have been described in more detail by Evans [35] and have led to the successful use of the materials in demanding applications such as tappet facings in internal combustion engines, screw conveyor bearings and scraper blades in the mining industry and extrusion dies in the metallurgical industry [36].

The transformation toughening effect can have a dramatically beneficial influence on wear resistance, as demonstrated by Fischer *et al* [37] who found that the wear resistance of yttria-stabilized zirconias is proportional to the fourth power of the fracture toughness. In contrast, several investigators have found minima in the wear resistance between room temperature and about 500 °C [38][39] while others demonstrated high wear rates of zirconia ceramics under various test conditions, particularly at high sliding speeds and applied loads [40][41][42][43]. In these cases, the high wear rates were explained in terms of the large-scale tetragonal-to-monoclinic transformation and subsequent delamination of the near-surface layer. The picture that emerges is that under lower loads, temperatures and sliding speeds, partial transformation of the tetragonal phase in the near-surface regions of zirconia ceramic inhibits microfracture and improves wear resistance. Under more severe sliding conditions, however, the transformation is more complete and affects a thicker subsurface layer. The volume expansion associated with the transformation then results in spalling and delamination of the transformed layer, thus increasing the wear rate [44].

In practice, wear of ceramics is clearly a complex phenomenon since mechanisms such as plastic deformation, microfracture, fatigue and tribochemical reactions may occur simultaneously [45] and are affected strongly by operating conditions and the environment.

Direct environmental effects include stress-corrosion cracking which is known to increase the wear rate of alumina in water [46]. A similar mechanism has been observed in zirconia

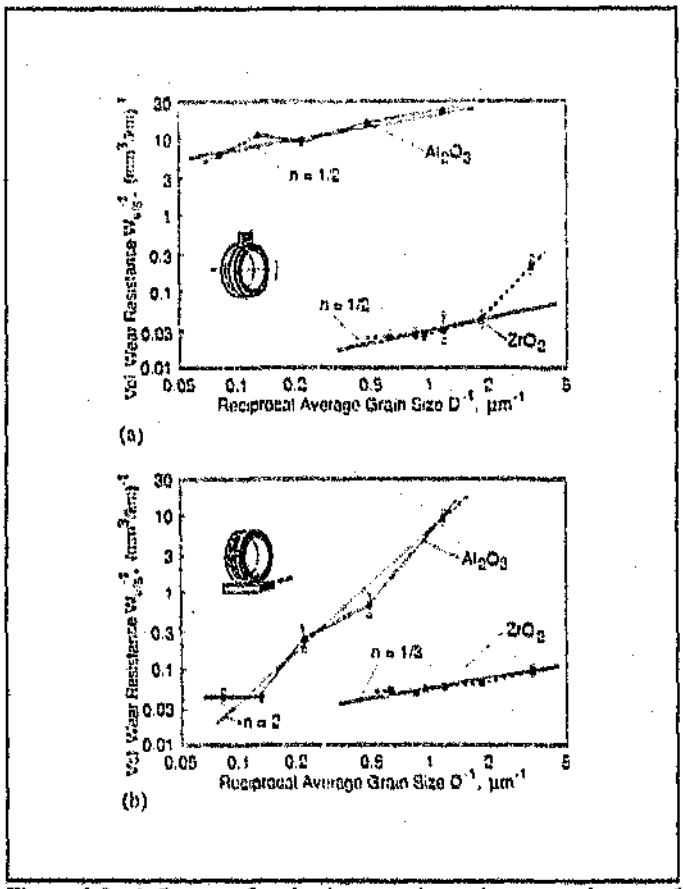

Figure 2.3: Influence of grain size on volumetric wear resistance of alumina and zirconia during (a) unidirectional and (b) reciprocating sliding contact. (after Zum Gahr *et al* [32])

Zirconia ceramics display a unique microstructural effect which has an overriding influence on fracture and wear properties. ZrO_2 exists in three crystallographic structures, namely cubic above 2370°C, tetragonal above 1170°C and monoclinic below 1170 °C [33]. The tetragonal or cubic phase can be stabilized over the entire temperature range by additions of MgO, CaO, Y_2O_3 (yttria) and CeO_2 (ceria); such ceramics are termed fully stabilized zirconias (FSZ). However, by carefully selecting the level of these additions and controlling the microstructure, varying proportions of the tetragonal phase can be retained to room temperature in a metastable form (tetragonal zirconia polycrystals, TZP, or partially stabilized zirconia, PSZ). In these ceramics, the application of localized thermal and/or mechanical stresses can cause

dry sliding since the silica layer is easily sheared, reduces the coefficient of friction and thus inhibits microfracture. Eventually, the surfaces may become smooth enough to enable hydrodynamic lubrication at very low sliding speeds and wear becomes negligible [27].

Most ceramics exhibit low thermal conductivity, diamond being the notable exception. Fracture due to thermal shock can thus occur as steep temperature gradients are developed in the surface due to frictional heating [28]. This mechanism is of particular importance in high-speed, dry sliding and/or high temperature applications. Winer and Ting [29] studied these aspects and proposed a thermomechanical wear model wherein fracture is caused by a combination of mechanical and thermal stresses and is influenced by the temperature-dependent mechanical properties of the ceramic.

It will be apparent from the preceding discussion that intergranular fracture and fracture on the scale of the ceramic grain size are most important under practical contact conditions. It is thus not unexpected that ceramic material microstructure and properties exert a strong influence on friction and wear. Ajayi and Ludema [30] found that the extent of damage and wear on a grain size scale was significantly different for ceramics such as silicon nitride, silicon carbide, alumina and zirconia due to the influence of microstructure. Nevertheless, macroscopic damage mechanisms such as transverse spalling were found to be similar for these ceramics, and therefore might still lend themselves to modelling based on fracture mechanics and friction theory considerations. Ajayi and Ludema [31] extended their work by showing that materials with weak grain boundaries (three different aluminas) were predominantly by grain pullout and so exhibited higher wear rates than a material with stronger grain boundaries (silicon carbide). Zum Gahr *et al* [32] demonstrated a strong influence of grain size on wear resistance for alumina and, to a lesser extent, for zirconia ceramics (Figure 2.3). Note also the vast difference in the behaviour of alumina in unidirectional *vs* reciprocating sliding. This demonstrates the relevance of the present work on engineering ceramics since most published studies were carried out on unidirectional pin-on-disc tribotest machines.

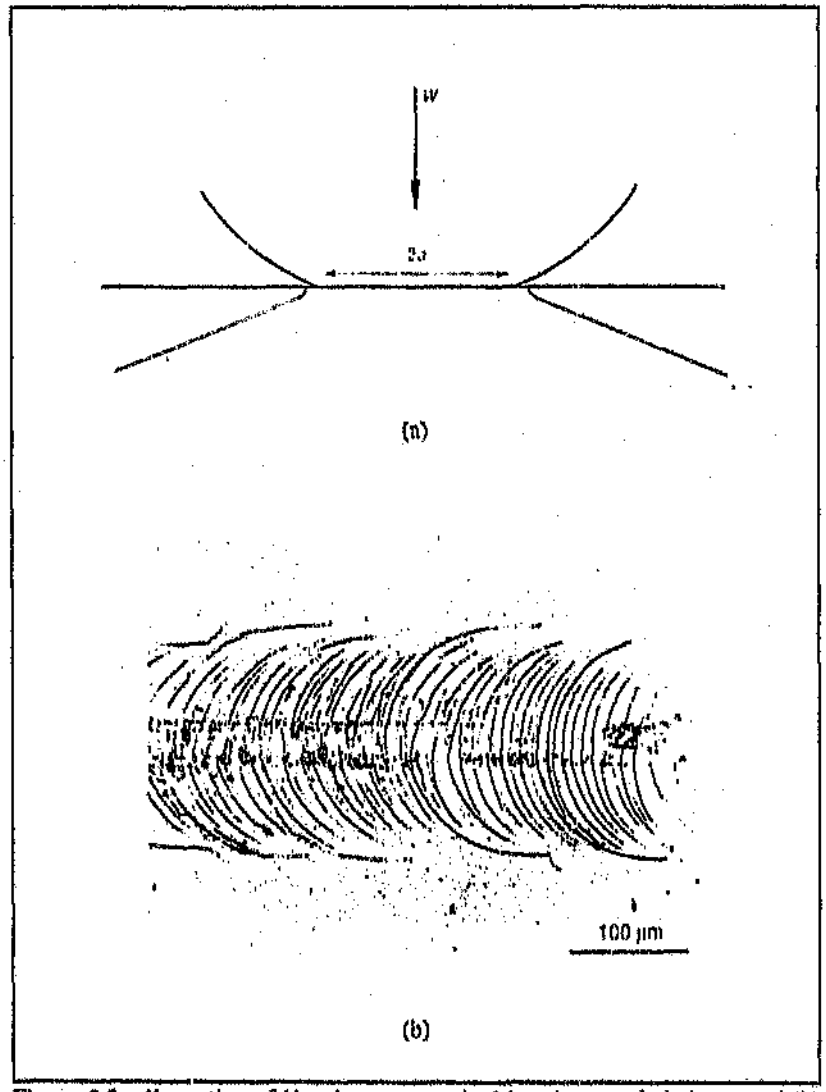

Figure 2.2: Formation of Hertzian cone cracks (a) under a static indenter and (b) during sliding, (as presented by Hutchings [15])

present work, since the stress ... are completely different.

Apart from plastic deformation and brittle fracture, ceramics can wear by tribochemical reactions or corrosion. For example, Si_3N_4 reacts with water to form silica and silica hydrates which are relatively soft and can be easily removed from the surface by mechanical action [26]. Nevertheless, the wear rate is generally reduced by this mechanism compared to

friction greater than 0.3, these stresses reach the surface of the ceramic where they reduce the fracture initiation stress, as mentioned previously, and promote fracture. Under these conditions, fracture is typically on a small scale and occurs along the grain boundaries, leading to the removal of individual ceramic grains and a roughening of the surface.

Under concentrated (counterformal) but elastic contacts below a blunt indenter, contact conditions are intermediate between the above two extremes, brittle fracture occurs on a larger scale and can be understood in terms of the Hertz elastic stress distribution. For a sphere pressing against a plane, it can be shown that the maximum tensile stress σ_{rmax} occurs at the surface and just at the edge of the circle of contact:

$$\sigma_{rmax} = (1 - 2\upsilon)\, p_{mean} \qquad (2.3)$$

where p_{mean} is the normal stress applied over the contact area and υ is Poisson's ratio. This tensile stress component causes a Hertzian cone crack to initiate and propagate when a certain critical normal load is exceeded (Figure 2.2(a)). The strong influence of friction on this critical fracture load was confirmed recently by Sliney [21] who demonstrated that ion-plated silver films lowered the coefficient of friction between diamond and alumina and thereby reduced fracture. When fracture does occur, it tends to appear in the form of arc-shaped cracks which intersect the contact surface transverse to the sliding direction (Figure 2.2(b)).

Other fracture mechanisms which have been observed include subsurface crack initiation and propagation [22][23] as well as the related fracture and fragmentation of the ceramic surface through fatigue [24][25]. These studies showed that fracture can occur at loads and stresses which are below the critical levels for spontaneous fracture by the initiation of cracks at material defects, such as pores, and/or by the progressive accumulation of dislocations in the material. Brookes and Parry [25] demonstrated that such mechanisms are active even when sliding under softer metal indenters. The fatigue mechanisms are dependent on the frequency of the applied stress cycles; this illustrates the importance of selecting the correct methodology in laboratory tests. Evidently, it will be dangerous to rely on data acquired from unidirectional pin-on-disc tests if a reciprocating component is being investigated, as in the

importance in metal-ceramic sliding systems. Such 'tribo-' or 'third body-' films can have a dramatic effect on ceramic friction and will be discussed in more detail in Section 2.2.4.

2.2.2 Fracture and wear

At least three basic particle detachment mechanisms can be distinguished for ceramics [16]: plastic deformation, brittle fracture and corrosion or wear by a 'tribochemical' mechanism. Brittle fracture undoubtedly leads to the highest wear rates and can thus be regarded as the most important mechanism.

The most severe contact conditions occur with rough sliding surfaces or sharp indenters (particles) where high localized loads and plastic deformation are experienced by the ceramic surface. Where the depth of deformation exceeds a critical value, vertical median vent cracks tend to form directly under the contact zone during the loading cycle [4]. Lateral cracks form during the unloading cycle, driven by residual stresses in the deformed zone beneath the contact, and these often extend beyond the contact zone. Evans, Lawn and Marshall [17][18] [19][20] studied these crack field intensively and suggested that material removal occurs when the radial cracks (or the median vent cracks) and the lateral cracks intersect to cause spalling. They proposed a model which relates the wear volume, V per unit sliding distance s to the fracture toughness K_c, hardness of the wearing surface H, elastic modulus E, and applied load P_n as follows:

$$V = P_n^{1.125} K_c^{-0.5} H^{-0.625} \left(\frac{E}{H}\right)^{0.8} s \qquad (2.2)$$

However, in most practical sliding systems, surfaces in contact tend to be conformal and smooth, for example sliding bushings and mechanical seal rings. Localized stresses tend to be low, the contact is characterized by elastic stress fields and the above model is not applicable. Nevertheless, as a result of friction at the interface, significant tensile stresses occur near the ceramic surface at the trailing edge of the contact [15]. At coefficients of

Under high applied loads or concentrated (counterformal) contacts, plastic deformation and fracture of the ceramic surface occurs, which results in roughening of the surface. Fracture provides an additional mechanism for the dissipation of energy, the contribution to friction by mechanical interlocking of asperities increases and thus the coefficient of friction increases, sometimes by a factor of four or more [9]. An example is shown in Figure 2.1 for a diamond indenter sliding on a single crystal of silicon carbide [14, 15] (a more detailed discussion on friction and wear transitions is provided in Section 2.2.3). It is important to note that fracture initiation is influenced by the tangential friction stress [8]. For coefficients of friction greater than 0.3, the maximum shear stress is located at the surface of the ceramic rather than below, which lowers the fracture initiation stress and promotes fracture.

Apart from fracture, the second important factor which governs ceramic friction is the formation of surface films by chemical reaction or material transfer. Non-oxide ceramics such as silicon carbide (SiC) and silicon nitride (Si_3N_4) are susceptible to oxidation when sliding in air while oxide ceramics such as alumina (Al_2O_3) and zirconia (ZrO_2) form hydrated surface films in the presence of water or water vapour [14, 15]. Material transfer and the compaction of loose wear debris on the sliding surfaces is commonly observed and is of particular

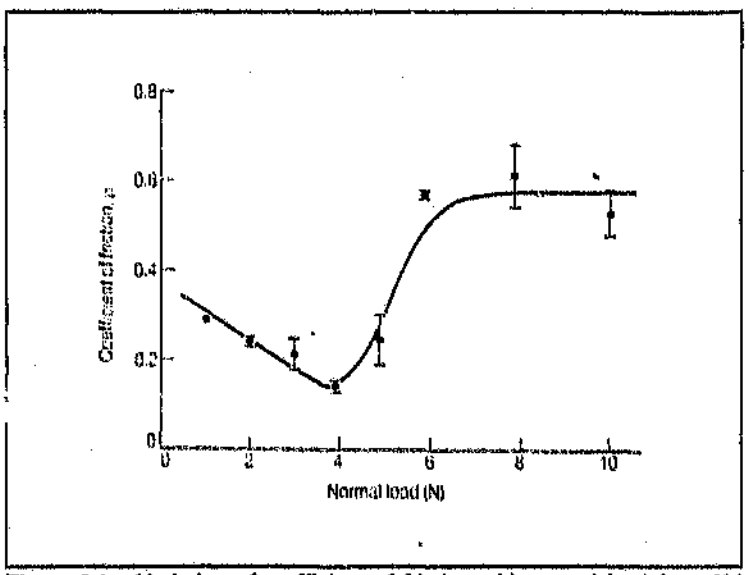

Figure 2.1: Variation of coefficient of friction with normal load for a 60° diamond cone sliding on a silicon carbide single crystal. (as presented by Hutchings [15])

2.2 Basic Concepts in Ceramic Friction and Wear

2.2.1 Sliding friction

Sliding friction in this context may be defined as the resistance to motion by one solid body over another. The friction force is usually proportional to the applied load, N:

$$F = \mu N \tag{2.1}$$

where the proportionality constant, μ, is the friction coefficient. Under sliding conditions, the frictional force must be overcome over the entire sliding distance. The resulting energy is dissipated as frictional heating of the sliding surfaces and through other processes such as surface deformation and fracture, which have recently been discussed in detail by Tabor [13].

There is now general agreement [10] that a number of microscopic mechanisms are responsible for generating friction, namely adhesion, mechanical interaction of surface asperities (interlocking), ploughing of asperities through the mating surface, deformation and/or fracture of surface and near surface layers, and interference and local plastic deformation as a result of trapped debris (third body effects [14]). The relative contributions by each mechanism to friction depends on the nature of the materials in contact, the applied loads and speeds, as well as the environment.

Ceramics, because of their high hardness, exhibit only very limited plastic flow at room temperature and thus the contribution to friction by plastic deformation is small under low applied loads. Moreover, the ionic or covalent nature of ceramic bonding limits adhesion between ceramics. In the absence of oxygen, the coefficients of friction for ceramics are thus lower than for comparable metal-metal contacts [15]. In unlubricated sliding in air, ceramics typically show friction coefficients between 0.25 and 0.8, which are comparable to those for metallic sliding couples separated by continuous metallic oxide films.

decades, very little published information is available on polycrystalline diamond composite materials (PCD). The low coefficient of friction and low wear rates of diamond make PCD materials attractive for use in highly loaded machine components in agressive environments, such as thrust bearings in down-hole motors which are used in drilling oil and gas wells. There is a strong need for an improved understanding of the tribological characteristics of PCD to facilitate the development of these and other sliding components.

Against this brief historical background, the present study focused on two aspects:

i. the generation of previously unavailable laboratory friction and wear data which can be used with confidence in the design and development of specific hydraulic mining equipment; and
ii. an improved understanding of the interrelationship between operating parameters, environment and friction and wear behaviour, particularly for PCD materials.

Being focused on specific industrial applications, namely reciprocating elements in hydraulic rockdrills and thrust bearings in down-hole motors, the study is limited to water-lubricated engineering ceramics sliding against AISI 440C stainless steel, as well as various polycrystalline diamond material couples in dry and water lubricated sliding contact.

In this chapter, published information on important aspects of the friction and wear of engineering ceramics and diamond, which relate to the work described in this thesis, is discussed.

layers, such as adsorbed films and transfer layers, in controlling friction and wear was soon confirmed. Good reviews on the state-of-the-science at this time were published by Cranmer in 1987 [8] and Buckley in 1989 [9]. Cranmer identified the following primary research needs [8]:

i. generation of labo : tory friction and wear data which is applicable to industrial applications;
ii. better characterization of the test materials, particularly the worn surfaces, to elucidate chemical surface effects and transfer layer formation, especially in metal-ceramic sliding contacts; and
iii. the development of new high-temperature lubricants for ceramics.

Despite efforts in these directions during the late 1980's and early 1990's, the friction and wear behaviour of ceramics remains relatively poorly understood, compared to metals [10]. There is no adequate unified theory which describes the relationship between friction, wear, operating conditions and environment. Reliable prediction of ceramic performance in field applications based on theoretical cor .iderations or laboratory tests is largely impossible, unless the essential conditions experienced in the field are closely matched in the laboratory tests. A further aspect to the problem is the poor reproducibility of many laboratory tribotests, as confirmed by recent round robin tests on metal-ceramic sliding couples carried out by various laboratories within the framework of the Versailles Project on Advanced Materials and Standards (VAMAS) [11][12].

As a result of the historical focus on internal combustion engines and aerospace applications, comparatively little information is available on water-lubricated metal-ceramic sliding systems. These are of interest in many applications, particularly in the mining industry, and thus one part of the present work examines such tribological couples in some detail.

The tribological knowledge base is considerably more patchy in the case of synthetic diamond materials. Although numerous basic studies on the friction and wear of natural diamond single crystals and polycrystalline synthetic diamond films have been carried out over the past

In the case of alumina, it is known that water can increase the extent of fracture by a stress-corrosion mechanism [46][94]. Where this is the dominant effect, the wear rate would clearly be expected to increase, as observed by Wallbridge *et al* [64, 82, 84, 89], Kapelski [87] and Scott [48]. However, it has been equally well documented that alumina is susceptible to hydrolysis [83, 84][95][96][97]. In the presence of liquid water or at relative humidity levels above approximately 20%, a more or less continuous film of aluminium hydroxide (boehmite, Al(OH)) is formed on the alumina surfaces. This could occur directly by reaction with the alumina surface itself or, and this is more plausible, indirectly through reaction between water and finely divided alumina wear debris. The imposed friction stress modifies the hydroxides to a layered structure which is easily sheared and is effective in reducing the friction coefficient and protecting the underlying surfaces from fracture and wear [98]. Where these effects override the stress corrosion effects, the friction coefficient and wear rate would be expected to decrease, as observed by Sasaki [83], Gates *et al* [84], Perez-Unzueta *et al* [; Takadoum [86] and Jeng *et al* [89].

The influence of water on the friction and wear behaviour of zirconia ceramics is poorly understood. It has been suggested that the presence of water reduces the surface energy and increases crack propagation rates, fracture and wear, analogous to alumina ceramics, although no direct evidence was provided [47][48]. Nevertheless, empirical evidence is now accumulating which appears to confirm that zirconia ceramics are susceptible to some kind of stress corrosion mechanism in water. On the other hand, Lancaster *et al* [99] recently observed a reduction in the wear rate of PSZ sliding in water and attributed this effect to tribochemical reactions. Once again, no direct evidence was provided to support this hypothesis and the possibility of formation of softer, lubricious layers on zirconia ceramics has yet to be proved [49].

Silicon based ceramics are much more reactive in water than alumina or zirconia ceramics. The formation of tribochemical surface films composed of SiO_2 or hydrated silicates on these materials has been confirmed by many investigators [100][101][102][103][104][105][106][107]. Furthermore, although the ceramics wear by microfracture at low and intermediate humidities, the crack propagation velocity in Si_3N_4, for example, remains unchanged with

Table 2.3: Summary of previous work on the effect of water or increasing relative humidity for various ceramic sliding couples

Combination	Test Configuration	Environment	Effect of water on		Reference
			Friction	Wear rate	
Al_2O_3/itself	Pin/disc	Varying rh	Decrease	Decrease	[83]
	4-ball	Water	Decrease	Decrease	[84]
	Pin/disc	"	"	Increase	[64]
	Pin/disc	Varying rh	Decrease	Decrease	[85]
	Pin/disc	"	Decrease	Decrease	[86]
	Ball/disc	"	Increase	Increase	[87], as referenced in [88]
	Ball/plate (reciprocating)	Water	Decrease	Decrease	[89]
	Pin/plate (reciprocating)	"	"	Increase	[48]
Si_3N_4/itself	Pin/disc	Varying rh	Decrease	Decrease	[83]
	Pin/disc	Water	Decrease	Decrease	[90]
	Pin/disc	Water	Unchanged	Decrease	[26]
SiC/itself	Pin/disc	Varying rh	Decrease	Decrease	[83]
	Fretting	"	Decrease	Decrease	[91]
ZrO_2/itself	Pin/disc	Varying rh	Increase	Increase	[41]
	Fretting	"	Unchanged	Decrease	[92]
	Pin/plate	Water	Increase	Increase	[48]
	Pin/ring	"	Decrease	Increase	[45]

iv. the alteration of the deformation properties of the surface layers of the materials (chemomechanical effects).

When present as a liquid, water may flush debris out of the sliding interface and thus impede the formation of third-body films. There appears to be general agreement that this results in an increase in wear rate but a decrease in friction coefficient [93]. Wear rates will also increase if surface fracture increases due to a stress-corrosion effect. On the other hand, tribochemical reactions between water and the ceramic surface or the wear debris may result in the formation of more tenacious protective surface films with a concomitant decrease in wear rate.

ceramic, followed by the progressive agglomeration and densification of these particles into small cylinders by a rolling action. The cylindrical debris particles are usually oriented transverse to the rolling direction and may thus provide an additional, low resistance mechanism of velocity accommodation across the contact by acting like miniature roller bearings. Indeed, the presence of these particles has been associated with a significant drop in friction coefficient [78].

There appears to be general agreement in the literature that the presence of well-developed third-body surface layers which exhibit load carrying capacity is beneficial in reducing the wear rate of the first bodies [79]. However, the influence of such layers on the friction coefficient appears to depend both on the nature of the film and the location and mode of velocity accommodation across the interface. Clearly, friction coefficients may be expected to drop if the third-body film is mechanically weak and velocity accommodation occurs by shear across the third body. On the other hand, well-developed 'beds' of debris on the sliding surfaces are often associated with significant increases in friction coefficient, probably as a result of ploughing and abrasion effects [79][80]. Velocity accommodation sites and mechanisms have recently been discussed in more detail by Alexeyev [81] and Berthier [82].

Tribochemical effects - the influence of water

It has become clear that most engineering ceramics are prone to tribochemical reactions or modifications of their surface mechanical properties under the influence of adsorption and other mechanisms. However, there is considerable disagreement in the literature concerning the influence of water on friction and wear compared to dry sliding, as illustrated in Table 2.3.

These ambiguities may be explained in terms of the influence of water on:

i. debris agglomeration and the formation of third-body surface films;
ii. the formation or changes in the structure of tribochemical surface films;
iii. the extent of crack growth and fracture; and

suggests that they may be effective in reducing friction and wear.

Table 2.2: Microhardness of tribofilms and lapped parent surfaces on several ceramics, along with bulk and contact temperatures (°C)

Material	Hardness ($HV_{0.01}$)		Bulk temperature	Contact temperature
	Lapped surface	Tribofilm		
Alumina	2 200 ± 100	-	210	1350 - 1450
WRA	2 500 ± 100	1 750 ± 150	215	T > 1450
SiC	3 100 ± 150	800 ± 150	195	T > 1100
SiSiC	2 600 ± 150	1750 ± 150	200	T > 1100

Third-body films form in a somewhat different way on silicon based ceramics. It is well-known that silicon nitride and silicon carbide oxidize easily at high temperatures [74][75][76]:

$$Si_3N_4 + 3\ O_2 \Rightarrow 3\ SiO_2 + 2\ N_2 \qquad (2.5)$$

Tribofilms on these materials are therefore usually composed of silica (SiO_2), which is formed by direct oxidation of the ceramic surface. Similarly, film formation on sialon involves chemical reaction of the surface combined with mechanical shear to form a homogeneous film comprising fine, crystalline sialon fragments in a silica matrix, which is usually amorphous [72]. Despite the fact that tribochemical reactions play a much more prominent rôle than mechanical comminution and compaction of wear debris, the TTA is applicable to tribofilms formed on these ceramics in the sense that the films also display load carrying capacity and are able to accommodate the sliding velocity through plastic deformation or internal shear mechanisms.

It has also been well documented that cylindrical wear debris is generated on silicon-based ceramics which are subjected to reciprocating motion [77][78]. The likely mechanism of formation involves the detachment of small particles from the silica surface layer on the

forces are involved in the agglomeration and attachment process and that these forces are sufficiently strong to prevent the tribofilm from being removed during sliding contact. Pursuing this argument and based on extensive studies of alumina, zirconia, silicon nitride and silicon carbide in dry sliding, they suggested that the nature of the tribofilms depends on the bonding type of the ceramic (Figure 2.10). For two ionically bonded ceramics sliding together (e.g. alumina or zirconia), continuous and adherent films are generally formed because the van der Waals forces are strong in such couples. On the other hand, these forces are relatively weak in the case of covalently bonded ceramics, such as silicon nitride or silicon carbide, and thus no distinct films or only individual particle reattachment are observed. Patchy tribofilms occur when combinations of ionic and covalent materials are in sliding contact.

Blomberg *et al* [70] attempted to characterize the mechanical properties of tribofilms formed on alumina, whisker reinforced alumina (WRA), and two silicon carbides by microhardness indentation methods. Although the porous film on alumina could not be evaluated, the remaining films exhibited hardnesses significantly lower than those of the parent surfaces (Table 2.2). The indentations were associated with plastic flow of the tribofilms, which

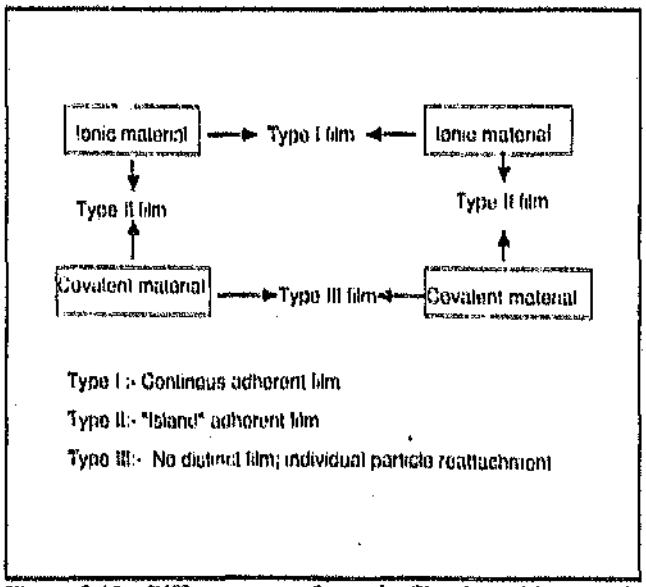

Figure 2.10: Different types of transfer film formed by ceramic sliding couples. (after Ajayi and Ludema [73])

i. detachment of wear debris from the two 'first bodies' which are in contact (e.g. by fracture or delamination);

ii. entrapment of some proportion of the wear debris within the contact zone; and

iii. the gradual filling of surface valleys (Abbot's volume) with debris. When Abbot's volume is full, the debris spills over onto the sliding surfaces and separates them. At this point, a third-body interfacial layer is formed which is associated with a certain load carrying capacity.

The central argument in the third-body approach is that debris particles entrapped in the contact zone are 'transported' at velocities which differ from particle to particle and are not necessarily parallel to the imposed sliding direction. The sliding velocity between the first bodies can thus be accommodated across the thickness of the third body (or interfacial layer) by these velocity gradients. Therefore, it should be possible to describe the friction and wear behaviour of materials in terms of the rheological properties of the third body, analogous to lubrication theory. Unfortunately, no suitable technique exists to measure the rheological properties of third-body films directly, and so recent studies have focused on elucidating their structure and likely mechanical properties.

Blomberg and coworkers [70][71][72] demonstrated that tribofilms formed on unreinforced alumina in dry sliding consist of small alumina fragments, typically 10 - 100 nm in diameter. These fragments comprised α-alumina crystals and did not undergo any phase change during formation. The films were porous, poorly adherent and, in agreement with the TBA, appeared to have been formed by mechanical fracture of the alumina surface, followed by milling and compaction of the wear particles. No binder phase was detected and the films were described as either 'well-sintered' through the thermomechanical interaction of high contact pressures and temperatures, or more loosely adherent and forming a particle bed on the underlying surface.

In contrast, Ajayi and Ludema [73] suggested that the driving force for debris agglomeration is the high surface energy of the small particles, which is reduced when particles bind to a surface or to each other. They went on to show that van der Waals and electrostatic attractive

studies should endeavour to identify friction and wear transitions which may be important to the particular application. Where relevant, these could be presented in the form of simple two-dimensional transition diagrams such as graphs of wear or friction against applied load, depending on which is considered the more important. Due consideration was given to transition phenomena in the present work.

2.2.4 Surface film formation and environmental effects

So far it has become clear that wear of ceramics is a complex phenomenon which does not lend itself to simple modelling. From the preceding sections, it would appear that apart from fracture, the formation of third-body interfacial films and tribochemical effects critically influence friction and wear. Through such mechanisms, the environment (i.e. lubricant presence and composition, temperature) exerts a strong influence on tribological behaviour by shifting the location of friction and wear transitions. It is thus relevant to discuss the rôle of third body films and tribochemistry in more detail for alumina, zirconia and silicon-based ceramics which are of interest in the present work.

Wear debris and the formation of third-body layers

Third-body interfacial layers composed of compacted wear debris have been observed in numerous studies on alumina [61][62][63][64] and zirconia [42][47][65][66][67][68][69] under unlubricated sliding conditions. In all cases, the friction and wear behaviour of the ceramics was explained in terms of the formation and removal of these layers. (As discussed previously, however, the behaviour of zirconia ceramics is complicated by phase transformations in the near-surface regions).

Godet [14] realized that the mechanical action of wear debris in the contact zone - one factor which is common to different materials in different types of sliding contact. In an attempt to rationalize these aspects, he developed the 'third-body approach' (TBA) to wear. He distinguished three stages in the formation of third-body interfacial layers:

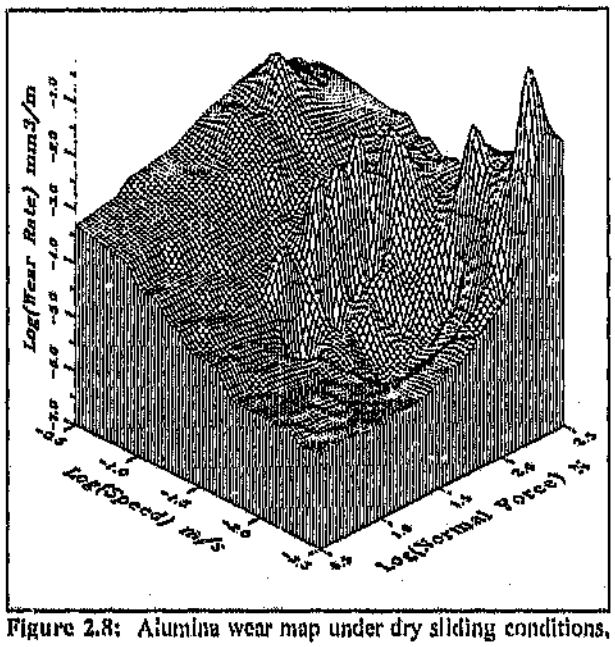

Figure 2.8: Alumina wear map under dry sliding conditions, determined using a step loading test procedure. (after Hsu *et al* [55])

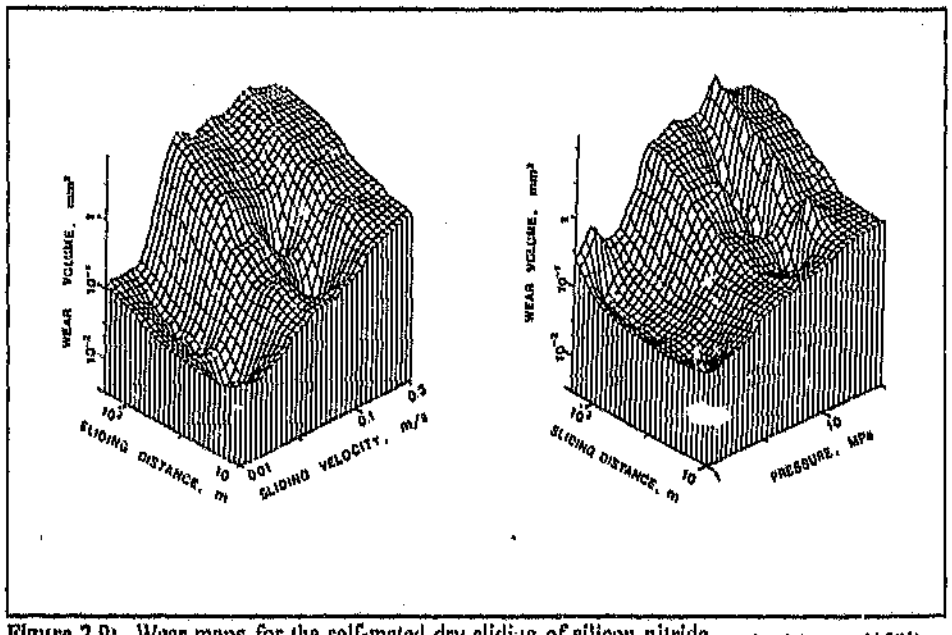

Figure 2.9: Wear maps for the self-mated dry sliding of silicon nitride. (after Lim *et al* [59])

In an attempt to visualize tribological transitions and the complex interrelationships between operational variables and friction and wear rates, the concept of 'wear mapping' was developed. Wear maps or transition diagrams were originally referred to by Tabor [53], who attributed the idea to Johnson, and essentially represent three-dimensional plots of wear rates against combinations of operational parameters such as load, speed and sliding distance over a wide spectrum of tribological conditions. They are generated for particular material couples and are useful to the design engineer for the identification of critical operating limits.

For the construction of wear maps, the independent variable of the tribosystem are classified into continuous variables (load, speed, temperature and time) and discrete variables (material, lubricant, environment, contaminants) with wear rate being the dependent variable. According to Hsu *et al* [55], five three-dimensional wear maps can be drawn for each allowed combination of discrete variables, namely graphs of wear against (i) speed and load, (ii) speed and temperature, (iii) speed and time, (iv) load and temperature, and (v) load and time. The complete set of maps then fully describes the tribological characteristics of the system.

This illustrates a key weakness of wear maps, namely their requirement for vast amounts of data. With the traditional tribotesting approach, each data point on the map represents one test at a particular set of experimental conditions; thus the generation of wear maps with an adequate resolution becomes extremely time-consuming and expensive. Hsu *et al* [55][57][58] recognized this and developed a step loading technique, using a unidirectional pin-on-disc test machine, in order to generate data faster. They demostrated the technique by deriving wear maps for alumina (an example is shown in Figure 2.8). Recently, wear maps for self-mated silicon nitride under dry sliding conditions were also published by Lim *et al* [59] (Figure 2.9) and Dong and Jahanmir [60] but these were constructed using traditional methods.

In summary, it must be concluded that three-dimensional wear maps for ceramics have not yet been developed to a level where they can be widely used. Few are currently available and, since they are time-consuming and expensive to generate, selected laboratory studies such as the one described in this thesis will be required for some time to come to obtain the data and understanding required by specific applications. It is equally evident, however, that such

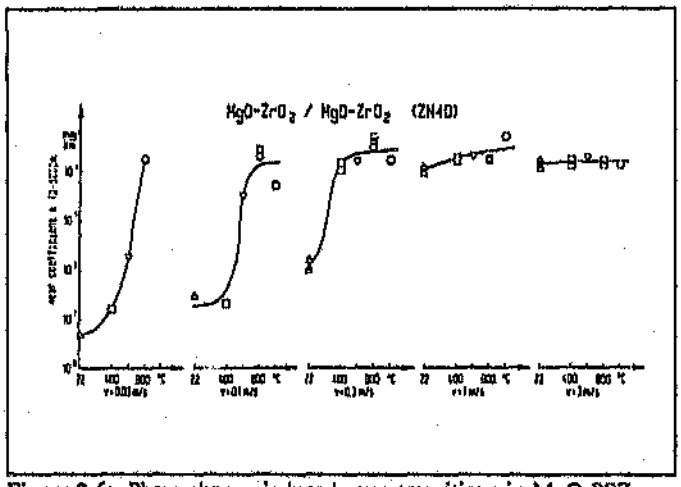

Figure 2.6: Phase-change induced wear transitions in MgO-PSZ as a function of sliding speed and ambient temperature. (after Woydt *et al* [56])

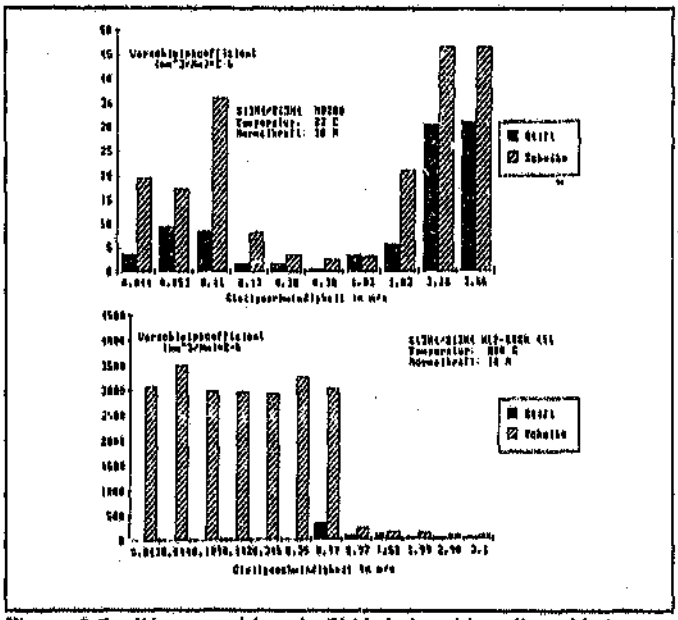

Figure 2.7: Wear transitions in Si_3N_4 induced by tribooxidation. (after Woydt *et al* [56])

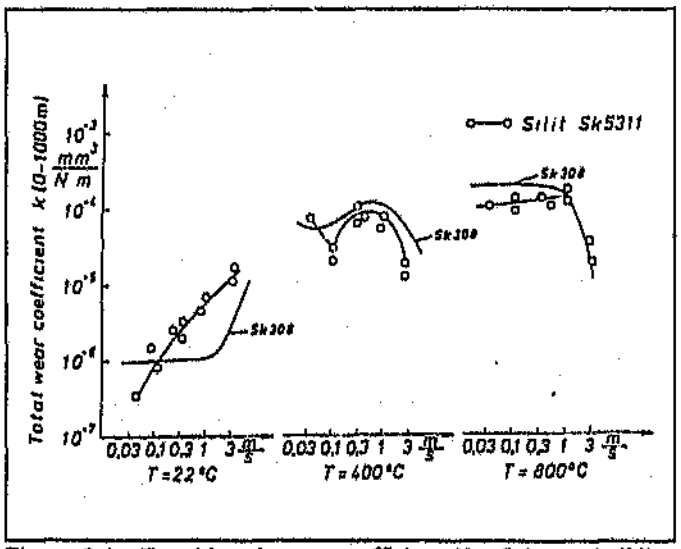

Figure 2.4: Transitions in wear coefficient, K, of the total sliding system for self-mated Si-SiC under unlubricated sliding. (after Woydt *et al* [56])

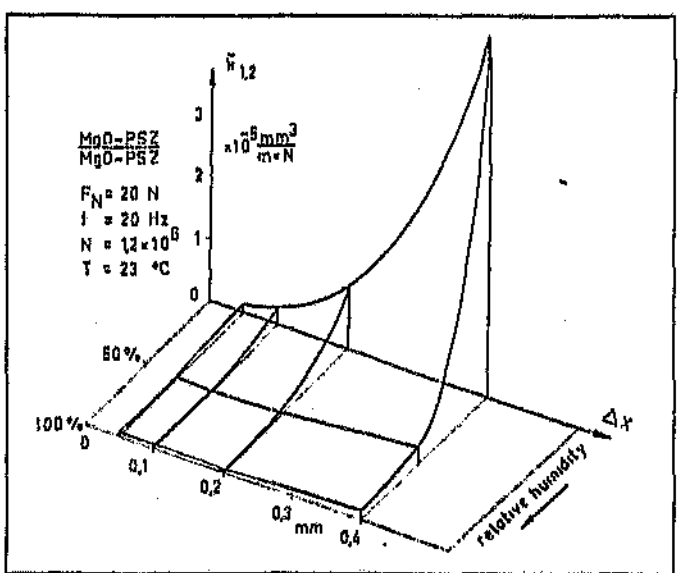

Figure 2.5: Humidity- and stroke length-dependent wear transitions for self-mated MgO-PSZ under unlubricated fretting. (after Woydt *et al* [56])

Analogous to metals in sliding contact, wear transitions in ceramics are characterized by sharp changes in wear rate with changes in load, sliding speed, or environmental conditions (temperature, lubricant composition, etc.). Mild wear is typically characterized by smooth sliding surfaces and low friction forces and wear mechanisms are dominated by plastic deformation or tribochemical reactions, leading to low wear rates. In severe wear regimes, ceramic surfaces are roughened, friction coefficients are higher and wear mechanisms are dominated by brittle fracture, leading to higher wear rates. The dimensionless wear coefficient K typically varies between 10^{-4} and 10^{-2} in the severe wear regime and is two or more orders of magnitude lower in the mild wear regime [15]. The variations in the data reported in Table 2.1 may thus be attributed to wear rate transitions and illustrate the difficulty associated with extrapolating ceramic performance for a particular application from even a relatively large body of literature data.

Woydt *et al* [56] have investigated transition phenomena extensively and recently classified transitions as follows (note that in all diagrams referred to here, the *volumetric* wear coefficient k is used, rather than the dimensionless wear coefficient):

i. stress-induced surface fatigue transitions, for example Si-SiC materials sliding under unlubricated conditions (Figure 2.4);
ii. humidity-dependent transitions resulting from the mechanical and chemical formation of third body surface layers, for example fretting of MgO - partially stabilized zirconia (MgO-PSZ), (Figure 2.5);
iii. transitions induced by temperature- and pressure-dependent phase transformations of the ceramic microstructure, typified by the unlubricated sliding of MgO-PSZ pairs at different temperatures and sliding speeds (Figure 2.6); and
iv. transitions induced by tribooxidation, which may cause increased or decreased wear: for example, the formation of Si-O-N surface layers on silicon nitride pairs in unlubricated sliding (Figure 2.7).

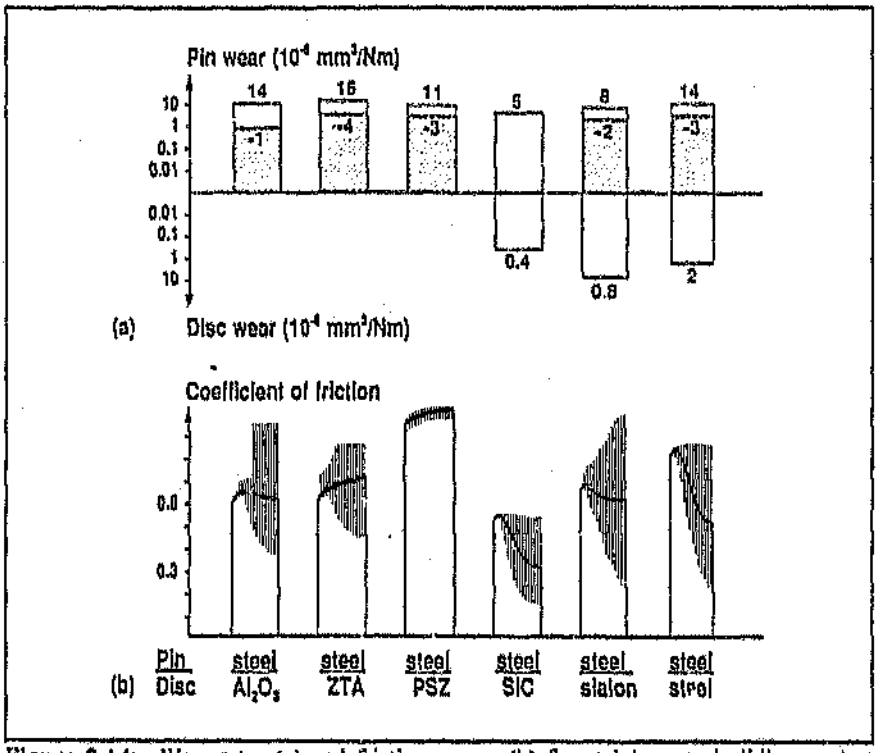

Figure 2.14: Wear rates (a) and friction curves (b) for stainless steel sliding against ceramics and itself under 10 N load and 0,1 m/s velocity in water. Transfer layer formation on the ceramic discs is represented by shadowed columns in (a). The friction curves represent 2500 m of sliding and the shadowed areas represent their amplitudes. (after Andersson *et al* [148])

it is clear that the precise characteristics, mechanisms of formation and rôle of such layers are not adequately understood yet.

Where the ceramic surface is not adequately protected by a transfer layer, chemically-assisted damage to the ceramic has been reported, leading to increased wear rates. For example, He *et al* [150] showed that zirconia ceramics are less resistant to wear in water and surmised that this may be the result of water-assisted phase transformation and fracture. Yang and Bahadur [151] studied the behaviour of alumina-based ceramics against tool steel and found that, in the absence of a well-developed transfer layer, the alumina suffered stress-corrosion damage.

The chemical interaction between steels and silicon-based ceramics is less strong than for oxide ceramics, leading to very little transfer layer formation [148]. As in unlubricated

to increase significantly with increasing humidity in the case of Ti and Al. The effect was attributed to enhanced oxidation of the metal surfaces at higher humidities, which increases adhesion between the ceramic and metal oxides. Nevertheless, the lubricating effect of adsorbed water vapour was confirmed in experiments with Ag sliders.

In broad agreement with these basic studies, Papaphilippou *et al* [145] showed that the friction and wear behaviour of ductile cast iron against alumina is dominated by an oxidational wear mechanism. At low humidity levels (25% RH), the interfacial wear debris contained significant amounts of metallic debris and wear coefficients were high due to abrasive wear. With increasing humidity levels up to 80% RH, both the friction and the wear coefficients decreased significantly, which was attributed to more extensive oxidation and better protection of the wear surfaces. The effect was more pronounced at low sliding velocities while for high velocities (0,6 - 0,7 m/s), humidity had only a slight effect on the wear coefficient.

When used as a liquid lubricant, it has been shown that water is not effective in preventing tribological phenomena such as material transfer and tribochemical reactions, which have been described in previous sections of this review [146][147][148]. In the case of oxide ceramics sliding against hardened or stainless steels, the formation of ferrous transfer layers is commonly observed which often resemble those observed under unlubricated conditions [148][149]. Typical friction and wear results obtained by Andersson and co-workers [148] for stainless steel sliding on a variety of engineering ceramics are summarized in Figure 2.14.

In contrast with this earlier work, He *et al* [150] very recently found that copious transfer of hardened steel (AISI 5200) to form thick and relatively continuous transfer layers only occurred on zirconia-toughened alumina (ZTA), but very little transfer occurred on zirconia ceramics (TZP). They also found that the coefficient of friction for the steel-alumina couples was a factor of 2 higher than that of the steel-zirconia couples.

Despite these ambiguities, there is fairly good agreement in the literature that metallic transfer layers are effective in protecting the underlying ceramic surface and reducing damage to the ceramic, although their presence may result in higher coefficients of friction. Nevertheless,

the rates of these two processes become comparable, whereas stable friction coefficients are observed when either of the two processes are dominant.

In the case of Si_3N_4 sliding against steel, the formation of a SiO_2 transfer layer on the steel surface has been reported [116][140] and the friction and wear behaviour is dominated by tribochemical effects, analogous to self-mated Si_3N_4.

The influence of humidity and water lubrication

It is evident from the preceding discussion that metal transfer to the ceramic surface appears to occur by interfacial bond formation, followed by rupture of cohesive bonds in the metal. This model is supported by the work of Takadoum *et al* [141][142], who studied pure Cu, Ni, Ti and Al in sliding contact with Al_2O_3, Si_3N_4 and PSZ, and demonstrated that the magnitude of the coefficient of friction and the extent of metal transfer is related to the oxidation activity of the metal. In the case of copper-ceramics and nickel-ceramics systems, increasing relative humidity in the range of 20% to 90% resulted in a significant decrease in the measured coefficients of friction. In contrast, the relative humidity level had no significant effect in the case of the chemically more reactive aluminium and titanium, where the coefficient of friction was found to be constant at ~0,60 and ~0,80 respectively. Takadoum *et al* speculated that the reduction in friction coefficient for copper- and nickel-ceramics systems is related to the lubricating effect of an adsorbed water vapour film. More active metals, they argue, are covered with more stable oxides and the adhesion of this water vapour film is reduced, resulting in much lower sensitivity to increasing humidity levels.

Similar results were obtained by Demizu *et al* [143][144], who found the friction coefficients of pure metals against Al_2O_3, ZrO_2 (TZP), SiC and Si_3N_4 to correlate strongly with the Gibbs free energy of ionization of the metals, particularly in very humid air (90% RH); that is, the more active metals showed higher coefficients of friction. For metals such as Cu, Ni, Fe and Cr, which are relatively unreactive compared to Ti and Al, the friction coefficient decreased slightly or was not greatly influenced by increasing humidity in the range 10% to 90% RH. However, in contrast with the findings of Takadoum *et al*, the friction coefficient was seen

2.3.3 Surface film formation and environmental effects

Analogous to ceramic/ceramic sliding couples, material transfer and other third-body effects such as interfacial oxide layer formation also occur in metal/ceramic sliding systems and, as indicated in Figure 2.12, play a fundamental rôle in controlling friction and wear. The basic mechanisms of third-body formation and their influence on tribological characteristics have been described in Section 2.2.4 and are broadly similar for metal/ceramic sliding.

Dry sliding

In sliding against oxide ceramics such as Al_2O_3 and ZrO_2, metal is commonly transferred to the ceramic surface to form a more or less continuous third-body layer [45][68][115][134] [135][136]. When sliding against ferrous alloys, the transfer layer is mainly composed of iron oxides and adheres firmly to the ceramic substrate [119][137]. There appears to be general agreement in the literature that such transfer films prevent direct metal-ceramic contact and thus dominate the friction behaviour of the sliding couples and protect the underlying ceramic from further damage. In the case of ductile and grey cast iron, it has been shown that graphite from the cast iron can act as a solid lubricant at the interface and lead to a further reduction in ceramic wear rate [138].

In view of the strong adhesion between the metallic transfer films and the ceramic substrates, most investigators have attributed the formation of the films to chemical interaction between the metal and the ceramic. Zhou *et al* [115] recently studied the unlubricated unidirectional sliding wear behaviour of high chromium cast iron with various matrices against Al_2O_3 and ZrO_2, and confirmed that the extent of metallic transfer film formation was related to the adhesive energy between the ceramics and the cast irons. Direct evidence for chemical interaction between Al_2O_3 and EN24 steel was provided by Ravikiran and Pramila Bai [139], with metal transfer and iron oxide formation at low sliding speeds and the formation of a spinel-type solid solution between iron oxide and alumina at high speeds. Furthermore, these investigators attributed observed oscillations in the friction coefficient to the competing processes of transfer layer formation and depletion. They argued that oscillations occur when

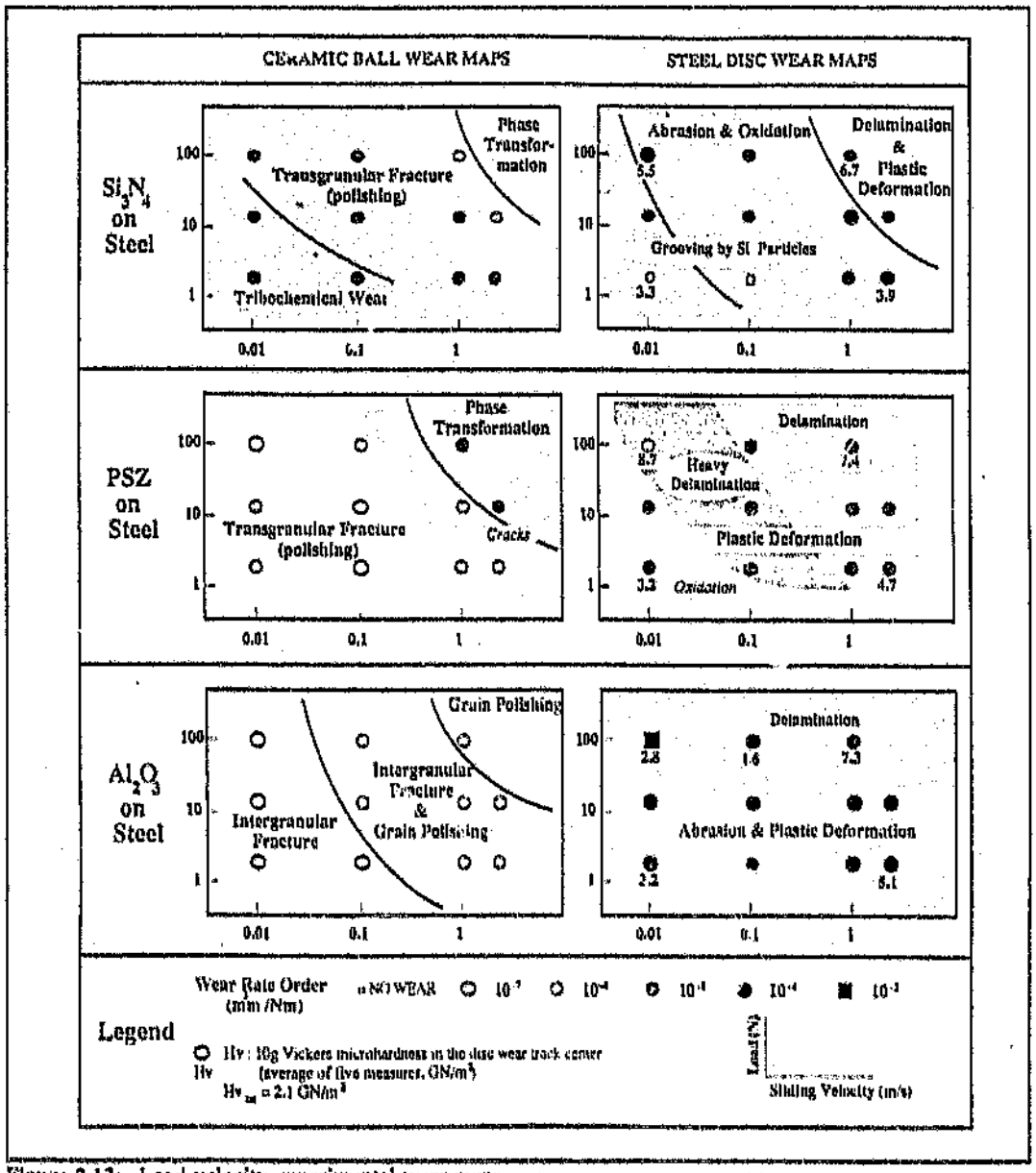

Figure 2.13: Load-velocity experimental wear maps (after Gautier and Kato [133])

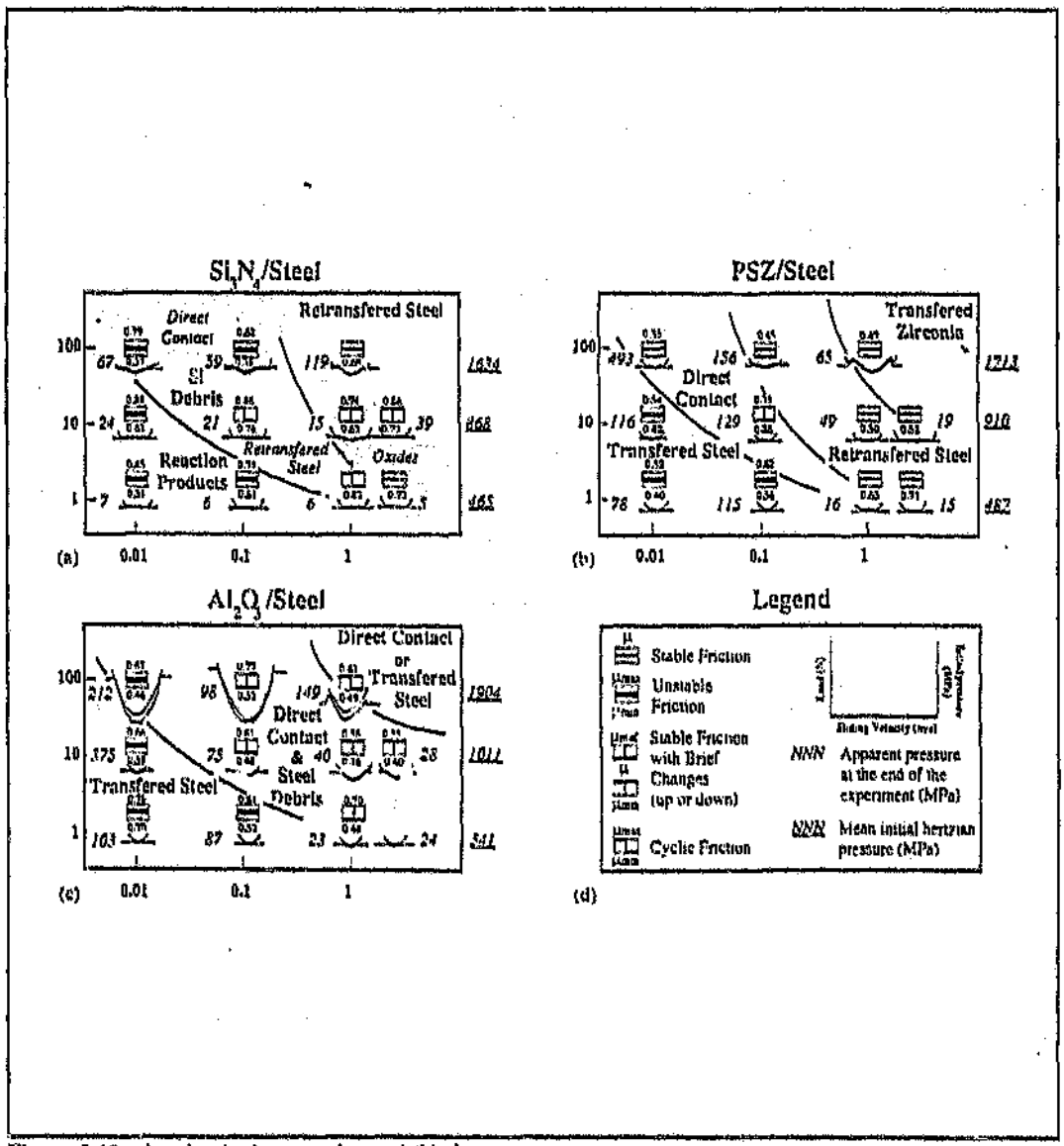

Figure 2.12: Load-velocity experimental friction maps (after Gautier and Kato [133])

wear mechanism map for different ceramics, such as that derived by Lim and Ashby [132] for steel/steel wear (Figure 2.11).

This complexity is demonstrated by the load-velocity friction and wear maps developed by Gautier and Kato [133] for alumina, PSZ and Si_3N_4 in unlubricated, unidirectional sliding against steel. The maps provide an excellent summary of typical friction and wear data for these sliding systems and are shown in Figures 2.12 and 2.13.

Referring to Figure 2.12, it will be seen that the coefficient of friction is rarely stable for any of the sliding systems throughout the test period. It is therefore meaningless to quote a single coefficient of friction for a particular metal/ceramic sliding system. Nevertheless, there appears to be a general trend towards increasing stability with increasing sliding speed and applied load. This may be related to the formation of thicker, more well-developed transfer layers under these conditions, or the occurrence of direct contact between the substrate materials. The interfacial material properties and contact conditions may thus be more stable and well-defined, leading to more stable friction coefficients.

The friction and wear maps reveal a further important characteristic, namely that lower coefficients of friction are not necessarily associated with lower wear rates. In fact, particularly the Si_3N_4- and PSZ-steel couples exhibit generally lower friction coefficients at higher sliding speeds and applied loads, where increased overall wear rates are experienced.

Gautier and Kato [133] compared their results to data published previously in the open literature and found general agreement. They further demonstrated that a linear relationship appears to exist between the wear rate of the ceramic or the steel sliding partner and the term μWv, where μ is the coefficient of friction, W the applied load and v the sliding velocity. This term represents the frictional energy generated at the sliding interface, which controls the growth rate of interfacial oxides and the onset of softening and melting.

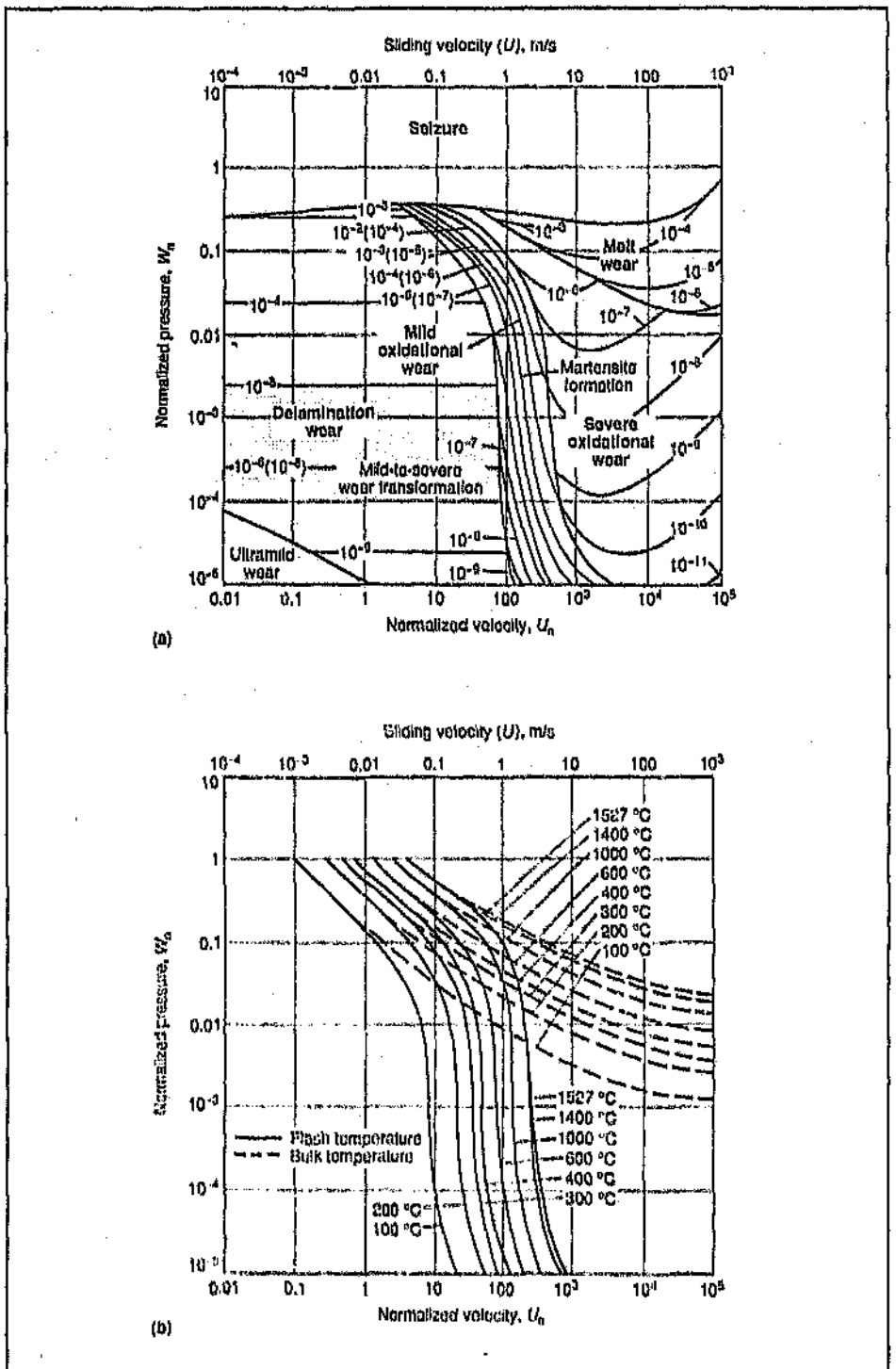

Figure 2.11: (a) Pressure-velocity wear map for steel pairs in unidirectional, unlubricated sliding; and (b) temperature map for similar steel pairs sliding under similar conditions. (after Lim and Ashby [132])

Lim and Ashby [132] developed a wear mechanism map for steel-on-steel wear in unidirectional, unlubricated sliding which illustrates the different wear regimes as a function of sliding speed and applied load (Figure 2.11). They also found that the severity of wear and the boundaries between wear regimes correlate well with the general surface and contact flash temperatures expected at particular values of load and speed (Figure 2.11 (b)). Although limited in that it applies only to a pin-on-disc system, this map is very useful to engineers in predicting the likely wear mode of a particular steel-steel sliding system.

The wear mechanisms described above are fundamentally controlled by the energy dissipation at the interface (which depends on the sliding speed, the applied load and the friction coefficient) and thus also occur in metal-ceramic sliding systems.

Abrasive wear of the metallic counterbody by the ceramic asperities has also been reported, for example in steel/alumina and steel/silicon nitride systems [133][117]. This is not unexpected in view of the high hardness of the ceramics compared to steels and other alloys. However, the mechanism appears to be relevant only where the ceramic surfaces are rough (e.g. ground) and contact loads are relatively low. Moreover, most ceramics tend to show improvements in surface roughness with increasing sliding distance, unless significant surface fracture occurs, by mechanisms such as plastic deformation and tribochemical reaction. Together with the rapid formation of metallic transfer layers on most ceramics (see Section 2.3.3), which may be accelerated by abrasion, this effect will tend to limit abrasive damage on the metallic counterface to the early run-in stages of sliding contact.

<u>Friction and wear data</u>

Metal/ceramic sliding pairs are susceptible to transitions in friction and wear rate, analogous to metal/metal and ceramic/ceramic sliding systems, which are a function of the sliding conditions. It is clear from the preceding discussions, however, that the wear of ceramics also strongly depends on the material characteristics of the ceramic itself (chemical nature, fabrication route, mechanical properties, etc.), and is probably more complex than metallic wear. It would therefore seem difficult if not impossible to derive a single pressure-velocity

combinations of high sliding speed (~ 0,5 m/s or more) and applied load (~ ≥ 30 N in a pin-on-disc or ball-on-disc test). Examples include spalling of a transformed surface layer in zirconia ceramics as well as surface microfracture of alumina ceramics [114][115]. Analogous to ceramic-ceramic wear, the extent of surface fracture appears to decrease with increasing ceramic fracture toughness.

For silicon-based ceramics sliding against metals, the dominant wear mechanism at lower sliding speeds is tribooxidation, as discussed before [116][117][118]. At higher speeds and applied loads, localised fracture is observed on the surfaces of silicon nitride [119] and silicon carbide [120], which results in an increase in friction coefficient and wear rate.

In addition to the established mechanisms described above, a few investigators observed abrasive wear on zirconia ceramics [121] and silicon nitride [122]. It is thought that this is attributable to ceramic wear debris particles which move through the sliding interface or become embedded in the metal counterface. Nevertheless, the other wear mechanisms are usually dominant.

Metallic counterbody wear

Under most practical contact conditions, the unlubricated wear of metals is dominated by two primary mechanisms. Firstly, oxidational wear occurs where the real contact areas of the metals are covered by a protective oxide film, typically 3 - 4 μm thick, from which wear particles are detached during sliding [123][124][125][126][127]. The mechanism is associated with little subsurface plastic deformation and low wear rates and typically occurs at combinations of relatively low applied loads and sliding speeds or low loads and high speeds. As sliding conditions become more severe (e.g. high loads/ high speeds or high loads/ low speeds), a transition occurs to plasticity-controlled wear mechanisms which are characterised by severe subsurface plastic deformation and high wear rates. Material loss then occurs by asperity adhesion and shear [15], nucleation and growth of subsurface cracks leading to delamination wear [128][129][130][131], and various forms of surface fatigue.

hydraulic cycle of a water-powered rockdrill. While it is relatively straightforward to replace the steel reciprocating spool with a ceramic component, it is presently not cost effective to do so in the case of the spool housing because of its complex shape.

The following sections describe previous published work on the friction and wear characteristics of metal-ceramic sliding couples. Emphasis is placed on highlighting similarities and differences compared to ceramic-ceramic systems. In addition, some key friction and wear data are presented.

2.3.2 Friction and Wear

Ceramic counterbody wear

As described earlier, material loss and wear of engineering ceramics occurs mainly by tribochemical reactions (for non-oxide ceramics), fracture and, to a lesser extent, by plastic deformation. Tribochemical reactions are dependent on the environment while the latter mechanisms are controlled by the stresses which are generated in the ceramic surface during sliding. Environmental parameters are largely independent of the counterface material composition, while the stress state in the sliding elements is a function of the applied load and sliding speed. It is thus not surprising that these fundamental ceramic wear mechanisms occur in metal-ceramic sliding couples as well.

Nevertheless, the stress distribution in the ceramic is a function of the mechanical properties of the counterface material. It will be readily appreciated that the surface asperities on softer metallic materials will deform plastically when loaded against a hard ceramic surface. The applied load is thus distributed more effectively than in the case of ceramic counterbodies, which results in less concentrated contacts and lower stresses in the mating ceramic surfaces. As might be expected, many investigators thus reported no damage or only polishing and very mild wear of the ceramic element (e.g. unlubricated sliding of alumina against tool steel [113] and zirconia ceramics against BS.970:1991 826M40 (EN26) steel, brass and cast iron [68]). Significant damage and surface fracture is typically only observed under severe sliding conditions, which occur at

increasing humidity [108]. The tribochemical formation of protective surface films is thus the dominant effect in all cases, which explains the more consistent results obtained for these ceramics.

Nevertheless, some instabilities in friction and wear coefficients can occur. Very recent work by Takadoum *et al* [109] demonstrated that protective hydrated silica films are formed by aggregation of wear debris, rather than by direct oxidation of the ceramic surfaces (i.e. the mechanism follows the third body approach discussed earlier). As might be expected, the friction coefficient and wear rate were seen to increase significantly when the wear debris was continually removed from the interface. These findings are in agreement with and explain results from earlier work by Yamamoto and Ura [110]. In reciprocating sliding, much of the protective film is removed during each stroke and unless the film can be re-formed rapidly enough, friction and wear coefficients increase [111]. A further source of instability has been reported very recently by Andersson and Blomberg [112] who showed that silicon monoxide (SiO) is formed on SiC within narrow operational regimes and appears as a loose powder on the sliding surface. This debris is unable to produce a protective tribofilm and is associated with higher friction coefficients and wear rates.

2.3 Metal-Ceramic Sliding Systems

2.3.1 Introduction

The previous sections have focused on ceramic-ceramic sliding couples in order to introduce and discuss the basic response of different ceramics to tribological stresses. In recent years, metal-ceramic sliding systems have gained in industrial importance for a number of reasons. There is increasing interest in the substitution of ceramics for more traditional materials in engineering systems, even in technologically conservative industries such as mining and minerals handling. This frequently leads to metal-ceramic sliding interfaces since the substitution of both sliding partners is often impractical due to the relative brittleness of the ceramics. Cost considerations further mitigate against the use of ceramics for both sliding partners in many cases. A typical example is the spool valve assembly which controls the

As described by Wilks and Wilks [179], some work has been done on PCD in sliding contact with steel, in response to the use of PCD as a cutting tool. Not surprisingly, the dominant parameters which determined wear rates were found to be the roughness of the PCD surface and chemical wear and transfer of steel to the PCD. The latter effect is probably related to the presence of the cobalt binder phase since no material transfer was observed with single crystal diamond.

Again, no systematic study could be found in the open literature of the wear of PCD compacts in sliding contact with similar materials. It would, however, be reasonable to assume that the mechanisms outlined above would also be operative in this case, depending on the contact conditions such as PCD roughness, contact temperature and contact pressure.

- Abrasive wear: This occurs as a result of rubbing against abrasive rock surfaces such as s ndstone and results in a smooth wear flat on the PCD compact by the fracture and cleavage mechanisms described earlier.

- Mechanical fatigue: Microchipping of single or multiple diamond crystals occurs as a result of cyclic applied loads which break the bonds between the diamond particles. Where thermal effects are negligible, the wear resistance of PCD increases with decreasing diamond grain size.

- Thermal-Physical: As described earlier, PCD exhibits thermal instability at temperatures above ~ 730 °C. At these temperatures, the microchipping wear mode changes to severe thermal degradation and the pull-out of entire diamond grains. This is caused by internal stresses between the diamond grains which are the result of differential thermal expansion of diamond and the cobalt binder phase.

  Below 730 °C, increasing temperatures increase the rate of microchipping and the rate of wear.

- Thermal-chemical: In the presence of oxygen, diamond begins to graphitize at temperatures above ~ 875 °C. However, due to the presence of the cobalt catalyst phase, conventional PCD compacts can begin to graphitize at temperatures around 700 °C, as described earlier.

Studies of the wear of PCD cutters have often tended to focus on the temperature-related wear mechanisms due to their prevalence in drilling applications [188].

an industrial finishing process, much of the research work has concentrated on the polishing of single crystal diamond using a cast iron scaife loaded with diamond grit [180]. Under these conditions, the rate of polish (i.e. the resistance to abrasive wear) is strongly dependent on the crystallographic orientation of the polished face and the direction of abrasion. This arises because abrasive wear and polishing of diamond occurs primarily by a microscopic cleavage process, and diamond cleaves preferentially along {111} cleavage planes. It is interesting that graphitization as a primary diamond wear process is now generally rejected in favour of mechanical chipping and cleavage ([181], as quoted in reference [182]).

It has also been shown that softer materials such as steel and even aluminium can cause wear of diamond [183]. This points to a fatigue mechanism which causes the formation and growth of small cracks in the diamond surface which eventually result in material loss.

Chemical wear occurs when diamond is brought into sliding contact with materials which have a high affinity for carbon [179]. A typical well-known example is the machining of ferrous alloys, which results in very high wear rates of the diamond tool and is thus generally avoided.

PCD composite materials are essentially isotropic due to their polycrystalline structure and therefore exhibit no wear anisotropy. Nevertheless, many of the diamond crystallites present themselves to the wearing counterface in very abrasion resistant orientations and this caused initial difficulties in the polishing of these materials. However, it has since been shown that PCD can be polished more rapidly on a scaife than single crystal diamond, provided the scaife is kept adequately charged with diamond abrasive [184]. This is due to the abrasive particles being pressed into the metal binder regions where they then also damage the less resistant edges of the PCD diamond grains.

Besides polishing, most of the work on PCD has concentrated on the wear of this material in cutting and particularly drilling (of oil and gas wells) since these are the most common applications of PCD [161][185][186][187]. The primary wear modes which have been identified are briefly described below.

coefficient of friction and explained this effect in terms of the generation and annihilation of dangling bonds on the diamond surfaces during sliding. In experiments with silicon carbide sliding against diamond coatings, Jahanmir *et al* [173] attributed low friction to the formation of graphite at the sliding interface.

The overriding influence on friction, however, appears to be the surface roughness of the diamond coating [174][175][176]. Friction coefficients are high (~ 0,5) for rough coatings (R_a > 200 nm) and similar to that for single crystal diamond (~ 0,05) for smooth coatings (R_a ~ 1 nm). A review of the tribological characteristics of diamond coatings and technological challenges associated with their industrial use has recently been published by Bull and Matthews [177].

Only very limited work has been published on the friction characteristics of PCD. Field and Freeman [178] studied the friction of syndite (a De Beers PCD with cobalt binder) against various metals and alloys and found that, in general, friction is lowest for diamond, highest for amborite (a De Beers cubic boron nitride composite) and intermediate for syndite. Feng [169] examined the friction of copper, tungsten carbide and cobalt on syndite and found, not surprisingly, that material transfer and roughness effects dominate the behaviour with softer materials. With tungsten carbide, the friction coefficient was lower at ~ 0,4 and did not vary greatly with syndite roughness. The effects were explained in terms of ploughing and adhesion, with transfer also playing a significant rôle.

To the best of the writer's knowledge, however, no systematic study of PCD friction and wear has been published in the open literature which explores the tribological mechanisms and operational limits associated with these materials. The present study therefore aims to make a contribution in this area.

2.4.4 Wear of diamond

Diamond is susceptible to two main forms of wear: mechanical or abrasive wear and chemical wear, as outlined in a recent review by Wilks and Wilks [179]. In view of its importance as

incubation period, compared to unlubricated and paraffin lubricated couples (Figure 2.17). This clearly shows that adhesion effects are important in diamond tribology. It is suggested that diamond surfaces in air are covered with a chemisorbed layer of H or OH, followed by an adsorbed layer of water. No dangling bonds are therefore available on the diamond surfaces and adhesion and friction is reduced.

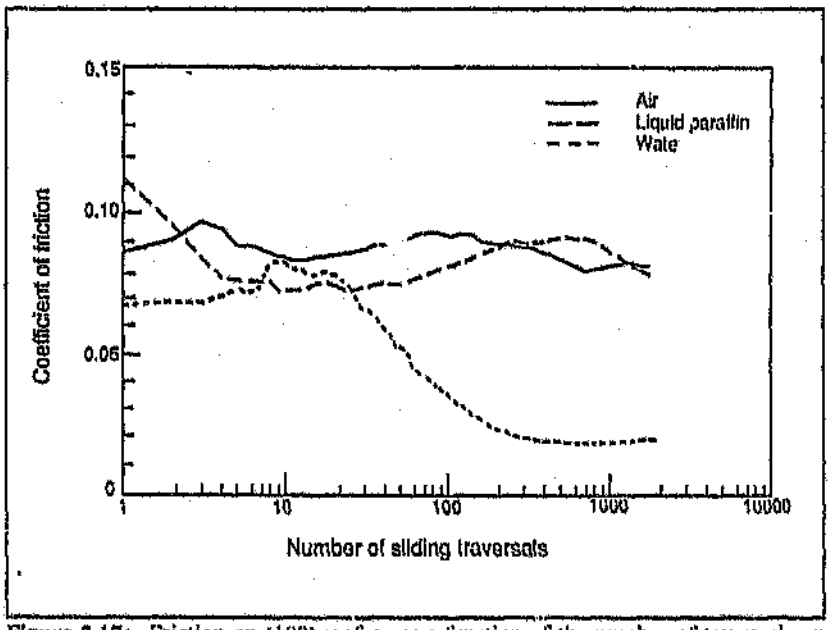

Figure 2.17: Friction on (100) surface as a function of the number of traversals on the same track. (after Feng and Field [171])

It is thus clear that the mechanism of diamond friction must involve both asperity interaction effects as well as adhesion. Additional effects include surface and subsurface fracture once a critical contact pressure level is exceeded, as well as the possibility of plastic deformation. However, no definitive description of the processes has yet been developed.

Friction of diamond coatings and PCD

Polycrystalline diamond coatings do not incorporate any second phases and would thus be expected to behave in a fundamentally similar way to single crystal diamond. Indeed, Gardos and Soriano [172] demonstrated that the adsorption of hydrogen is important in lowering the

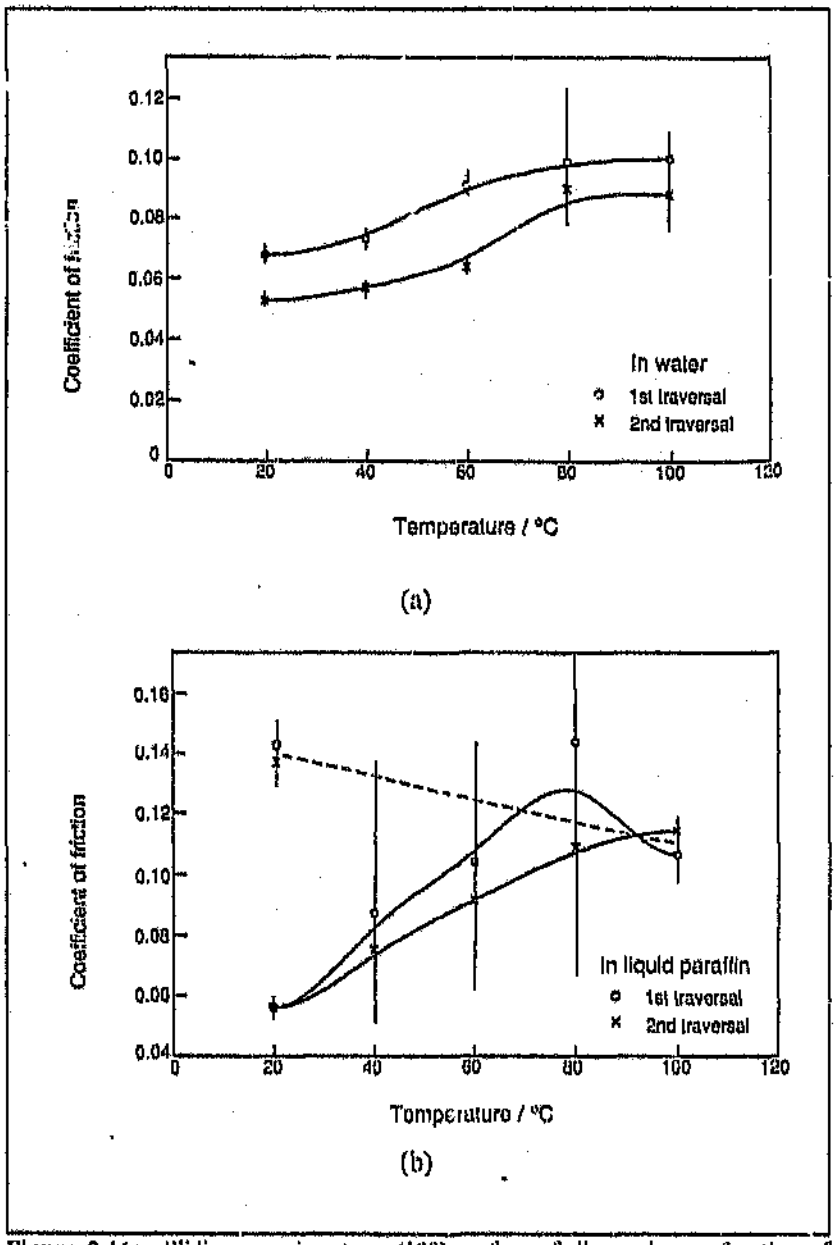

Figure 2.16: Sliding experiment on (100) surface of diamond as a function of temperature: (a) in the presence of water and (b) liquid paraffin. (after Feng and Field [170][171])

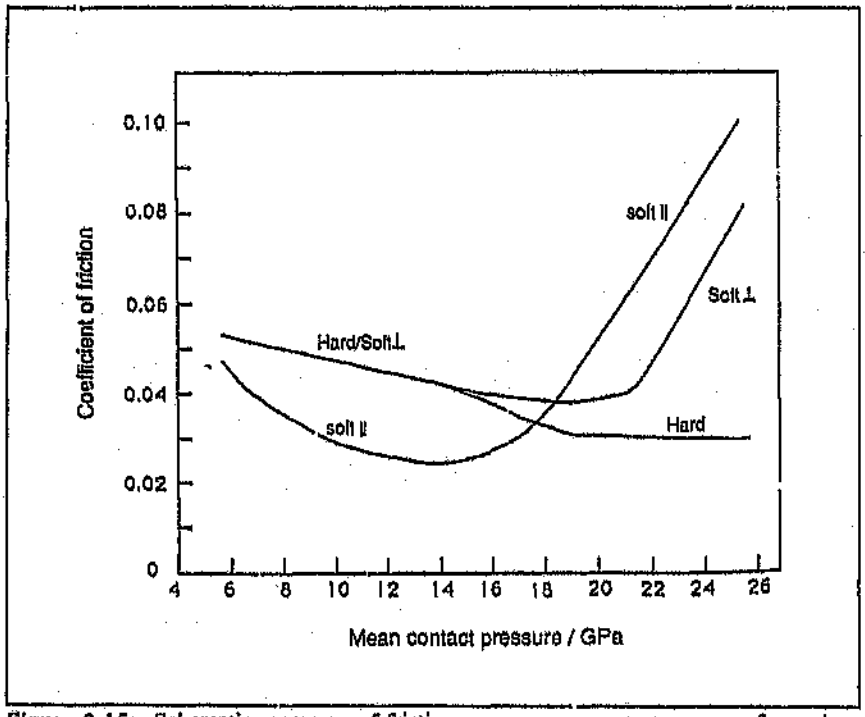

Figure 2.15: Schematic summary of friction versus mean contact pressure for various styli sliding on the (001) face of a diamond. Soft ∥ implies sliding in the <100> direction parallel to the polish lines, soft ⊥ implies sliding in the <010> direction orthogonal to the polish lines and hard refers to sliding in the <110> direction. (after Samuels and Wilks [168])

rise and fall over one another. They further described several energy dissipation mechanisms to account for the observed frictional loss, the most plausible of which would appear to be elastic vibration of the asperities after each disengagement. This model is successful in describing most of the above effects.

However, recent work by Feng and Field [170][171] demonstrated a marked effect of temperature and the presence of water on friction behaviour. In single reciprocating traversal experiments, they found that increasing the temperature in the presence of water resulted in a significant increase in the coefficient of friction (Figure 2.16 (a)). A similar effect was found for liquid paraffin; however, in contrast to the behaviour with water, the friction coefficient remained at a high value on cooling (Figure 2.16 (b)). For multiple traversals, the friction coefficient of water lubricated diamond couples decreased markedly after an initial

the <110> or cube diagonal direction and highest along the <100> or cube edge direction [163][165]. The frictional anisotropy is smaller on the (110) face and virtually non-existent on the (111) face. Enomoto and Tabor [166] showed that the applied load on the sliding diamond indenter needs to exceed a certain threshold level before the anisotropy effect becomes significant.

The magnitude and symmetry of the friction coefficient also depends on the direction of polishing relative to the crystallographic orientation of the samples [167]. Bearing in mind that material is removed during polishing by a small-scale chipping or cleavage process, which results in surface roughness features of the order of 5 nm in height, this result suggests that surface topography is an important parameter governing diamond friction behaviour.

The literature is divided concerning the influence of applied load on the magnitude of the friction coefficient. Using a rounded stylus as sliding element, Enomoto and Tabor [165] found that the coefficient of friction increased with increasing applied load. In contrast, using the tip of a natural octahedron as slider, Casey and Wilks [166] found that the friction coefficient was independent of the applied load, which suggested an influence of stylus shape. Further experiments by Samuels and Wilks [168] revealed that these discrepancies were related to different contact pressure regimes used in the previous work. Using styli of various radii but under similar contact pressure conditions, they showed that the coefficient of friction decreases or remains virtually constant on the (100) and (110) surfaces in the 'hard' direction (Figure 2.15). ('Hard' here refers to the ease of polishing of the diamond in this direction). This trend has since been confirmed by Feng [169].

Influence of lubricants

It is generally accepted that the friction of diamond is much lower in air than in vacuum, probably as a result of adsorbed surface layers. Moreover, the coefficient of friction remains unaffected by conventional lubricant oils. To explain this result and the geometric effects discussed in the previous section, Casey and Wilks [166] and Samuels and Wilks [167] proposed a 'ratchet-type' friction mechanism, where the asperities of the interacting surfaces

- Single crystal diamond begins to graphitize at at an increasing rate at temperatures above ~ 1200 °C in inert or reducing atmospheres and above ~ 875 °C in the presence of oxygen [161]. In PCD composites, the presence of the catalyst phase, usually cobalt, leads to thermal instability at temperatures above ~ 700 °C [155]. Degradation of the composite then occurs by the differential thermal expansion of cobalt and diamond, as well as graphitization of the diamond, catalyzed by cobalt.

To overcome the limitations imposed by the thermal instability of traditional PCD, thermally stable PCD composites were developed and commercialized in the early 1980's [155]. These are manufactured either by leaching out the cobalt phase after sintering, or by choosing a binder phase which becomes inert with respect to carbon after sintering. An example of the latter material is marketed by De Beers under the trade name 'Syndax' and contains silicon as the binder phase. Although much of the silicon in the diamond network is present in the form of silicon carbide, a significant amount of free silicon remains in these areas [163]. As will be seen in Chapter 5, this is important in the friction and wear behaviour of this material.

2.4.3 Friction of diamond

Most of the work on the friction and wear of diamond have been carried out using single crystal specimens of natural or synthetic diamond. While these basic studies have served to elucidate some of the important aspects of diamond tribology, they are limited in that the small specimen size has necessitated the use of very low sliding speeds. An excellent concise review of the friction behaviour of diamond has recently been published by Tabor and Field [164].

Friction of diamond in air

There is general agreement in the published literature that the coefficient of friction of self-mated diamond sliding in air typically lies between 0,05 and 0,15, depending on the crystal orientation and surface roughness. On the (100) face, the friction coefficient is lowest along

2.4.2 PCD: Synthesis and properties

PCD composites are made by a high temperature, high pressure process similar to that used in the commercial manufacture of synthetic diamond grit. Micron-sized diamond powder as the starting material is thoroughly mixed with a metallic catalyst or binder phase, typically cobalt, and enclosed in a protective metal can [161]. Alternatively, and this is the more usual method, the diamond powder is placed into a recess in a previously sintered WC-Co compact, from which the required catalyst is obtained by melting and extrusion of the Co binder phase. The sample is first pressurized to a typical pressure of 5 Gpa and then heated to the carbon/catalyst eutectic temperature, which is typically 1500 °C. Sintering of the mixture occurs by dissolution of the diamond crystals at their edges and points of contact, followed by epitaxial growth of diamond on faces and sites of low-angle contact between crystals. The binder phase is thus effectively excluded from the crystal contact points and true diamond-diamond bonds are formed. This characteristic distinguishes PCD composites from more familiar composite materials such as WC-Co where no true intergrowth of the hard phase occurs [162]. At the completion of the process, small pockets of binder phase remain in the interstices of the continuous diamond network. Nevertheless, the typical diamond concentration in PCD is 90 - 97%.

The resultant composite is traditionally in the format of a disc, consisting of a thin layer of PCD (~ 0,7 mm thick) integrally bonded to the WC-Co substrate during the high pressure, high temperature cycle. Some important characteristics of PCD are outlined below.

- PCD approaches the hardness of single crystal diamond but exhibits isotropic mechanical properties as a result of the random orientation of diamond crystals.

- Residual stresses in the PCD layer are high as a result of differential thermal contraction of diamond, Co and WC-Co during cooling from the sintering phase [161]. These can cause spontaneous delamination of the layer from the WC-Co substrate when subjected to impact loads.

industrial applications [154]. Today, synthetic diamond is available in a number of forms:

- loose grit: which is used in cutting, grinding and polishing and drilling applications and accounts for the majority of synthetic diamond used in industry (current market is estimated at around 400 million carats or 80 tonnes per annum, of which synthetic grit accouts for about 90% [155]);

- coatings: which consist of polycrystalline diamond and are designed for a wide variety of applications including wear resistant coatings, electronic applications and the production of free-standing films for optical applications; and

- composites: also known as polycrystalline diamond (PCD) composites, where diamond crystals are sintered into a dense structure in the presence of a metallic binder or catalyst phase. The resultant cylindrical compacts are widely used as cutting tools and inserts for oil and gas well drill bits and are the materials of interest in the present work.

Diamond grits are usually commercially manufactured by subjecting a mixture of graphite and a metal solvent, such as cobalt, nickel, iron or alloys of these, to high pressures and temperatures of ~ 5 GPa and 1500 °C, respectively. Polycrystalline diamond or diamond-like coatings can be produced using chemical vapour deposition (CVD) and other techniques, but most industrial applications are still very much in the development phase. Further details on the development history, manufacturing methods and applications of these materials can be found in references [154], [156], [157], [158], [159], [160].

The synthesis and essential properties of polycrystalline diamond (PCD) composites will be discussed in more detail in the following section, since this is important for developing an understanding of the tribological characteristics of these materials.

sliding, the behaviour of these ceramics is dominated by tribochemical effects and the formation of silica surface reaction layers. Polishing of the ceramic has been observed until the surfaces became smooth enough to facilitate hydrodynamic lubrication, even at relatively low sliding speeds of 0,1 m/s.

2.4 Synthetic Diamond Materials

2.4.1 Introduction

Diamond possesses a face-centred cubic structure in which the carbon atoms are tetrahedrally coordinated and covalently bonded [152]. This is responsible for the unique combination of mechanical and elastic properties of diamond. Referring to Table 2.4, it will be seen that the hardness, elastic modulus and thermal conductivity of diamond are higher than that of any other known material, while its friction coefficient in self-mated sliding is lower than that of most other materials [153]. These and other properties make diamond an attractive material for electronic applications (e.g. heat sinks), optical applications (e.g. x-ray windows),

Table 2.4: Some key properties of diamond compared to selected engineering ceramics.

Property	Diamond	Alumina	Zirconia
Hardness (GPa)	56 - 108[1]	11 - 22	10 - 14
Young's Modulus (GPa)	1000	340 - 410	196 - 216
Friction coefficient (self-mated, in air)	0,05 - 0,15[1]	0,6 - 0,7	0,6 - 0,7
Thermal conductivity (W/cm.°C)	20		

NOTES: 1. Values depend on crystallographic orientation.

biological applications (e.g. coated heart valves to prevent wear and biological fouling) and tribological applications (e.g. cutting and grinding tools).

Over the past 40 years, considerable research effort has thus gone into the development of diamond synthesis technologies in order to facilitate and expand the use of diamond in

written in machine code to achieve maximum speed, reads a burst of digital data over a number of reciprocating cycles from each channel and performs an averaging function. The length of this data burst for each channel is specified in the test parameter set-up stage. For the wear depth data, the subroutine simply calculates the mean of this data burst. The advantage of this approach is that variations in the data due to vibrations or variations in specimen height are averaged out for each data point.

For the friction force data, the process is slightly more complex since the sign of the signal changes from positive on the forward stroke, to negative on the return stroke. The subroutine thus calculates the average of the absolute values of the data burst. The need for writing this subroutine in machine code now becomes clear. In order to obtain meaningful friction force data, the routine had to be capable of reading the transducer data fast enough to resolve a number of individual reciprocating cycles at the maximum design reciprocating frequency of the machine.

In summary, the machine code subroutine reads a burst of raw digital data from each of the two A-D converter channels at preselected sampling intervals and calculates a meaningful average for each data burst. This average is then returned to the main programme and represents the y-value of the data pair for that particular sampling interval. For each channel, the cumulative time elapsed for each sampling interval is calculated and represents the x-value of the data pair.

Immediately after sampling, the raw friction and wear data pairs are converted into data pairs representing cumulative sliding distance vs. friction force and cumulative sliding distance vs. wear depth, using the necessary test parameters and calibration constants. These data points are then plotted on the computer screen in real-time to provide the investigator with a graphical view of the progress of the test. This is particularly useful when investigating friction and wear transition phenomena, where it is sometimes desirable to terminate the test before and after a transition to enable detailed wear surface analyses.

Following the above operations, all four data pairs are then stored on disk in ASCII format

Option 2 is used to fit a polynomial to acquired data, which can subsequently be plotted together with the data using the **Graphics** options. The remaining options were not required in the present work and are currently not supported. However, the menu structure has been designed to allow for easy extension of the programme to incorporate these features.

Graphics:
1. Setup graph
2. Plot curve(s)
3. Select output device
4. Change graph aspect ratio

The programme supports the simultaneous plotting of multiple data sets on x-y graphs with two y-axes. Option 1 is used to set up the graph, i.e. to define axis scales and labels, select the line and marker type for the different data sets, and to define with respect to which y-axis each data set is to be plotted. Option 2 is used to then plot the graphs. A notable feature is that the x-axis and the left-hand y-axis are scaled automatically by default, based on the x and y values in the data set. This enables rapid plotting of any given data set without the need to first manually scale the graph. Furthermore, a cursor is provided with the graph on the computer screen. This can be moved along the plotted curve using the arrow keys and is useful for finding the x-y coordinates for any given point on the curve.

Output devices like printers can be specified with Option 3, the default device being the computer screen. However, this option is now inoperative since it was found to be more convenient to print graphs using the plotting functions in QuattroPro™. The aspect ratio of the graph as it appears on the computer screen can be adjusted using Option 4.

3.3.3 Data acquisition and storage

The analog signals from the friction force and wear depth transducers are converted into digital data using an A-D converter card. The computer programme interrogates the two channels of the A-D card at sampling time intervals which are specified during the test parameter set-up stage (Option 1, Test sub-menu). At each interval, a small subroutine,

Option 2 is used to run a test automatically, where the computer starts and then terminates the test once the test duration specified in Option 1 has elapsed and continuously acquires and stores friction and wear data during the test. Option 3 provides for manual control where the machine can be started and stopped using selected computer keys.

(ii)	**Disk Utilities:**	Data files:	1.	Load files from disk
			2.	Save files on disk
			3.	Catalog disk (i.e. list files)
		TCON files:	4.	Load files from disk
			5.	Save files on disk
			6.	Catalog disk
			7.	Specify directories
			8.	Display default file structure

Note: TCON files list the selected conditions for each friction and wear test, together with the test name and date on which the test was conducted.

Edit/Enter data:	1.	Data entry from keyboard
	2.	Append/insert data to file
	3.	Delete points
	4.	Edit data points
	5.	List points

These options can be used to enter data using the keyboard, and to list and modify the data selectively.

Manipulate data:	1.	Transform data stepwise
	2.	Polynomial regression
	3.	Interpolation on existing derived curve
	4.	Integrate/differentiate data
	5.	Calculate arithmetic mean / RMS value

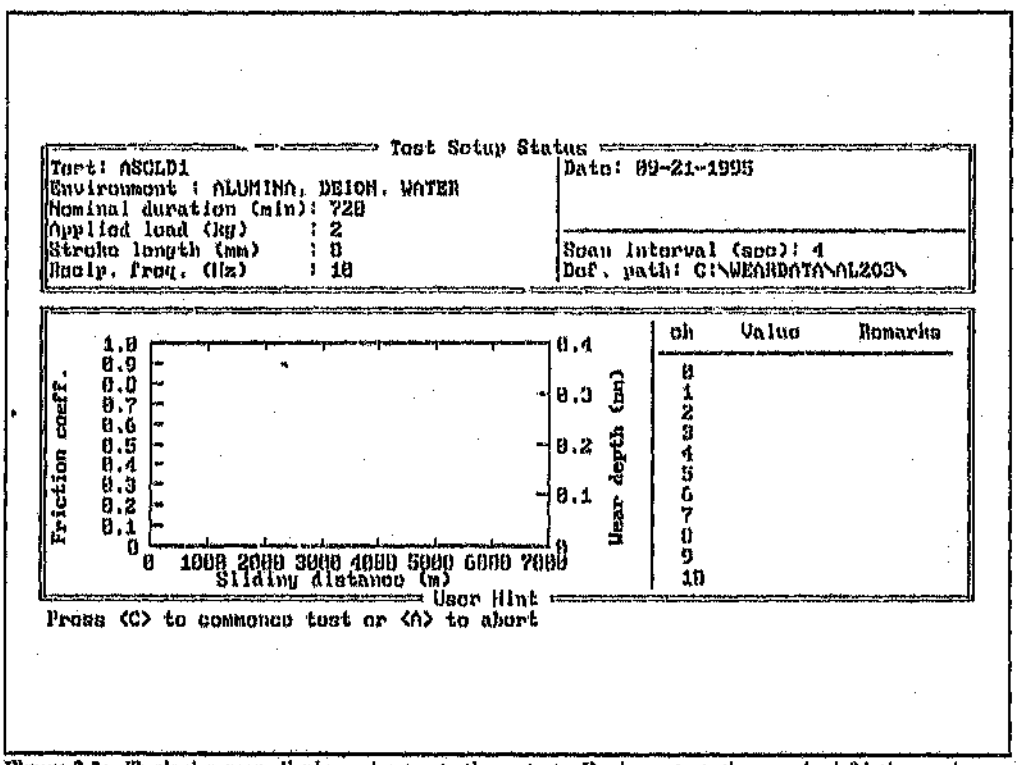

Figure 3.3: Typical screen display prior to starting a test. During a test, the acquired friction and wear data is displayed graphically and numerically in the centre window.

reciprocating frequency, test duration, data file name and test description. These parameters are subsequently used with the calibration constants derived in the calibration routine (Option 4) to calculate sliding distance and the coefficient of friction from the raw data obtained from the transducers. The conditions for data acquisition are also selected in this step; more about this in Section 3.3.3. Finally, the user can specify lower and upper limits for each data channel, in user-selected units. For example, in the case of wear depth the limits might be 0 and 0,4 mm, respectively. The programme then monitors the values of the acquired data while executing the test and will terminate the test automatically when any one limit is exceeded. This feature is required to protect the machine against potential damage when running tests unattended. On termination, a message will appear in the 'Remarks' column in the centre display window (see Figure 3.3) which indicates on what channel and for what reason the termination occurred.

3.3.1 Menu structure

There are two menu levels, namely the **main menu** which lists the options available and five **sub-menus** which are used to execute the various options (these are discussed in more detail in the following section). The sub-menus are accessible either from the main menu, or directly from any other sub-menu by 'hot keys'. When displaying a sub-menu, the screen is divided into three windows:

- Top window: which provides information concerning the number of data files loaded in memory, date, time, and data file path;
- Centre window: which lists the sub-menu concerned; and
- Bottom window: which provides relevant information to the user, such as a list of 'hot-keys' to be used for accessing the various sub-menus directly as well as any error messages.

These windows are also used while the Test sub-menu is displayed, or while executing a test (Figure 3.3). In these cases the top menu provides a summary of the selected test conditions, the centre window is used for displaying the Test menu or acquired data in real-time mode, and the bottom window provides relevant user information.

3.3.2 Sub-menus

The five sub-menus and the associated options available are listed below.

(i) **Test Menu:**
1. Setup test conditions
2. Run test automatically
3. Manual override
4. Calibrate data acquisition channels

Option 1 is used to define a set of test parameters, including applied load, stroke length,

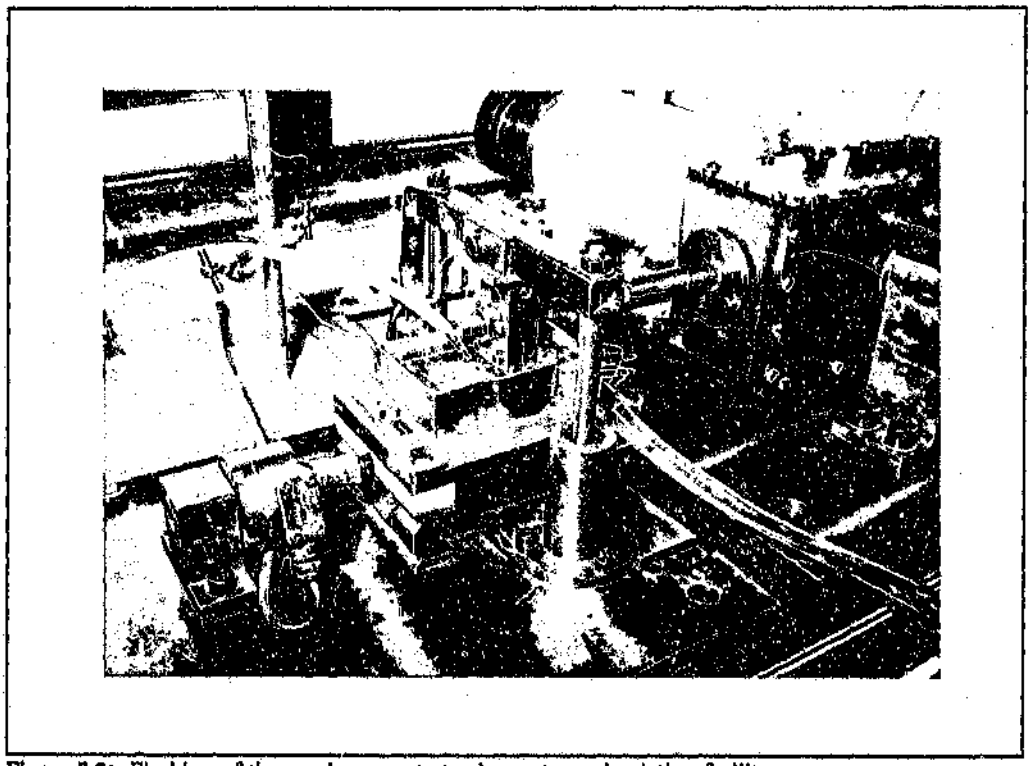

Figure 3.2: Flushing of the specimen contact using water recirculating facility.

- continuous monitoring of user-selected data limits on all activated channels with automatic test termination if any limit is exceeded;
- real-time plotting of data from any two activated channels;
- simultaneous data acquisition from up to 11 channels;
- automatic processing of raw data;
- automatic activation and termination of experiment, based on user-selected test duration.

A listing as well as a compiled, executable version of the programme is provided on the computer disk provided with this thesis.

follower in the oscillating head. The load frame is located in linear rolling element bearings and extends through the cast iron baseplate of the machine. It is loaded beneath the plate by dead weights.

The friction force is measured by a load cell attached to the stationary specimen stage assembly. The supports which carry the specimen stage are machined in such a way that they deflect elastically under the influence of the friction force. This guarantees a well-defined, linear response of the load cell to the friction force.

The total wear depth of the sliding system is monitored by an inductive linear variable differential transducer (LVDT) which measures the downward displacement of the load frame.

Since components in hydro-powered mining equipment operate in water, the completed test system also incorporates a water recirculation facility to provide flushing of the specimen contact during testing (Figure 3.2). The temperature of the water may be controlled to within 1°C from room temperature to 100°C by means of an integrated heating arrangement.

3.3 Computer Software Development

A PC-based computer programme was written in Microsoft Turbo-Basic™ to facilitate automated test control and continuous data acquisition. The program includes the following main features:

- user-friendly menu structure with position-sensitive help in some areas;
- continuous on-screen information regarding test conditions, data acquisition parameter status and test status;
- maximum data acquisition rate of 16 kHz, which is required to resolve the friction force over single reciprocating cycles and may be varied by the user using several delay functions;
- automatic data storage throughout a test;

maintenance, which indicates the effectiveness of the design measures.

To facilitate the changing of specimens, the scotch yoke housing is carried in a trunnion and the entire assembly may be rotated about the drive shaft axis. The trunnion is formed by a stub shaft on the front housing cover, and a ball bearing mounted in the rear of the housing, running on the drive shaft.

Wear in the mechanism is taken up automatically by a hydraulic piston, which is attached to the moveable rear sliding plate in the crosshead and keeps the block running with zero clearance. This is also important to prevent backlash and inaccuracies in stroke length. Oil is fed to the piston by the same pump that supplies the injectors. The feed pressure is regulated by a bypass valve. If required, the hydraulic system may be converted to manual operation to reduce complexity. The ability to adjust the mechanism for wear is retained with manual operation.

The lower, fixed specimen is clamped in a stainless steel bath using a simple vee-block arrangement. The bath, in turn, is mounted on a baseplate and may be moved laterally to alter the relative positions of the fixed and the moving specimen. Several experiments may thus be run on the same fixed specimen. A facility is also provided for adjusting the vertical position of the bath with respect to the reciprocating specimen. This is used to accommodate fixed specimens of different thickness and is necessary since the reciprocating arm needs to be accurately horizontal to avoid asymmetric friction behaviour on the forward and reverse strokes.

The baseplate incorporates electric tube heaters for elevated temperature testing and is mounted on elastically deformable supports to enable measurement of the friction force. The specimen stage assembly and the drive system are mounted on separate cast iron baseplates to reduce vibration transmission from the drive system.

The normal load is applied to the top specimen by means of a load frame and a roller cam

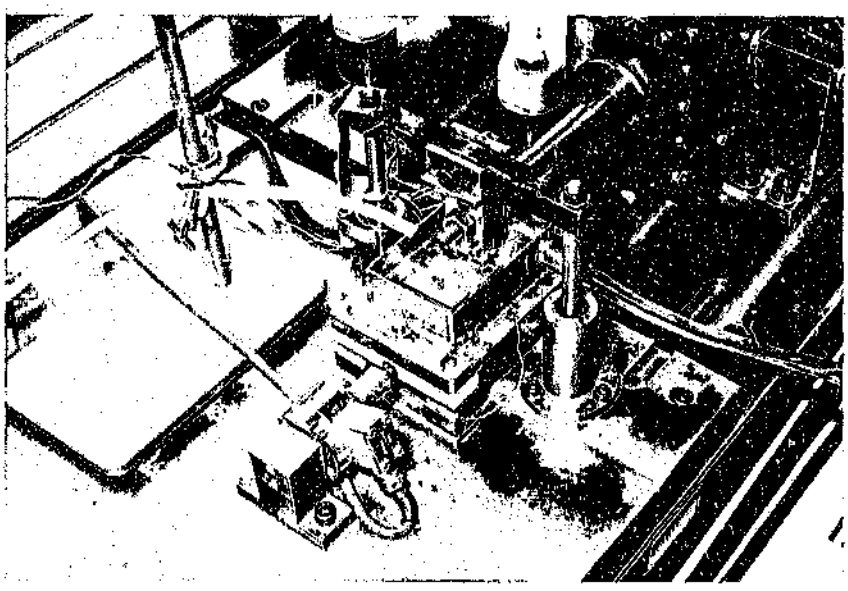

(c)

Figure 3.1 (cont.)

The oil is recirculated through the housing from a 20 l reservoir, using a hydraulic pump.

The scotch yoke mechanism is driven by a double cam arrangement, consisting of the crankpin on the driveshaft which fits into an off-centre recess at the rear of a phosphor bronze cam. This cam, in turn, rotates in the sliding block in the cross head and is locked onto the crank pin by means of a bolt. By varying the relative position of the cam on the crank pin, the throw of the square sliding block and, therefore, the stroke length of the crosshead may be adjusted steplessly between 0 and 8,5 mm.

The drive shaft is carried in a bearing block and is belt-driven by a 1,5kW dc electric motor. The motor speed may be varied using a solid state speed controller to set the reciprocating frequency in the range 0 - 50 Hz.

The machine has now operated satisfactorily for a number of years without requiring

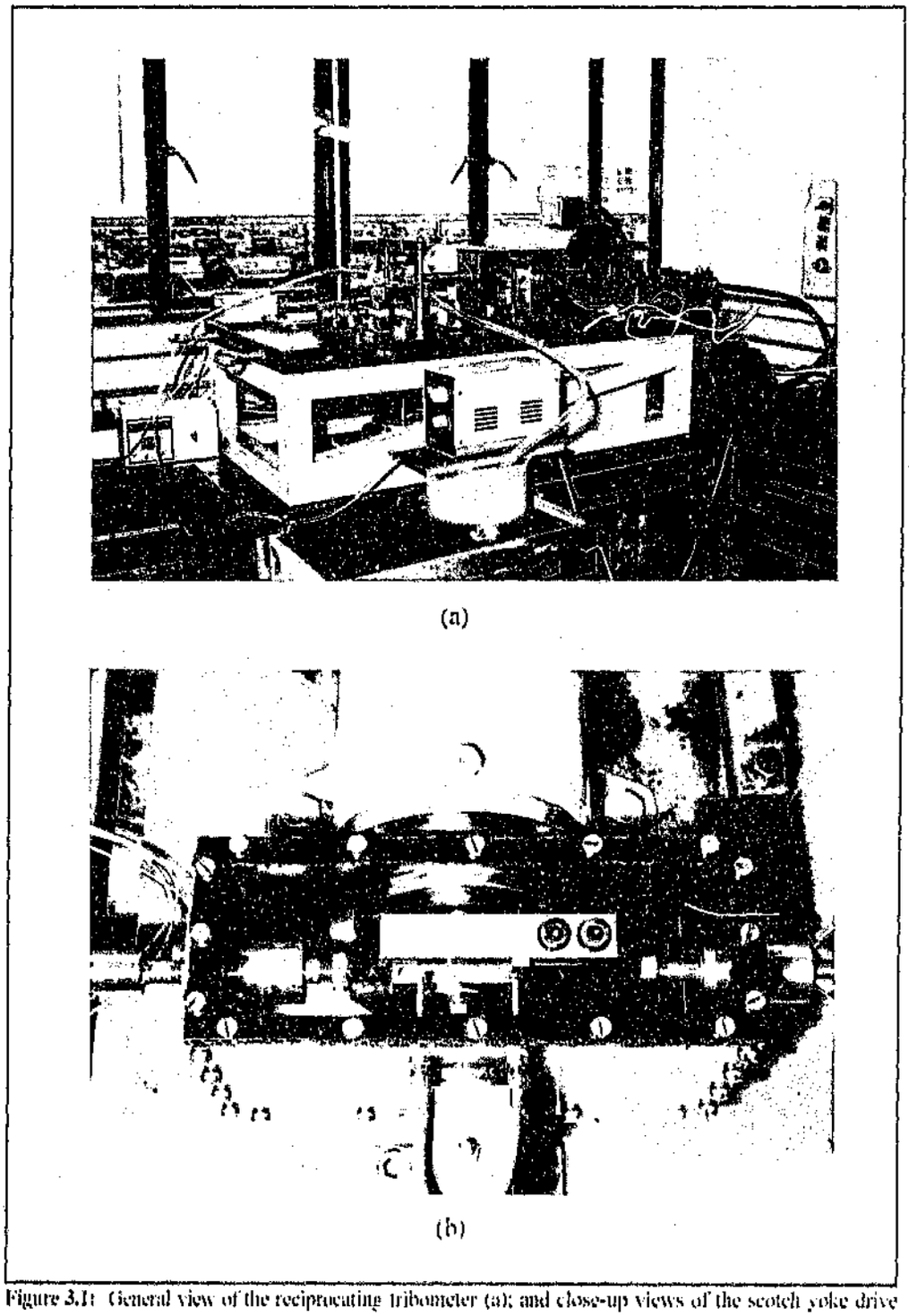

(a)

(b)

Figure 3.1: General view of the reciprocating tribometer (a); and close-up views of the scotch yoke drive system (b) and the specimen stage assembly (c).

- specimen heating facility.

While the frequency and stroke length ranges were easily determined from the operational conditions of relevant components, the applied load range was more difficult to define. No reliable data could be found concerning typical loads on the sliding surfaces of reciprocating components in hydro-powered equipment. It was thus decided to specify a load range much wider than that typically used in previous laboratory investigations (see Chapter 2), in order to accommodate all loads which could reasonably be used with metal-ceramic sliding couples. Other specifications such as the specimen contact geometries and environmental control facilities were selected to make the machine as flexible as possible and accommodate the needs of both the present and future research programmes.

The detailed design drawings are presented in Appendix A while the completed tribometer is shown in Figure 3.1.

The top specimen is held in a simple clamping arrangement in a moving head (Figure 3.1(c)), which is oscillated horizontally by a scotch yoke drive assembly (Figure 3.1(b)). In principle, the latter consists of a square block, which is driven by an overhung crankpin on the drive shaft and slides in a slotted crosshead. The vertical motion of the block is thus 'absorbed' in the slot, so that only the horizontal reciprocating motion is transferred to the crosshead. Compared with other types of drives, the main advantages of the scotch yoke system are:

- compact design;
- no lateral forces are imposed on the output shaft, thereby reducing the stresses on machine components; and
- no linkages are required.

A disadvantage is that the system incorporates a number of sliding surfaces, primarily between the sliding block and the slotted crosshead. For this reason, both the sliding block and the crosshead are made from hardened carbon steel. To ensure adequate lubrication, the mechanism is enclosed in a housing and hydraulic oil is injected into the sliding interfaces.

CHAPTER 3

3. DEVELOPMENT OF HIGH-SPEED RECIPROCATING TRIBOMETER

3.1 Introduction

One part of the present work focused on a laboratory study of various metal / ceramic sliding couples for use in high pressure, high frequency oscillating hydro-powered stoping equipment like water hammers and rock drills. A review of relevant work published in the open literature revealed that the mode of sliding can exert a significant influence on the friction and wear characteristics of ceramic and metal/ceramic sliding couples (e.g. Figure 2.3, Chapter 2). It was concluded that a conventional pin-on-disc test arrangement, which is characterized by unidirectional sliding of the samples, is unsuitable for the present work. A high speed reciprocating tribometer was therefore developed to simulate the essential contact and sliding motion conditions experienced by the components under consideration.

3.2 Specifications and Design

The test machine had to facilitate the measurement of friction force and wear of the test material couples under controlled sliding conditions. Important parameters like reciprocating frequency, stroke length and applied load had to be variable over a range compatible to the operating conditions of oscillating components in hydro-powered equipment. The selected parameter ranges and additional specifications are listed below:

- Frequency of oscillation: 0 - ~50 Hz
- Stroke length: 0 - ~9 mm (variable)
- Normal load: 0 - ~250 N
- Specimen configuration:
  - ball-on-flat (point contact)
  - cylinder-on-flat (line contact)
  - flat-on-flat (area contact)
- Environmental control:
  - specimen bath for liquid environments

4.1.2 Test environment

Most experiments were conducted in deionized water to evaluate the tribological response of the test couples without the complicating influence of corrosion or other effects. However, South African mine waters can be highly corrosive due to low pH, high levels of chlorides and sulphates and high levels of dissolved solids. Some exploratory friction and wear experiments were therefore conducted in a synthetic solution with typical mine water composition to evaluate the influence of water chemistry.

4.2 Experimental Details

4.2.1 Materials

In all experiments, a point contact geometry was employed with an AISI 440C stainless steel ball as the top, moving specimen and a ceramic disc as the lower, stationary specimen.

AISI 440C stainless steel

Hardened AISI 440C stainless steel ball bearings (10mm in diameter) were procured from Goodfellow Metals Ltd in England and were used in the as-received condition. The microstructure was examined by preparing a cross-section of a number of balls according to standard metallurgical techniques. As shown in Figure 4.1, the typical structure comprised carbide precipitates in a martensitic matrix, as expected for this material. The hardness of the material at 58 HR_c was typical of AISI 440C in the hardened condition.

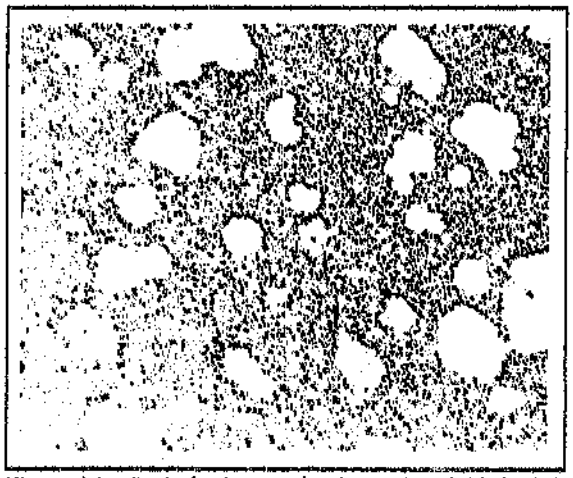

Figure 4.1: Optical micrograph of a sectioned AISI 440C stainless steel ball, 100x magnification.

in size) with less than 10% of cubic phase present in the form of larger grains (4 - 8 μm) [190]. Since a much higher proportion of metastable and transformable tetragonal phase is retained in the structure, 3Y-TZP exhibits a much improved toughening effect compared to PSZ.

- Ce-TZP: where the tetragonal phase is stabilized with 12 mol% ceria (CeO_2) additions. The microstructure of the material is similar to that of 3Y-TZP but the transformation from the tetragonal to the monoclinic phase occurs at lower stresses. Ce-TZP thus generally exhibits improved toughness compared to 3Y-TZP.

In summary, under the influence of any given mechanical stress, the extent of the phase transformation and the toughening effect increases in the order PSZ - (3Y-TZP) - (Ce-TZP).

Silicon based ceramics

It is now well-known that the friction and wear behaviour of silicon based ceramics like silicon nitride and silicon carbide is dominated by tribochemical effects and the formation of a silica-based surface layer. Although this has generally been associated with low coefficients of friction but increased wear rates (Chapter 2, Sections 2.2 and 2.3), some workers have reported high friction coefficients for these materials sliding against themselves or various metals in high humidities [100][144]. Less appears to be known about the behaviour of these ceramics when sliding against steel, although reduced adhesion and transfer layer formation compared to oxide ceramics has been reported. In particular, little work has been reported on SiAlON (silicon-aluminium-oxynitride), although similar effects are suspected [191].

Against this background, two silicon based ceramics were selected for evaluation, namely SiAlON (silicon-aluminium-oxynitride) and silicon nitride (Si_3N_4).

fracture toughness implies that the material should exhibit low wear in applications where impact loads are relatively low. Further, considerable local expertise existed on the processing, characterization and testing of this material. The selection of alumina for this study therefore afforded an opportunity to gain experience in the tribological testing and analysis of ceramics, before proceeding to more complex and less well-understood materials.

Zirconia based ceramics

Zirconia ceramics exhibit a phase transformation from the tetragonal to the monoclinic phase when subjected to mechanical stress (Chapter 2, Section 2.2.2). This is analogous to the martensitic transformation in steels and provides increased resistance to fracture and impact. Zirconia ceramics may therefore be suitable for application in reciprocating hydro-powered equipment where some impact loads are present. However, some reports in the literature suggest that the volume expansion associated with the phase transformation (which usually results in toughening) may lead to surface fracture and reduced sliding wear resistance, while other investigators found an increase in wear resistance (Chapter 2, Sections 2.2.3 and 2.3.2). Further, little work has been reported on the influence of this effect on the friction characteristics of these materials, particularly when sliding against steels.

Against this background, three zirconia ceramics were selected for the present work, exhibiting varying degrees of transformation toughening:

- PSZ: partially-stabilized zirconia, where the cubic phase is stabilized with small additions (~ 3 wt%) of MgO. The microstructure of commercially available Mg-PSZ materials is complex and typically consists of stable cubic zirconia grains with transformable tetragonal zirconia precipitates within the grains as well as at the grain boundaries.
- 3Y-TZP: tetragonal zirconia polycrystal, where the tetragonal phase is stabilized with 3 mol% yttria (Y_2O_3) additions. This material consists primarily of fine tetragonal grains (usually ~ 0.75μm

CHAPTER 4

4. METAL-CERAMIC SLIDING COUPLES

4.1 Introduction

As outlined in Chapter 1, Section 1.1, it was uneconomical to consider replacing the steel housings of reciprocating components in hydro-powered gold mining equipment with ceramic materials. For this reason, AISI 440C stainless steel was selected as the sliding counterface material for the ceramics.

Despite significant development work, the detailed operating conditions of reciprocating components in water-powered rock drills and hammers are still relatively ill-defined [189]. Uncertainty exists particularly around the applied loads and impact conditions due to the dynamic nature of the mining operating environment. What is clear is the fact that wear in components such as valves and actuating pistons causes internal leakage of the hydraulic fluid (water), which results in inefficient operation and eventual failure of the machine. Further, smooth friction behaviour during sliding is more important for these components than a low friction coefficient *per se*, since stick-slip motion results in erratic operation of the machine. An improved metal-ceramic sliding couple should therefore exhibit a compromise between low wear rates and smooth friction behaviour, with perhaps some bias towards the latter property.

4.1.1 Materials selection

Against the above background, a range of engineering ceramics was selected for study.

<u>Alumina</u>

Alumina has been extensively studied as a model polycrystalline oxide ceramic and is commonly available in various shapes at low cost. A combination of high hardness and low

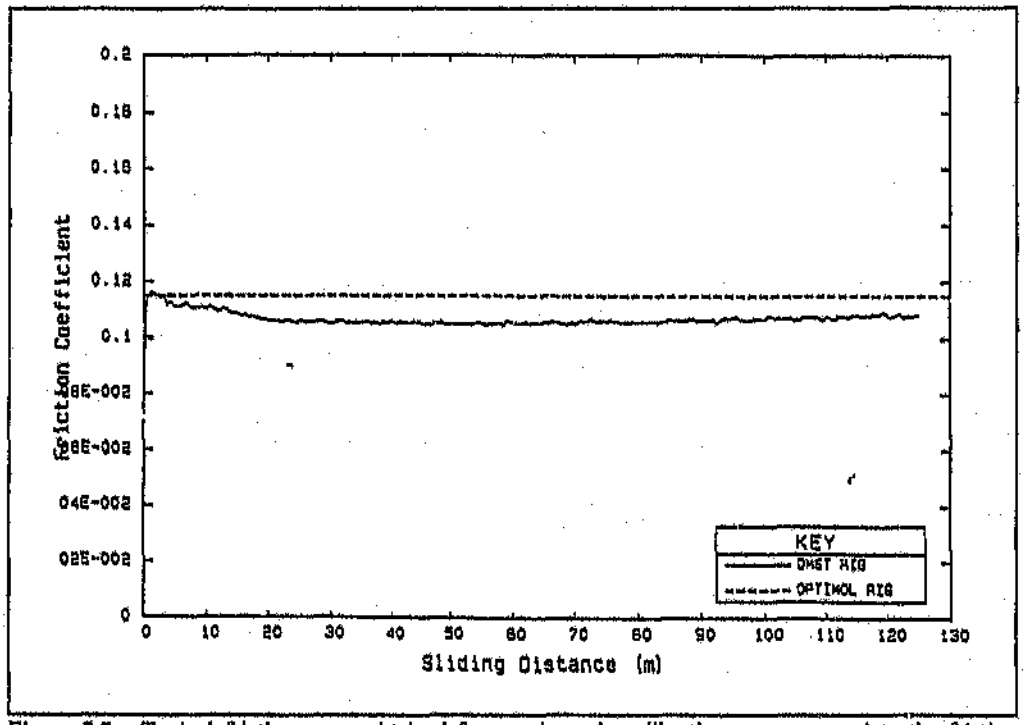

Figure 3.7: Typical friction curve obtained from a dynamic calibration run compared to the friction coefficient specified for the commercial Optimol SRV reciprocating sliding test rig.

GmbH, Germany). These samples were supplied by Optimol and the compositions of the steel and the lubricant were not disclosed.

The standard calibration test conditions on the Optimol SRV machine are an applied load of 200 N, reciprocating frequency of 50 Hz, stroke length of 1 mm and a test duration of 1 hour. In the present case, the same test conditions were used, except for a shorter test duration of 20 min. This was selected since the friction coefficient obtained from the Optimol rig was found to stabilize at its characteristic value after about 2 min.

The friction trace obtained from a typical dynamic calibration run is shown in Figure 3.7. It can be seen that the stable friction coefficient value of 0,11 $\pm$ 0,002 showed excellent agreement with the value of 0,115 given for the Optimol SRV system.

The wear depth LVDT was calibrated simply with a micrometer screw. As for the friction transducer, the transducer response was linear over the distance used.

3.5 Summary

A high-speed reciprocating tribometer was developed and tested, as well as a computer programme to facilitate automatic test control, data acquisition and processing. The main aims of the machine, namely to provide meaningful friction and wear data in a reciprocating mode and over a range of sliding conditions, were satisfactorily achieved. Vibration analyses indicated that reciprocating frequencies between 25 and 35 Hz should be avoided unless further vibration-reducing measures are employed. Some suitable measures were identified. Excellent agreement in measured dynamic friction coefficients was found with a commercially available tribometer, using a standard test arrangement with known friction behaviour.

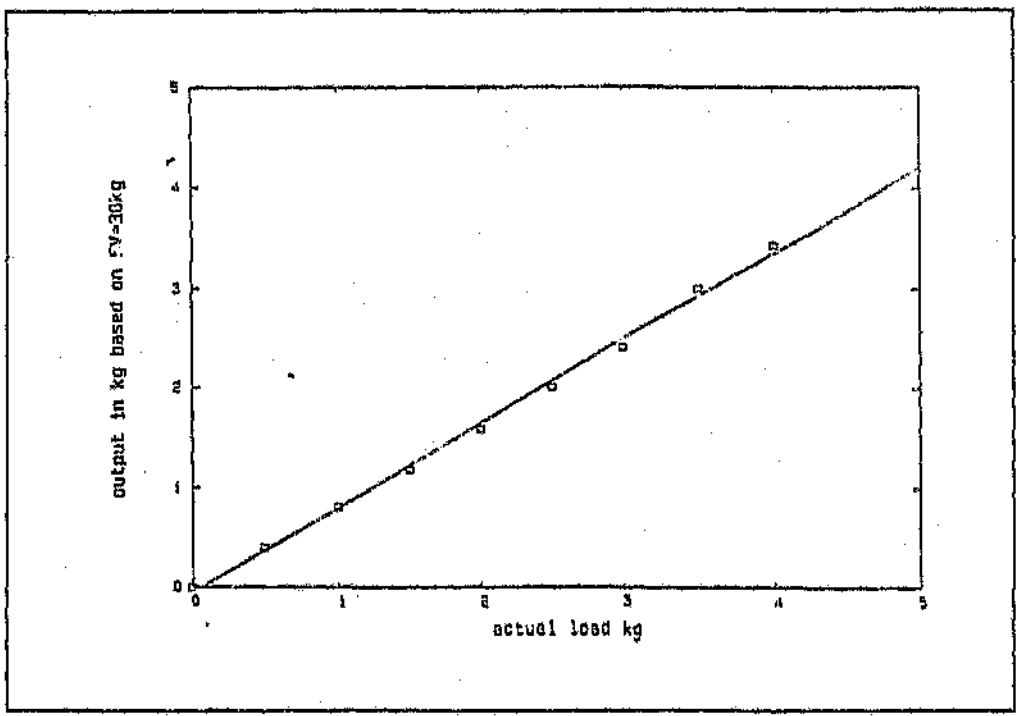

Figure 3.6: Typical static calibration curve for friction force transducer system.

force was lost in the system, presumably mostly in the elastic specimen stage supports.

More importantly, however, the load-output response was linear over the load range considered. The transducer output could therefore be related to the actual friction force at the specimen contact by a simple linear calibration function.

Having achieved satisfactory results from the static calibration results, the next step was to calibrate the tribometer dynamically against a material combination with known friction behaviour. This was necessary to verify whether effects like vibrations or unavoidable, small errors in specimen alignment were likely to influence the measured friction coefficients significantly. The selected couple comprised a standard steel ball and disc combination which is used together with a standard lubricant to calibrate the well-known Optimol SRV reciprocating tribometer. (This machine is also capable of reaching high frequencies but at much smaller stroke lengths of 3mm maximum, and is commercially available from Optimol

The following general conclusions could be drawn from the vibration analysis:

- Without implementing further vibration-reducing measures, meaningful results may be obtained if the machine is run at relatively low frequencies (< 20 Hz) and critical speed ranges are avoided.

- For frequencies below about 40 Hz, the mounting of the base plates should be rigid to ensure an accurate stroke length. Therefore, isolation of the specimen stage from the drive system by using resilient rubber mounting is not considered practical. At higher frequencies, such a mounting may bring benefits as the inertia of the plates reduces inaccuracies in the stroke to acceptable levels.

- Reductions in transmitted vibration may be achieved through improved balancing of the reciprocating masses and by increasing the mass of the drive system mounting.

Many of the recommendations suggested by the analysis have been implemented. For example, most tests in the present series were conducted at frequencies below 20 Hz and the machine components were supported on heavy cast iron base plates. Cast iron was selected since this material exhibits superior vibration damping characteristics compared to steel.

3.4.3 Static and dynamic calibration

The friction measurement system was calibrated by applying known static loads to the specimen stage in the specimen contact plane. This procedure was repeated regularly throughout the test programme. A typical calibration curve is shown in Figure 3.6. Based on the construction of the amplifier, an output of 5 V was equivalent to a load of 30 kg on the transducer. This implies that the calibration curve shown in Figure 3.6 should have exhibited a slope of 1 if no portion of the friction force was lost in the mechanical system. In fact, the slope was close to 0,84 which implied that close to 16% of the actual friction

Initial tests confirmed that significant vibrations were transmitted to the specimen stage from the drive system at particular frequencies. The vibrations of the specimen stage and the transducer support were approximately equal and exhibited a frequency which correlated with the excitation frequency. The first natural frequency of the system, measured at the specimen stage by exciting it into free vibration, was found to be approximately 30 Hz. Accordingly, the amplitude of the specimen stage and transducer vibration exhibited a peak at about 30 Hz.

When the base plate of the specimen stage assembly was supported on resilient rubber pads, the natural frequency dropped to about 9 Hz. In the absence of a friction force, the maximum displacement amplitude was then reduced to about 30% of that obtained for a stiff support. Unexpectedly, however, this maximum amplitude occurred not at the natural frequency, but somewhere between 15 and 50 Hz.

In order to assess the influence of specimen stage vibration on the output from the friction force transducer, the signal from the transducer was monitored together with the signal from one of the accelerometers. With the machine running without specimen contact (i.e. zero friction force), the momentary value of the measured force signal appeared to have a random distribution with no discernible component close to the excitation frequency. The scatter associated with the signal appeared to be unaffected by resonance in the system and increased approximately linearly with increasing reciprocating frequency. As was the case in the earlier force analysis, the magnitude of the scatter was of the order of a typical friction force at a frequency of 50 Hz.

When the base plate of the specimen stage was supported on resilient rubber pads, the maximum scatter in the measured force signal was reduced to about 30% of that obtained for a rigidly mounted plate. At particular frequencies (24 and 50 Hz), the scatter was reduced even further to approximately 2 - 5% of the typical friction force. However, the resilient mounting resulted in oscillation of the base plate with amplitudes of up to 1mm. As tests run with specimen contact showed, this led to inaccuracies in the stroke and an unsatisfactory friction force signal.

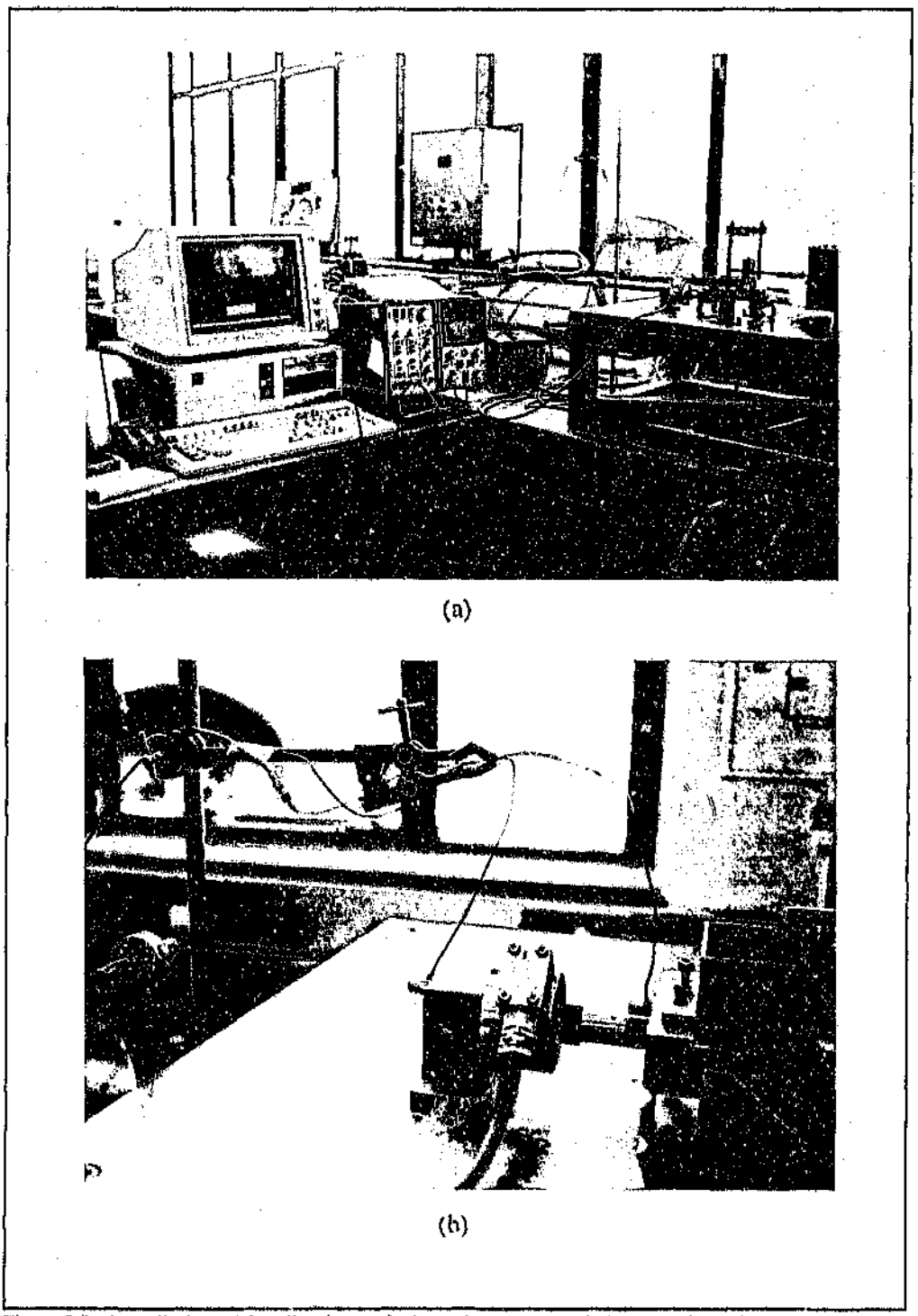

(a)

(b)

Figure 3.5: Overall view of the vibration analysis equipment (a) and close-up view of the accelerometers (b).

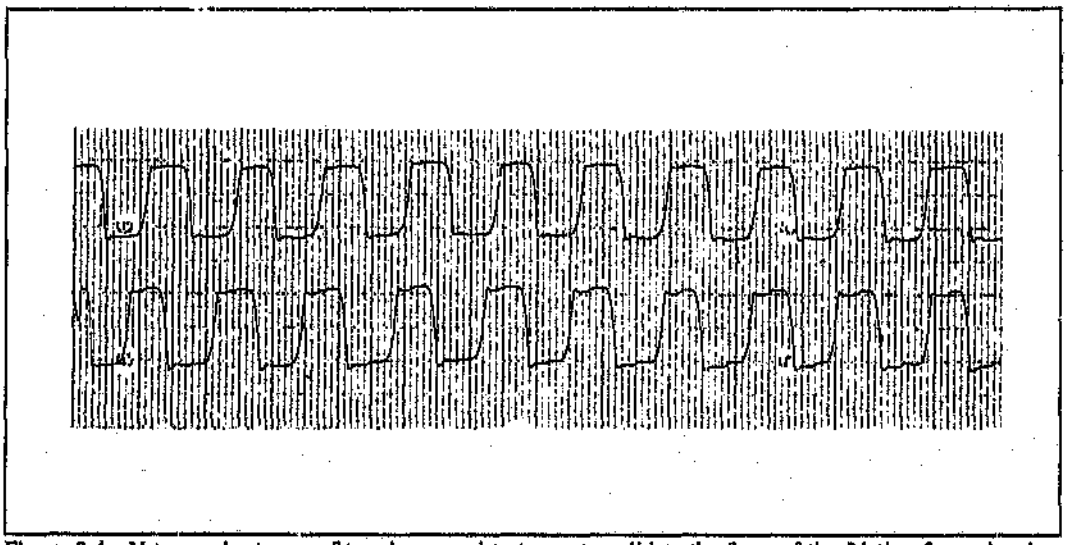

Figure 3.4: Y-t recorder traces of two low-speed tests run to validate the form of the friction force signal.

3.4.2 Vibration analysis

A series of trials was run to assess the vibration characteristics of the tribometer. This involved running the machine both with and without specimen contact with an oscilloscope connected to the friction force transducer. It was found that significant vibrations were transmitted from the drive system to the transducer at particular reciprocating frequencies. At the maximum frequency of 50 Hz, the amplitude of the transducer output was of the order of a typical friction force amplitude.

To study this effect in more detail, it was decided to perform a more comprehensive vibration analysis using two accelerometers and a storage oscilloscope. The arrangement is illustrated in Figure 3.5. Since the horizontal component of the imbalance generated in the drive system far outweighed the vertical component, attention was focused on horizontal vibration. While not entirely correct, this approach was justified for reasons of economy for the present survey investigation.

A vibration test involved running the tribometer through its entire speed range without specimen contact (i.e. with zero friction force) while recording the accelerometer outputs.

in separate files. They can thus easily be imported into standard graphics and spreadsheet packages such as QuattroPro ™ for further data manipulation, if required, and printing of graphs. The programme also automatically appends the appropriate data channel number to the user-defined file name and assigns different file extensions to the data files: '.raw' for the raw digital data and '.dat' for the transformed data. The test conditions are stored in a separate file under <filename.con>. This enables the user to load a previously defined set of test parameters for subsequent tests without having to manually re-specify any parameters. To further streamline the operation of the tribometer, the programme retains a test parameter set in memory until it is replaced by a new parameter set.

3.4 Commissioning of Tribometer

3.4.1 Data acquisition system

As a first step in the commissioning procedure, the load cell/dc amplifier system performance was assessed. After zeroing, the machine was left for 24 hours to assess zero drift. During this time, the zero point reading drifted by 0,001 V or 0,02% of the maximum amplifier output, which was considered to be acceptable. The tribometer was then run at a frequency of 3 Hz while the signal from the friction transducer was monitored by a y-t recorder. As can be seen from Figure 3.4, the friction trace approached a square wave, which indicated that the dynamic coefficient of friction was relatively constant over the sliding strokes. The friction coefficient also exhibited a small peak at the start of every stroke, showing that the system was sensitive enough to detect the static coefficient of friction as sliding initiated at these positions.

The friction measuring system exhibited little hysteresis, especially under dynamic loading conditions. Under static loading, the zero signal 'crept' in the direction of the applied load by 0,01 V or 0,2% of the maximum output, which was considered to be acceptable.

Satisfactory operation of the data acquisition software was verified by monitoring known voltages applied to the A-D converter.

Table 4.4: Apparent contact pressure (MPa) for Sialon and Si_3N_4 under various loads.

Material	Ground ceramics			Polished ceramics		
	20 N	30 N	50 N	20 N	30 N	50 N
Sialon	4,6	6,2	9,1	8,8	9,9	10,5
Si_3N_4	4,1	5,5	7,0	9,1	11,5	12,9

and 9,9 MPa (ground, 50 N and polished, 30 N), but were observed at pressures of 10,5 MPa (polished, 50 N).

It can of course be argued that the actual contact pressure may be very much higher on the ground surfaces as a result of their greater roughness. However, it was observed that the grinding scratches were filled with metallic debris from the steel ball. This effect tended to smooth the contact surface and contributed to a more even distribution of the applied load. Nevertheless, the retention of metallic debris on the ceramic surface certainly resulted in a more complex sliding interface compared to the polished ceramics, and may also have played a rôle in maintaining lower friction coefficients.

Based on these results, it would appear that the load carrying capacity (LCC) of the tribochemical surface films in terms of apparent contact pressure is ~ 10,5 MPa for Sialon and ~ 13 MPa for Si_3N_4. In view of the different compositions of the ceramics, it is likely that the higher sensitivity and lower LCC observed for Sialon is associated with differences in the chemical composition of the triboflms.

A similar trend towards longer run-in periods and greater scatter and oscillation in friction coefficient with increasing applied load was observed for ground PSZ surfaces. As will be discussed in Section 4.4, this could be attributed to a complex interplay between polishing and fracture on the ceramic surfaces and the formation of metallic transfer layers.

surfaces. However, at an applied load of 50 N the oscillating nature of the friction coefficient suggested that these films were overloaded in the case of Sialon and close to overloaded in the case of Si_3N_4, with the processes governing film formation and depletion becoming comparable. To support this explanation, a sliding experiment was performed on polished Si_3N_4 under a load of 80 N. No oscillations were observed and the steady state friction coefficient was substantially higher than that obtained at lower loads, and similar to that obtained during the run-in phase (Figure 4.8). This result confirmed that the tribochemical surface films were unable to accommodate loads in excess of about 50 N under the sliding conditions used, resulting in a transition from low to high coefficients of friction.

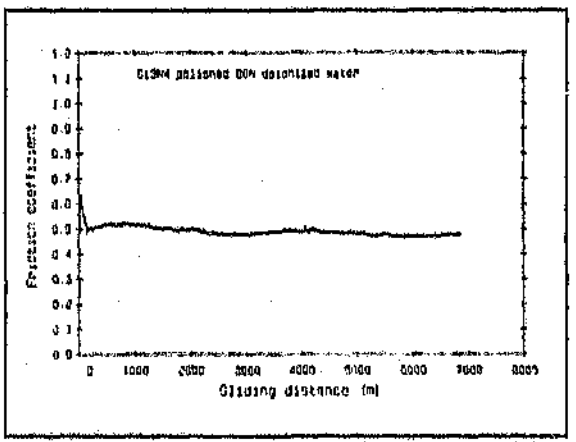

Figure 4.8: Friction trace obtained for AISI 440C sliding against polished Si_3N_4 under a load of 80 N. Note absence of oscillations and high coefficient of friction.

No large-scale oscillations in friction coefficient were observed on ground Sialon and Si_3N_4 surfaces worn under a load of 20 N. This is not inconsistent with the above explanation and can be attributed to differences in contact pressure. The steel balls experienced significantly more wear when tested against the ground ceramics compared to the polished ceramic surfaces, due to the greater surface roughness of the former. The effect on the apparent final contact pressure, as calculated from the wear scar diameters on the steel balls, is summarized in Table 4.4.

Clearly, the contact pressures were significantly lower for the ground surfaces than for the polished surfaces. For ground Si_3N_4, the contact pressure at 50 N was in fact lower than that for polished Si_3N_4 tested under a load of 20 N, which provides an explanation for the fact that no oscillations were observed in the former case. Sialon appears to be more sensitive to contact pressure, as indicated by the fact that no oscillations occurred under pressures of 9.1

increased with increasing applied load and occurred to a greater extent on 3Y-TZP and Ce-TZP than on PSZ, resulting in more extensive transfer layer formation which appeared to reduce both the scatter and the value of the friction coefficient (Section 4.4).

The silicon based ceramics, Sialon and Si_3N_4, generally exhibited the lowest scatter and the lowest and most consistent friction coefficients. However, extended run-in periods associated with high coefficients of friction were observed for polished surfaces subjected to a load of 50 N. Following the initial run-in period, the friction coefficient oscillated between the low, steady-state and the high, run-in values (Figure 4.7). This trend was more marked for Sialon than for Si_3N_4. Detailed analysis of the wear tracks (Section 4.4) revealed that the periods characterized by high friction were not associated with any macroscopic damage on the ceramic surfaces, such as fracture, or the formation of metallic transfer films.

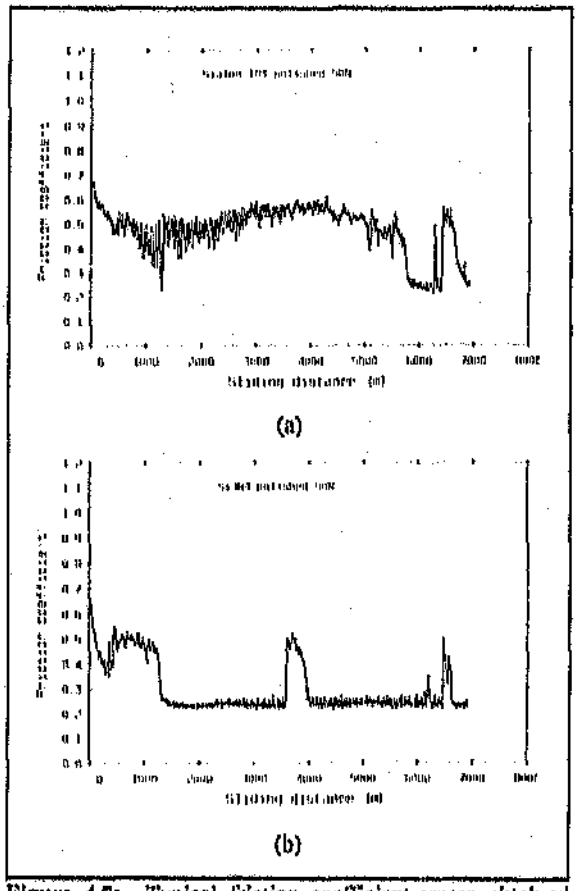

Figure 4.7: Typical friction coefficient traces obtained under a load of 50 N for (a) polished Sialon and (b) polished Si_3N_4.

It is well-known that silicon based ceramics tend to form SiO_2-based surface films during sliding contact, which are generally thought to be lubricious (Sections 2.2 and 2.3). No information could be found on the mechanical properties or load-carrying capacity of such films, however. The low friction coefficients and steady friction behaviour observed in this work tend to confirm that lubricious SiO_2 tribofilms were formed on both Si_3N_4 and Sialon

picture of the surface films. Two sets of XPS measurements were performed on each wear scar, one on the as-worn scar and one after sputter cleaning with argon ions, in order to examine the surface and bulk composition of any surface layers.

4.3 Friction and Wear Results

4.3.1 General friction behaviour

The friction traces obtained for the various material couples are presented in Appendix B. A brief examination of these graphs shows that a distinct two-phase behaviour was observed in most cases, corresponding to a 'run-in' and a 'steady-state' period. The run-in phase was characterized by the rapid development of a 'steady-state' surface on the sliding elements by processes like the removal of surface contaminants and, more significantly, the formation of surface tribofilms, which is discussed in more detail in Section 4.4. Rapid initial wear of the steel ball and, in some cases, the ceramic counterface occurred to establish a well-defined area contact (Section 4.3.3). Consequently, the contact pressure decreased during the run-in phase to a value which could be accommodated by the material couples through steady-state processes like the formation and wear of third-body films.

In general, the steady-state phase was reached within 1000 m or less of sliding. In the case of ground alumina surfaces, however, the run-in phase could be as long as 4000 m whereas more than 5000 m of sliding was required to reach steady-state on ground PSZ surfaces. These results confirmed the need for long test durations to obtain meaningful data.

The scatter in the friction coefficient was generally ± 0.03 or less, particularly for the polished ceramic surfaces. Notable exceptions were the ground PSZ and the ground 3Y-TZP surfaces, which exhibited much greater scatter and less consistent friction behaviour particularly at lower applied loads. For the zirconia ceramics, the scatter tended to decrease in the order PSZ > (3Y-TZP) > (Ce-TZP). These trends are probably related to the combined effects of mechanical polishing, surface fracture and the formation of a metallic transfer layer, composed of compacted wear debris originating from the steel ball. In particular, surface fracture

results obtained for ground and polished alumina under an applied load of 50 N.

As may be expected, the contact pressure fell rapidly in the initial phase of the test in both cases due to initial rapid wear of the steel ball. As the test progressed and the apparent contact area increased, the wear depth increased more slowly which, in turn, caused the contact pressure to decrease at a lower rate.

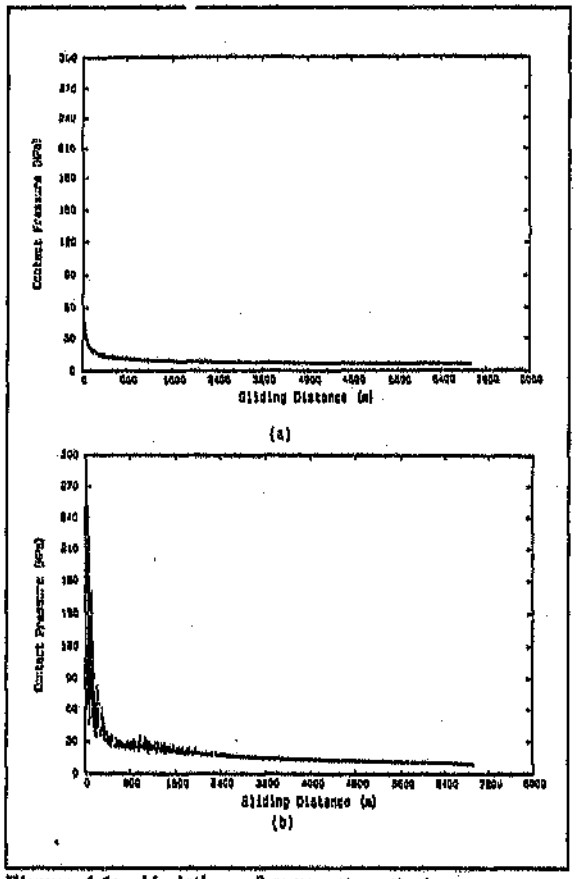

Figure 4.6: Variation of apparent contact pressure as a function of sliding distance for AISI 440C steel sliding on (a) ground and (b) polished alumina.

4.2.3 Analytical techniques

Microscopy

On completion of a test, the ceramic discs and the steel balls were examined with the unaided eye to determine the macroscopic regularity of the wear tracks. More detailed analyses of the wear scars were performed using low magnification optical and high magnification scanning electron microscopy (SEM). Prior to the SEM examination, the ceramic specimens were sputter coated with gold.

Surface analysis

The energy dispersive X-ray (EDS) attachment on the SEM as well as X-ray photoelectron spectroscopy (XPS) was used to characterize the chemical composition of the worn surfaces and any transfer layers. The latter technique is capable of identifying the oxidation states of elements and facilitated the identification of oxides and hydroxides to obtain a more complete

friction coefficient. Consequently, a 12 hour duration was employed for all subsequent friction and wear experiments, corresponding to a sliding distance of 6912 m.

A ball-on-flat contact geometry with initial nominal point contact was selected for all experiments in order to minimize alignment difficulties and avoid the need for an initial running-in period to achieve repeatable specimen contact conditions. A disadvantage of this arrangement is the fact that the apparent contact area increases and the apparent contact pressure decreases as the ball wears. The extent of this variation depends on the wear rate of the ball which, in turn, depends on numerous factors such as the counterface material and surface roughness. In the context of the present work, an attempt was thus made to establish how the contact pressure varies throughout a test.

From geometrical considerations, it can be shown that the worn area on the ball at any point in the test is adequately approximated by:

$$A = \pi (2 R h - h^2) \tag{4.1}$$

where R is the radius and h is the wear depth of the ball.

The apparent contact pressure can then be determined simply by dividing the applied load by the apparent contact area calculated from equation (4.1).

In the present test series, the combined wear of the steel and ceramic specimen is monitored by means of a linear variable differential transducer (LVDT), which measures the downward displacement of the load frame. It is thus generally not possible to substitute this measured wear depth directly in equation (4.1). However, in the case of the AISI 440C-alumina couple, the alumina wears so little that the measured wear depth is very close to the actual wear depth on the steel ball, and it becomes appropriate to use equation (4.1). Figure 4.6 shows the

Table 4.3: Test matrix used for the friction and wear tests.

	Surface Finish					
	Ground			Polished		
	Applied load (N)			Applied load (N)		
Material	20	30	50	20	30	50
Al_2O_3	✓	✓	✓	✓	✓	✓
PSZ	✓	✓	✓	✓	✓	✓
3Y-TZP	✓	✓	✓	✓	✓	✓
Ce-TZP	✓	✓	✓	✓	✓	✓
Sialon	✓	✓	✓	✓	✓	✓
Si_3N_4	✓	✓	✓	✓	✓	✓

$NaNO_3$	940 ppm
Na_2SO_4	2515 ppm
NaCl	475 ppm.

The pH of this mine water was 6,7.

Prior to each test, the specimens were ultrasonically degreased in acetone. The AISI 440C stainless steel ball was then clamped in the reciprocating head while the ceramic disc was mounted in the stationary specimen stage. Both specimens were then cleaned again by wiping with tissue paper soaked in acetone. After setting the stroke length with a digital displacement gauge, the required test parameters were entered in the computer program and the test started. For each experiment, fresh solution was used to flush the contact region.

In the first test series on alumina, a test duration of 1,75 hours was used, corresponding to a sliding distance of 1000 m. This was based on typical test conditions reported in the open literature and seemed to be sufficient for the friction coefficient to stabilize. However, an exploratory experiment run for 12 hours to study the occurrence (or otherwise) of surface fatigue indicated that up to 1500 m of sliding are generally necessary to achieve a steady

Table 4.2: Surface roughness values of ground and polished ceramic discs.

Material	Surface roughness (μm R_a)	
	Ground	Polished
Al_2O_3	0,2	0,04
PSZ	0,2	0,03
3Y-TZP	0,3	0,02
Ce-TZP	0,2	0,01
Sialon	0,4	0,04
Si_3N_4	0,6	0,02

4.2.2 Tribological test conditions and procedures

The actual loads experienced by reciprocating components in water-powered mining equipment are ill-defined due to the dynamic nature of the operating environment. As a first step, detailed examinations of the damage which is typically developed on such components were conducted, followed by exploratory ball-on-disc reciprocating friction and wear tests in an attempt to simulate this damage. It was concluded that a load range of 20 to 50 N would adequately represent the load conditions experienced by such components.

The final selected test matrix is shown in Table 4.3. A frequency of 10 Hz and a stroke length of 8 mm was selected (i.e. an average sliding speed of 0,16 m/s) to reduce vibration and hydrodynamic lubrication effects.

In these experiments the contact was flushed with deionized water to simulate the essential conditions found in hydro-power equipment. Exploratory experiments to study the influence of water chemistry were conducted in a synthetic mine water, Unisel [193], which was a relatively agressive electrolyte prepared by dissolving a number of salts in distilled water:

$CaCl_2.2H_2O$	3411 ppm
$Mg(NO_3)_2.6H_2O$	1170 ppm

Ceramic material properties

The density and porosity of the ceramics was measured by the Archimedes method, which involved weighing the specimens dry and in air, under water, and wet and in air. Mechanical properties like hardness and fracture toughness were determined by indentation techniques, using a Vickers diamond indenter under loads of 10 - 20 kg. The results, representing the average of at least 5 measurements, are summarized in Table 4.1.

Table 4.1: Material properties of the experimental ceramics

Material	Bulk density (g/cm^3)	Apparent porosity	Hardness (GPa)	Toughness ($MPa.m^{1/2}$)
Al_2O_3	3,98	0,036	18,61	3,35
PSZ	8,85	0,011	8,85	~9,1 *
3Y-TZP	6,10	0,023	12,10	~11,0 *
Ce-TZP	6,27	0,253	9,61	~13,0 *
Sialon	3,24	0,392	13,64	~5,0 *
Si_3N_4	3,31	0,169	13,56	~4,5 *

* fracture toughness could not be measured accurately from indentations; these are typical literature values.

Surface preparation

Being ball bearings, the AISI 440C steel balls were highly polished and were used without any further surface preparation, apart from cleaning prior to testing.

The ceramic discs were ground and polished; the R_a values for each material are summarized in Table 4.2. These surface preparations were selected for practical reasons since they are the ones most likely to be used on actual machine components.

zirconia (≤ 0,75 μm) with a very small proportion of larger cubic zirconia grains (Figure 4.4).

Ce-TZP

The Ce-TZP specimens were prepared from commercial 12-Ce powder obtained from Tosoh Corporation, Japan. Sample powders were milled in iso-propyl alcohol with ZrO_2 grinding media. PEG was added as a binder to a level of 2wt%. Sample discs were first uniaxially pressed at 40 MPa and then cold isostatically pressed at 400 MPa. The discs were fired in air at 1 400°C for 4 hours, using heating and cooling rates of 200°C/hour.

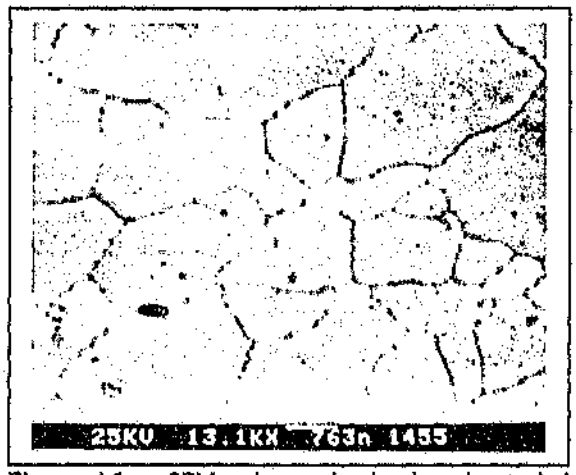

Figure 4.5: SEM micrograph showing the typical microstructure of Ce-TZP ceramic.

The microstructure of the material is shown in Figure 4.5 and consisted of tetragonal zirconia grains 1 - 2 μm in size, with occasional larger grains (up to 3 μm). This microstructure is typical for Ce-TZP and has been commonly observed by other workers [192].

Silicon based ceramics

Sialon 101 specimens in the form of square discs (approximately 14x14x7mm) were cut from a plate specimen obtained from Vesuvius Sialon, England.

Si_3N_4 specimens were obtained from Iscar (Pty) Ltd in the form of cutting tool tips and were used in the as-received condition after suitable surface preparation.

Australia, in the form of 40mm diameter rods. Disc specimens were cut from these rods using a diamond blade.



Figure 4.3: SEM micrograph showing the typical structure of the Mg-PSZ ceramic.

The microstructure of the material was typical of a commercial Mg-PSZ ceramic and consisted of large cubic zirconia grains with tetragonal zirconia precipitates clearly visible at the grain boundaries (Figure 4.3). (The intra-grain tetragonal precipitates were too small to be resolved by scanning electron microscopy).

3Y-TZP

The 3Y-TZP specimens were produced using pre-mixed powder from Toyo Soda, Japan. Round pellets 40 mm in diameter were uniaxially pressed under a load of 35kN. After cold isostatic pressing, the pellets were sintered for optimum toughness using the following heating schedule:

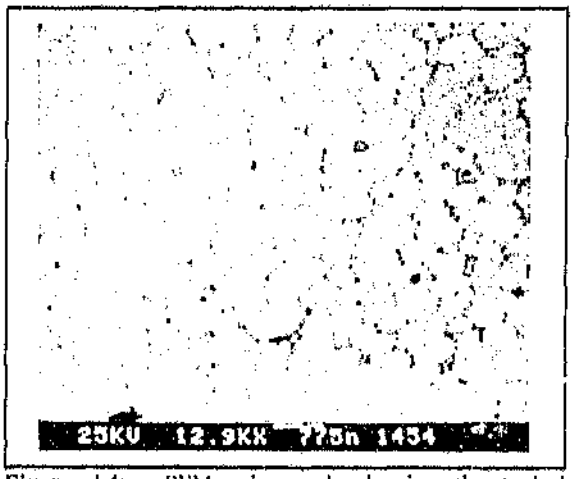

Figure 4.4: SEM micrograph showing the typical microstructure of 3Y-TZP ceramic.

- heat at 5°C/min to 1 500°C, soak for 5 hours; and
- cool at 5°C to room temperature.

As expected, the microstructure of the material consisted of very fine grains of tetragonal

A Leco analysis of the carbon content was performed by an independent laboratory. At 0,99 wt%, the carbon content was within the range specified for AISI 440C stainless steel (0,95 - 1,2 wt%). A check of the remaining elements using a Scanning Auger Microprobe revealed a chromium content of 17,1wt% which is also within the range specified (16,00 - 18,00 wt%).

Alumina

Alumina discs were prepared from 99,5% pure alumina powder (designated RCHPDBM) mixed with 0,03 wt% MgO and 4 wt% polyethylene glycol (PEG) as binder. Cylindrical pellets were uniaxially pressed for 30 seconds under a load of 15 kN and then sintered using the following heating schedule to yield fully dense discs, 25mm in diameter:

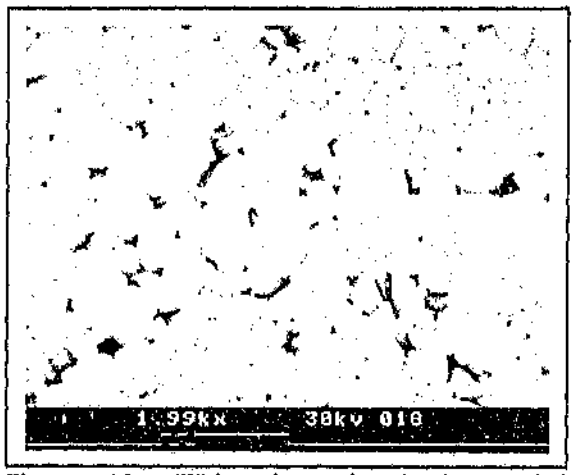

Figure 4.2: SEM micrograph showing typical microstructure of an alumina disc.

- heat at 5°C/min to 300°C, soak for 2 hours;
- heat at 5°C/min to 900°C, soak for 1 hour;
- heat at 5°C/min to 1 500°C, soak for 3 hours; and
- cool at 5°C/min to room temperature.

The microstructure of the resulting material is shown in Figure 4.2 and consisted of alumina grains between ~2 and ~6 μm in size. The material appeared to be relatively brittle, as indicated by the intergranular removal of whole grains during the polishing process.

Partially stabilized zirconia (PSZ)

The Mg-PSZ ceramic (toughness-optimized TS grade) was obtained from Nilcra Ceramics.

the silicon based ceramics at all applied loads. This was attributed to the greater tendency towards surface fracture damage and metallic transfer layer formation on these materials. Wear on the silicon based ceramics occurred primarily by a tribochemical wear mechanism and no surface fracture damage or significant metallic transfer layer formation was noted. The stabilized wear rates were thus significantly lower for these materials compared to the oxide ceramics (Figure 4.12 (b)).

A notable exception to this general trend is Sialon, which behaved in a similar way to Si_3N_4 at low loads, but exhibited wear depths and wear rates similar to the oxide ceramics at a load of 50 N. This was attributed to the fact that Sialon underwent a transition in friction and wear behaviour at a load around 50 N, as indicated also by the friction results (Section 4.2.1). At this load, the silicon-containing tribofilms on the Sialon surface would appear to become unable to support the applied stresses, resulting in a significant increase in friction and wear rates. A similar transition also occurs on Si_3N_4, but at somewhat higher loads, as confirmed by the high friction coefficients obtained under a load of 80 N (Section 4.2.1).

Another significant feature of these results is the fact that the stabilized wear rates are quite similar for both ground and polished ceramic surfaces. This suggests that it may be possible to utilize the ceramic components in the ground rather than the polished condition (except alumina, which shows no surface roughness improvement during sliding), if the higher wear rate during the run-in phase can be accommodated. Fine polishing of ceramic materials is an expensive process and thus this may have significant economic benefits.

Furthermore, the wear rates of the oxide ceramics are considered to be sufficiently similar for both ground and polished surfaces that the selection of a suitable material couple for hydropower equipment can be made on the basis of friction behaviour, rather than wear rate. (Recall that a smooth friction behaviour and low coefficients of friction are important in these components to avoid stick-slip motion). Nevertheless, based on their lower stabilized wear rates, the silicon based ceramic-AISI 440C couples should outlast equivalent couples with oxide ceramic by 30 - 50 % and should thus be given preference.

for alumina. This result is attributable to the fact that polishing was less effective and occurred at a slower rate on these materials. The wear depth curves were characterized by longer run-in periods than the oxide ceramics, which indicated that a longer sliding distance was required to achieve a steady-state surface. A rougher surface was thus maintained on the wear track for a longer time period, resulting in more wear on the steel ball during the run-in period than in the case of the oxide ceramics. This trend was more pronounced for Si_3N_4 than for Sialon, which provides an explanation for the lower wear depths exhibited by Sialon.

The lower rate of polishing may be related to the higher hardness of Sialon and Si_3N_4 compared to the zirconia ceramics (~13,6 GPa compared to ~ 9 GPa for PSZ and Ce-TZP and 12 GPa for 3Y-TZP). Tribochemical wear of the silicon based ceramics by oxidation and dissolution of the ceramic surfaces probably also contributed to polishing. However, residual grinding scratches were observed over most of the wear track, indicating that the rate of material removal by this process was evidently lower than that due wear on the steel ball or that due to the mechanical polishing mechanisms active on the zirconia ceramics.

To summarize, it thus appears that the sliding couples involving Sialon and Si_3N_4 experienced greater wear than the oxide ceramics in the early stages of the tribotests due to a lower rate of surface polishing and a longer run-in phase. If this explanation is correct, the oxide ceramics would be expected to exhibit generally higher wear rates than the silicon based ceramics in the steady-state portion of the test, since the overall wear depths were similar for both. By referring to Figure 4.11 (b), it will be seen that this was indeed the case, particularly at high loads of 50 N.

Notwithstanding the similar overall wear depths, the silicon based ceramics would thus be expected to outlast the oxide ceramics by up to 30 % under similar operational conditions. This result vindicated the present analysis approach of quantifying the stabilized wear rate as well as the overall wear of the sliding couple, rather than relying only on measurements of the overall wear of the individual sliding elements.

For polished ceramic surfaces, the oxide ceramics exhibited generally greater wear depths than

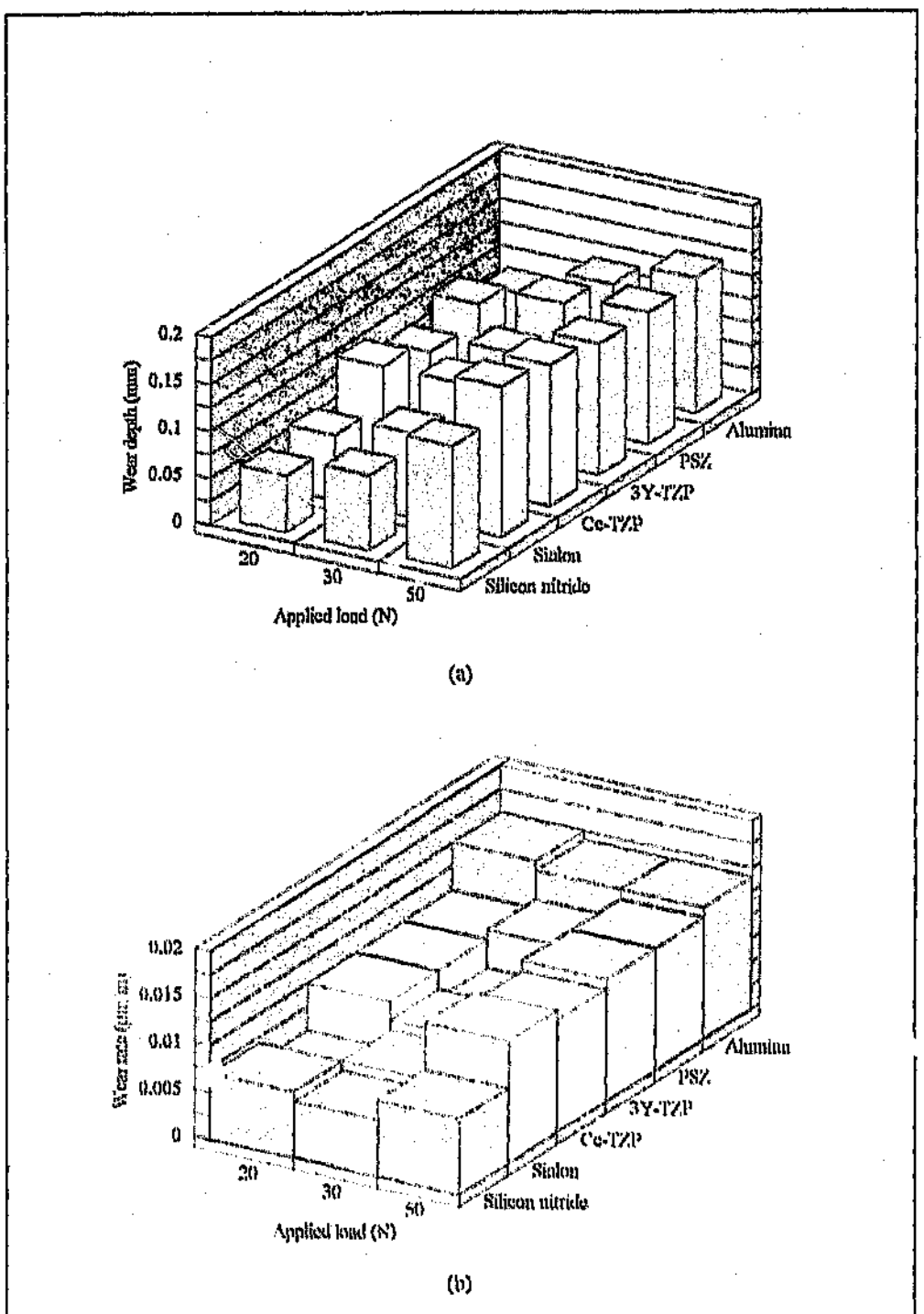

Figure 4.12: Total wear depth (a) and stabilized wear rates (b) for sliding couples involving polished ceramic surfaces.

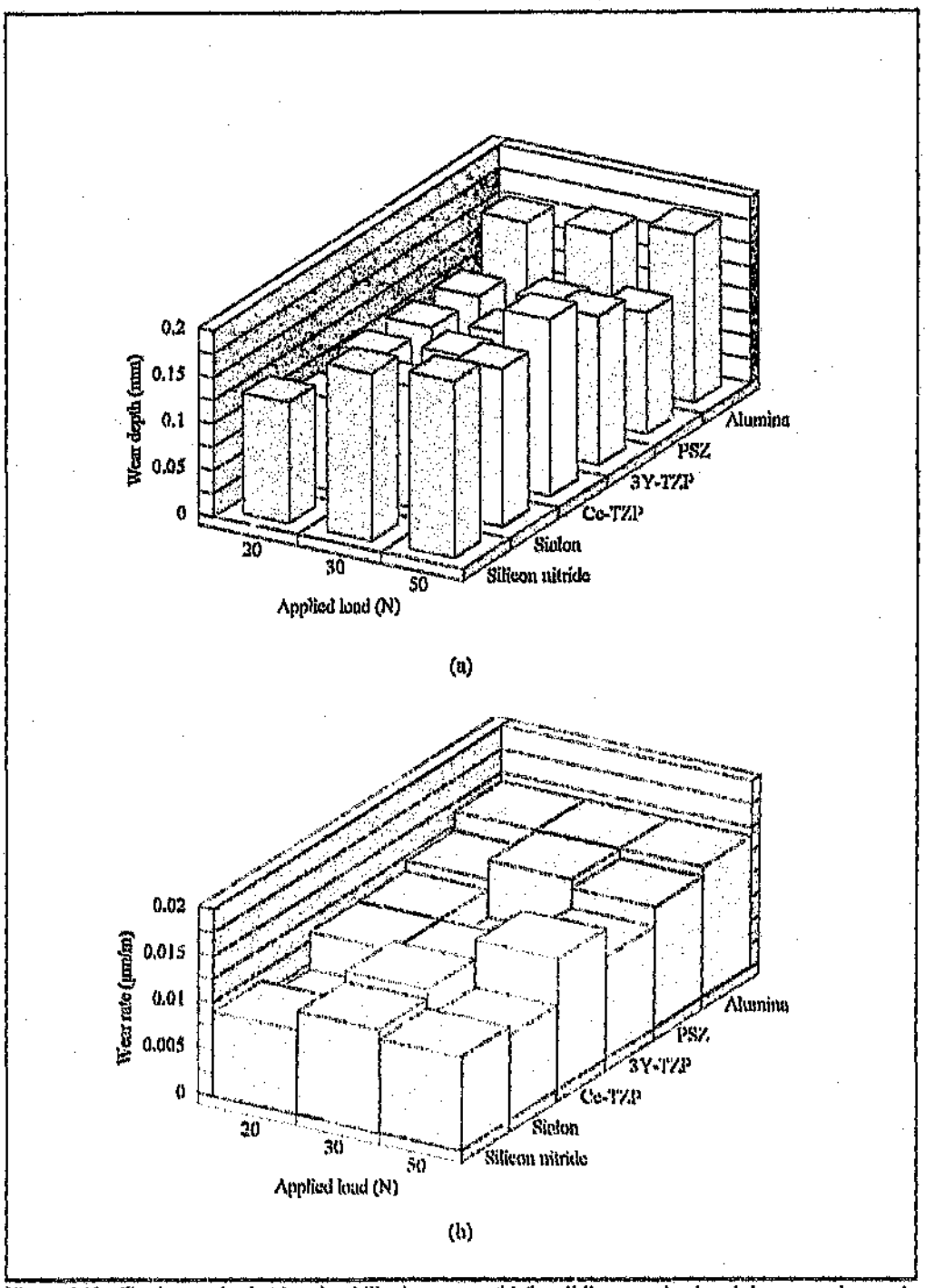

Figure 4.11: Total wear depth (a) and stabilized wear rate (b) for sliding couples involving ground ceramic surfaces.

Table 4.6: Summary of wear depth and steady-state wear rate results obtained for the various sliding couples.

		Surface finish and applied load (N)					
		Ground			Polished		
Material	Parameter	20	30	50	20	30	50
Al_2O3	Wear depth (mm)	0,15	0,16	0,18	0,09	0,12	0,14
	Wear rate (µm/m)	0,014	0,014	0,014	0,015	0,014	0,014
PSZ	Wear depth (mm)	0,11	0,12	0,13	0,11	0,13	0,14
	Wear rate (µm/m)	0,012	0,014	0,013	0,010	0,011	0,013
3Y-TZP	Wear depth (mm)	0,11	0,12	0,16	0,9	0,11	0,14
	Wear rate (µm/m)	0,011	0,008	0,011	0,010	0,007	0,013
Ce-TZP	Wear depth (mm)	0,12	0,13	0,19	0,11	0,11	0,15
	Wear rate (µm/m)	0,011	0,011	0,014	0,010	0,008	0,012
Sialon	Wear depth (mm)	0,10	0,14	0,17	0,07	0,09	0,16
	Wear rate (µm/m)	0,007	0,012	0,009	0,005	0,007	0,013
Si_3N_4	Wear depth (mm)	0,13	0,18	0,19	0,06	0,08	0,13
	Wear rate (µm/m)	0,009	0,011	0,010	0,007	0,006	0,006

However, under an applied load of 50 N, the wear depth for the zirconia ceramics increased in the order PSZ - (3Y-TZP) - (Ce-TZP), with the wear depth for Ce-TZP becoming similar to that for alumina. This is thought to be related to the increasing amounts of fracture damage observed on the latter materials at these higher loads. In the case of 3Y-TZP and Ce-TZP, most of the polished region of the wear track worn under a 50 N load was roughened again by surface fracture, resulting in increased abrasion of the steel ball as evidenced by the presence of thick metallic transfer layers in these areas.

The silicon based ceramics showed wear depths of a similar magnitude to those for the zirconia ceramics, despite the fact that only polishing and no fracture damage occurred in the wear tracks, which could have contributed to wear of the steel ball. In fact, in the case of Si_3N_4 the wear depths at applied loads of 30 and 50 N were even larger and similar to those

Analogous to the friction results, the wear depth traces showed a distinct two-phase behaviour, characterized by a more or less pronounced run-in phase followed by a steady-state phase (Figure 4.10). During the run-in phase, the wear depth increased rapidly and this was associated with the formation of a well-defined area contact between the specimens. As outlined in Section 4.2.2, the contact pressure between the specimens dropped rapidly during this stage of a test. During the steady-state phase, the contact pressure decreased at a much lower rate and the wear rate was essentially constant.

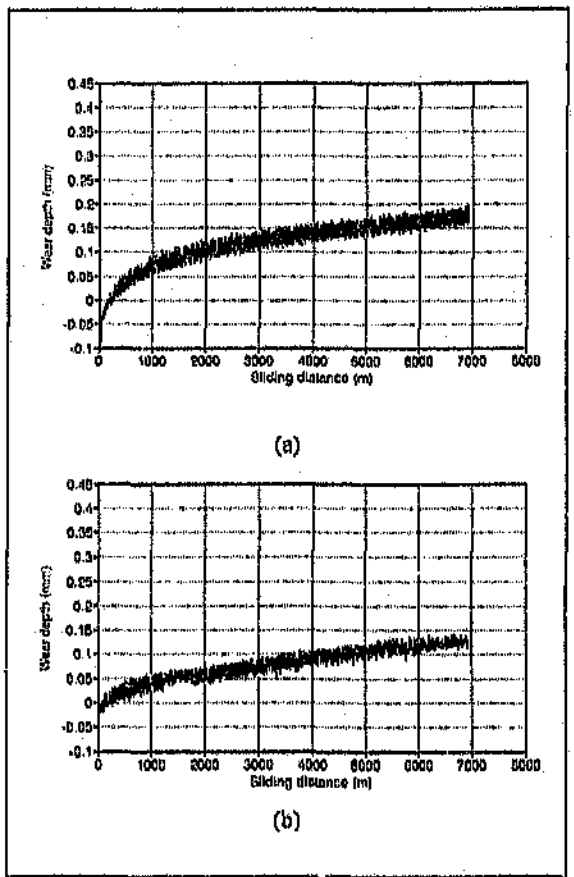

Figure 4.10: Typical wear depth traces for (a) ground and (b) polished alumina (dry sliding, 50N load).

To characterize the wear behaviour of the various couples, the total wear depth for the test as well as the steady-state wear rate (in μm/m of sliding) was determined from these traces. The results are summarized in Table 4.6 and shown graphically in Figures 4.11 and 4.12.

In the case of ground ceramic surfaces, alumina showed the highest wear depth of the oxide ceramics at all loads. This is probably related to the high hardness of alumina and the consequential high wear rate on the steel ball by abrasion and adhesion. The zirconia ceramics showed generally lower wear depths and this was attributed to the polishing effect observed on these materials, which improved the average surface roughness over the wear track and thus reduced the contribution to the wear depth by abrasive wear of the steel ball.

This approach was deemed unsuitable for the present work for a number of reasons:

i. Metal-ceramic sliding couples are often charaterized by the formation of metallic transfer layers on the ceramic counterface. While material is removed from the metal counterface, it is thus not necessarily lost from the sliding system and, in the form of a transfer layer, continues to contribute to the accommodation of applied load and interfacial sliding. Mass loss measurements on the ceramic counterface do not take this into account, unless measurements are performed before and after removal of any transfer layers (which is typically not done).

ii. In the hydropower systems under consideration, the increase in clearance between the sliding components is of prime importance since this determines the leakage rate of the hydraulic fluid. Thus, while localized surface fracture damage may occur on the ceramics, the function of the components may remain essentially unimpaired if the resulting surface irregularities are filled and smoothed by a metallic transfer layer. Simple mass loss measurements provide no information on these processes and their influence on total clearance loss.

iii. Finally, pronounced run-in behaviour is observed for metal-ceramic sliding point contacts, which is the geometry used in the present work. Mass loss measurements performed at the end of a test incorporate the rapid wear which takes place during run-in and provide no information on the steady-state wear rate of the total couple.

In the light of these considerations, it was decided to quantify wear using the LVDT measurements of the wear depth resulting from the combined wear of the steel ball and the ceramic counterface. These measurements take into account the effects of transfer layer formation and the like and provide a relevant indication of the increase in clearance between the sliding partners.

Polished ceramic surfaces

The alumina, 3Y-TZP and Ce-TZP ceramics exhibited a decreasing trend in friction coefficient with increasing applied load. This was associated with a concomitant increasing trend in the extent of metallic transfer layer formation, which suggests that such layers were beneficial in reducing friction. Similarly, for the zirconia ceramics a decreasing trend in friction coefficient was observed in the order PSZ > (3Y-TZP) > (Ce-TZP) at applied loads of 30 and 50 N. The extent of surface fracture and metallic transfer layer formation increased in the same order, which tends to confirm this relationship.

The friction coefficients exhibited by Sialon and Si_3N_4 were again significantly and consistently lower than those of the oxide ceramics and remained unaffected by the applied load. This was attributed to the formation of lubricious Si-containing surface films and the absence of significant surface damage and metallic transfer layers.

Furthermore, the friction coefficients for the polished Si_3N_4 and, to a lesser extent, Sialon surfaces were very similar to those for the ground surfaces, particularly for higher applied loads. This is consistent with the findings of Denape *et al* [196], who found that the friction response of Si_3N_4 sliding on steel was influenced by the ceramic surface roughness over only a short transitory stage. The effect was ascribed to the polishing of the ceramic surfaces during sliding, which was confirmed in this work.

4.3.3 Wear results

During a review of the published literature (Chapter 2), it was noted that most investigators quantified wear by means of mass loss or dimensional measurements on each of the two sliding elements. The data was then typically reported in the form of volume loss, or in terms of wear coefficients for each element (i.e. in $mm^3/m.N$ or, if the dimensionless wear coefficient is used, in terms of $mm^3/m.N$ multiplied by the hardness of the sliding material).

similar in appearance to those observed on alumina, and covered a large proportion of the wear track area. The stabilized friction coefficients for these materials and their dependence on applied load were therefore similar to those for alumina, since much the same conditions prevailed at the sliding interface.

At low loads (20 N), polishing was less effective on 3Y-TZP than on Ce-TZP. This is attributable to the higher hardness of this material (12,1 GPa compared to 9,61 GPa) since the solubility of zirconia in water, like that of alumina, is too low for tribochemical polishing [195]. Therefore, polishing of zirconia surfaces must occur mainly by mechanical processes such as microabrasion and plastic deformation, which are controlled by material hardness. The grinding scratches on 3Y-TZP were thus retained over a greater proportion of the wear track area, resulting in a higher coefficient of friction. With increasing load, the wear track surfaces became very similar in appearance to the Ce-TZP wear tracks, resulting in similar coefficients of friction.

On the PSZ surfaces, the centre of the wear track was polished effectively at all applied loads, due to the relatively low hardness of the material (8,85 GPa). Surface fracture occurred in localized regions of the central portion of the wear track and metallic transfer layers were formed only in small patches. The surfaces exhibited a similar appearance at all applied loads, which provides an explanation for the apparent insensitivity of the friction coefficient to this parameter.

The silicon based ceramics showed a slight decreasing trend in friction coefficient with increasing load, probably as a result of more extensive polishing of the wear tracks. The friction coefficients were consistently and significantly lower than those for the oxide ceramics. This is attributable to the formation of lubricious Si-containing films on the ceramics and the absence of significant surface fracture damage and thick metallic transfer films (although residual grinding scratches were in many cases filled with compacted wear debris).

In the case of alumina, no improvement in surface roughness by polishing occurred at any applied load. This is most likely related to the high hardness of the material, since polishing of alumina occurs primarily by mechanical processes such as microabrasion. The surface irregularities were filled with metallic debris from the steel ball, eventually leading to the formation of transfer films at all loads. According to the theoretical description by Bowden and Tabor [194], the friction coefficient in the presence of an interfacial film is given by:

$$\mu = \frac{\tau_f}{H} \tag{4.2}$$

where τ_f is the shear strength of the film and H is the hardness of the metallic layer in the case of a thick layer, or the hardness of the softer sliding element (in this case the steel) where the interfacial layer is thin. In the present case for alumina, relatively thick and continuous metallic transfer layers were observed at all loads. Therefore, the hardness and shear strength of the layers would have approached constant values and thus constant friction coefficients were obtained.

A more complex combination of processes like polishing, surface fracture and the formation of metallic transfer layers occurred on the zirconia ceramics (more details are provided in Section 4.4). Polishing was observed in the centre of the wear tracks, resulting in the removal of grinding scratches and a significant improvement in surface roughness. If this were the only effect, the friction coefficients for these materials would be expected to be significantly lower than those for alumina, due to the reduced contribution of asperity interlocking to the friction coefficient. However, the polished area covered only a portion of the wear track and the grinding scratches were partially retained near the edges of the track. Despite the fact that the scratches tended to be filled with metallic wear debris, these areas could thus have contributed towards a higher friction coefficient.

Furthermore, the roughness in the polished centre regions of the wear tracks on 3Y-TZP and Ce-TZP was increased again as a result of surface fracture, particularly at higher applied loads. These damaged areas were associated with thick and continuous metallic transfer films

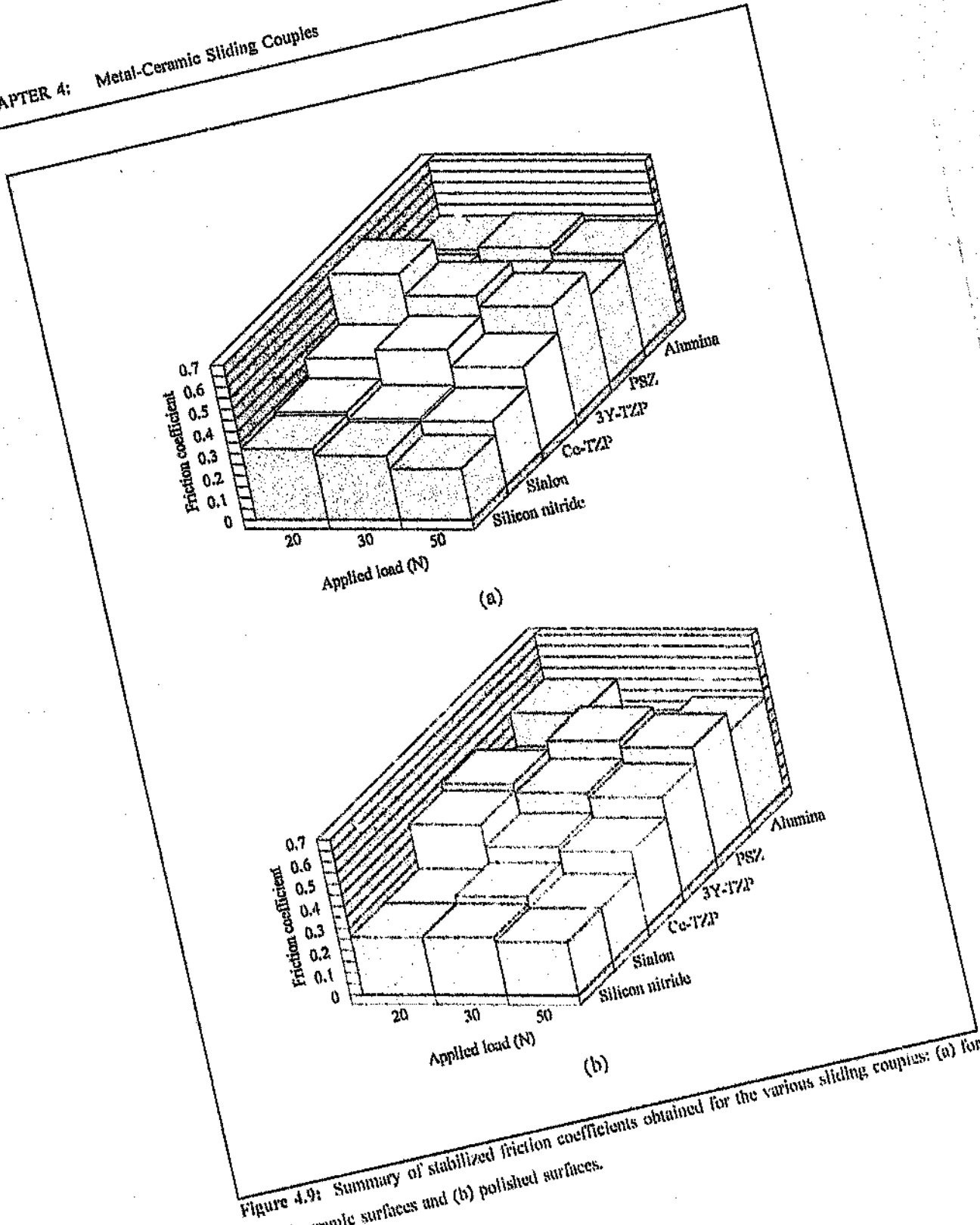

Figure 4.9: Summary of stabilized friction coefficients obtained for the various sliding couples: (a) for ground ceramic surfaces and (b) polished surfaces.

4.3.2 Friction coefficient results

To provide a comparative basis, the stabilized coefficients of friction were determined from the steady-state portion of the friction traces. The results are summarized in Table 4.5 and shown graphically in Figure 4.9.

Table 4.5: Stabilized friction coefficients for AISI 440C stainless steel sliding against the various ceramics.

Ceramic surface finish	Applied load (N)	Friction coefficient for ceramics					
		Al_2O_3	PSZ	3Y-TZP	Ce-TZP	Sialon	Si_3N_4
Ground	20	0,45	0,43	0,65	0,42	0,33	0,32
	30	0,46	0,4	0,55	0,46	0,3	0,29
	50	0,43	0,4	0,5	0,38	0,29	0,23
Polished	20	0,5	0,35	0,49	0,46	0,26	0,26
	30	0,36	0,53	0,45	0,36	0,29	0,26
	50	0,42	0,5	0,43	0,34	0,24	0,24

The repeatability of these coefficients was generally within ± 0,02, except for the zirconia ceramics, particularly PSZ, where the repeatability was typically no better than ± 0,04 as a result of large-scale fluctuations in the friction behaviour.

Ground ceramic surfaces

For ground ceramic surfaces, the coefficients of friction exhibited by the oxide ceramics were generally similar and, with the exception of 3Y-TZP, appeared to be largely independent of the applied load. This is consistent with the findings of He *et al* [150] and is attributable to the development of very similar transfer layers on the ceramics.

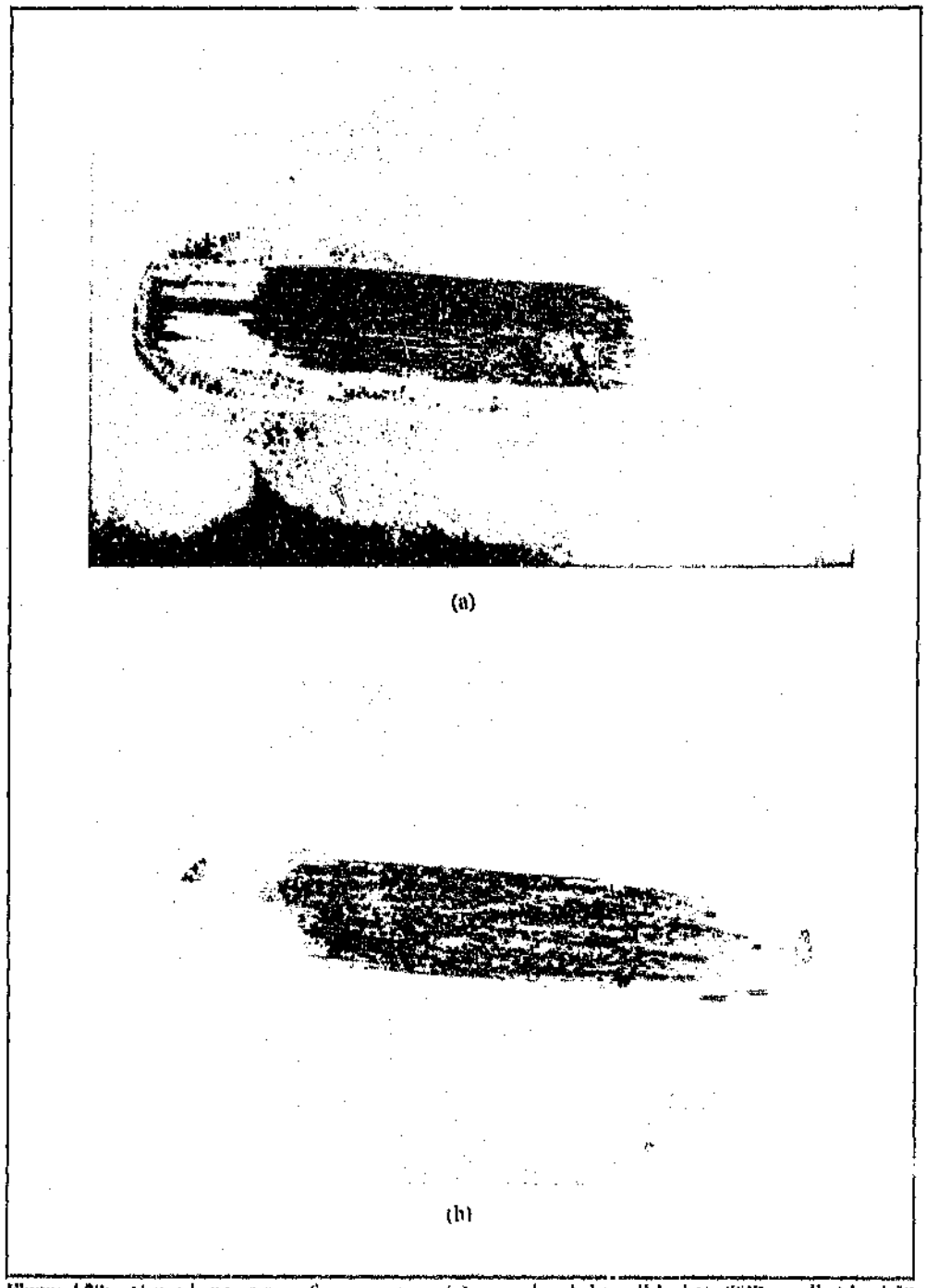

Figure 4.20: General appearance of wear scars on (a) ground and (b) polished Co-TZP (applied load 50 N, magnification 8x).

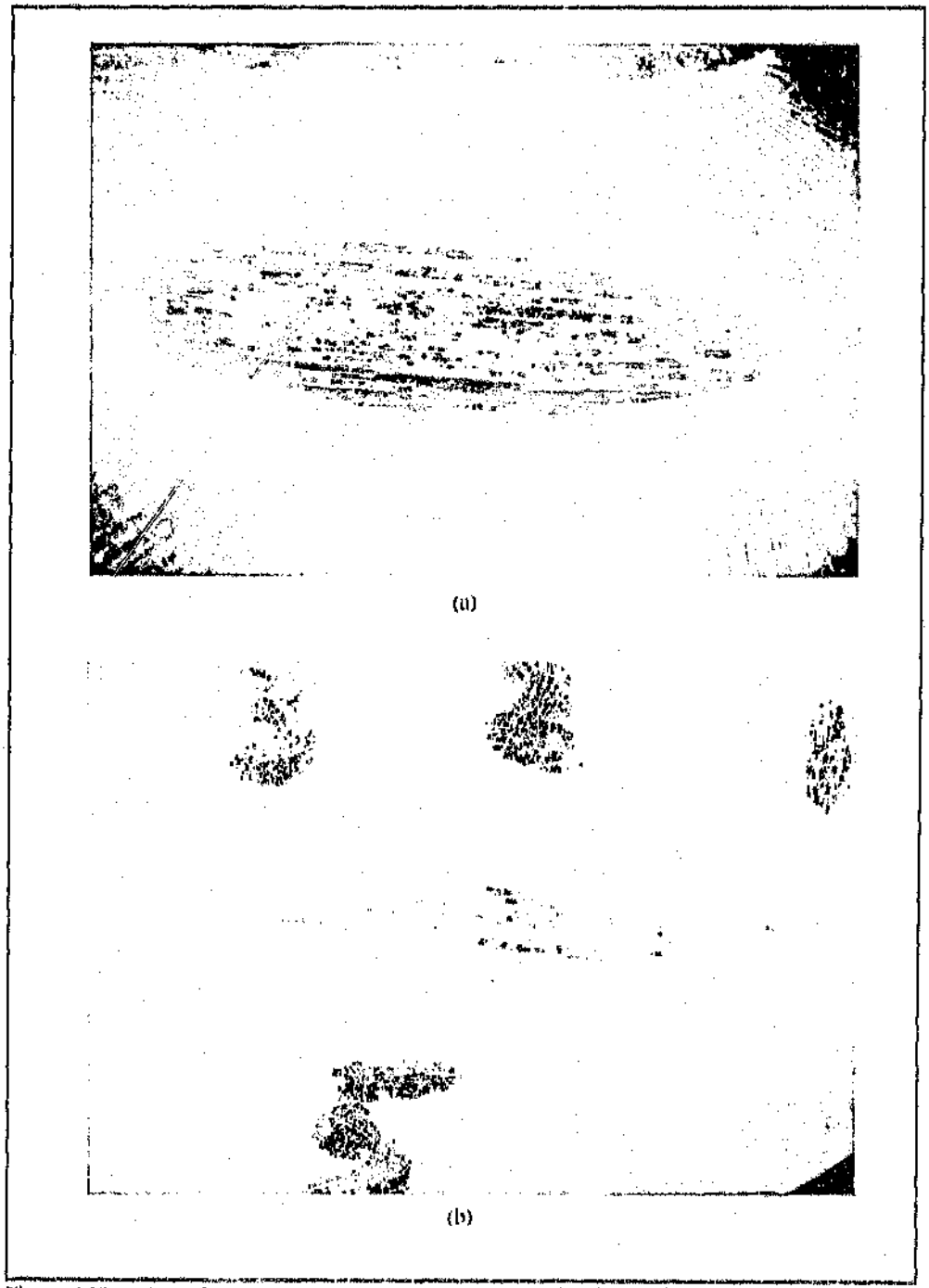

Figure 4.19: General appearance of wear scars on (a) ground and (b) polished 3Y-TZP (applied load 50 N, magnification 8x).

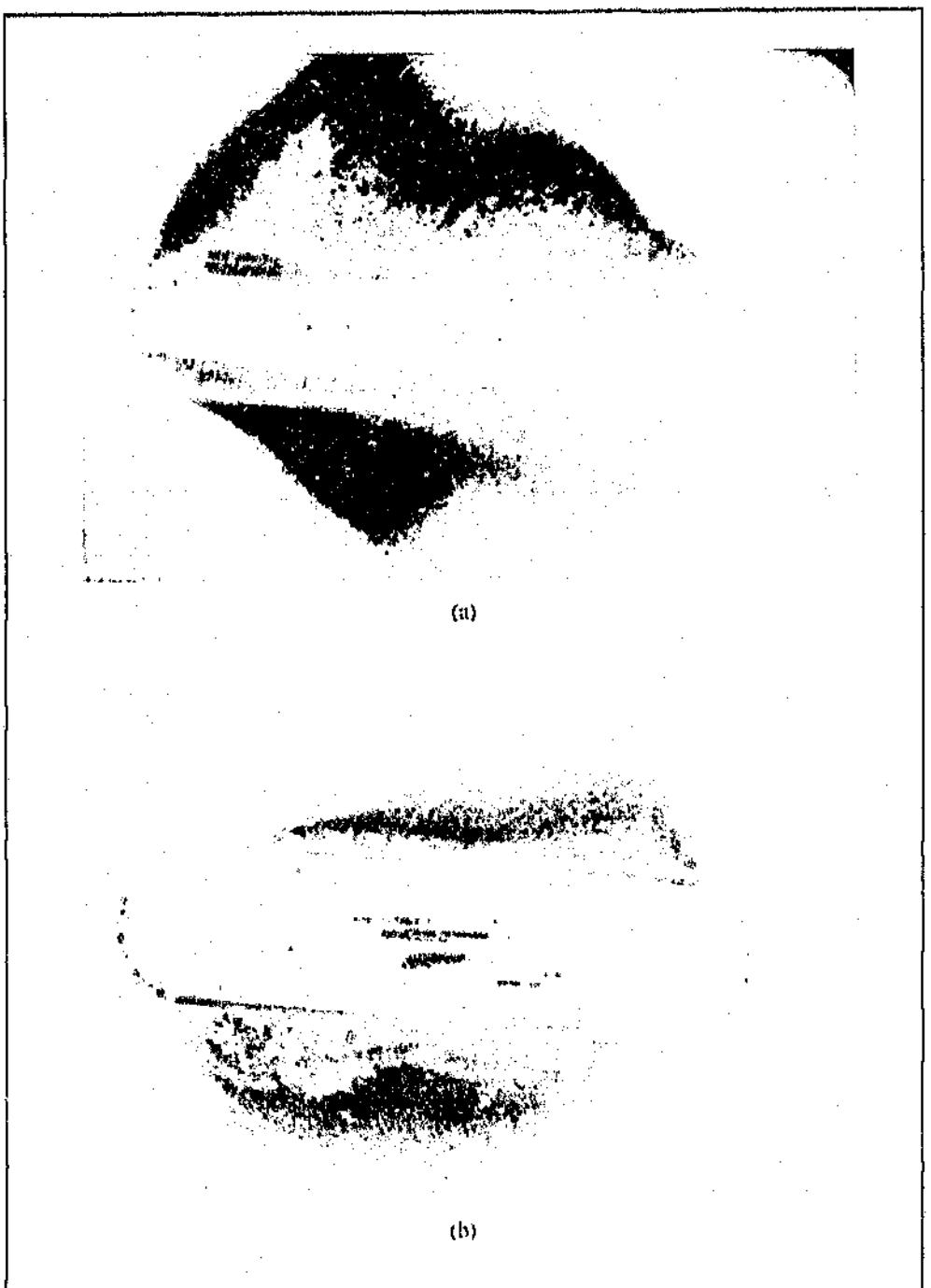

Figure 4.18: General appearance of wear scars on (a) ground and (b) polished PSZ (applied load 80 N, magnification 8x).

Table 4.9: XPS analysis results obtained on polished alumina after 6912 m of sliding under a load of 50 N.

Peak	Binding energy (eV)	Species	Sensitivity factor	Atomic %
C (1s)	285	-	0,2	20,0
Al (2p)	75,2	Alox	0,1	29,0
O (1s)	530	-	0,61	50,4
Fe (2p)	714,4	FeOOH / Fe_2O_3	1,76	0,6
			Total	100

low-speed sliding conditions used in this work.

The formation of lubricious aluminium hydroxides when sliding in water has been reported by numerous workers [84][97][149]. However, the formation of such compounds could not be confirmed in the present analyses and it is considered unlikely that they played a major rôle in determining friction and wear behaviour.

4.4.2 Zirconia ceramics

The general appearance of typical wear scars generated on ground and polished surfaces of the zirconia based ceramics under a load of 50 N is shown in Figures 4.18 - 4.20. The ceramics clearly tended to develop a characteristic surface finish during sliding which was largely independent of the original surface roughness. There was a trend towards increasing fracture in the wear scars, associated with the formation of metallic transfer layers, in the order PSZ - (3Y-TZP) - (Ce-TZP). These aspects were studied in more detail using SEM, and the findings are discussed below under separate headings.

Table 4.7: XPS analysis results obtained on polished alumina after 48 m of sliding under a load of 50 N.

Peak	Binding energy (eV)	Species	Sensitivity factor	Atomic %
C (1s)	285	-	0,25	15,6
Al (2s)	118,8	Al_2O_3	0,23	22,4
O (1s)	530,9	-	0,61	57,8
Fe (2p)	710,2	FeOOH / Fe_2O_3	1,76	2,5
Cr (2p)	577,2	CrOOH	1,53	1,7
			Total	100

Table 4.8: XPS analysis results obtained from a typical wear track on polished alumina after 6912 m of sliding under a load of 50 N.

Peak	Binding energy (eV)	Species	Sensitivity factor	Atomic %
Analysis on the as-worn surface				
C (1s)	285	-	0,25	27,0
Al (1s)	119,1	Al_2O_3	0,23	8,6
O (1s)	531,1	-	0,61	53,5
Fe (2p)	710,1	FeOOH / Fe_2O_3	1,76	6,6
Cr (2p)	577,1	CrOOH	1,53	4,3
			Total	100,0
Analysis after sputtering				
C (1s)	285	-	0,4	58,2
Al (2s)	119,2	Al_2O_3	0,61	39,8
O (1s)	530,5	-	1,76	1,9
Fe (2p)	709,2	FeO		
Cr (2p)	576,7	Cr_2O_3		
			Total	100

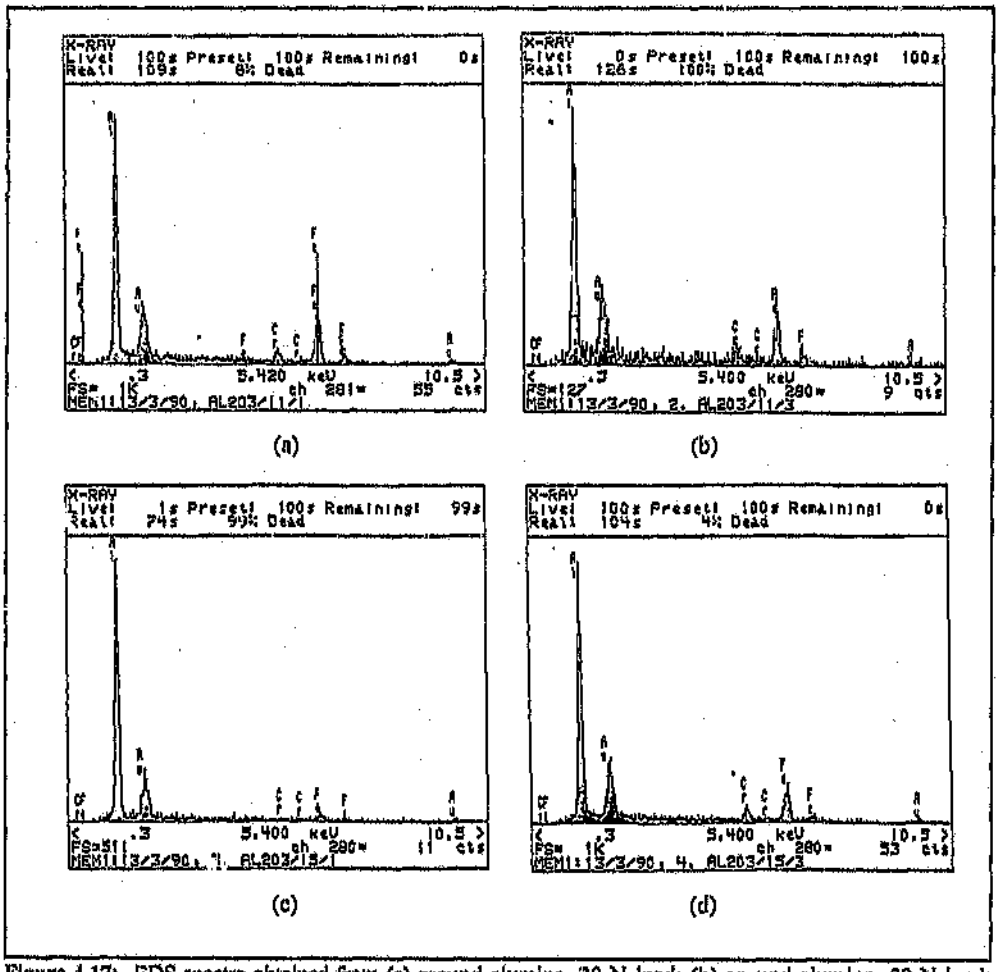

Figure 4.17: EDS spectra obtained from (a) ground alumina, 20 N load; (b) ground alumina, 50 N load; (c) polished alumina, 20 N load; and (d) polished alumina, 50 N load, confirming that transfer layers on these surfaces originated from the steel ball.

A further XPS analysis was thus performed on a carefully selected area of the wear track worn for a sliding distance of 6912 m, where very few pores were present. The results indicated the presence of small amounts of $FeOOH/Fe_2O_3$, but a relatively large proportion of a complex aluminium oxide which could not be uniquely identified (Table 4.9). This result provided tentative evidence for some form of direct chemical interaction between the oxide debris originating from the steel ball and the underlying alumina ceramic surface. The formation of an aluminium-iron oxide spinel could not be confirmed, possibly due to the lower contact temperatures which would be developed under the water-lubricated, relatively

oxide (Fe_2O_3) and chromium oxide (Cr_2O_3), which are relatively hard even when compared to alumina (~10 GPa for Fe_2O_3 [198] and ~12.7 GPa for Cr_2O_3 [199] against 19 GPa for the alumina surface). The oxides could thus easily have acted as a polishing medium by abrading the alumina on a small scale.

EDS analyses confirmed that the transferred material on both ground and polished alumina surfaces originated from the steel ball (Figure 4.17). The presence of such layers on polished, undamaged alumina surfaces indicated that strong adhesion and possibly some chemical interaction between the steel and the alumina had occurred. This is plausible in view of the fact that alumina is known to form solid solutions with iron oxides [200]. Direct analytical evidence for such effects is scarce, however, and appears to be limited to reports of the formation of an aluminium-iron oxide spinel at high sliding speeds [139]. To study these aspects, detailed XPS analyses were performed on polished alumina surfaces which were worn against AISI 440C stainless steel for various sliding distances under an applied load of 50 N.

After 48 m of sliding, a very faint transfer layer was visible on the alumina surface. The XPS data indicated that this layer comprised FeOOH and/or Fe_2O_3 (the binding energies for FeOOH and Fe_2O_3 overlap) and CrOOH (Table 4.7). This may be attributed to hydration of oxide wear debris since deionized water was used as lubricant. The layers formed after 4032 and 6912 m of sliding were more well-developed and exhibited similar compositions. Not surprisingly, the outer surfaces of these layers contained FeOOH/Fe_2O_3 and CrOOH, whereas the bulk of the layers, analyzed after sputtering the top surface of the layer away with argon ions, comprised mainly FeO and Cr_2O_3 (Table 4.8). Significant amounts of Al_2O_3 were also detected in all these analyses, which suggested that either some intermixing of debris from the steel ball and the alumina substrate occurred, or that the transfer layers were thin and patchy. The XPS analysis spot size is quite large (~ 1 mm^2) and thus the results could have been dominated by signals originating from thicker patches of steel oxide debris compacted into the pores on the ceramic.

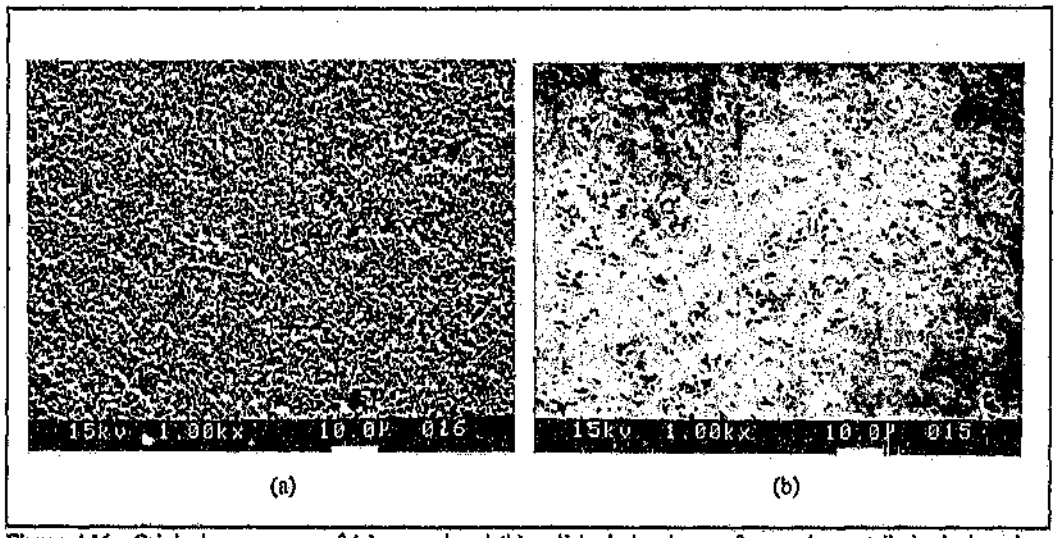

Figure 4.16: Original appearance of (a) ground and (b) polished alumina surfaces prior to tribological testing.

On the polished alumina surfaces, fairly continuous, dark brown metallic transfer layers were clearly seen under the optical microscope (Figure 4.13), but were not obvious under the scanning electron microscope (Figure 4.15). The transfer layers were thus very thin and smooth in the centre of the wear tracks. Thick, cracked transfer layers similar to those found on the ground ceramic were only developed in the low-stress regions at the edges of the wear scar (Figures 4.15 (b) and (d)).

Furthermore, shallow pits similar in shape to the alumina grains in the microstructure were commonly observed on the wear tracks, particularly at lower applied loads (arrowed in Figure 4.15 (a)). Some of the pits exhibited abrasive grooves which often terminated at the pit boundary. The development of similar grain relief has been reported by Wallbridge *et al* [64] and Gee [197] in studies of the sliding wear of self-mated alumina, and can be ascribed to anisotropic wear of the ceramic. Mild abrasive wear on a very fine scale was suggested by Gee [197] as a possible mechanism for the formation of grain relief.

In the present case, some loose wear debris was present in the sliding interface, as indicated by the fact that such debris was compacted in the irregularities on the ceramic surface, analogous to ground alumina. As will be shown later, much of the debris comprised iron

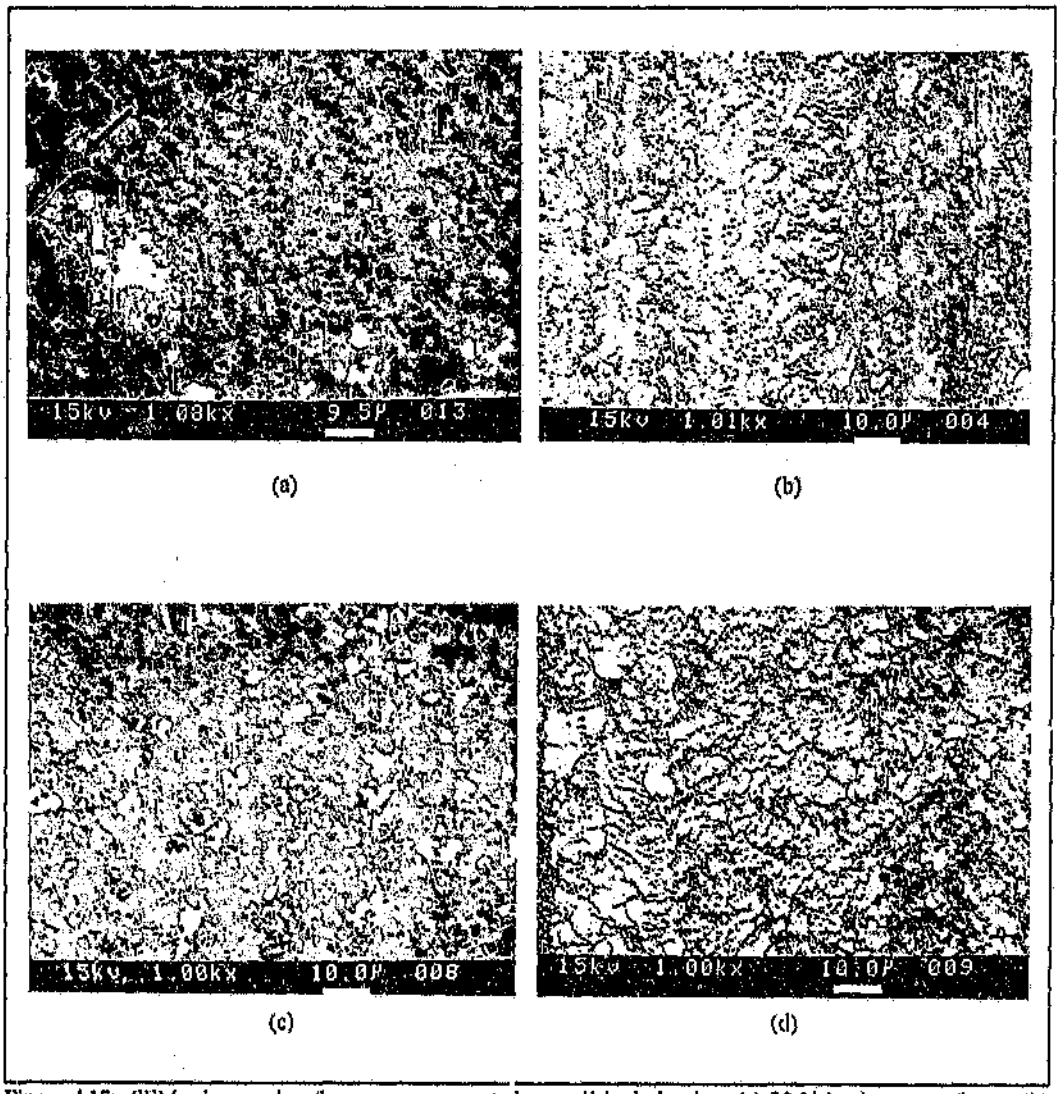

Figure 4.15: SEM micrographs of wear scars generated on polished alumina: (a) 20 N load, centre of scar; (b) 20 N load, edge of scar; (c) 50 N load, centre of scar; and (d) 50 N load, edge of scar.

although perhaps only semi-continuous, carried much of the applied load and also contributed significantly towards accommodating the relative sliding motion between the AISI 440C steel ball and the alumina disc. As outlined in the foregoing sections, the layers thus played a major rôle in determining the friction and wear behaviour of the material couple.

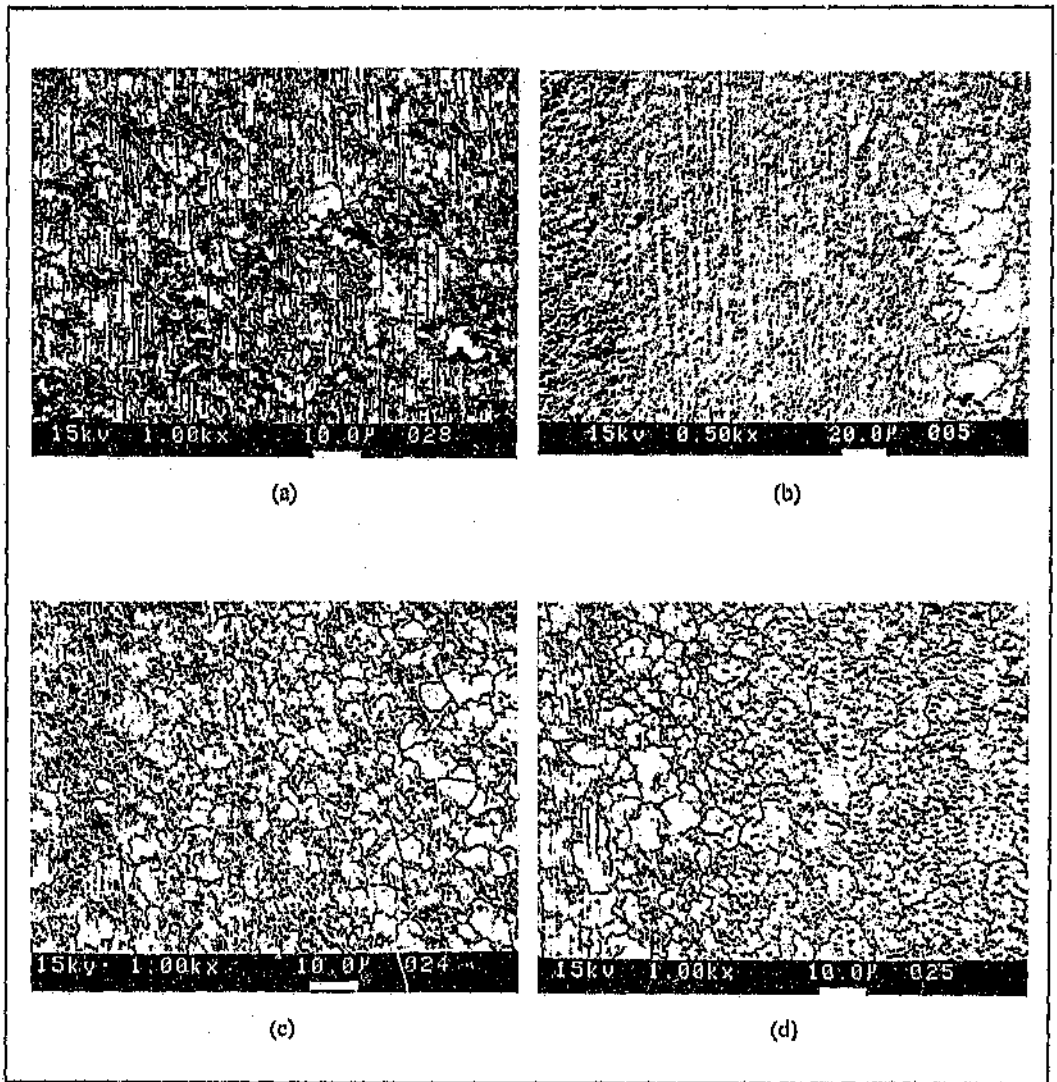

Figure 4.14: SEM micrographs of wear scars generated on ground alumina surfaces: (a) 20N load, centre of scar; (b) 20 N load, edge of scar, (c) 50 N load, centre of scar; and (d) 50 N load, edge of scar. Lighter areas are the metallic transfer layer, darker areas the alumina surface.

An extensive network of cracks in the films suggested that they were mechanically relatively weak. Abrasive score marks and cracks were observed in the direction of sliding, indicating that some loose metal oxide and/or ceramic debris was present in the sliding interface. There was also some evidence for plastic deformation of the films (illustrated in the left-hand portion of Figure 4.14 (d)). The presence of these features indicated that the transfer layer,

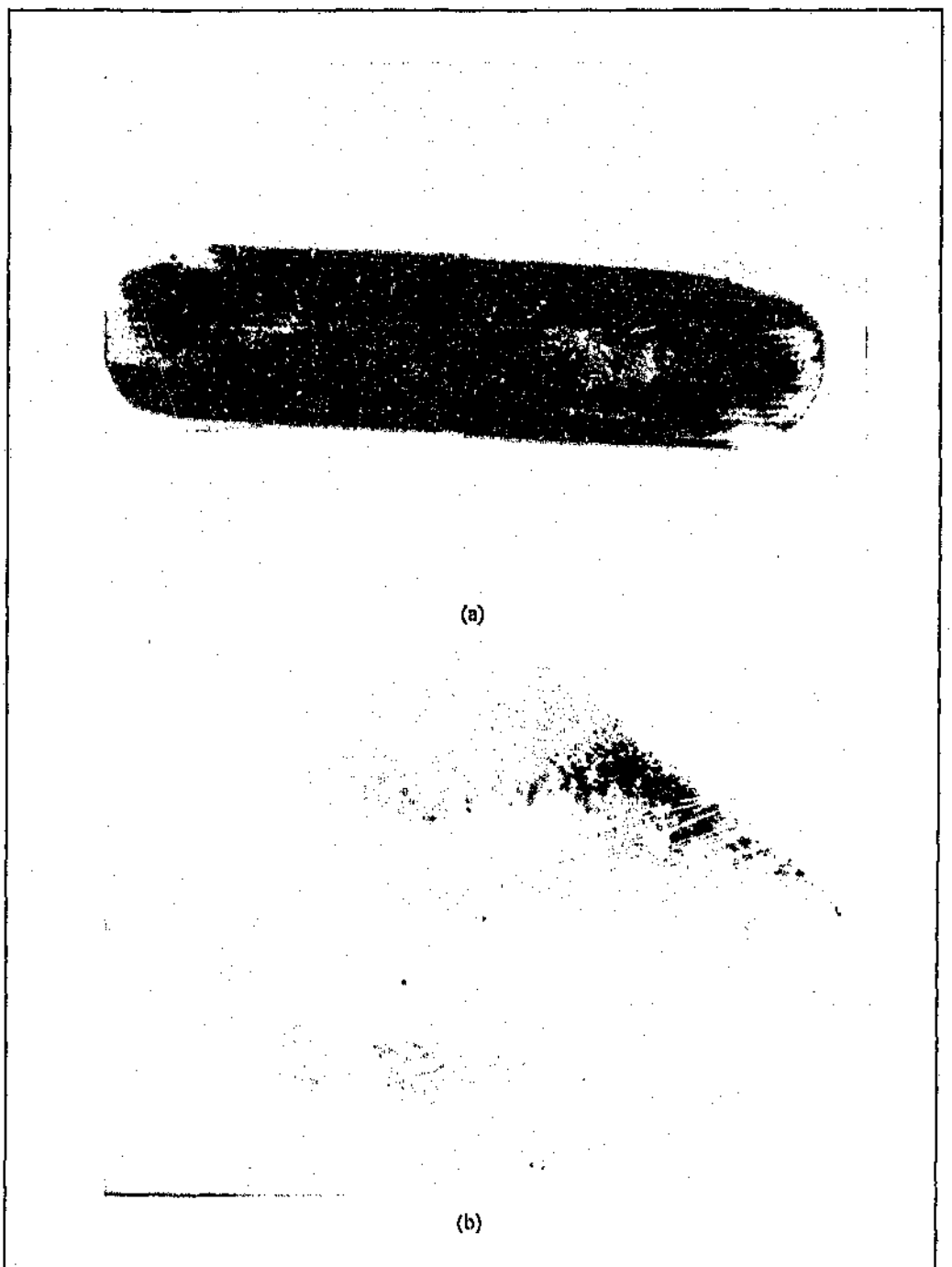

Figure 4.13: General appearance of wear scars on (a) ground and (b) polished alumina (load 50 N, magnification 50 x).

4.4 Wear Scar Development and Tribofilm Formation

4.4.1 Alumina

A general view of the wear scars produced on ground and polished alumina surfaces under a load of 50 N is shown in Figure 4.13. It should be noted that the appearance of these scars was similar to those produced on comparable alumina surfaces under lower loads of 30 and 20 N. Significant material-transfer layers were formed on both the ground and the polished surfaces.

Closer examination using scanning electron microscopy (SEM) revealed that for a given ceramic surface finish, the appearance of the wear scars and the transfer layers was indeed similar for different applied loads (Figures 4.14 and 4.15). As noted earlier, this was thought to be the primary reason for the apparent insensitivity of the friction coefficient to the applied load for these material couples.

On the ground alumina surfaces, semi-continuous metallic transfer layers were observed under all applied loads (Figure 4.14). Metallic debris filled the irregularities on the ceramic surface and was compacted in these areas to form coherent transfer layer patches. (Similar layers have been observed by Ramakiran and Bai [149] in their study of water-lubricated sliding of alumina against steel). Although the average surface roughness in the centre of the wear track was thus improved (compare with the original ground surface, Figure 4.16 (a)), the higher asperities on the alumina surface still protruded above the transfer film (seen as dark grey areas in Figures 4.14 (a) and (c)). Little or no polishing of these asperities appeared to occur, probably due to the high hardness of alumina. As suggested in Section 4.3.3, this provides an explanation for the higher stabilized wear rates observed for this material couple.

Thicker transfer films were developed at the edges of the wear track, where they covered the ceramic surface completely (Figure 4.14 (b) and (d)). As might be expected from the pressure distribution across the circular contact area, the films were less well-compacted in these regions.

after sputtering compared to 3Y-TZP. This supported the qualitative observation that the transfer layers tended to be thicker on Ce-TZP as a result of increased surface fracture.

4.4.3 Silicon-based ceramics

The general appearance of typical wear scars generated on ground and polished surfaces of Sialon and Si_3N_4 under a load of 50 N is shown in Figures 4.33 and 4.34. Evidently, polishing in the centre of the wear track was somewhat less effective than on the zirconia ceramics. As indicated in Section 4.3, this may be related to the relatively high hardness of the silicon based ceramics, which would reduce the rate of polishing by mechanical processes such as plastic deformation and abrasion. Further, many researchers have shown that at high humidities, material removal on these ceramics occurs primarily by a tribochemical oxidation mechanism, which is promoted by the presence of water and interfacial stresses [26][101][148][207]. The resultant hydrated SiO_2 tribofilms generally reduced the wear rate of silicon nitride by the suppression of microfracture (by reducing friction) on the wearing surfaces. Since no obvious fracture damage was observed on the present wear tracks, the polishing rate may thus have been further reduced by the presence of such tribofilms.

The wear tracks were studied in more detail using SEM and surface analytical techniques, and the findings are discussed below under separate headings.

Sialon

As observed in the optical micrographs, Sialon exhibited significantly less effective polishing on ground surfaces than the zirconia based ceramics (Figure 4.35). Although the surface roughness was improved in the centre of the wear scars, the original grinding scratches were still visible in many cases. Material was transferred from the steel ball onto the Sialon ceramic and was deposited in the valleys of the grinding scratches (Figure 4.35 (b)). Analogous to the zirconia based ceramics, transfer thus appeared to occur by a mechanism of oxidative wear and abrasion of the steel ball, followed by mechanical compaction of loose wear debris on the ceramic surface. However, since no macroscopic fracture damage occurred

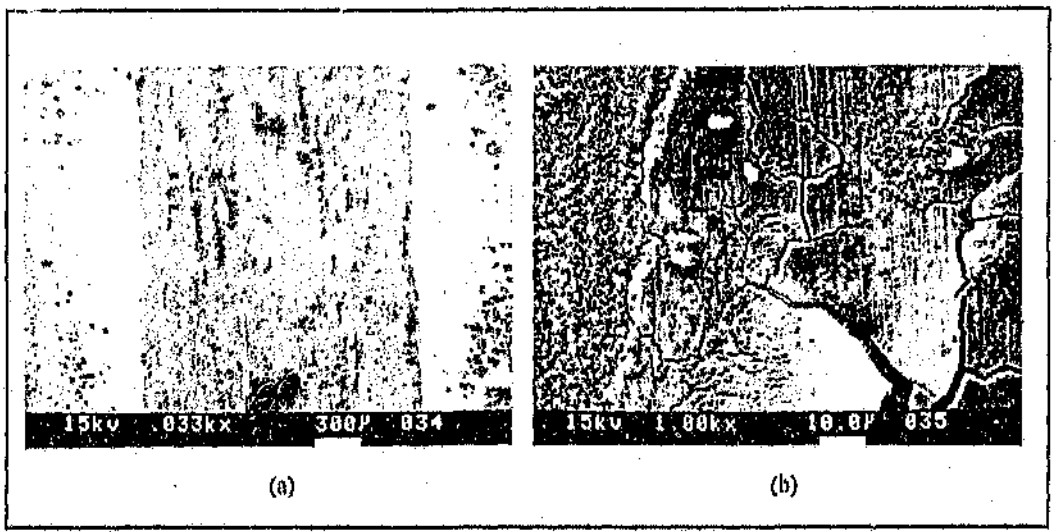

Figure 4.32: Wear track generated on a ground Ce-TZP surface under a load of 50 N; (a) general view and (b) centre of track.

Table 4.12: XPS analysis results obtained on a polished Ce-TZP wear track after 6912 m of sliding under a load of 50 N.

Peak	Binding energy (eV)	Species	Sensitivity factor	Atomic %
Analysis on the as-worn surface				
C (1s)	285	-	0,2	26,8
Zr (3p)	333	ZrO_2	0,4	26,1
O (1s)	530,1	-	0,61	45,0
Fe (2p)	710,7	Fe_2O_3	1,76	2,1
			Total	100,0
Analysis after sputtering				
Zr (3p)	332,6	ZrO_2	0,4	50,2
O (1s)	530	-	0,61	43,8
Fe (2p)	709,2	FeO	1,76	4,3
Cr (2p)	575,4	CrO_2	1,7	1,3
Ce (3d)	886,5	Ce	6,5	0,4
			Total	100

be understood since the tetagonal-to-monoclinic (*t-m*) phase transformation in Ce-TZP occurs more easily (i.e. at lower applied stresses) than in 3Y-TZP, as outlined earlier. A similar trend in fracture propensity with ceramic stability was observed by Becker et al [206] who studied the wear of zirconia ceramics with different toughness values against an SAE 4620 steel ring.

As a result of increased fracture, more well-developed transfer layers were also formed compared to 3Y-TZP, although the morphology of the layers and their mechanism of formation appeared to be largely similar (Figure 4.31). Moreover, as for the other zirconia based ceramics, polishing on the ground surfaces was so effective that the wear scars generated were indistinguishable from those formed on polished surfaces (Figure 4.32).

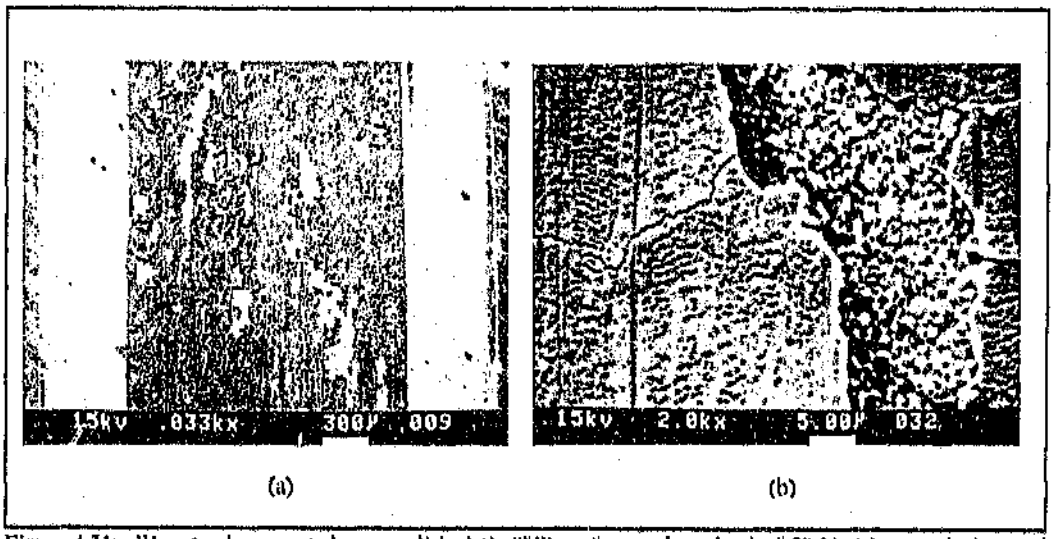

Figure 4.31: Wear track generated on a polished Ce-TZP surface under a load of 50 N; (a) general view and (b) centre of track. (Darker areas = transfer layer).

XPS analyses confirmed that the transfer layers were composed of iron and chromium oxides, much like those formed on 3Y-TZP (Table 4.12). After sputtering, FeO was observed in the bulk of the layers rather than Fe_2O_3 which occurred on the as-worn surface. This suggested that further oxidation of the deposited iron oxides may have occurred after completion of the test. Further, considerably more iron and chromium oxide was detected on these wear scars

XPS analysis showed that the layers comprised mainly Fe_2O_3 (Table 4.11). In contrast to PSZ, the layers were not penetrated after sputtering which confirmed the visual observation that the layers were thicker and more continuous than those formed on PSZ.

Table 4.11: XPS analysis results obtained on a polished 3Y-TZP wear track after 6912 m of sliding under a load of 50 N.

Peak	Binding energy (eV)	Species	Sensitivity factor	Atomic %
Analysis on the as-worn surface				
C (1s)	295	-	0,2	27,3
Zr (3p)	333	ZrO_2	0,4	28,3
O (1s)	530	-	0,61	41,2
Fe (2p)	710	Fe_2O_3	1,76	3,2
			Total	100,0
Analysis after sputtering				
Zr (3p)	332,6	ZrO_2	0,4	58,2
O (1s)	530	-	0,61	39,8
Fe (2p)	710	Fe_2O_3	1,76	1,9
			Total	100

Near the edges of the wear scars, the surface was polished and little or no surface fracture or material transfer was evident. Analogous to PSZ, transfer layers were thus associated with areas of high surface roughness, suggesting that they were formed primarily by the compaction of loose metal oxide wear debris. This may be ascribed to the relatively low chemical compatibility of AISI 440C stainless steel and 3Y-TZP.

Ce-TZP

The same observations outlined for 3Y-TZP also apply to Ce-TZP, which is not surprising in view of the microstructural similarities between the materials. However, the extent of surface fracture in the wear scars appeared to be somewhat larger than for 3Y-TZP. This can

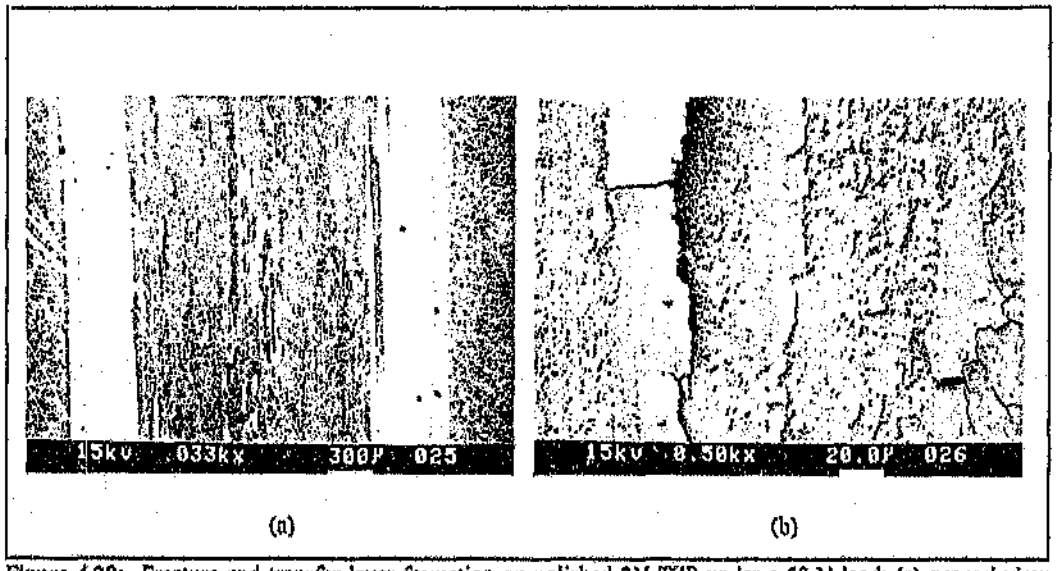

Figure 4.29: Fracture and transfer layer formation on polished 3Y-TZP under a 50 N load: (a) general view and (b) centre of wear track.

detected large relative amounts of Fe and Cr, confirming that they were formed from debris originating from the steel ball (Figure 4.30).

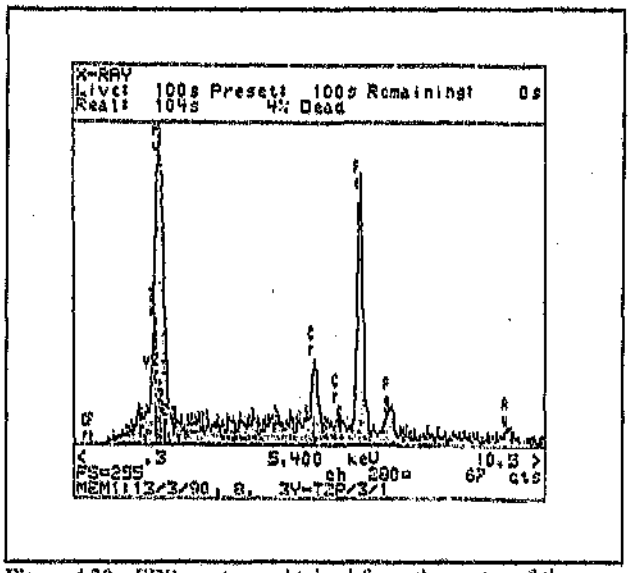

Figure 4.30: EDS spectrum obtained from the centre of the wear track shown in Figure 4.29.

On the other hand, Tucci and Esposito [69] detected no phase transformation in 3Y-TZP ceramics tested in unidirectional sliding in air. They suggested that this was related to high transient (flash) temperatures at the sliding interface, which reduced the driving force for the transformation. Nevertheless, extensive surface fracture leading to wear did occur, which was attributed to the low thermal shock resistance of 3Y-TZP. Further, Bundschuh and Zum Gahr [39] studied the influence of temperature on the wear of 3Y-TZP ceramics and suggested that the maximum driving energy for transformation may occur at medium temperatures around 250 °C. They argued that the tendency for phase transformation should be relatively low at temperatures substantially above or below this temperature range. However, the potential influence of the environment on the transformation driving force was neglected since all tests were conducted under unlubricated sliding conditions. Based on these arguments, Bundschuh and Zum Gahr [39] attributed the reduced wear rates observed at temperatures around 250 °C to transformation-induced plasticity.

In the present work, the sliding contacts were continuously flushed with water and flash temperatures would have been relatively low. It is considered unlikely, therefore, that a substantial reduction in transformation driving force and/or fracture as a result of thermal shock would have occurred, as proposed by Tucci and Esposito [69]. Indeed, in contrast to the work by Bundschuh and Zum Gahr [39] the presence of water in the sliding interface may in fact have increased the transformation driving force, as suggested by Sasaki [202]. Finally, Guillou *et al* [205] recently demonstrated that the size of the near-surface transformation zone in Ce-TZP increased as the number of stress cycles increased on a point contact. Eventually, intergranular fragmentation and spalling occurred at the edges of the contact zone. In the present work, transformation of the 3Y-TZP surface could thus have been further enhanced by the large number of stress cycles experienced by the ceramic as a result of the reciprocating sliding motion. In view of these considerations, the suggestion that the observed fracture damage on the 3Y-TZP wear tracks was related to the transformation and subsequent spalling of a surface layer is reasonable.

The areas damaged by fracture were associated with the formation of smooth, continuous metallic transfer layers which were also seen to delaminate (Figure 4.29). EDS analyses

primarily by oxidation wear (i.e. by the removal of wear debris from oxide layers on the ball) with a small contribution by fine-scale abrasion. Some larger, more angular ceramic wear debris particles were also noted, formed by surface fracture.

3Y-TZP

As for PSZ, effective polishing occurred on the ground 3Y-TZP surfaces. Similar improvements in surface finish during sliding has been reported by other investigators [49]. However, for comparable loads, a greater amount of surface fracture was observed in the centre of the wear scar. Further, the morphology of the damage was different and no preferential grain boundary fracture or the formation of striated pits was noted. Instead, the damaged areas were roughened uniformly on a scale similar to the grain size of the 3Y-TZP material (Figure 4.28). With increasing applied load, the extent of surface fracture also increased, but the appearance of the damaged areas remained unchanged. This is thought to be related to the different microstructures of the ceramics. As described earlier, in PSZ ceramics only tetragonal precipitates are transformed under the influence of applied mechanical stresses. Since these precipitates are located at the grain boundaries and within cubic grains, the grains can absorb some of the resultant compressive stresses. In 3Y-TZP, however, the microstructure comprises mainly very small tetragonal grains, which are metastable and transform as a whole to the monoclinic phase when the applied stress exceeds a certain threshold value. A brittle surface layer is thus formed on the ceramic which can be easily removed during sliding since it is not restrained by the bulk of the material. Similar results and observations have been reported by a number of previous investigators [40][43][204].

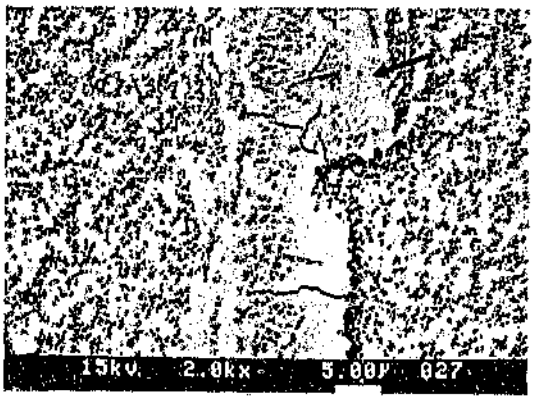

Figure 4.28: Typical fracture damage in the centre of 3Y-TZP wear scars. (Dark layer is a metallic transfer layer).

XPS analyses showed that the transfer layers comprised only iron and chromium oxides and no evidence of chemical interaction between the steel ball and the PSZ surface was found (Table 4.10). After sputtering, no metal oxides were detected, indicating that the layer had been penetrated.

Table 4.10: XPS analysis results obtained on typical transfer layers generated on PSZ after 6912 m of sliding under a load of 50 N.

Peak	Binding energy (eV)	Species	Sensitivity factor	Atomic %
C (1s)	285	-	0,2	22,3
Cr (2p)	576	CrO_2	1,7	3,2
Zr (3d)	183,6	ZrO_2	1,1	49,0
O (1s)	530	-	0,61	20,4
Fe (2p)	710	FeOOH / Fe_2O_3	1,76	5,1
			Total	100

In summary, it can be concluded that material deposition on PSZ occurred mainly by the mechanical compaction of wear debris, rather than by direct adhesion and chemical interaction between the steel and PSZ counterfaces. This is in accordance with the findings of He *et al* [150], who observed that only very thin metallic transfer layers formed on Y-TZP surfaces in the absence of significant surface fracture damage.

The metallic debris itself was extremely small and the particles exhibited an irregular morphology (Figure 4.27). This suggested that debris from the steel ball was formed

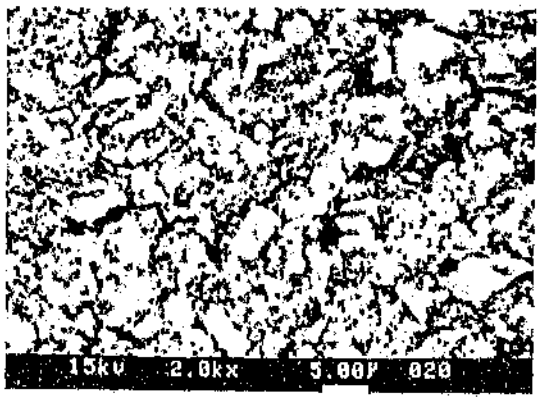

Figure 4.27: Typical loose wear debris at the edges of the PSZ wear scars.

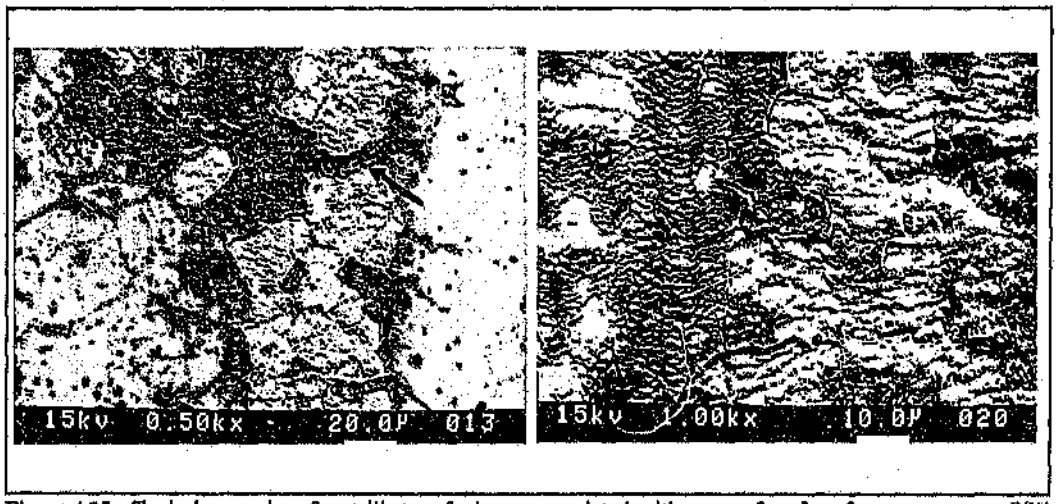

Figure 4.25: Typical examples of metallic transfer layers associated with areas of surface fracture on worn PSZ surfaces.

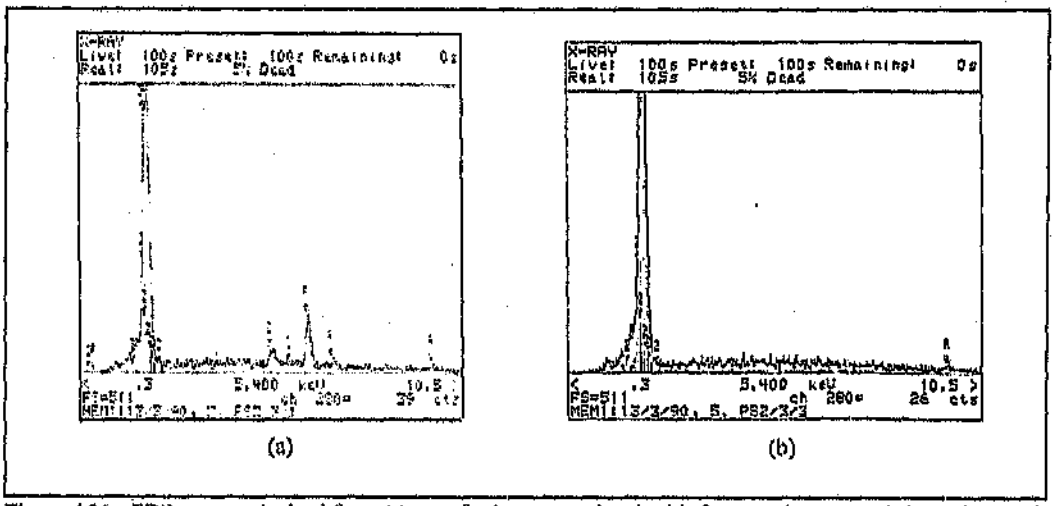

Figure 4.26: EDS spectra obtained from (a) transfer layer associated with fracture damage and (b) undamaged, polished area on worn PSZ ceramic.

These observations were confirmed by EDS spot analyses. In particular, Fe and Cr was detected in the transfer layers, while no Fe or Cr was found on the wear scars in areas which were well polished and free from significant surface fracture (Figure 4.26).

bonds. In this way, the phase transformation from tetragonal to monoclinic zirconia could have been promoted, as described recently by Sasaki [202].

Rainforth and Stevens [203] recently studied Mg-PSZ in unlubricated sliding contact against steel and reported similar pitting damage when the applied mechanical stress exceeded a certain threshold value. The formation of striated pits was attributed to the initiation and coalescence of microcracks due to the transformation of tetragonal precipitates within the PSZ grains to the monoclinic phase. Transformation occurred preferentially along the [100] directions, which could account for the localized occurrence of these pits in the present work. Some material removal also appeared to occur by abrasion, as indicated by numerous small grooves on the wear scars in the direction of sliding (Figure 4.23). This was probably caused by loose, hard Fe- and Cr-oxide as well as fine PSZ wear debris which became trapped between the sliding surfaces.

It was noticeable that no well-developed surface layers were formed on polished regions of the PSZ surfaces. Material deposition invariably appeared to be associated with regions of high surface roughness. Grinding scratches at the edge of the wear scar were partially filled with material originating from the steel ball, while the areas between the scratches remained essentially free from transferred material (Figure 4.24). (On polished PSZ surfaces, thicker transfer layers were formed by debris compaction in the low-stress areas near the wear track edges, analogous to alumina). Similarly, metallic transfer layers were commonly associated with areas of surface fracture in the centre of the wear scar (Figure 4.25). Partial delamination of these layers appeared to occur regularly, leading to wear.

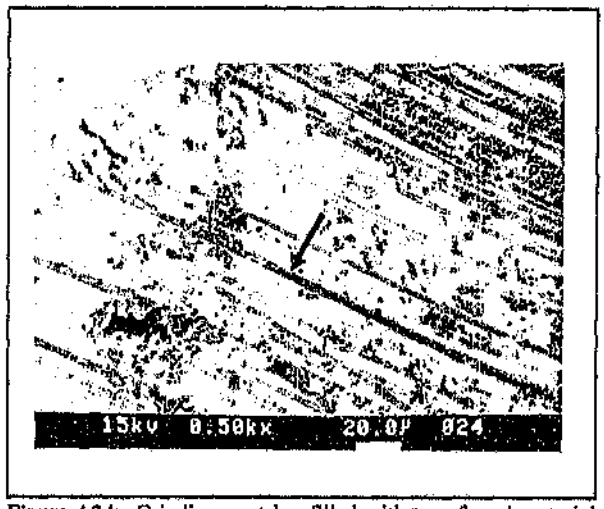

Figure 4.24: Grinding scratches filled with transferred material at the edge of a wear track on ground PSZ.

brittle monoclinic phase as described earlier.

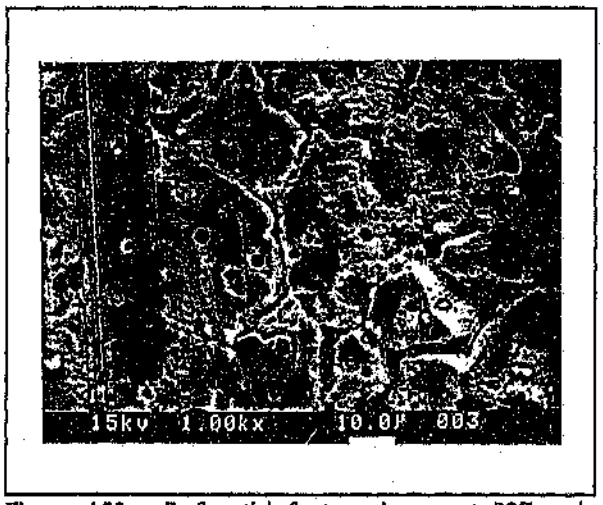

Figure 4.22: Preferential fracture damage at PSZ grain boundaries.

Another characteristic feature was the presence of striated pits on the wear tracks, where small scale fracture was seen to occur on individual PSZ grains (Figure 4.23). Their formation was attributed to the transformation of metastable tetragonal precipitates within the grains, which is associated with a volume expansion (> 3%) of the precipitates. When the extent of transformation exceeded a certain threshold, the associated compressive stresses could not be accommodated within the grain anymore, particularly since the wearing surface of the grains was unrestrained, and fracture occurred within the grain. The possibility also exists that the affected grains protruded slightly above the contact surface due to the volume expansion of the transformed precipitates. The cyclic nature of subsequent sliding contacts could then have contributed to fracture damage by a spalling fatigue mechanism.

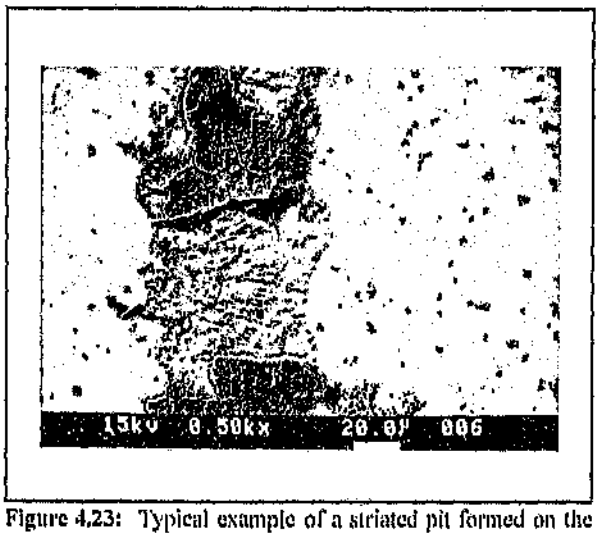

Figure 4.23: Typical example of a striated pit formed on the PSZ surfaces.

Since the mechanisms of damage were similar, the formation of striated pits and preferential grain boundary fracture tended to occur in combination. This type of fracture damage could have been exacerbated by the presence of water through a mechanism involving the adsorption of OH^- ions at the surface and the resultant breaking of the Zr-O-Zr

PSZ

In contrast to alumina, the central area of the PSZ wear tracks was polished effectively during sliding. In fact, the polished region of a wear scar on a ground surface was essentially indistinguishable from that formed on a polished surface. Close inspection of grinding scratches which had been partially removed suggested that the polishing mechanism involved plastic deformation of the PSZ at the edges of the grinding scratches, with possibly some contribution by fine-scale abrasion and fracture (Figure 4.21).

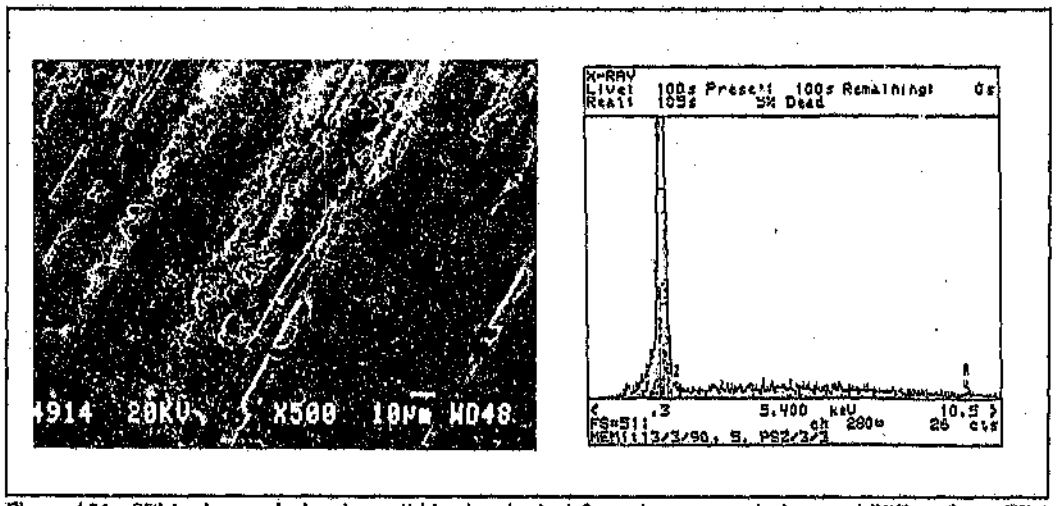

Figure 4.21: SEM micrograph showing polishing by plastic deformation on a typical ground PSZ surface. EDS spectrum shows lack of transferred material.

Non-uniform wear of the PSZ surface occurred within the polished wear track regions at all applied loads (although the severity of damage increased with increasing load), characterized by preferential fracture and localized material removal at the grain boundaries (Figure 4.22). This type of damage has also been observed on PSZ tappet facings in diesel engines [201] and is related to the presence of tetragonal zirconia precipitates at the grain boundaries. When the applied stress exceeds a particular threshold value, these precipitates transform to the more

on the steel surfaces, similar to those found in the present work, was promoted in the presence of sulphate due to the following initiating reaction:

$$Fe + SO_4^{2-} \rightarrow FeSO_4 + 2e \qquad (4.3)$$

Hydrolysis of the iron sulphate could then occur in the presence of water to form iron hydroxides.

Further, Bugarcic [211] reported that the smooth, thin and transparent reaction layers formed on the steel surfaces could be removed by running water.

Less work appears to have been done on the influence of chlorine-containing compounds, although Kotvis and Tysoe [212] found that the addition of ~2% chlorinated hydrocarbon to a pure hydrocarbon lubricant increased the load carrying capacity (LCC) of steel-steel couples by up to three times. It was suggested that the additive decomposed to form chloride at the sliding interface, subsequently leading to the formation of a halide, probably $FeCl_3$. The presence of this chloride was confirmed by XPS analyses and was linked to the observed increase in LCC.

Similar effects have been observed on metal-ceramic sliding couples. For example, Tanita *et al* [213] studied the efficacy of the extreme pressure additive zinc dithiophosphate (ZnDTP) in SiC-steel and Si_3N_4-steel sliding systems. They confirmed the formation of iron phosphate in the former couple and zinc sulphide in the latter couple, and related the formation of these reaction layers on the steel counterface to a reduction in wear rate. Interestingly, the friction coefficient was reduced by the zinc sulphide layer in the case of the Si_3N_4-steel couple while that of the SiC-steel couple remained unaffected. This tends to confirm the apparent lubricious nature of sulphur-containing compounds. These findings are supported by the work of Gates and Hsu [214], which indicated that sulphur-containing additive compounds tend to decrease friction and wear of self-mated Si_3N_4 lubricated by paraffin oil. However, in contrast to the apparent beneficial effect of chlorides on steel surfaces, they found that chlorine-containing compounds tended to increase wear and had a slight increasing effect on the

For Sialon, the total wear depth was reduced while the stabilized wear rate remained unaffected. Together with the friction results, this suggested that the 'load carrying capacity' of the interfacial tribofilms was slightly increased, leading to more consistent friction behaviour and lower wear. Si_3N_4 exhibited a lower total wear depth, but a substantially increased stabilized wear rate compared to the results obtained in deionized water. The couple would thus be expected to exhibit a shorter operational lifetime in Unisel than in deionized water, although the lifetime would be similar to that of the remaining metal-ceramic couples. The lower wear depth was attributable to a reduced running-in phase.

These results suggest that the constituents in the Unisel synthetic mine water modified the tribofilms and/or the interfacial contact conditions in some way in the case of alumina and the silicon-based ceramics. The lack of a measurable effect on friction and wear in the case of the zirconia ceramics can be understood since these materials exhibited significant levels of surface fracture damage, which led to increased surface roughness and the formation of thick, cracked metallic transfer films. It is likely that these larger-scale effects would have dominated the friction and wear behaviour and masked any influence of the water chemistry, such as reduced levels of adhesion.

In contrast, the tribofilms formed on the unfractured surfaces of alumina and the silicon-based ceramics were extremely smooth and probably not much thicker than 1 μm [111]. Small-scale effects due to lubricant composition may thus easily have exerted a measurable influence on the contact conditions.

The mechanisms by which lubricant additives or chemical contaminants influence friction and wear of ceramics are generally not well understood, particularly for aqueous solutions. Nevertheless, it is well-known that the presence of chlorines and sulphur containing compounds tends to decrease friction and wear of metal sliding couples. For example, Wei and Spikes [210] showed that increased levels of sulphur in diesel fuels resulted in a marked decrease in wear of self-mated BS970:1991 534A99 (EN31) steel in reciprocating sliding. Similarly, Bugarcic [211] found that SO_2 decreased the coefficient of friction between various steel-steel sliding couples at high humidities (> 70%). It was suggested that the formation of lubricious ferric hydroxide layers

solutions (pH values between 1 and 3). These solutions were simple in composition, containing just one chemical species such as NaOH, KOH, and HCl. The Unisel synthetic mine water solution used in this work was much more complex in composition and was close to neutral with a pH value of 6,7. It is possible, therefore, that the conflicting results may be attributable to a complex interaction of competing effects of the different Unisel constituents. Furthermore, the influence of the different chemical species on friction and wear may be different for metal-ceramic compared to self-mated ceramic sliding couples. For example, it was shown in the previous sections that relatively strong adhesion appears to occur between AISI 440C steel and alumina when sliding in deionized water. The presence of chemical species such as chlorides and sulphates in the sliding interface, possibly in the form of adsorbed films on the sliding surfaces, may have reduced this adhesion and led to a reduction in friction and wear rates.

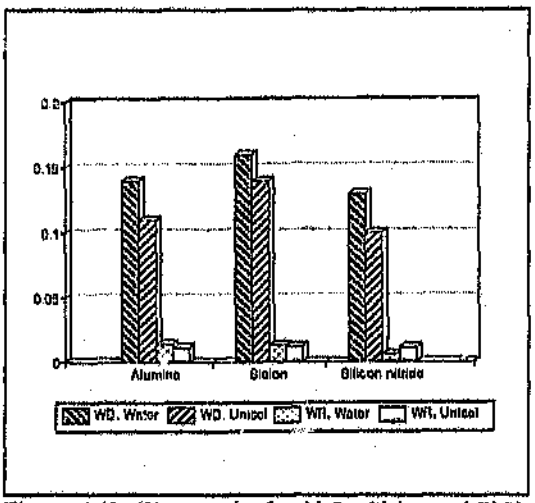

Figure 4.42: Wear results for Al_2O_3, Sialon and Si_3N_4 sliding in deionized water and Unisel (WD = wear depth in mm, WR = wear rate in µm/m sliding).

Table 4.16: Comparison of wear results obtained for alumina, Sialon and Si_3N_4 when lubricated with Unisel synthetic mine water and deionized water.

Lubricant	Parameter	Ceramic counterface material		
		Al_2O_3	Sialon	Si_3N_4
Deionized water	Wear depth (mm)	0,14	0,16	0,13
	Wear rate (µm/m)	0,014	0,013	0,006
Unisel	Wear depth (mm)	0,11	0,14	0,10
	Wear rate (µm/m)	0,011	0,012	0,011

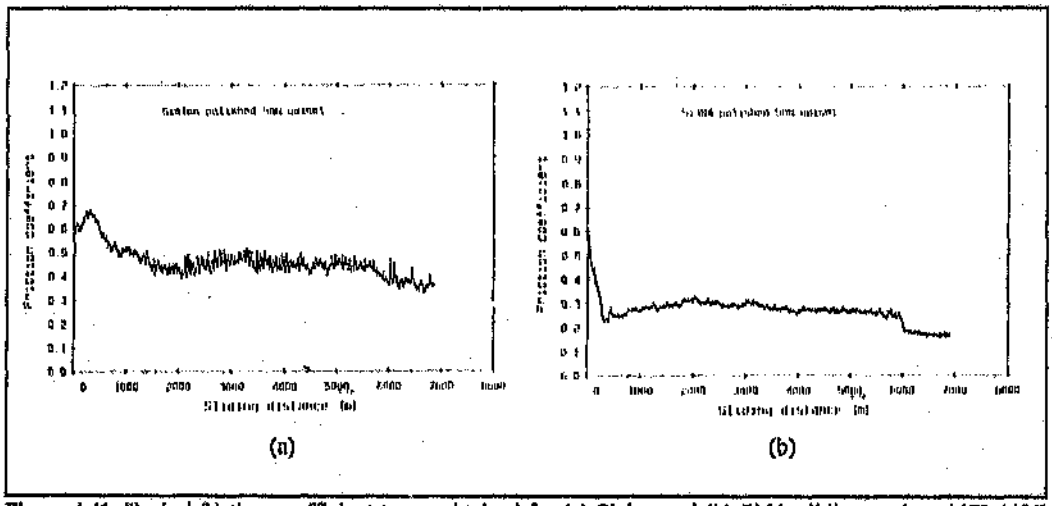

Figure 4.41: Typical friction coefficient traces obtained for (a) Sialon and (b) Si_3N_4 sliding against AISI 440C in Unisel synthetic mine water solution.

In the case of Sialon, the friction coefficient in Unisel fell between the high and low-level values obtained under deionized water lubrication (recall that the friction coefficient oscillated in deionized water). In contrast, Si_3N_4 exhibited a friction coefficient similar to the low-level value obtained in deionized water. For both materials, the friction coefficient trace in Unisel showed no oscillations and remained fairly constant at the steady-state values (Figure 4.41). Analogous results have been reported by Löffelbein *et al* [209], who observed short periods of increased friction in deionized water and ammonia solutions, but no oscillations in other solutions containing chlorides and sulphates. The test configuration in their case was self-mated sintered Si_3N_4 as well as hot-isostatically pressed (HIPped) and reaction-bonded Si_3N_4.

The wear results indicated no consistent effect of the Unisel solution on both the total wear depth and the stabilized wear rate for the zirconia ceramics, as also found by Löffelbein *et al* [209]. However, measurable effects occurred for alumina and the silicon-based ceramics (Table 4.16 and Figure 4.42).

In the case of alumina, the total wear depth and the stabilized wear rate decreased when sliding in Unisel, compared to deionized water. This is contrary to the results obtained by Sasaki [208] and Löffelbein *et al* [209] for self-mated ceramics lubricated by acidic aqueous

4.5.2 Results and discussion

A typical friction trace obtained for alumina sliding in Unisel mine water (composition given in Section 4.2.2, page 82) is presented in Figure 4.40. It can be seen that the steady state friction coefficient was reduced to ~0,15 compared to the value of ~0,43 exhibited in deionized water. Moreover, a much smoother friction profile was observed. This is in good agreement with the results obtained by Sasaki [208] for chloride solutions with pH levels between 1 and 3. Similarly, friction coefficients between 0,1 and 0,15 were also observed by Löffelbein *et al* [209] for self-mated alumina sliding in various sulphate, chloride, phosphate and hydroxide solutions. They measured higher friction coefficients in deionized water (~0,25) which is in broad agreement with the present work.

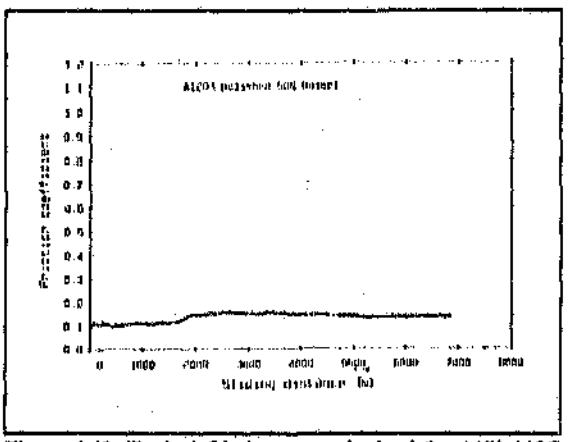

Figure 4.40: Typical friction trace obtained for AISI 440C sliding against alumina in Unisel solution under a load of 50 N.

In contrast, no consistent effect was observed for the zirconia ceramics and the friction coefficients remained essentially unchanged (Table 4.15). Again, this is consistent with results obtained by Löffelbein *et al* [209] for PSZ ceramics.

Table 4.15: Comparison of steady-state coefficients of friction obtained in deionized water and Unisel synthetic mine water solution.

Lubricant	Friction coefficient for ceramics					
	Al_2O_3	PSZ	3Y-TZP	Ce-TZP	Sialon	Si_3N_4
Deionized water	0,43	0,4	0,5	0,38	0,29 - - 0,5	0,23 - - 0,45
Unisel	0,15	0,45	0,43	0,4	~ 0,4	0 35

4.5 Influence of Water Chemistry

4.5.1 Introduction

The work described in the previous sections was conducted with deionized water as lubricant in order to obtain baseline information on the tribological properties of candidate material couples for hydro-powered mining equipment. However, South African mine waters typically contain high levels of chlorides and sulphates and high levels of dissolved solids, and can be highly corrosive due to low pH values. The influence of such variations in water chemistry on the tribology of ceramic and metal-ceramic couples has not been studied to any great extent, although isolated reports exist in the literature.

Sasaki [208] recently studied the influence of pH on the friction and wear characteristics of alumina under water lubricated conditions. The pH values were varied by adding hydrochloric acid and sodium hydroxide. The coefficient of friction was found to remain constant over a relatively wide range of pH values (~5 - ~9), but decreased at pH values outside this range. Conversely, the wear rate was found to be lowest in pure water and increased with increasing and decreasing pH.

Similarly, Löffelbein *et al* [209] recently examined the influence of acidic and basic aqueous solutions on the friction and wear behaviour of various ceramic sliding couples. Although some variations in friction and wear were observed, they reported no systematic effects and concluded that the nature of the solutions was of minor importance.

Against this background, some exploratory experiments were conducted in a synthetic mine water solution to verify whether or not an effect could be observed. Due to time and financial constraints, the experiments were limited to AISI 440C steel sliding against polished ceramic materials under a load of 50 N. Limited surface compositional analyses were undertaken to examine the influence of water chemistry on tribofilm composition.

The results obtained from XPS analyses of a wear scar generated on a polished surface under a 50 N load are presented in Table 4.14. While these analyses also indicated the presence of FeOOH, they confirmed the formation of a hydrated SiO_2 tribochemical film on the silicon nitride surface. The amounts of FeOOH were even smaller than those detected on Sialon, and it is reasonable to suggest that the silicious film dominated the tribological behaviour and was responsible for the superior friction and wear characteristics of the material couple, as outlined in Section 4.3.

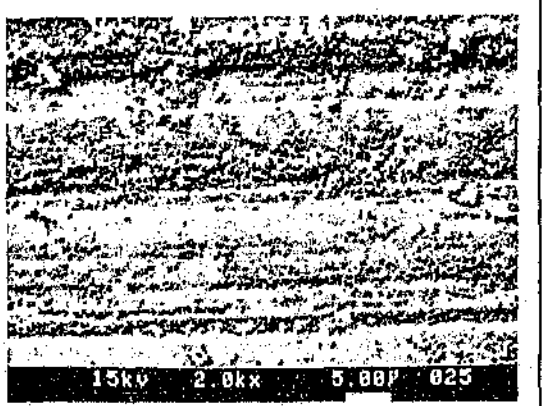

Figure 4.39: SEM micrograph of the original ground Si_3N_4 surface.

Table 4.14: XPS analysis results obtained on a polished Si_3N_4 wear track (6912 m of sliding, load 50 N).

Peak	Binding energy (eV)	Species	Sensitivity factor	Atomic %
Analysis on the as-worn surface				
C (1s)	285	-	0,2	29,5
Si (2p)	101,8	Silicate	0,17	27,8
O (1s)	531,8	-	0,61	23,9
N (1s)	397,2	-	0,4	17,0
Fe (2p)	711,6	FeOOH	1,76	1,8
			Total	100,0
Analysis after sputtering				
C (1s)	285	-	0,2	9,6
Si (2p)	103,2	SiO_2	0,17	32,5
O (1s)	533,0	-	0,61	31,8
N (1s)	398,8	-	0,4	20,3
Fe (2p)	712,2	FeOOH	1,76	5,8
			Total	100

In summary, the silicate layer was thus not effective in preventing adhesion completely between the steel ball and the Sialon counterface. However, the amounts of transferred metal present on the Sialon wear tracks were extremely small. For example, the fact that no metal was detected by EDS on polished Sialon suggested that the metallic transfer layers were significantly thinner than 1 μm, since that is the typical analysis depth of the EDS technique. It is likely, therefore, that the silicate layer dominated the friction and wear behaviour of the material couple, as was suggested in Section 4.3.

Silicon Nitride

The features observed on the silicon nitride wear scars were generally similar to those seen on the Sialon scars. Polishing was slightly more effective on the ground Si_3N_4 surfaces, however, and material deposition from the steel ball was reduced (Figure 4.38). The improvement in surface roughness, although not as dramatic as on the zirconia based ceramics, was evident by comparing the original ground finish (Figure 4.39) with a worn surface (Figure 4.38 (b)). Polishing appeared to occur by a similar mechanism to Sialon, i.e. mainly by tribochemical means, although some microfracture was also evident at the edges of the grinding scratches.

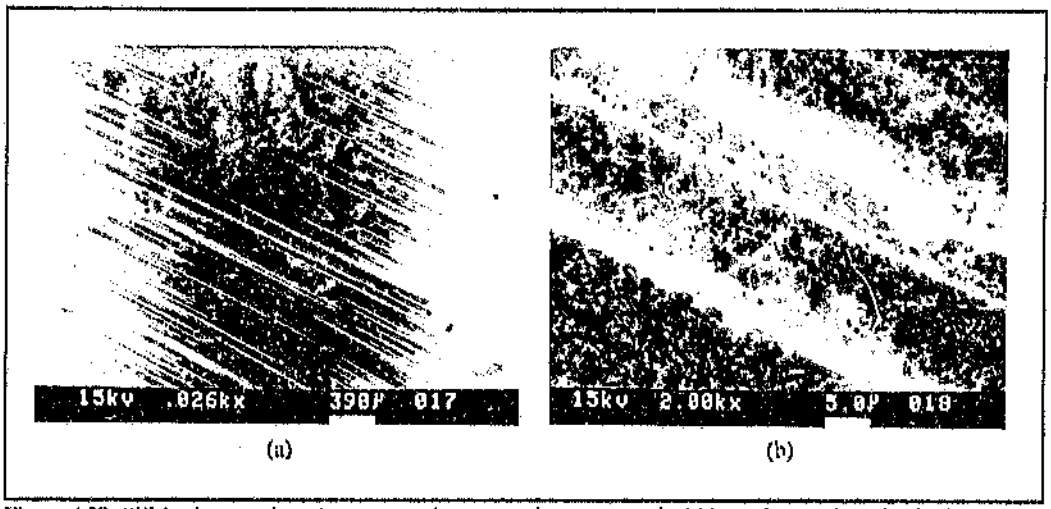

Figure 4.38: SEM micrographs of a wear track generated on a ground Si_3N_4 surface under a load of 50 N: (a) general view and (b) centre of track.

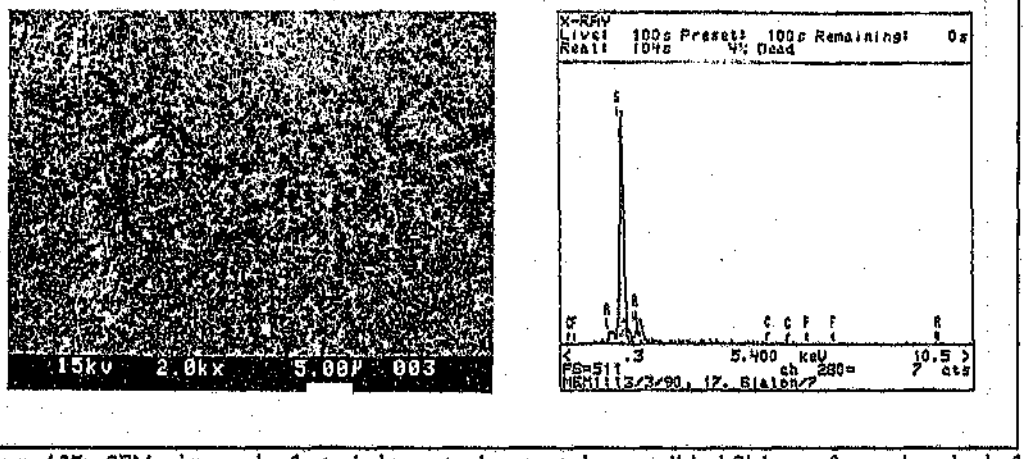

Figure 4.37: SEM micrograph of a typical wear track generated on a polished Sialon surface under a load of 50 N. The EDS spectrum shows no significant metal transfer from the steel ball.

Table 4.13: XPS analysis results obtained on a polished Ce-TZP wear track after 6912 m of sliding under a load of 50 N.

Peak	Binding energy (eV)	Species	Sensitivity factor	Atomic %
Analysis on the as-worn surface				
C (1s)	285	-	0,2	31,1
Si (2p)	101,2	Silicate	0,17	24,2
O (1s)	531,2	-	0,61	21,3
N (1s)	396,8	-	0,4	20,9
Fe (2p)	711,6	FeOOH	1,76	2,5
			Total	100,0
Analysis after sputtering				
C (1s)	285	-	0,2	5,8
Si (2p)	102	Silicate	0,17	34,1
O (1s)	531,4	-	0,61	29,4
N (1s)	397,6	-	0,4	21,9
Fe (2p)	709,4	FeO	1,76	8,8
			Total	100

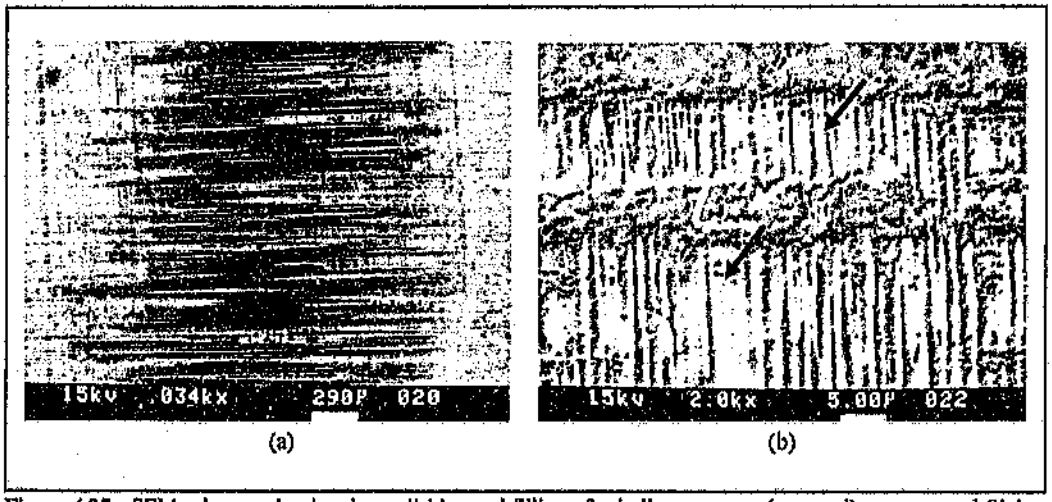

Figure 4.35: SEM micrographs showing polishing and filling of grinding grooves (arrowed) on a ground Sialon surface under a 50 N load; (a) general view and (b) centre of wear track.

in the wear track, the effect was much less marked than for the TZP ceramics. This is supported by the EDS analysis shown in Figure 4.36 which shows only a very small amount of Fe and Cr in the wear scar. Even less material transfer from the steel ball was observed on the polished Sialon surfaces (Figure 4.37).

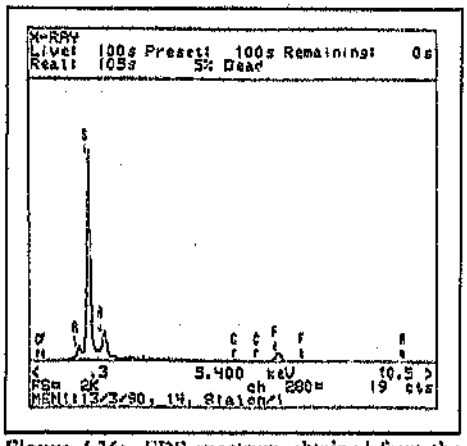

Figure 4.36: EDS spectrum obtained from the wear scar shown in Figure 4.35.

The results obtained from XPS analyses of a typical wear scar produced on a polished Sialon surface under a 50 N load are given in Table 4.13. These showed that a silicate layer was formed on the ceramic surface, probably by a tribochemical mechanism. The composition of this layer appeared to be relatively complex and/or non-stoichiometric, and could not be uniquely identified. Only small amounts of iron in the form of FeOOH and FeO were detected. Clearly, some transfer from the steel ball had occurred, but to a much lesser extent than on alumina or even the zirconia based ceramics.

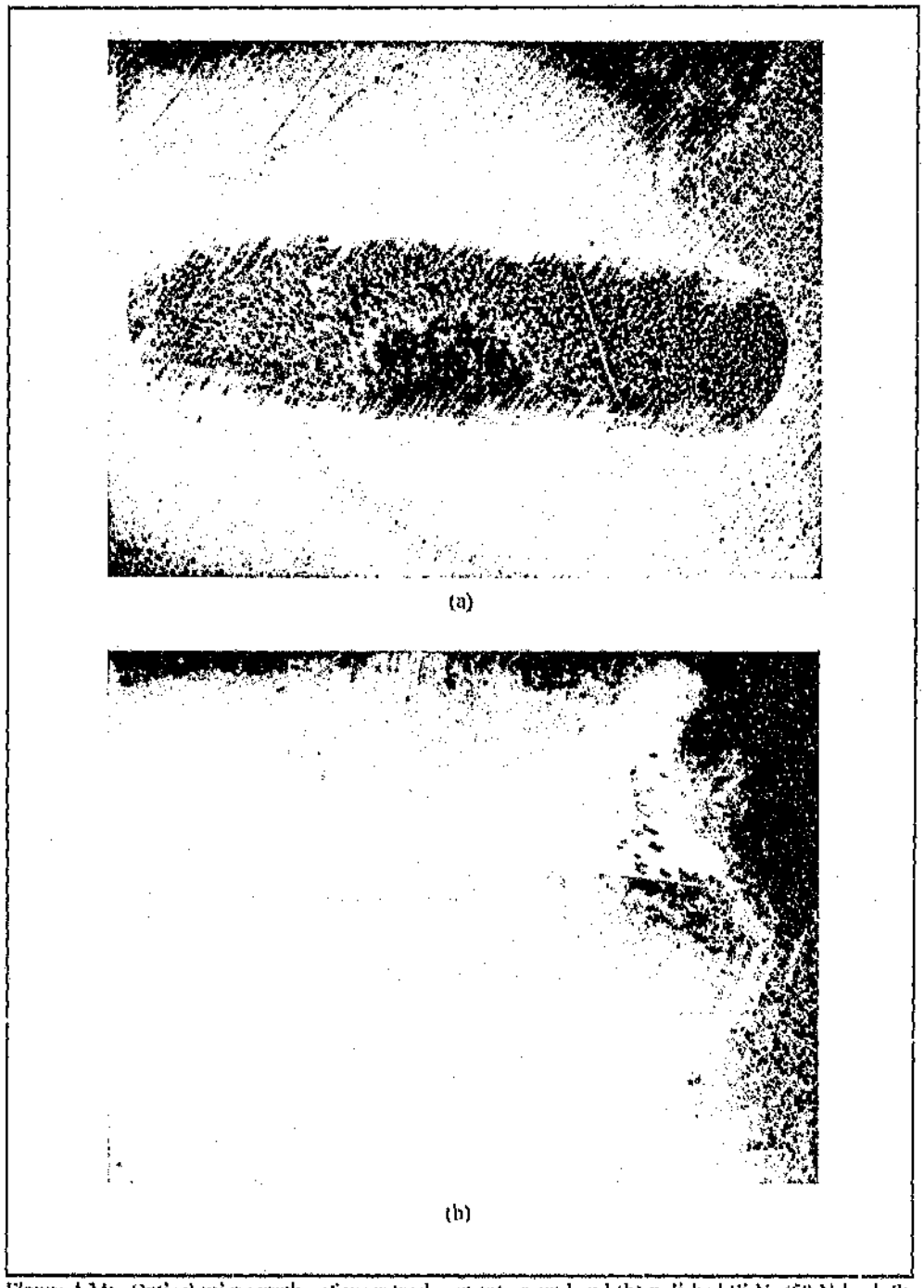

Figure 4.34: Optical micrographs of wear tracks on (a) ground and (b) polished Si_3N_4 (50 N load, 8x magnification).

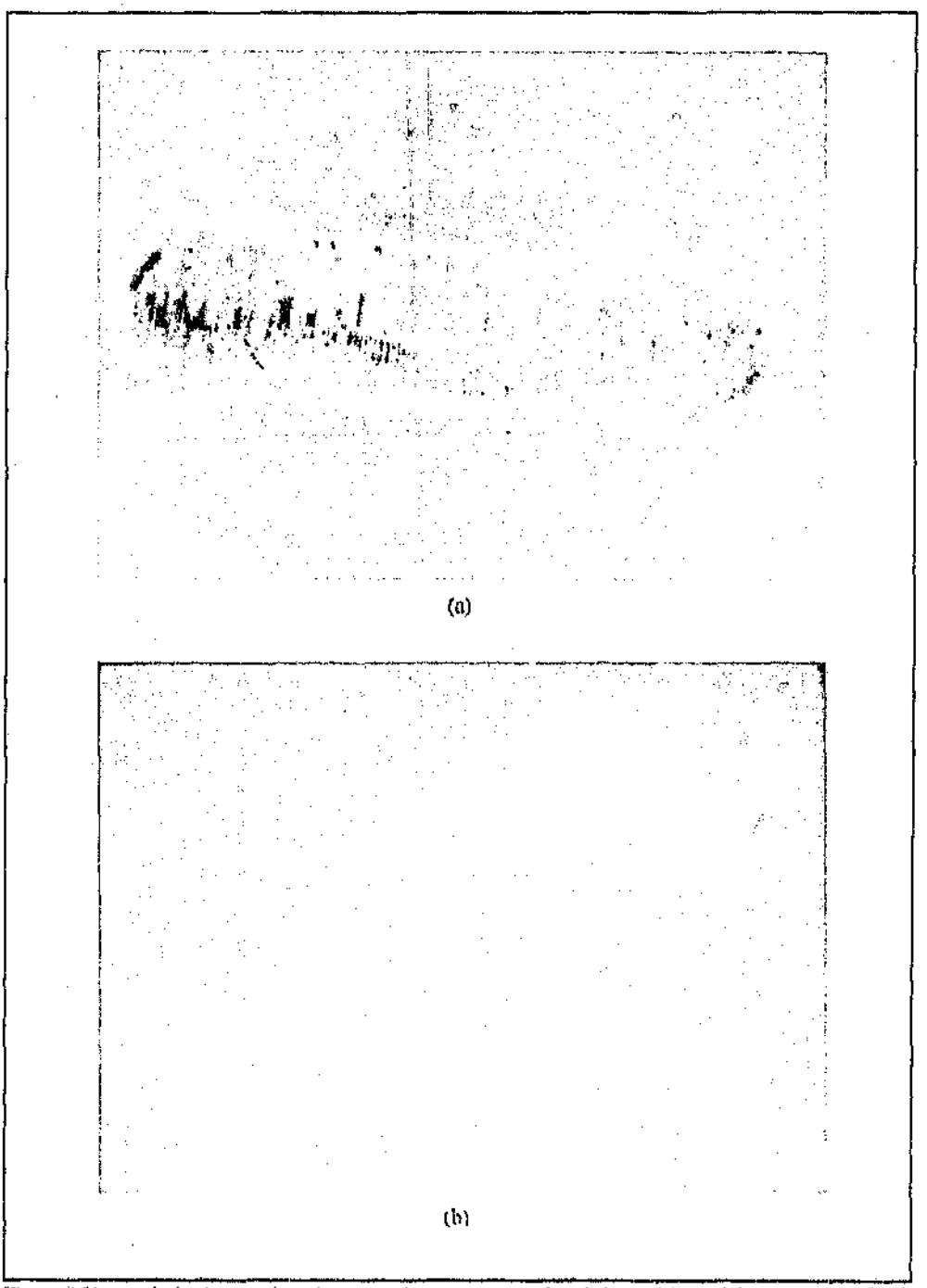

Figure 4.33: Optical micrographs of wear tracks on (a) ground and (b) polished Sialon 101 (50 N load, 8x magnification).

The effect was more marked on the pin than the disc, with the roughness across the sliding direction reaching 0,39 μm R_a as compared to 0,08 μm R_a along the sliding direction. The equivalent values for the disc are 0,29 μm R_a and 0,23 μm R_a.

Preferential wear of the inter-grain areas appeared to occur to a much larger degree than on Syndite, resulting in an etched appearance of the surfaces. Compositional analyses by EDS of granular wear debris which appeared to collect in the hollows yielded no x-ray peaks. Since the EDS system is unable to detect carbon, it is reasonable to suggest that the debris comprised mainly diamond fragments originating from the edges of the diamond grains in the PCD compacts. It is thus likely that the abrasive scoring on the PCD surfaces was caused by these extremely hard, loose debris particles as they became trapped in the sliding interface.

5.3.2 Specimen geometry effects

On self-mated Syndax, initial load carrying capacity (LCC) tests were done using **untapered** Syndax pins by increasing the applied load systematically from 186 to 3634 N (Figure 5.3). Up to about 3000 N (~47 MPa contact pressure), the friction coefficient remained constant at ~0,08 - 0,1. Beyond about 3000 N, severe grooving of the sliding surfaces occurred and the friction coefficient and pin temperature increased rapidly. These results suggested that the load carrying limit was about 3000 N with the present test configuration, limited by the influence of wear debris on the integrity of the sliding surfaces.

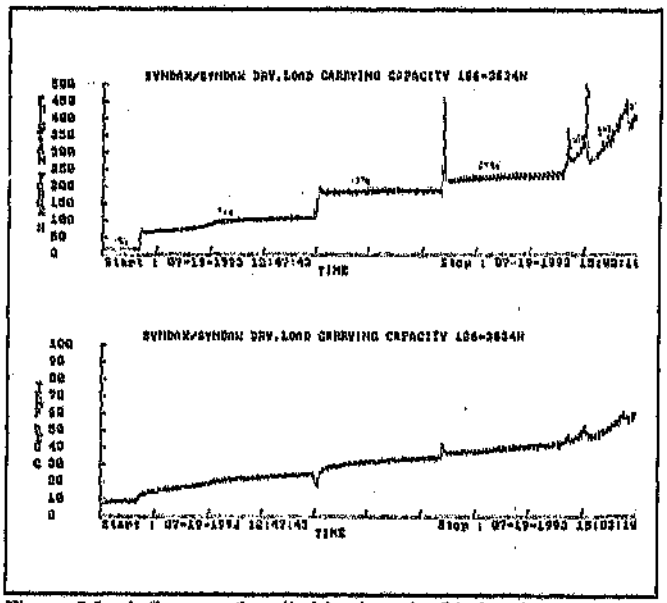

Figure 5.3: Influence of applied load on the friction force (top) and PCD temperature (bottom) for self-mated Syndax (untapered pin).

Closer examination of the Syndax pins confirmed that chipping occurred at the pin edges which were not bevelled. The debris so formed was dragged through the contact area and contributed to the scoring of the surfaces and probably limited the LCC. Additional



(a)

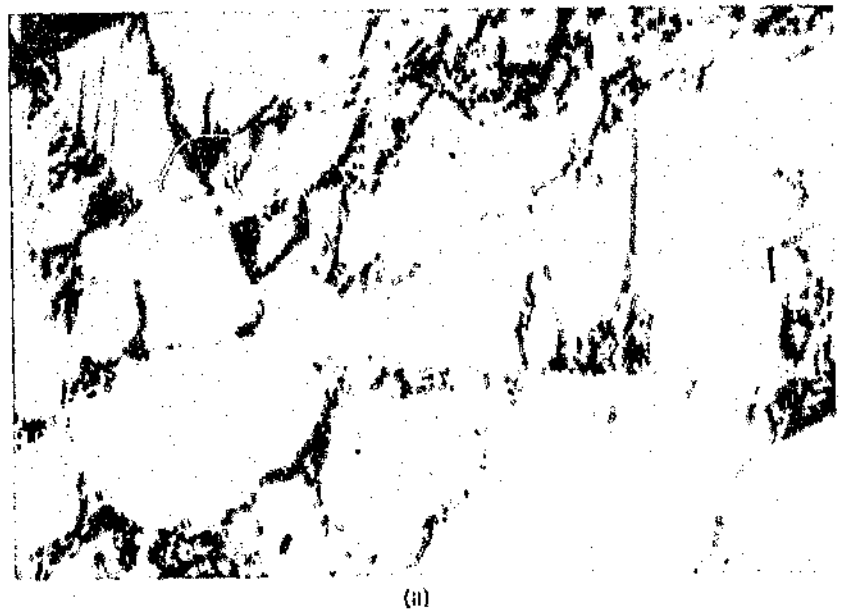

(a)

Figure 5.2: Optical micrographs of worn Syndax pin surfaces showing abrasive grooving on the diamond particles and preferential wear and accumulation of loose debris at the inter-grain areas; (a) 200x and (b) 1000x magnification.

chemical degradation of the diamond surfaces (although this was not confirmed). In fact, the further improvement in surface roughness with increasing load indicated that such a marginal overload condition is a prerequisite for efficient and rapid running-in of the PCD materials. The test parameter window for successful surface polishing is quite narrow, however, as exploratory tests showed that inceasing the applied load by too large an amount too early in the run-in process results in seizure of the couple and damage to the PCD surfaces.

Based on these results, a running-in procedure was devised which involved the step-wise increase of the applied load at a sliding speed of 0,13 m/s, while allowing enough time at each load for the friction coefficient and the surface roughness on both sliding elements to stabilize.

Self-mated Syndax

The initial running-in phase was conducted under a 186 N load, smaller than the 490 N load used previously for Syndite. After one hour of sliding, the surface roughness of the pin in the sliding direction had decreased from 0,40 μm R_a to 0,08 μm R_a, while the roughness of the disc had only decreased from 0,31 to 0,23 μm R_a. Similar trends had been observed for the Syndrill SD specimens with the pin polishing very rapidly, reaching 0,03 μm R_a within 2 hours of running, and the disc roughness lagging behind. In contrast to Syndite, the friction coefficient remained at a lower value of 0,12.

The initial running-in behaviour of self-mated Syndax thus seemed to mirror closely that of Syndite. In the second phase of running-in, the normal load on the Syndax pin was thus increased systematically to a maximum of 1200 N. The friction coefficient remained low at between 0,08 and 0,1 which was in stark contrast to Syndite which showed much higher friction coefficients of 0,2 - 0,4 when run for extended periods at 490 N.

Closer examination of the specimens during and after the running-in phase showed that scratches and grooves appeared on the pin and disc surfaces (Figure 5.2). As a result, the surface roughness depended on the test direction, being rougher across the sliding direction.

5.3 Unlubricated Sliding Behaviour

5.3.1 Run-in characteristics

Self-mated Syndite

This couple was used to develop a methodology for running-in PCD materials. Initial tests were conducted at a constant load of 490 N (contact pressure 7,7 MPa), and the resultant improvement in surface roughness with increasing test time is summarized in Table 5.1.

Table 5.1: Surface roughness values of the Syndite pin and disc run-in under a load of 490 N.

Run time (h)	R_a of pin (μm)	R_a of disc (μm)
0	0,15	0,27
2	0,03	0,10
4	0,06	0,11
8	0,01	0,07
14	0,02	0,04
18	0,03	0,05

The results showed that the Syndite pin was well-polished after only two hours, corresponding to 936 m of sliding. The disc, on the other hand, exhibited a rougher surface than the pin after 18 hours, although no further improvement in surface finish occurred after 14 hours of sliding. The couple was thus run for 4 hours under an increased applied load of 870 N (13,7 MPa contact pressure), which resulted in further improvements in surface roughness values to 0,01 μm R_a for the pin and 0,03 μm R_a for the disc. At this stage the couple was regarded as well run-in and ready for further investigation.

The friction coefficient (μ) increased and exhibited more scatter as the surface roughness improved. Eventually, μ fluctuated between 0,2 and 0,4 which is much higher than the value of ~0,1 which would be expected for self-mated diamond. This suggested that the Syndite couple was marginally overloaded during the run-in phase, possibly leading to some local

Dry sliding tests were conducted at a sliding speed of 0.13 m/s. After the running-in phase, the normal load was increased step-wise from 180 to ~4300 N (equivalent to contact pressures of 2.8 and 67.6 MPa) to evaluate the load carrying capacity of the sliding couples.

Water lubricated tests were also conducted at a sliding speed of 0.13 m/s. Exploratory experiments were also conducted at speeds of 1.9 and 3 m/s, but it was found that predominantly hydrodynamic lubrication conditions prevailed up to high loads with the highly polished PCD specimens. These conditions were unsuitable for assessing the performance of the material couples in the more important boundary lubrication regime, and the lower speed was thus chosen to reduce the influence of hydrodynamic lubrication.

Prior to testing, the surface roughness values of the pins and discs were determined using a Hommel T1000 surface profilometer. In contrast to Syndite, the values for Syndax specimens were found to be dependent on the test direction, and subsequent measurements were carried out both in and across the sliding direction. The samples were then ultrasonically cleaned in acetone before the first tests, but between tests the Syndax sliding surfaces were mostly simply washed with water and acetone. Tribofilms were removed from the sliding surfaces before testing with dilute hydrochloric acid, followed by a water and then acetone wash.

Thermocouples were fixed into the pins with epoxy in such a way that they were in direct contact with the rear of the PCD layer. The thermocouple output was continuously logged on a computer to give an indication of the PCD surface temperature during the tests. For any given test, the temperature was found to scale closely with the measured friction force. In the interest of simplicity and brevity, this thesis will thus concentrate on reporting the friction data since the temperature data did not serve to elucidate the friction processes further.

On completion of the tests, the sliding surfaces were examined under an optical microscope to study the surface features developed under particular experimental conditions. More detailed analyses of the friction and wear processes were carried out using scanning electron microscopy (SEM), while surface compositional analyses were conducted using energy dispersive x-ray analysis (EDS) and X-ray photoelectron spectroscopy (XPS).

When using pins such as the PCD compacts, with large flat areas that must be kept in contact with the turning disc, it is difficult to get the two sliding surfaces well aligned so that full pin area contact can be established. Furthermore, the PCD couples were expected to show only very limited potential for running-in due to the extreme hardness and wear resistance of these materials. Therefore, a self-aligning bearing with its axis vertical was fixed on the load arm to act as pin sample holder. The inner and outer races of the bearing were pinned together in such a way that rotation of the races with respect to each other was prevented, but limited relative movement in the horizontal plane was still possible. With the PCD pin held in this self-aligning sample holder, good area contact with the disc could be achieved and maintained without undue difficulty.

5.2.2 Experimental materials and methodology

Nominally, both the Syndite and the Syndax pins used were 13,44 mm diameter with 2 mm wide 5° taper edges so that the effective contact diameters were ~9 mm. The Syndite pins consisted of a 0,7 mm thick PCD layer with cobalt 'binder', bonded to a tungsten carbide backing. The total height of the pins was 8 mm. The Syndax pins consisted of a 5 mm thick PCD layer with silicon as binder phase, brazed to a mild steel backing pin. The Syndite counterface discs were 70 mm in diameter while the Syndax discs used were 56 mm in diameter. All sample materials were supplied by De Beers Diamond Research Laboratory (DRL), Johannesburg.

Initial experiments showed that the roughness of the lapped contact surfaces on the Syndite and Syndax specimens improved progressively with increasing test time and applied load. A run-in procedure was thus developed to provide a well-defined, steady-state surface finish on all specimens prior to testing. This consisted of running the unused material couples at a sliding speed of 0,13 m/s and periodically increasing the applied load. At each load, the couple was run until the friction coefficient stabilized, following which the test was stopped and the surface roughness measured on both sliding elements. The process was repeated until no further improvements in surface roughness were noted.

5.2 Test Equipment and Methodology

5.2.1 Test equipment

Thrust bearings are characterized by a unidirectional sliding motion, and thus a pin-on-disc (POD) rather than a reciprocating tribometer was utilized in the present work (Figure 5.1). In this machine, one element of the sliding couple is in the form of a pin and is fixed in a sample holder on a cantilever load arm. The pin is allowed to slide on rotating horizontal disc, which comprises the second element of the couple under investigation and is driven by a variable speed motor. The load on the pin can be varied and is applied by means of dead weights on the load arm.

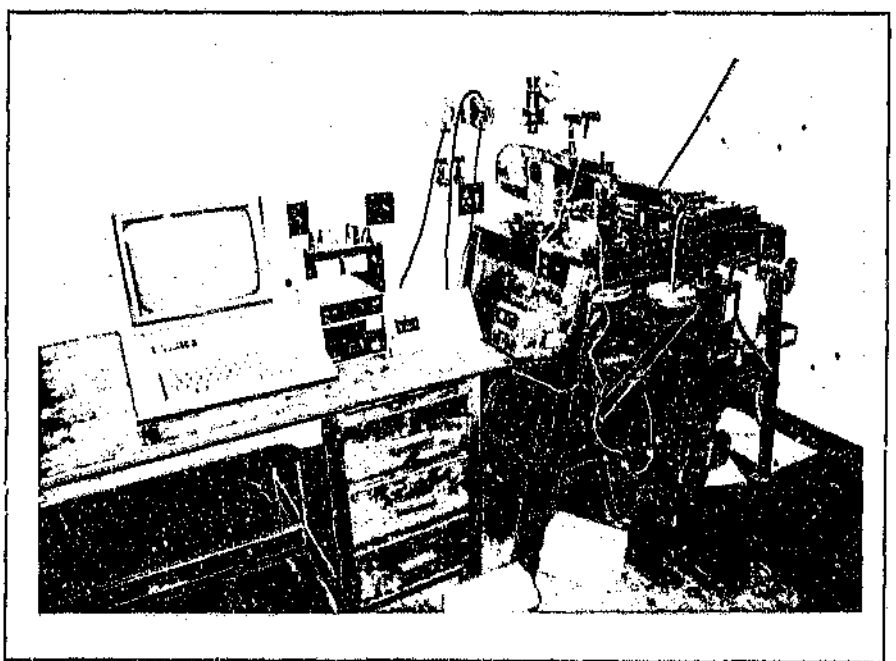

Figure 5.1: Pin-on-disc (POD) tribometer used in the present work.

The friction force and pin temperatures were constantly monitored and recorded by a computer.

CHAPTER 5

5. POLYCRYSTALLINE DIAMOND (PCD) SLIDING COUPLES

5.1 Introduction

Initial development work on PCD thrust bearings for down-hole drilling applications, conducted by the writer and co-workers, indicated that the friction behaviour of self-mated Syndite (De Beers PCD) sliding couples was quite unpredictable at high contact pressures. In some cases, rapid seizure of prototype bearings occurred without adequate warning. It was noted that this instability in friction behaviour was the performance limiting factor, and not wear of the bearing surfaces. Careful analysis of the worn surfaces suggested that the sudden increase in friction coefficient, followed by seizure, was associated with the formation of Co-rich tribofilms on the PCD surfaces. No reference to this phenomenon, or to the mechanisms underlying the effect of such layers on PCD friction and wear, could be found in the open literature.

It was known, however, that cobalt and other metals like iron tend to promote the chemical degradation of diamond to form graphite (Section 2.4.3 and 2.4.4). It was thus postulated that thermally stable PCD materials which do not employ conventional metallic binder systems should exhibit a more attractive friction and wear behaviour than Syndite at high contact pressures. An example of such a material is Syndax (De Beers trademark) which employs silicon as a binder phase.

This more detailed study was initiated to assess the tribological characteristics of various combinations of Syndax and SD 025 Syndite (Co-bonded PCD, diamond grain size 25 μm) under both dry and water lubricated conditions. Particular emphasis was placed on elucidating the mechanisms which determine the friction behaviour of these couples, in order to point the way towards the selection or development of PCD sliding couples for bearings with improved performance. Less attention was paid to quantifying wear since wear was not found to be the performance limiting factor for PCD bearings.

behaviour of alumina and the silicon-based ceramics. Based on available evidence, this was tentatively explained in terms of reduced adhesion and the promotion of iron oxide and hydroxide formation on the steel ball by the presence of sulphate. Adsorption effects may have played a significant contributory rôle, particularly in the case of the silicon-based ceramics. It was suggested that the influence of sulphate may have been more important in this regard than that of chloride. Further work on clarifying the precise mechanisms was suspended due to time contraints and a lack of funds, but is clearly indicated in view of the potential importance of these effects in improving the performance of these metal-ceramic sliding couples.

It was noted that metal-ceramic couples suitable for application in reciprocating components in hydro-powered stoping equipment need to exhibit a low friction coefficient and steady friction behaviour, coupled with an acceptable steady-state wear rate, in order to ensure satisfactory component operation and lifetimes. In view of these requirements, this work has demonstrated that the silicon-based ceramics were generally superior to the oxide ceramics. In deionized water, preference should be given to Si_3N_4 because of the apparent higher load carrying capacity and lower wear rate compared to Sialon. In mine waters which exhibit a similar composition to the synthetic Unisel mine water solution and which are typically used as the hydro-power working fluid, both Sialon and Si_3N_4 are considered to be equally suitable. In this case, even the AISI 440C-alumina couple would be suitable as a result of the beneficial influence of the mine water constituents on friction and wear, provided the poor fracture toughness of the alumina ceramic can be tolerated.

4.6 Summary

The friction and wear behaviour of a range of oxide and silicon-based ceramics sliding against AISI 440C stainless steel in deionized water was studied. All the sliding couples which were considered exhibited a pronounced two-phase friction and wear behaviour, characterized by a run-in and a steady-state phase. The wear results in particular showed that it is important to quantify not only the total amount of wear, as is commonly done, but also the steady-state wear rate, which is the more important parameter for assessing the long-term operational performance of the sliding couple.

It was confirmed that the oxide ceramics generally showed higher friction coefficients and wear rates compared to the silicon-based ceramics. This was explained in terms of different levels of adhesion between the sliding elements and the formation of interfacial metallic transfer films. In the case of zirconia ceramics, increased transformation toughening was found to be related to increased surface fracture damage and metallic transfer film formation. However, these films were beneficial in that they protected the underlying ceramic surface from further damage and determined the friction and wear behaviour.

The superior friction and wear behaviour of Sialon and Si_3N_4 was related to the formation of lubricious SiO_2-based tribochemical reaction films on these materials. The load carrying capacity of these films appeared to be limited, however, and oscillations in friction coefficient and increased stabilized wear rates were observed at loads of 50 N. The effect was more pronounced for Sialon and was probably related to the different nature of the tribofilms.

All ceramics except alumina developed a characteristic surface finish during sliding, which was essentially independent of the original surface roughness. This has important economic implications since these materials may be thus used in practical applications without prior polishing.

A short study on the influence of water chemistry dem[illegible]nat the presence of significant amounts of chloride and sulphate had a significant effect on the friction and wear

for silicon, as indicated by the relevant bond dissociation energies (Table 4.17, after Ref. [214]).

Table 4.17: Bond dissociation energies for selected silicon bonds

Bond	Dissociation energy (kJ/mol)	
	Mean	Range
Si-H	297	4
Si-Si	318	21
Si-C	435	21
Si-N	439	38
Si-Cl	439	50
Si-S	619	13
Si-O	770	13

In summary, the results obtained in this work suggested that the mechanisms by which the Unisel constituents influenced the friction and wear behaviour may have been similar for the alumina and silicon-based ceramics sliding against steel, and were largely concentrated on the steel ball (no obvious signs of increased chemical attack was noted on any of the ceramic surfaces). The influence of sulphates on the formation of iron oxides and hydroxides formed on the steel ball may be of particular importance in this regard. Similarly, adsorption effects may have played an important rôle, particularly in the case of the silicon-based ceramics. Again, sulphur-containing compounds may have had the dominant effect in this regard in view of the very strong affinity of sulphur towards silicon. However, it must be realized that these results are preliminary in nature and further work is indicated to clarify the nature of these mechanisms. In particular, detailed experiments using different solutions containing only chlorides or sulphates should be conducted, coupled with more detailed surface compositional analyses, to assess the relative rôle of each Unisel constituent. This work was suspended in the present case due to time constraints and a lack of funds.

friction coefficient.

Considering these findings, it is considered reasonable to suggest that similar processes may be responsible for the effects observed in the present work. Specifically, the reduction in friction and wear observed for alumina may be related to a reduction in adhesion between the AISI 440C steel and the alumina counterface. XPS analyses on the alumina surface revealed no significant differences in tribofilm composition compared to the surfaces tested in deionized water, and no significant amounts of sulphur or chlorine were detected. Similarly, there was no sign of iron chloride on the steel ball. It is likely, therefore, that the mechanisms responsible for the reduction in adhesion were related to adsorption effects of sulphur and/or chlorine containing species. Furthermore, the presence of sulphate in the Unisol solution may have promoted the formation of protective iron oxide and iron hydroxide films on the steel ball, as suggested by Burgacic [211]. It is interesting to note in this context that Löffelbein *et al* [209] also failed to detect any reaction layers or significant differences in tribofilm composition on various ceramic surfaces. They used a variety of analytical techniques including Auger spectroscopy, which has a similar analysis depth resolution to XPS. It would appear, therefore, that whatever reaction or adsorbed layers were formed may have been removed after termination of the test, or during the analysis procedure.

For the silicon-based ceramics, the stabilized friction coefficient was substantially unaffected by the Unisel solution, particularly for Si_3N_4. This may be understood since the tribological behaviour of these couples was determined mainly by a tribochemical reaction film and little adhesion occurred between the AISI 440C steel and the ceramic surfaces when sliding in deionized water. Like the AISI 440C-alumina couple, XPS analyses failed to detect any substantive differences in tribofilm composition on the ceramic, or the presence of reaction layers on the steel ball. It is possible, therefore, that the apparent increased load-carrying capacity of the couples, as evidenced by the absence of oscillations in the friction coefficient, may be related to increased iron oxide/hydroxide formation on the steel ball, analogous to the AISI 440C-alumina couple. This is supported by the fact that the stabilized wear rates were very similar for the three steel-ceramic couples. Nevertheless, adsorption effects may also have played a rôle since chlorine and particularly sulphur are known to have a strong affinity

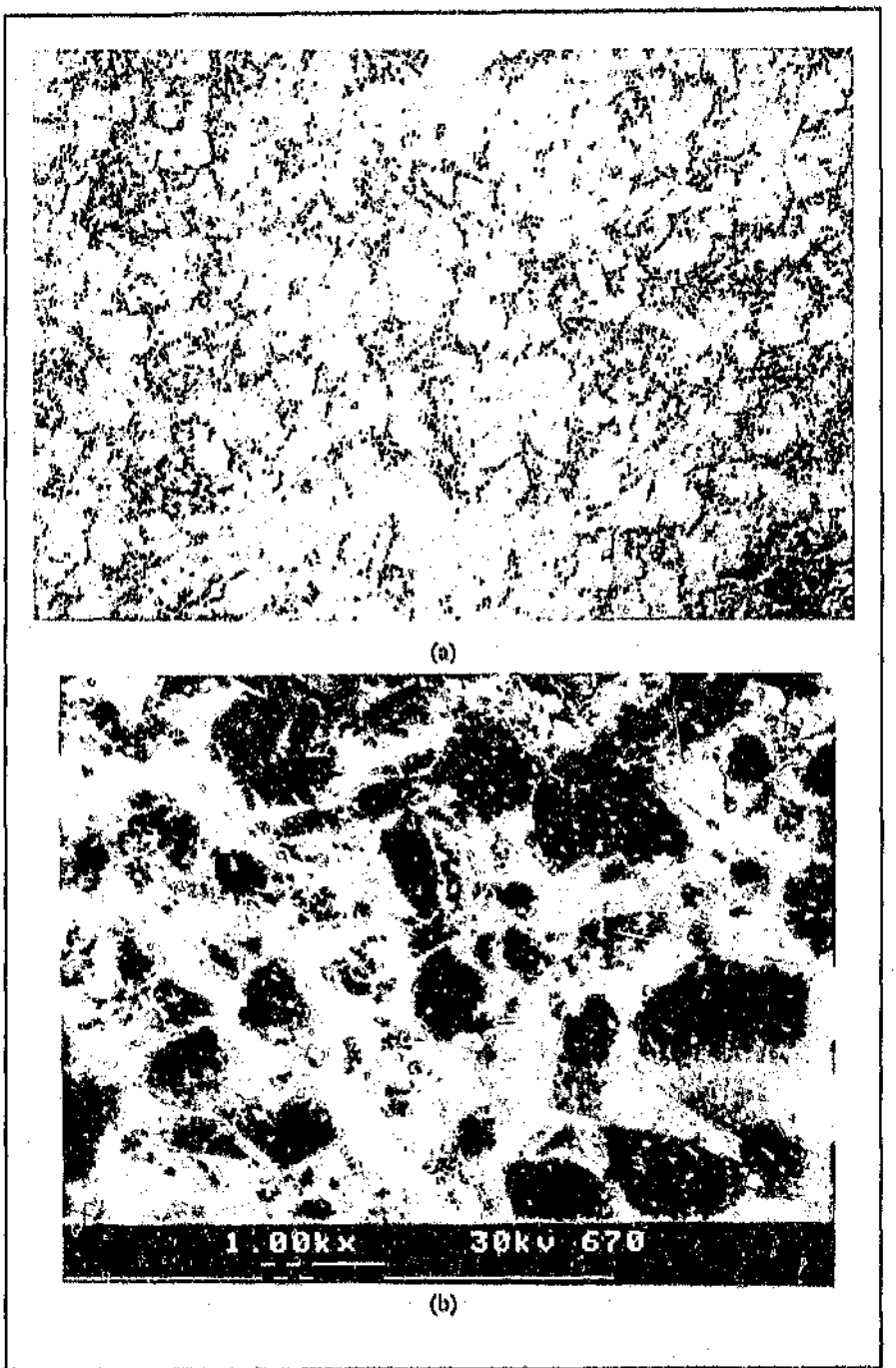

Figure 5.13: Typical appearance of Syndax disc from the self-mated Syndax couple under dry sliding: (a) optical micrograph (500x mag.), and (b) SEM micrograph

to the well-known 'tin-sweating' effect observed in bronze bearings. Further studies are required to determine the mechanistic details, but were beyond the scope of the present work.

As outlined in the previous section, the Co-rich tribofilms were associated with high friction coefficients. At somewhat lower loads where the layers were less well-developed and very patchy, erratic friction behaviour occurred as a result of stick-slip motion. While cobalt-induced degradation of the diamond surfaces may also have played a rôle in this regard, it is suggested that adhesion between the Co-rich tribofilms and/or shear of the films in the sliding interface were the dominant effects.

Self-mated Syndax

The Syndax surfaces were highly polished but exhibited evidence of preferential wear of the inter-grain areas (Figures 5.13 and 5.14). Some of the cavities in the binder phase regions may still be remnants from the original lapped surface, however. Wear debris accumulation and compaction was observed in some of the binder phase regions.

No obvious tribofilms were discerned by microscopic examination of the surfaces. EDS analyses on the polished diamond grains showed small amounts of Si, however, which suggests that very thin Si-rich tribofilms were formed (Figure 5.15).

The precise composition of the Si-rich films was not confirmed since these particular specimens could not be accommodated in the required analysis equipment (AES, XPS). Nevertheless, based on published information and own experience with ceramic friction and wear, it is probable that the films contained significant amounts of silicon oxides and hydroxides, both of which are comparatively lubricious. This would explain the fact that the films were not detrimental to the friction behaviour of the couple.

In summary, the low friction coefficients and high I.CC of the self-mated Syndrill couple were attributable to the absence of Co-rich tribofilms on the surfaces. Sliding contact occurred primarily between relatively clean diamond surfaces, some of which were covered

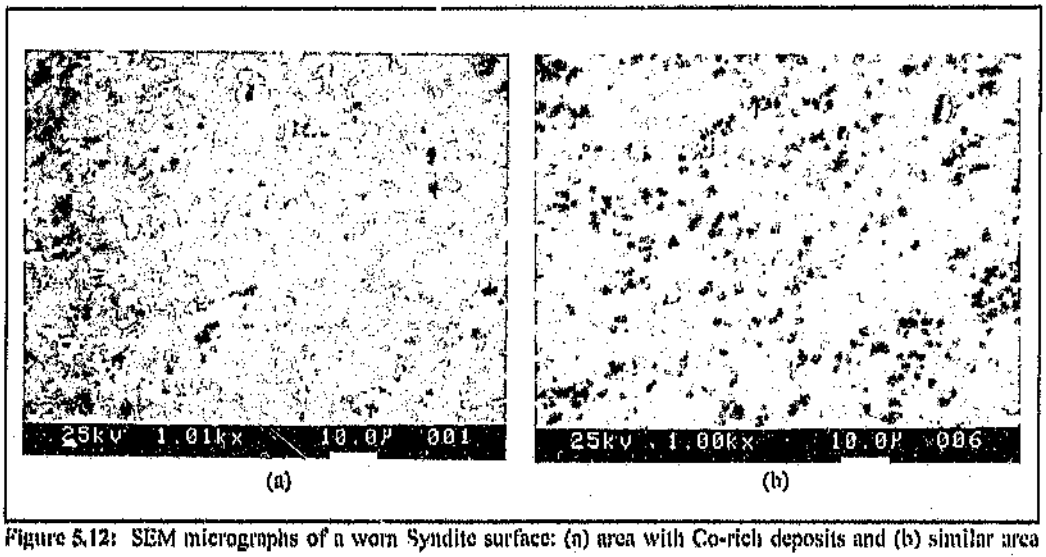

Figure 5.12: SEM micrographs of a worn Syndite surface: (a) area with Co-rich deposits and (b) similar area after cleaning with hydrochloric acid.

bulk to the sliding surface was the primary effect contributing to tribofilm formation. It is unlikely that mechanical extrusion of the binder phase by deformation of the near-surface PCD microstructure played a significant rôle in this process. Unlike tungsten carbide-cobalt (WC-Co) cermets, where this mechanism is commonly observed [215], Syndite is characterized by the true intergrowth or sintering of diamond particles to form a stiff, continuous diamond skeleton. The potential for microstructural deformation and concomitant mechanical binder phase extrusion is thus much lower in these materials.

It is more likely that binder phase migration was thermally activated by frictional heating and was sustained by a diffusion mechanism, probably involving the diffusion of vacancies into the PCD compact, analogous to a similar migration effect observed during the brazing of Syndite [216]. The underlying driving force for the mechanism may have been provided by the binder phase undergoing some chemical reaction(s) at or near the surface of the PCD compact (recall that AES and XPS analyses of the tribofilms showed the presence of binder phase oxides). Differential thermal expansion between the binder phase and the rigid diamond network probably played a lesser rôle, since PCD compacts contain sufficient microporosity after manufacture to accommodate such effects up to high temperatures (>700 °C) without binder phase exudation [217]. In summary, it is considered that the mechanism is analogous

Table 5.2: XPS results obtained from a typical, thick tribofilm on a Syndite surface.

Peak	Binding energy (eV)	Species
C (1s)	284,10	Graphite
	285,25	Diamond
Co ($2p_{3/2}$)	782,85	Co-oxide
W ($5p_{1/2}$)	38,3	W-oxide

films were quite continuous. Loose Co-rich binder wear debris most likely contributed to the formation of the films by agglomeration at surface discontinuities such as grain boundary regions, where it was compacted and smeared over the surface of the diamond grains. The latter effect may have become more prominent as the surface finish of the Syndite improved, probably because the discontinuities became smaller and less able to accommodate loose wear debris. The extent of tribofilm formation would then be expected to be similarly related to surface finish, which could explain the trend towards higher friction coefficients and more erratic friction behaviour with improved surface finish. The important rôle of loose wear debris was confirmed by the observation that the debris tended to form a compacted layer at the leading edge of the Syndite pin, at the interface between the edge taper and the sliding surface (Figure 5.11).

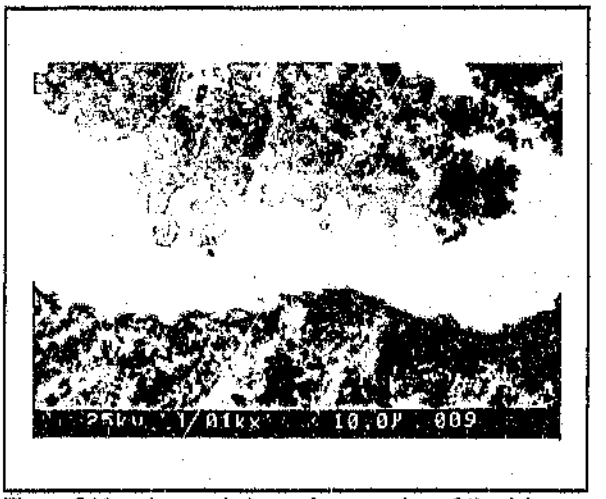

Figure 5.11: Accumulation and compaction of Co-rich wear debris at the leading edge of a Syndite pin.

Removal of the Co-rich tribefilms by etching with hydrochloric acid resulted in fairly deep valleys in the inter-grain regions (Figure 5.12). Nevertheless, the tribofilm could be re-formed rapidly even at low loads of 500 N where little further polishing and wear of the diamond grains occurred. This observation suggests that migration of the binder phase from the PCD

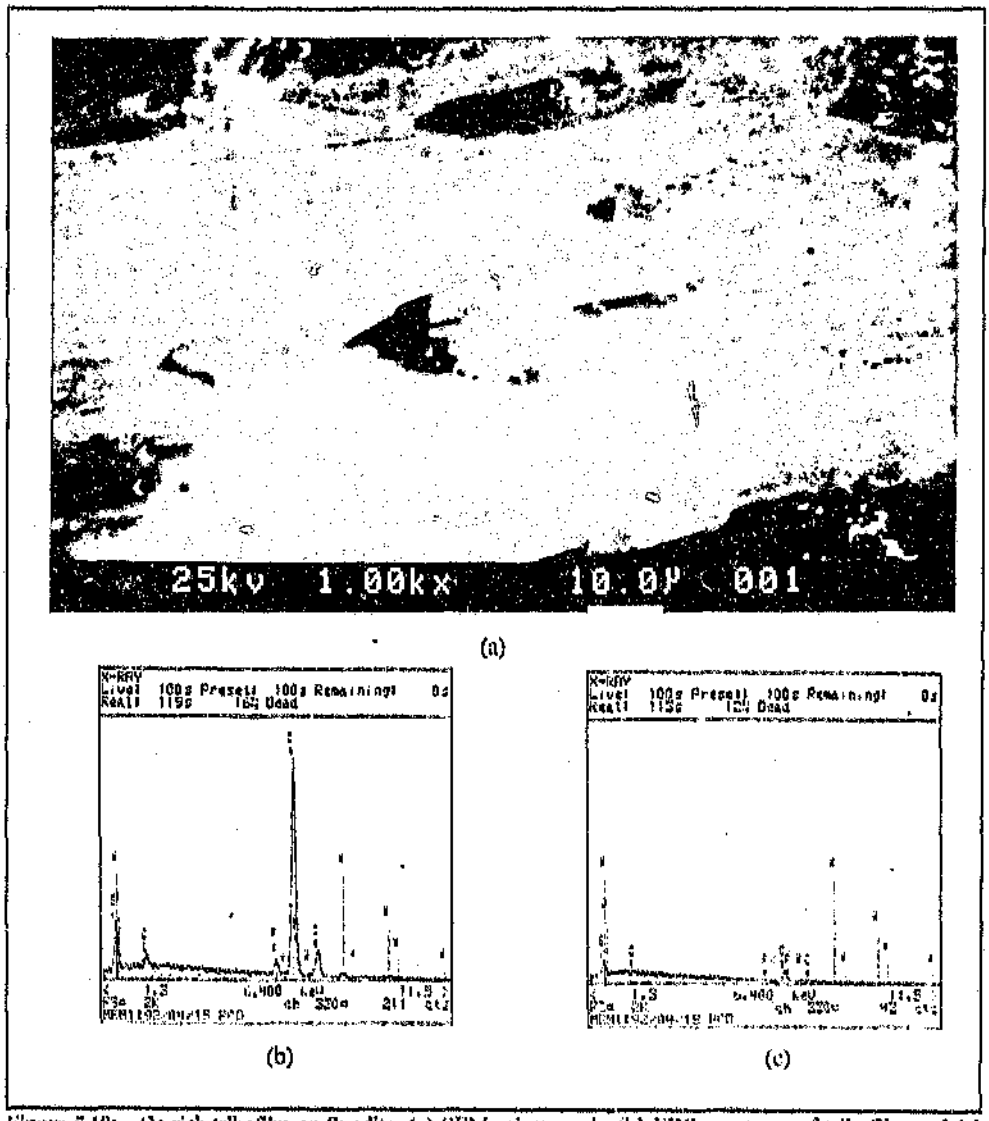

Figure 5.10: Co-rich tribofilm on Syndite: (a) SEM micrograph; (b) EDS spectrum of tribofilm and (c) EDS spectrum of polished diamond grain without tribofilms.

A small graphite peak was detected apart from the dominant diamond peak, suggesting that some graphitization of the diamond surfaces had occurred, possibly stimulated by the presence of the Co-rich tribofilm.

The surface films tended to form in patches with well-defined boundaries, within which the

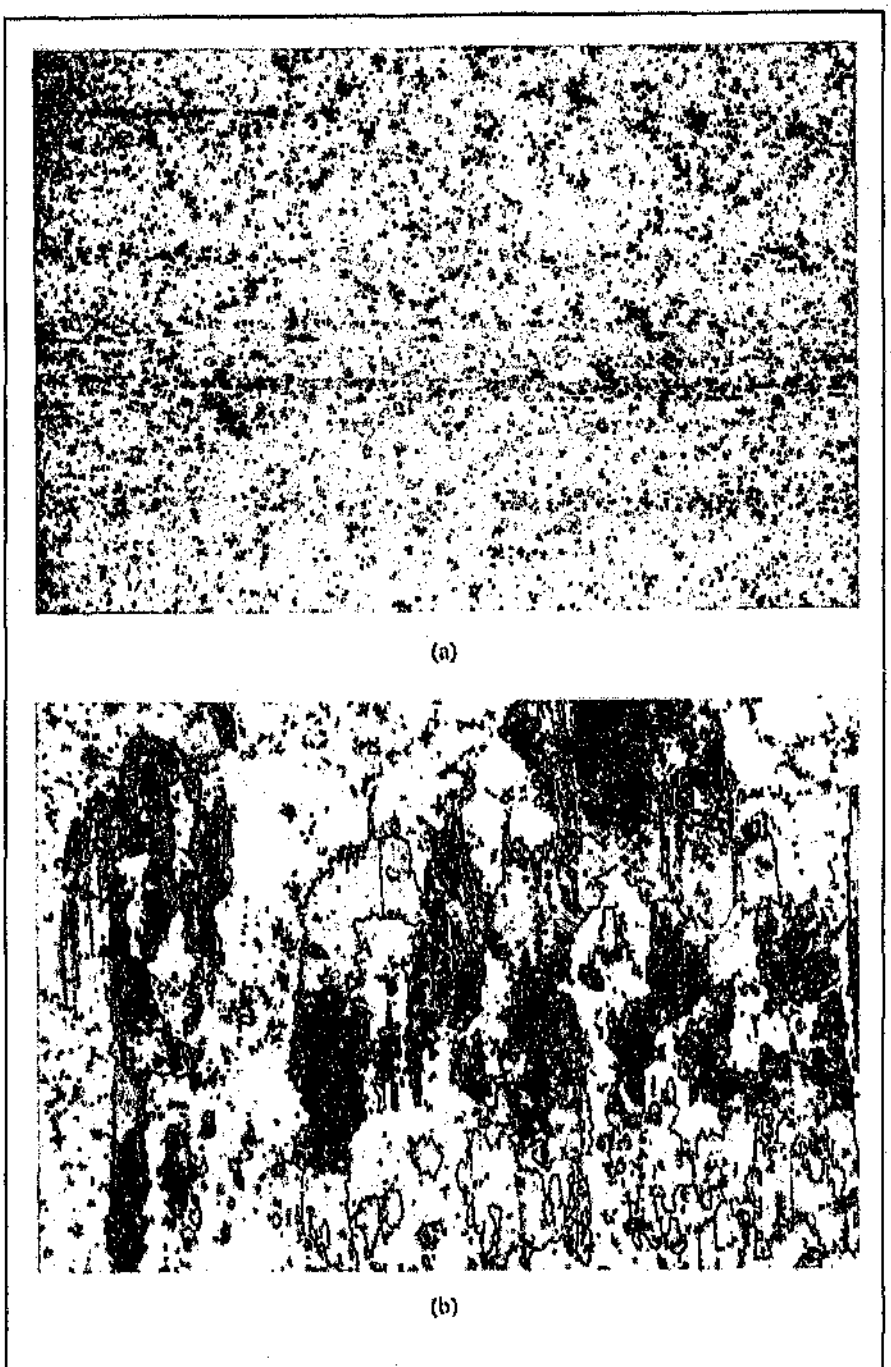

(a)

(b)

Figure 5.9: Well-developed tribofilms on (a) Syndite disc (140x mag.); and (b) Syndite pin (400x mag.).

5.3.4 Surface effects and tribofilm formation

Self-mated Syndite

Extensive tribofilm formation was observed on the Syndite disc and pin after completion of the LCC tests (Figure 5.9). These films were usually very thin, as indicated by their coloured appearance under the optical microscope, and were generally observed more easily by optical than by scanning electron microscopy.

Energy dispersive X-ray (EDS) analyses were conducted on a Syndite pin with a thick surface film smeared over part of the polished PCD surface, in order to determine the nature of these films (Figure 5.10). Little metallic contamination was found on diamond grains without the surface layer, while a high concentration of cobalt and tungsten, the constituents of the Syndite binder phase, was detected where the layer was present. More sophisticated analyses using Auger electron spectroscopy (AES), indicated that the approximate composition of the layer was Co 19%, C 41%, O 33%, W 7%, and Cl 0,6%. An analysis on a polished diamond grain without any apparent surface layer showed an approximate composition of Co 4%, C 87%, O 7%, and Cl 2%. Clearly, the surface layer was rich in Co with lesser amounts of W and originated from the Syndite binder phase. The high oxygen content detected by AES suggests that oxidation of some or all of the elements in the layer had occurred.

X-ray photoelectron spectroscopy (XPS) analyses were performed to examine the nature of the layer in more detail. The resultant spectra were relatively complex with carbon and oxygen exhibiting composite peaks. There is some uncertainty concerning the position of the W and particularly the Co peak, due to relatively large statistical errors associated with the peak analysis. In the latter case this uncertainty could be of the order of 1 - 2 eV. With this in mind, there was some evidence for oxidation of these tribofilm constituents, as suggested by the AES measurements (Table 5.2). A more precise determination of tribofilm composition would require a far more comprehensive study, which was beyond the scope of the present work.

2 and 4), it is probable that the silicon-rich tribofilm on the Syndax surface contained significant amounts of silicon oxides and hydroxides, which are relatively lubricious. This would explain the fact that the film did not appear to have a detrimental effect on the friction behaviour of the Syndax / Syndite couple.

<u>Syndite (pin) / Syndax (disc)</u>

Finally, this sliding couple also carried the maximum applied POD machine load of 4300 N (Figure 5.8). The friction coefficient remained essentially constant over the load range although variations occurred between 0,09 and 0,11. The results suggest that Syndite/Syndax may be slightly superior to Syndax/Syndite with respect to friction behaviour for low load applications and vice versa. Nevertheless, both couples are far superior to the self-mated Syndite couple and are better suited for unlubricated, high load sliding applications.

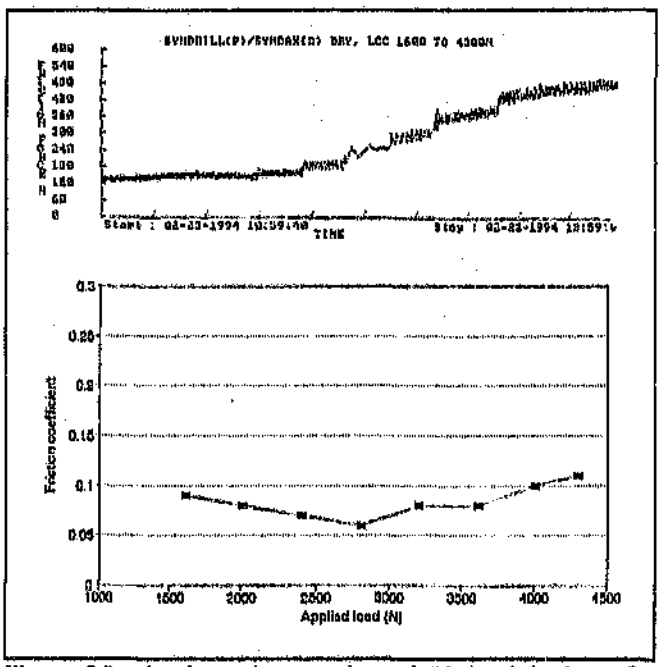

Figure 5.8: Load carrying capacity and friction behaviour of a Syndite (pin) / Syndax (disc) couple in dry sliding.

Detailed examination of the worn surfaces revealed silicon and cobalt-rich tribofilms on the Syndax surface, similar to those found on the Syndax/Syndite couple. The Syndite surface was essentially free from deleterious Co-rich tribofilms.

The superior friction characteristic of Syndax compared to Syndite is thought to be related to the absence of Co-rich or any other well-developed tribofilms on the sliding surfaces (Section 5.3.4). The friction behaviour is thus dominated by diamond-diamond contact, rather than by the properties of interfacial films.

Syndax (pin) / Syndite (disc)

This couple also sustained the maximum POD machine load of 4300 N, although the scatter in friction coefficient was significantly higher than for the self-mated Syndax sliding couple (Figure 5.7). Nevertheless, the friction coefficient also decreased over the load range used, from 0,16 at 1600 N to 0,07 at 4300 N, which is comparable to the self-mated Syndax couple.

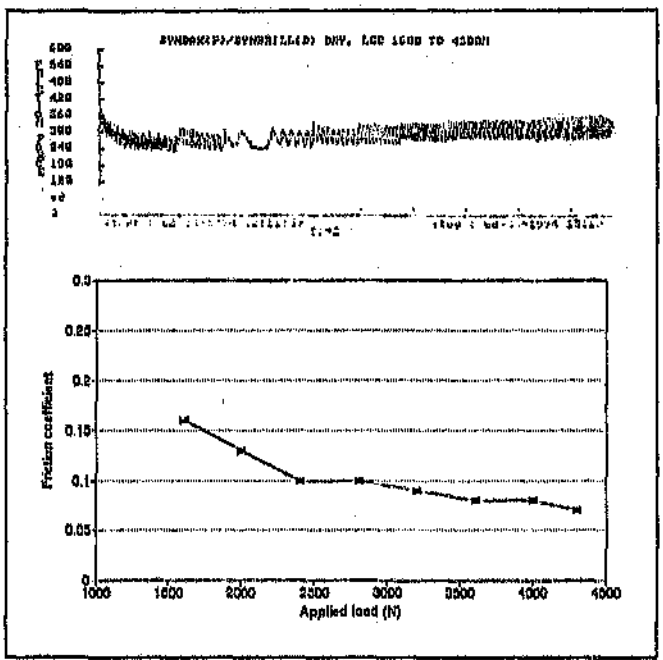

Figure 5.7: Load carrying capacity and friction behaviour of a Syndax (pin) / Syndite (disc) couple in dry sliding.

These results are perhaps surprising in view of the presence of cobalt in the Syndite material, which was seen to be related to the poor friction behaviour of self-mated Syndite. However, a detailed analysis of the worn surfaces revealed no Co-rich tribofilms on any of the sliding surfaces. A complex, patchy silicon and cobalt containing tribofilm was noted instead on the Syndax surface (Section 5.3.4). The cobalt was effectively 'bound' in this complex film, and thus adhesion between the surfaces as well as the potential for cobalt-induced decomposition of the diamond surfaces was reduced.

Based on published literature and own experience with ceramic friction and wear (Chapters

However, this may not have been the only mechanism, since removal of the tribofilms resulted in a dramatic decrease in friction even at low loads. Thermocouple measurements indicated that the temperature at the interface between the 0,7 mm thick Syndite layer and the underlying WC-Co support did not exceed 50 °C at these loads. In view of the high thermal conductivity of Syndite, it would appear unlikely that the surface temperature would have reached values around 700 °C under these conditions. It is suggested, therefore, that direct interaction or adhesion between the Co-rich tribofilms on the two sliding elements may also have significantly contributed to the observed effect of these films on Syndite friction behaviour, particularly at lower loads. Such interaction may have been further controlled by other properties of the tribofilms, such as thickness and shear strength.

Self-mated Syndax

Load carrying capacity (LCC) tests were performed using tapered Syndax pins by increasing the applied load systematically from 1600 N to about 4300 N. The sliding couple exhibited low friction coefficients and smooth friction behaviour up to 4300 N (67,6 MPa contact pressure), which is the maximum applied load that could be reached with the POD machine (Figure 5.6). In fact, the friction coefficient decreased from about 0,13 at 1600 N to 0,07 at 4300 N applied load, in contrast to the self-mated Syndite couple.

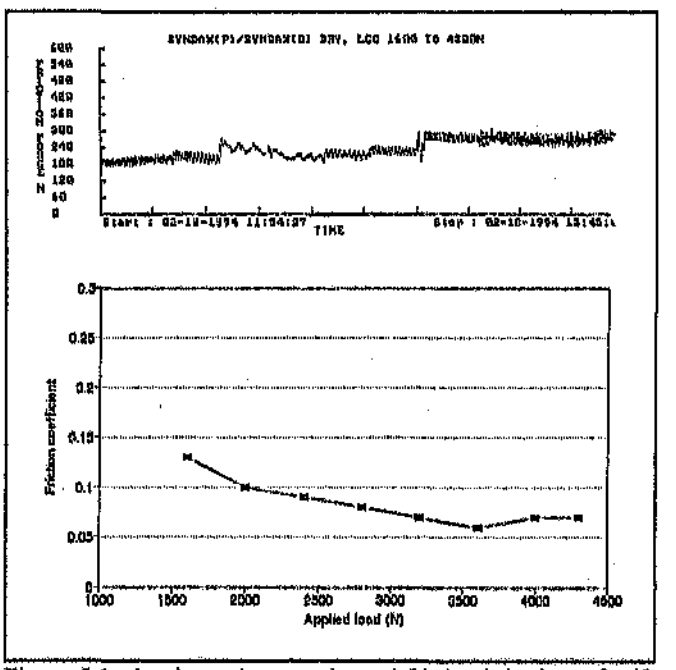

Figure 5.6: Load carrying capacity and friction behaviour of self-mated Syndax in dry sliding.

3200 N, which was defined as its load carrying capacity (LCC).

The increase in friction coefficient and associated scatter was seen to be related to the formation of a more or less continuous tribofilm on the Syndite surfaces, which appeared to originate from the Co-rich binder at the inter-grain areas. It was found that the film could not be removed with water or organic solvents, but could be readily and completely removed with dilute (~ 6M) hydrochloric acid. Detailed analysis of the tribofilm appearance and composition indicated that it was indeed rich in cobalt and originated from the binder phase (Section 5.3.4).

To study this effect further, additional experiments were conducted at various loads both before and after removal of the Co-rich films with hydrochloric acid. As shown in Figure 5.5, significantly lower friction coefficients were obtained with the cleaned specimens. This result confirmed the deleterious effect of the tribofilms on the friction behaviour of self-mated Syndite.

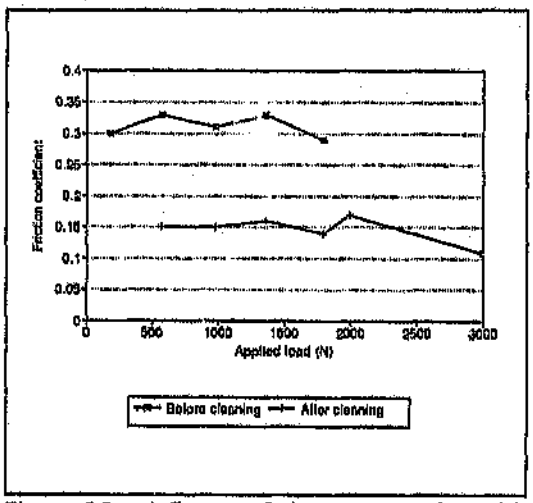

Figure 5.5: Influence of the presence of Co-rich tribofilms on the friction behaviour of self-mated Syndite.

Cobalt acts as a catalyst and is known to reduce the temperature at which diamond begins to graphitize in the presence of oxygen from ~875 °C to ~700 °C (Section 2.4.4). In the present case, the Syndite surfaces visually appeared shiny, black, with dark streaks in the areas where the Co-rich layers were present, and it is possible that this mechanism contributed to the observed effect. Indeed, XPS analyses suggested that a small amount of graphite was present on the Syndite surfaces.

experiments conducted with similar Syndax pins and discs before they were lapped flat suggested that loads in excess of 4000 N (62,8 Mpa contact pressure) could be sustained. In this case, however, the pin surface was slightly curved and the edge chipping effect described above did not occur. The surfaces of the specimens were also not grooved to the same extent.

In view of the edge chipping damage, the test series to determine the load carrying capacity of self-mated Syndax was repeated using pins with a 2 mm, 5° edge taper. This pin geometry was also used for all remaining tribotests, as indicated in Section 5.2.

5.3.3 Influence of load and load carrying capacity (LCC)

Self-mated Syndite

The influence of applied load on the friction behaviour of self-mated Syndite is shown in Figure 5.4. As observed during the run-in phase, the friction coefficients were relatively high (0,17 - 0,26) and were found to increase significantly beyond an applied load of 3200 N (50,3 MPa contact pressure). At higher loads, the friction coefficient also tended to increase with time for a given load and the scatter in the measured friction force increased, indicating that the Syndite couple was not sliding under steady state conditions. It was thus concluded that the maximum load which could be sustained by the couple with constant friction coefficient was

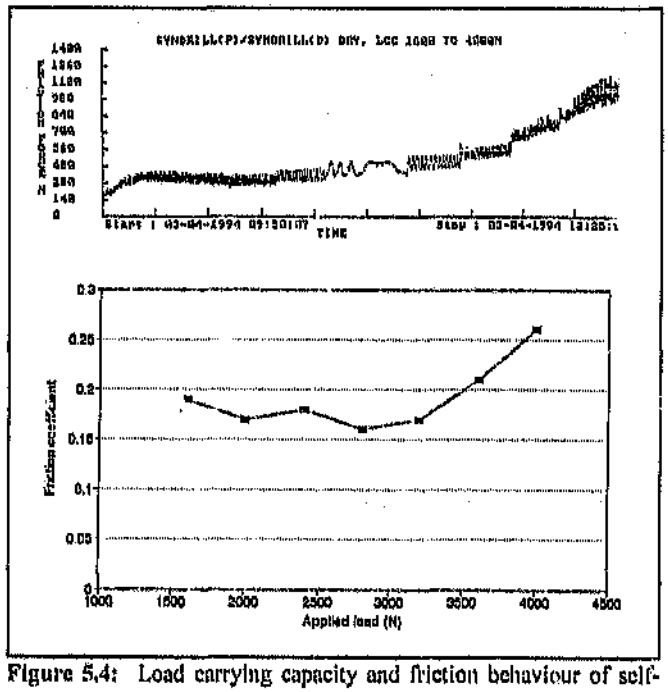

Figure 5.4: Load carrying capacity and friction behaviour of self-mated Syndite in dry sliding.

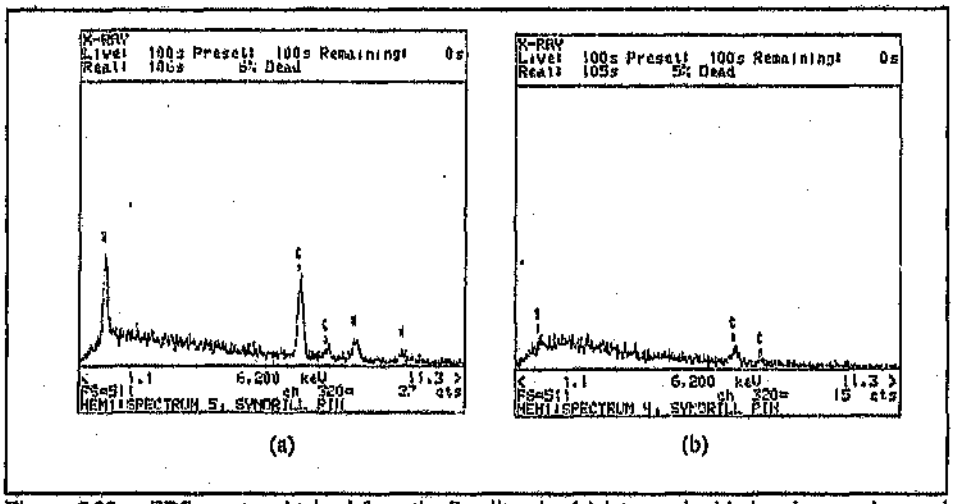

Figure 5.23: EDS spectra obtained from the Syndite pin: (a) inter-grain, binder phase region; and (b) typical polished diamond grain, showing absence of Co-rich tribofilms.

high affinity between Co and the Si-rich Syndax binder phase.

As for the Syndax (pin) / Syndite (disc) couple, the Co from the Syndite binder phase was thus bound in a complex Si-rich tribofilm on the Syndax disc. This effectively cleaned the Syndite surface, limited the formation and interaction of Co-rich tribofilms, and resulted in the low friction coefficients and high load carrying capacity observed.

5.3.5 Influence of drilling fluid constituents

It is normal practice to pump a drilling fluid down the drill pipe and through the drill bit to cool and lubricate the drill bit and flush the cuttings out of the borehole. These fluids are usually water-based clay (bentonite) muds. In order to ensure that the cuttings are carried out of the borehole efficiently, barite and/or haematite additions are also made to adjust the density of the drilling mud. The density required and thus the level of these additions depend on the depth of the borehole, and increase with increasing depth. For holes of about 2000 m in depth, the typical bentonite and barite contents would be of the order of 5 wt%, giving a mud density of ~1.3 g.cm^{-3}. Haematite is generally added only for extreme depths and where very high mud densities are required. Due to the nature of the application, the drilling mud

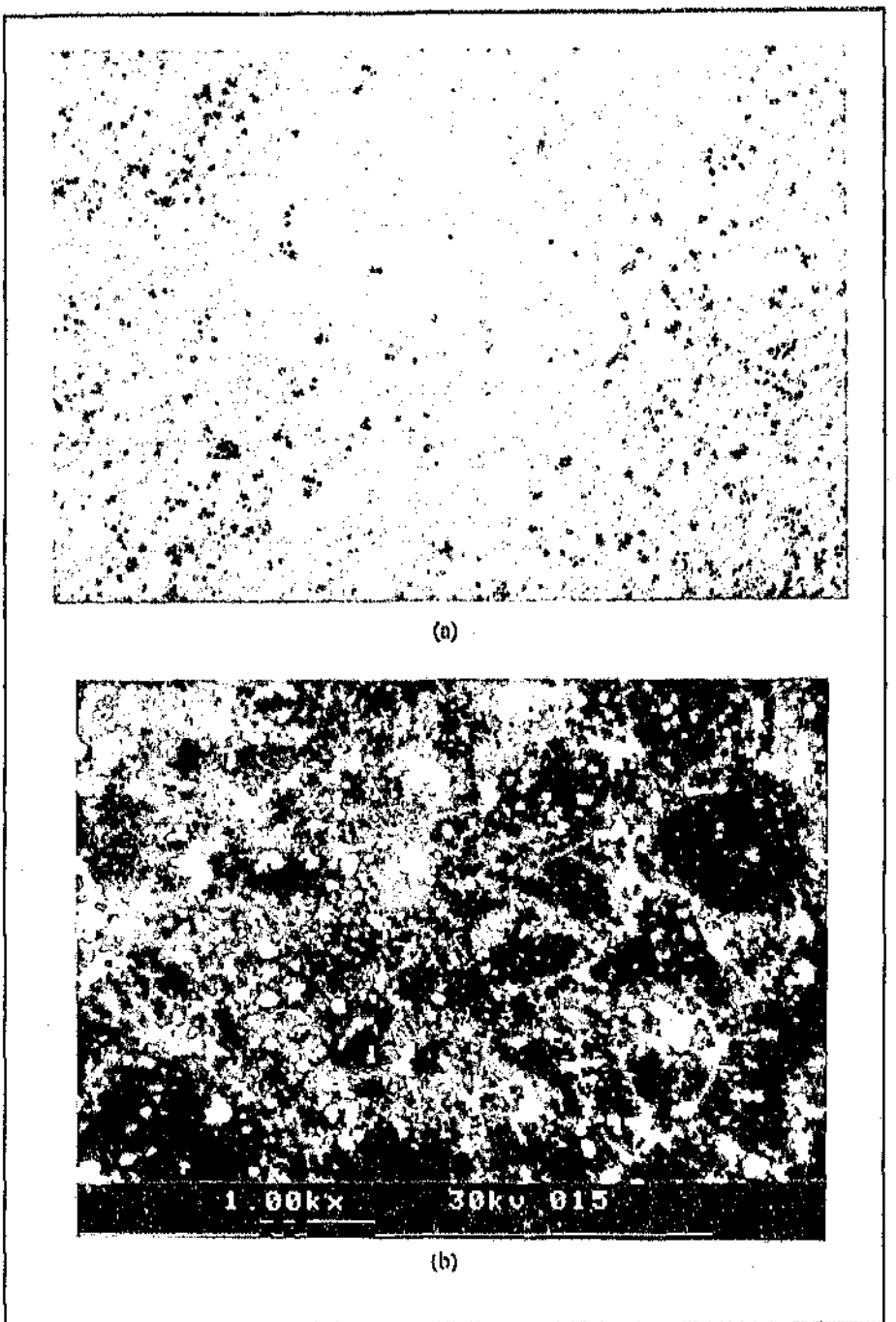

(a)

(b)

Figure 5.22: Optical micrograph (a), 200x mag.; and (b) SEM micrograph of the Syndite pin from the Syndite (pin) / Syndite (disc) dry sliding couple.

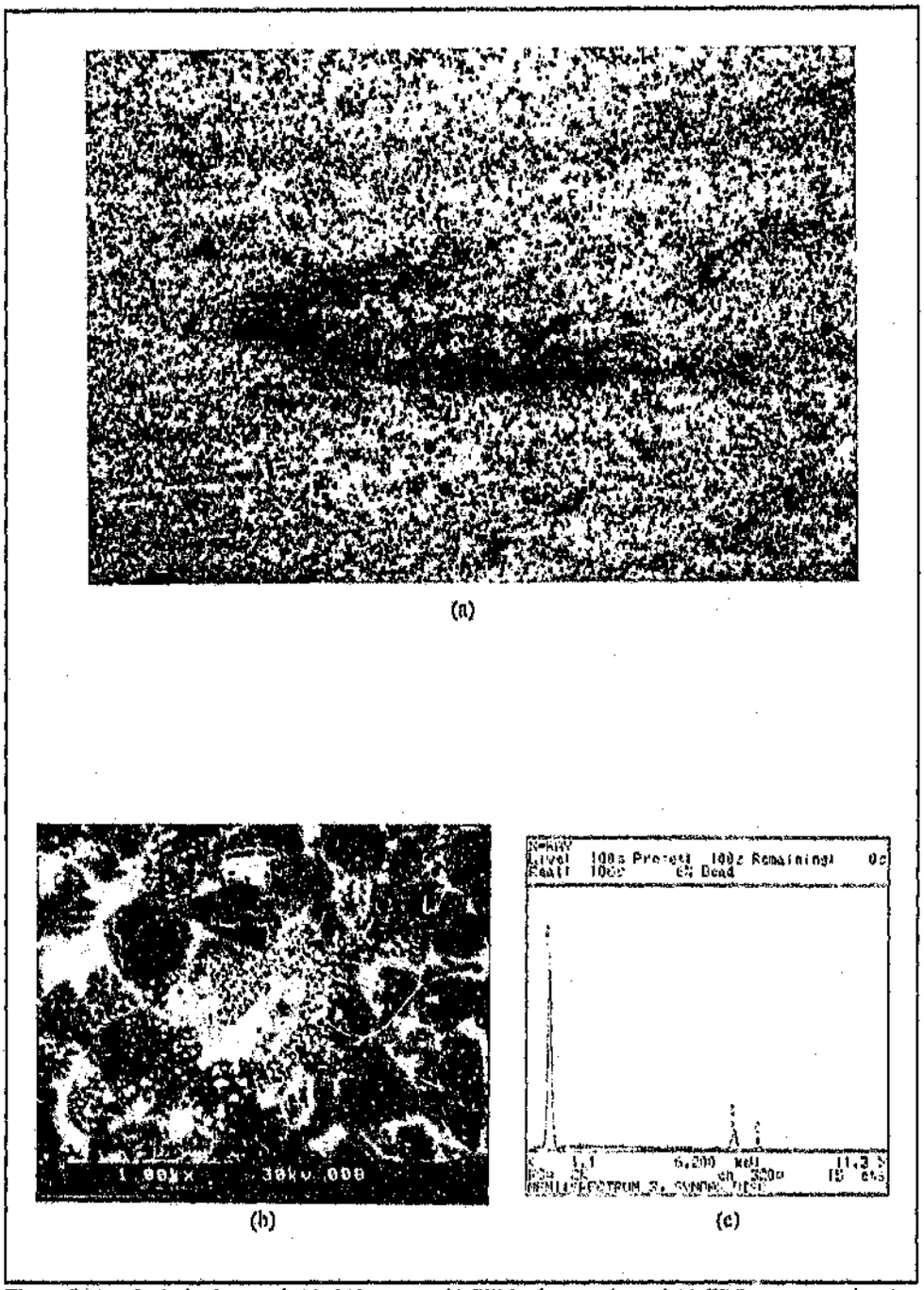

Figure 5.21: Optical micrograph (a), 200x mag.; (b) SEM micrograph; and (c) EDS spectrum, showing the formation of Si and Co-rich triboflms on the Syndax disc from the Syndite (pin) / Syndax (disc) dry sliding couple.

regions were denuded of Co (as shown in Figure 5.15). The complex debris formed in this way was then smeared over the Syndax diamond grains to form the observed tribofilms.

The mechanism outlined above may have involved direct interaction between the Syndax and Syndite binder phases, and/or reaction between loose debris originating from the binder phases. The presence of a significant amount of loose wear debris on the Syndite surface indicated that the latter process probably played a significant rôle. Further, the preferential transfer of Co to the Syndax surface would appear to have had the effect of protecting the Syndax binder phase regions from preferential wear. This may have been related simply to the accumulation of debris at the Syndax binder phase regions, and/or a modification in the mechanical properties of the Si-rich material in these areas as a result of the presence of Co and W. An analogous effect has been observed in WC-Co cemented carbide composite materials, where the accumulation of debris in the binder phase regions protected the binder phase from further wear [220].

Syndite (pin) / Syndax (disc)

The features noted on this material couple were similar to those on the Syndax (pin) / Syndite (disc) couple. The Syndax disc exhibited extensive tribofilm formation in the form of thick patches which were smeared over adjacent diamond grains and were often associated with loose particulate wear debris (Figure 5.21). EDS analyses showed that the films were rich in Si and Co; however, in contrast to the films found in the case of the Syndax (pin) / Syndite (disc) couple, no significant amounts of tungsten were detected (Figure 5.21 (c)). Nevertheless, it is likely that the films were formed by a similar mechanism.

The bulk of the Syndite pin area was highly polished and only some loose wear debris was present on the surface (Figure 5.22). No obvious tribofilms were noted. EDS analyses confirmed that appreciable amounts of Co and W were only present in the binder phase regions, while the diamond grain surfaces were essentially free of Co (Figure 5.23). The Co-rich binder phase was thus preferentially removed from the Syndite surface as a result of the

intensity of the peak measured at 101.35 eV was significantly higher than that of the peak at 783.75 eV, and was thus attributed mainly to a Si-containing compound. In particular, the peak could correspond to a complex metal-Si-O compound, since a compound of the form $Me_3SiOSiMe_3$ exhibits a peak at 100.9 eV and a compound of the form $(Me_2\ SiO)_4$ exhibits a peak at 101.6 eV according to the database. Although far from conclusive, these results thus provided some tentative evidence for a complex Si-Co containing compound in the tribofilm, as expected from the phase diagram. The determination of the exact nature of the compound would require a very detailed XPS study, which was beyond the scope of the present work.

Tungsten, a small amount of which is present in the Syndite binder phase, did not appear to have reacted with any of the other tribofilm constituents. There was some evidence to suggest, however, that it was present in the form of an oxide (Table 5.3).

The mechanism of tribofilm formation was clearly complex and involved a number of processes. Analogous to the Syndite couple, it is proposed that the binder phase on both the Syndax and the Syndite sliding elements was exuded from the structure under the influence of frictional heating. Although Syndax is a true composite where no diamond intergrowth is present, the network of diamond grains is extremely stiff as a result of the high volume fraction of diamond. It is thus considered unlikely that direct mechanical extrusion contributed significantly to binder phase migration.

In the case of self-mated Syndite, this mechanism resulted in the formation of Co-rich tribofilm patches on both sliding elements. In self-mated Syndax, the Si-rich binder phase became oxidized and was thus easily removed from the surfaces, resulting in low friction coefficients and preferential wear of the binder phase without the formation of thick tribofilms. However, in mixed Syndax / Syndite sliding couples the Co-rich binder phase of the Sydite evidently exhibited a strong affinity towards the Si-rich binder phase of the Syndax, as shown by the EDS and XPS analysis results. As a result, it was preferentially removed from the Syndite surface, reacting with the Si and accumulating at the binder phase regions of the Syndax surface. (This tends to be confirmed by the fact that the Syndite binder phase

(Table 5.3). The graphitization did not appear to have a negative effect on the friction coefficient or load carrying capacity under the test conditions used. This provides a further indication that the relatively poor performance of the self-mated Syndite couple was attributable mainly to adhesion and direct interaction between the Co-rich tribofilms formed on these materials, rather than tribofilm-induced chemical degradation of the diamond surfaces.

Table 5.3: XPS results obtained from a typical tribofilm on a Syndax surface after dry sliding against Syndite.

Peak	Binding energy (eV)	Species
C (1s)	284.80	Graphite
	286.00	Diamond
O (1s)	532.65	Silicon oxide
	534.10	Silicon oxide
	531.00	W-oxide, possibly WO_2 (?)
Si (2p)	101.35	Complex Si-metal compound, or Co (3s) peak
	103.60	Silicon oxide
	104.95	Silicon oxide
Co ($2p_{3/2}$)	783.75	? (some indications for a complex Co compound, but no match found in XPS database)
W ($2p_{3/2}$)	37.90	W or W-oxide

The Si data indicated that much of the tribofilm was heavily oxidized, which could account for the fact that the film did not have a deleterious effect on the friction coefficient or load carrying capacity of the sliding couple. The Co peak at 783.75 eV and one small peak at 101.35 eV, which was attributed to Si, could not be uniquely identified using the available XPS database. Interpretation was complicated by the fact that the Co peak at 783.75 eV was poorly defined due to relatively large statistical errors associated with the peak analysis. It is possible that this peak was indicative of the presence of Co in its metallic form, since the Co($2p_{3/2}$) peak appears at 778 eV [219]. Furthermore, for pure cobalt the Co(3s) peak appears at 101 eV but is much smaller in intensity than the Co($2p_{3/2}$) peak. In the present case, the

appeared to be effective in "neutralizing" or "binding" the Co, which suppressed the formation and interaction of Co-rich tribofilms on the diamond surfaces and thus led to the low friction coefficients observed on this material couple.

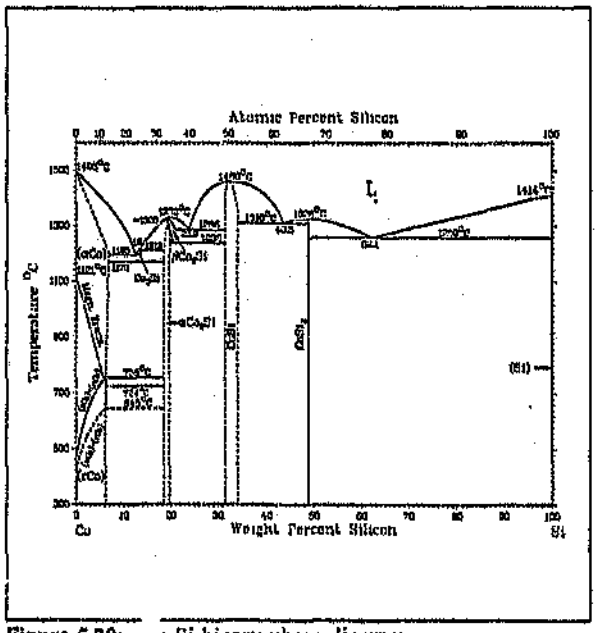

Figure 5.20: Co-Si binary phase diagram.

The strong interaction between Si and Co in the tribofilm can be understood by considering the relevant binary phase diagram (Figure 5.20, from Ref. [218]). This indicates that Si and Co form solid solutions as well as a number of intermetallic compounds over a wide range of compositions. In the present case, the EDS analyses suggested that the tribofilms contained significantly more Si than Co. By referring to the silicon-rich portion of the phase diagram, it can be seen that the tribofilm might thus be expected to contain a Si-Co containing compound, possibly similar to $CoSi_2$. The actual composition of such a compound would probably be more complex than $CoSi_2$, however, due to the more complex conditions prevailing at the sliding interface, as well as the presence of oxygen which also has a strong affinity towards Si. Nevertheless, the presence of such a compound would help to explain the effective binding of the cobalt in the tribofilm, which appears to prevent the formation of deleterious Co-rich tribofilms on the Syndite counterface.

Based on these considerations, the composition of the tribofilm was studied in more detail by conducting XPS analyses on the Syndax pin. The spectra obtained were again complex, with C, O, Si, and W exhibiting compound peaks. By resolving the peaks, it was found that most of the diamond surface on the Syndax pin was undamaged, although there was some evidence for localized graphitization, similar to that found on the self-mated Syndite surfaces

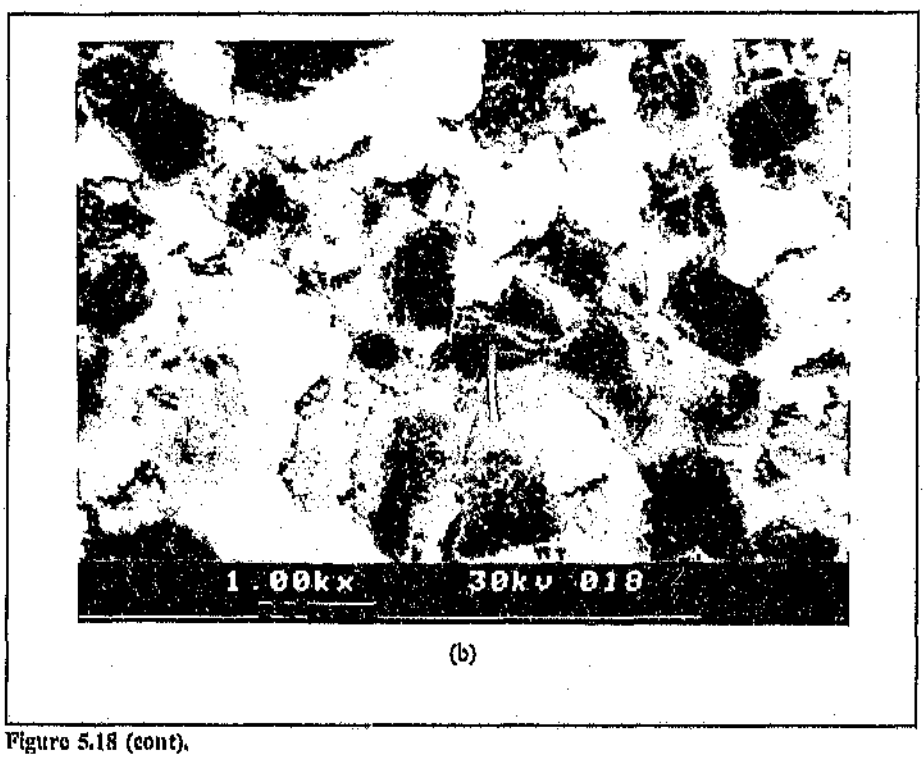

(b)

Figure 5.18 (cont).

Despite the interpretive difficulties, the EDS analysis showed that the films were rich in Si, but also contained significant amounts of Co and W (Figure 5.19). The high Si content could be deduced from the strong peak at around 1,8 keV, which is much too large in relation to the W L-lines between 8 and 10 keV to be attributable only to W. The tribofilms on the Syndax pin thus originated mainly from the Syndax binder phase (Si), but interacted strongly with Co and W from the Syndite binder phase during their formation. Material transfer occurred preferentially from the Syndite binder phase (Co/W) to the Syndax binder phase (Si), as evidenced by the fact that the films formed only on the Syndax surface. The extensive formation of these films

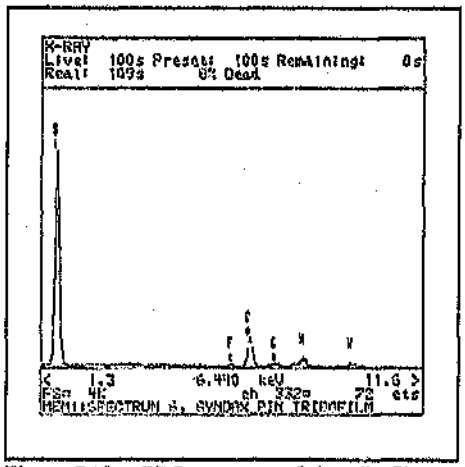

Figure 5.19: EDS spectrum of the tribofilm on the Syndax pin.

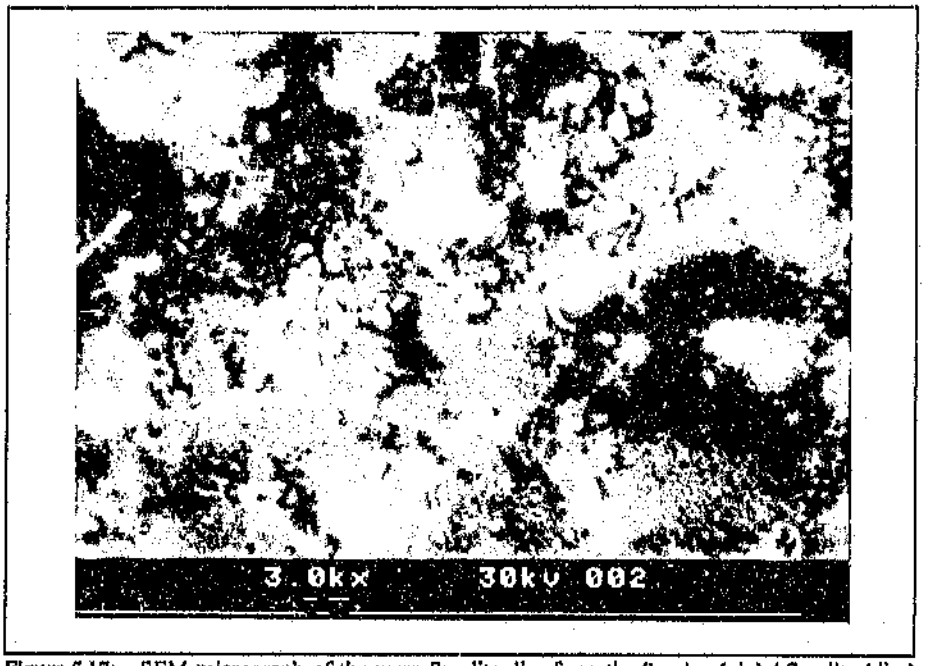

Figure 5.17: SEM micrograph of the worn Syndite disc from the Syndax (pin) / Syndite (disc) dry sliding couple, showing accumulation of loose wear debris on the surface.

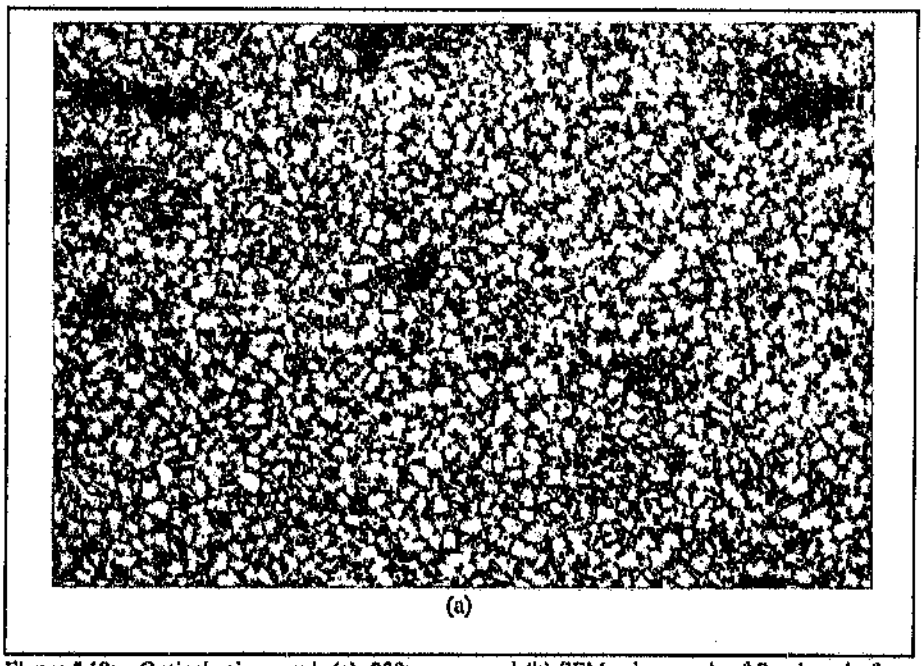

(a)

Figure 5.18: Optical micrograph (a), 200x mag.; and (b) SEM micrograph of Syndax pin from the Syndax (pin) Syndite (disc) dry sliding couple, showing extensive tribofilm formation.

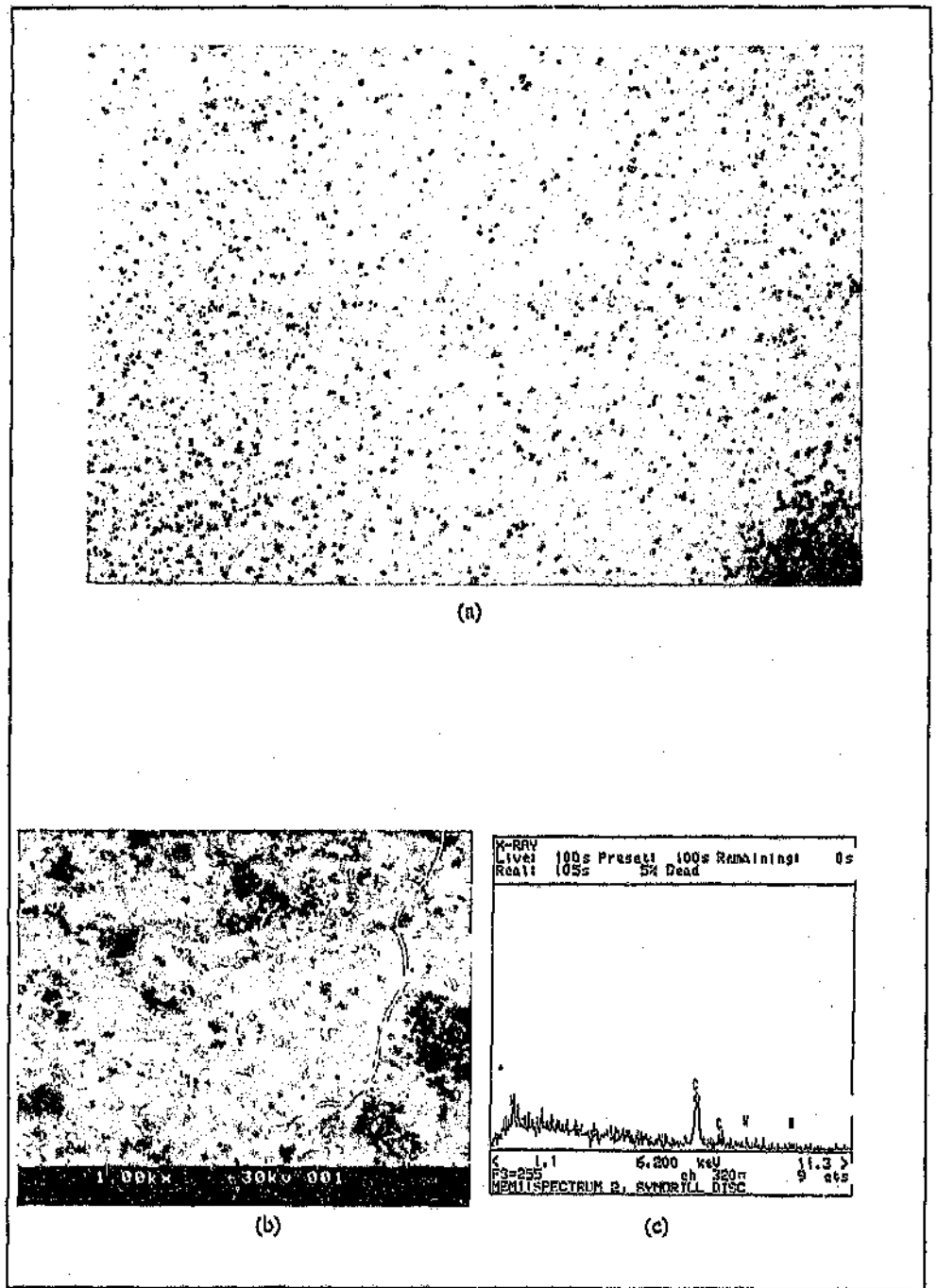

Figure 5.16: Optical micrograph (a), 200x mag.; (b) SEM micrograph; and (c) EDS spectrum of the worn surface of the Syndite disc from the Syndax (pin) Syndite (disc) dry sliding couple.

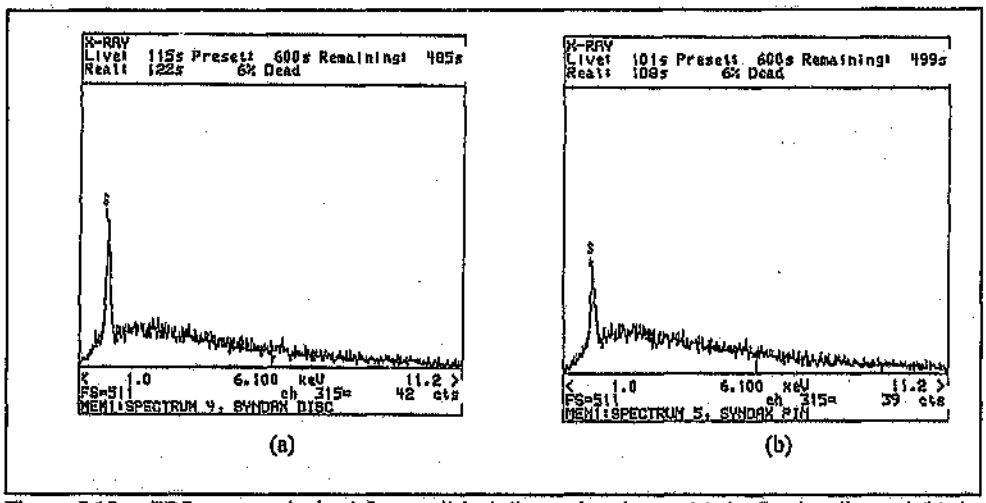

Figure 5.15: EDS spectra obtained from polished diamond grains on (a) the Syndax disc and (b) the Syndax pin from the self-mated Sydax dry sliding couple.

by thin and lubricious, Si-rich tribofilms.

<u>Syndax (pin) / Syndite (disc)</u>

Little Co-rich tribofilm formation was observed on the Syndite disc (Figure 5.16). The diamond surfaces were highly polished and some accumulation of particulate wear debris occurred on the sliding surface (Figure 5.17). This debris was not smeared over the surface and did not appear to be deleterious to the the friction behaviour of the material couple.

In contrast, the Syndax pin exhibited well-developed tribofilms (Figure 5.18). These films occurred in patches which were smeared over the diamond grains and appeared to originate at the binder phase regions. Energy dispersive x-ray (EDS) analysis of the films was somewhat complicated by the fact that the Si K_α line at 1.739 keV overlaps with the W M_α line at 1,774 keV. It was thus difficult to unambiguously identify Si, the Syndax binder phase, in the presence of W, which is contained in the Syndite binder phase. Tungsten could be identified uniquely by it's characteristic L-lines between 8 and 10 keV.

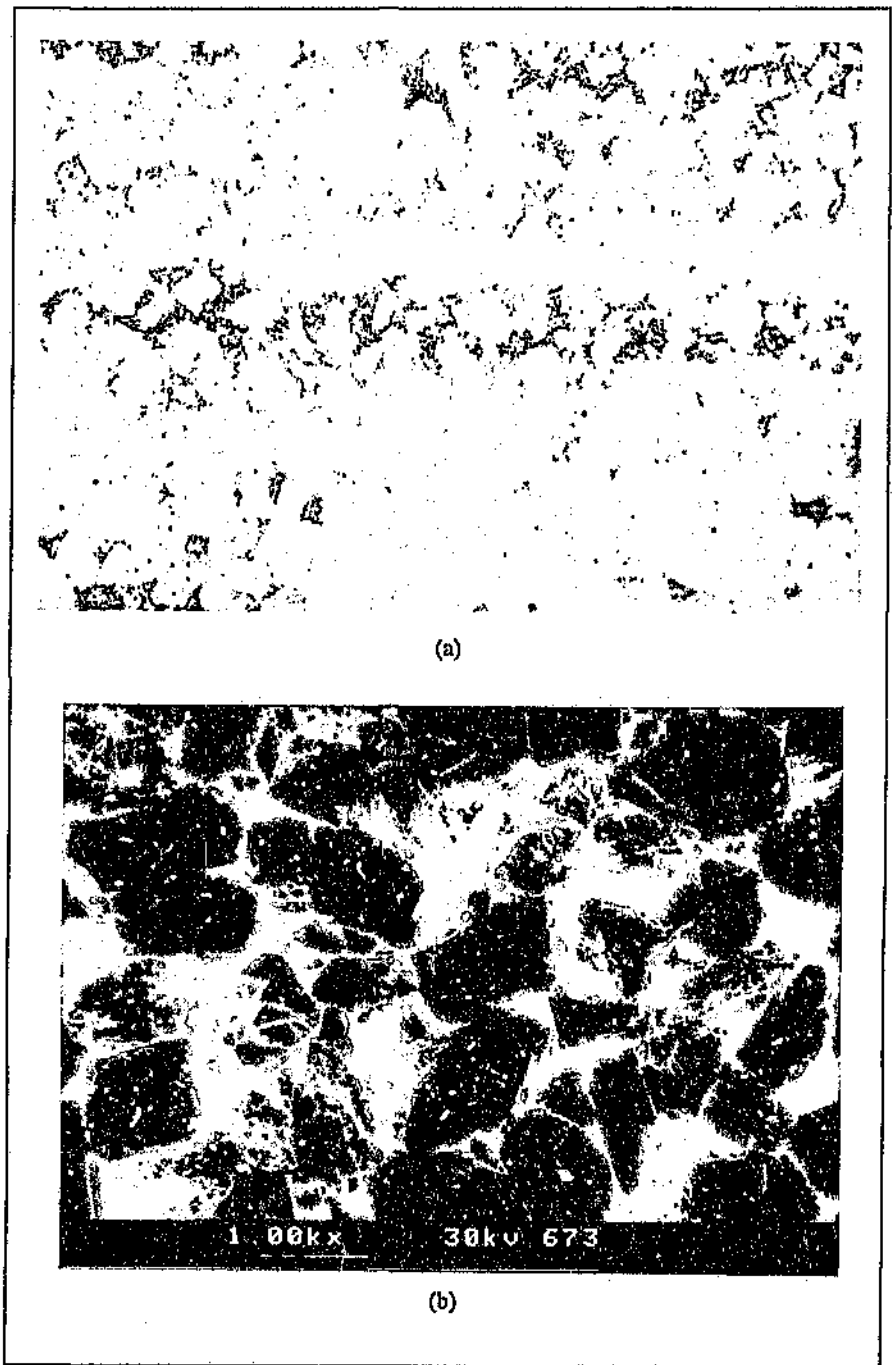

(a)

(b)

Figure 5.14: Typical appearance of the Syndax pin from the self-mated Syndax couple under dry sliding: (a) optical micrograph (500x mag.); and (b) SEM micrograph.

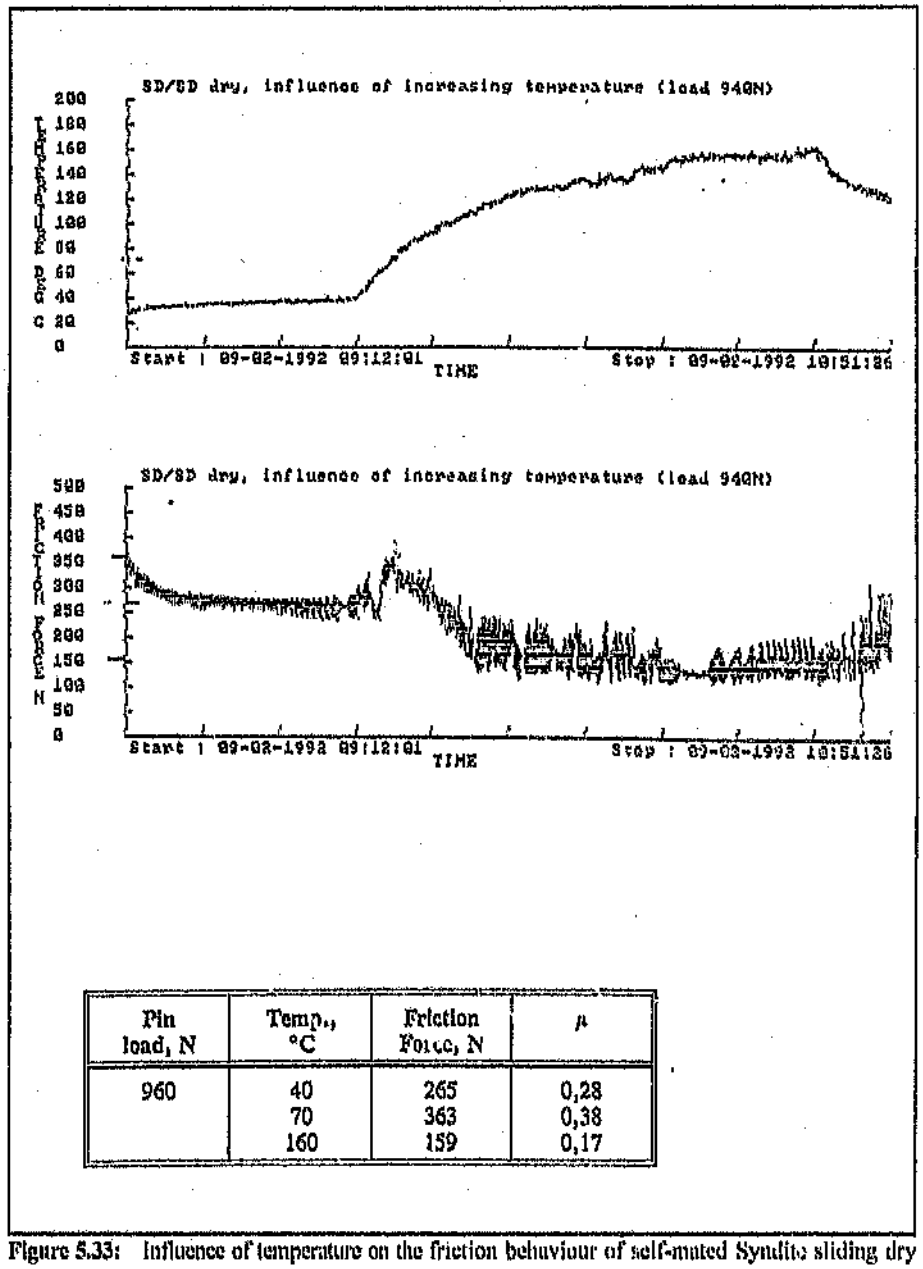

Pin load, N	Temp., °C	Friction Force, N	μ
960	40	265	0,28
	70	363	0,38
	160	159	0,17

Figure 5.33: Influence of temperature on the friction behaviour of self-mated Syndite sliding dry under a load of 960 N (contact pressure 15,1 MPa).

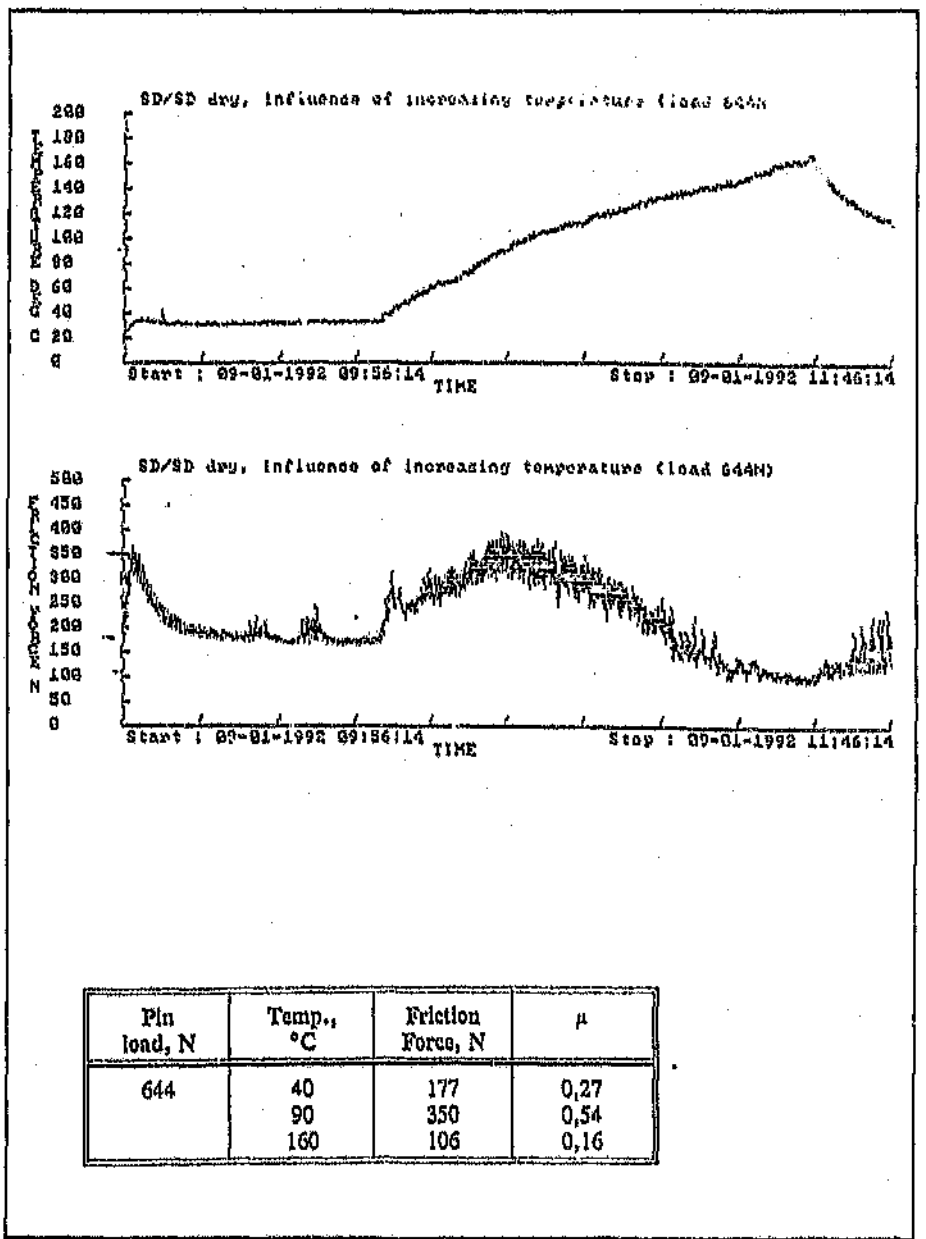

Pin load, N	Temp., °C	Friction Force, N	μ
644	40	177	0,27
	90	350	0,54
	160	106	0,16

Figure 5.32: Influence of temperature on the friction behaviour of self-mated Syndite sliding dry under a load of 644 N (contact pressure 10,1 MPa).

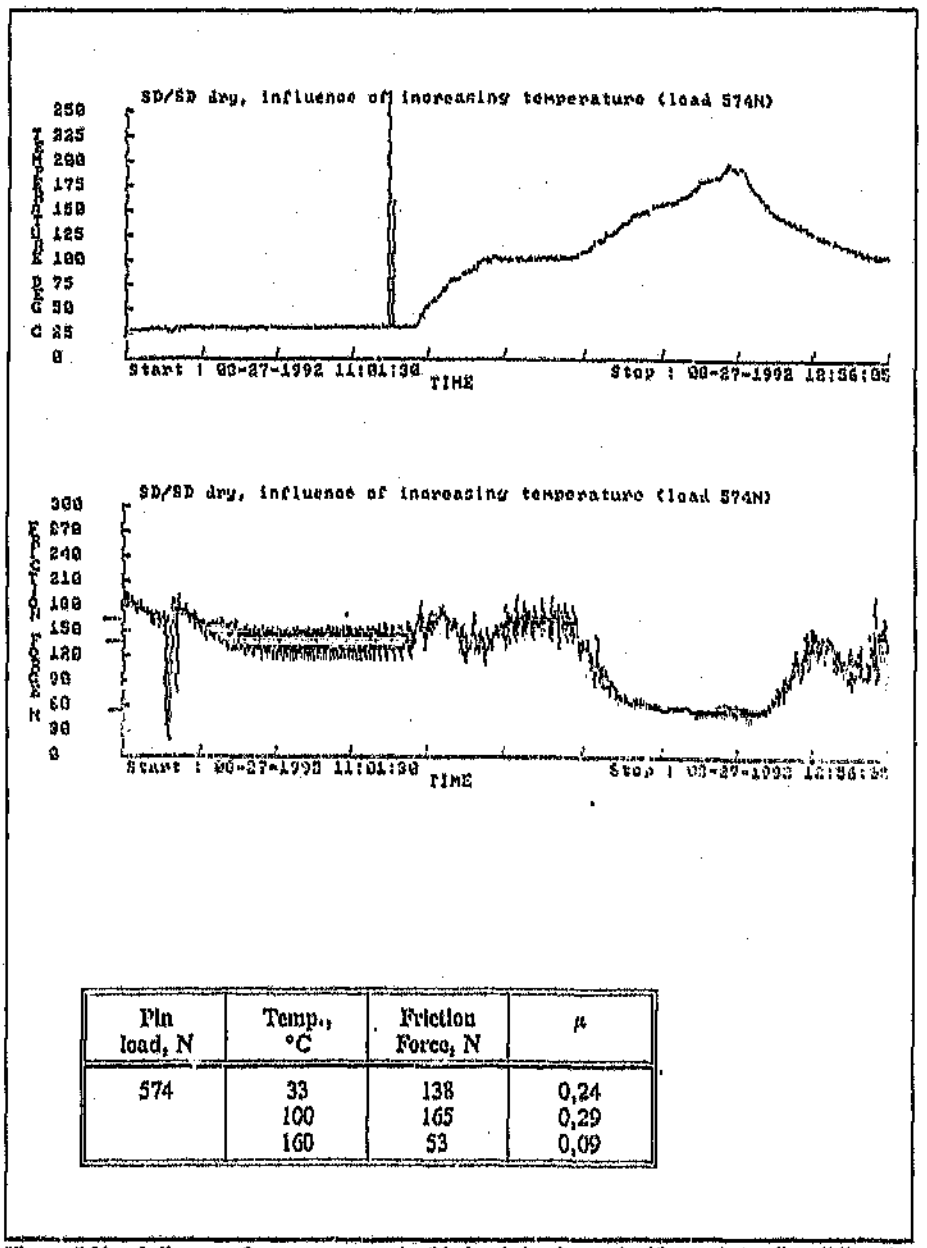

Pin load, N	Temp., °C	Friction Force, N	μ
574	33	138	0,24
	100	165	0,29
	160	53	0,09

Figure 5.31: Influence of temperature on the friction behaviour of self-mated Syndite sliding dry under a load of 574 N (contact pressure 9 MPa).

The same basic behaviour pattern was found in the four tests conducted (Figures 5.31 to 5.34). On commencement of the temperature increase, the friction force also started to increase and at the same time the fluctuations of the friction force signal increased. At times the associated vibrations were so severe that the whole POD tribometer was shaking. The friction force then reached a maximum value at some temperature between 60 °C and 100 °C, after which it and the signal fluctuations again started decreasing and reached an apparent minimum at a temperature of about 160° C. On allowing the system to cool down, the friction force and associated noisy vibrations again increased rapidly.

These results suggested that for a given applied load, the formation of the detrimental Co-rich tribofilms was indeed promoted by increasing temperature, which is in agreement with the proposed formation mechanism of these layers. The fact that the friction coefficient decreased at higher temperatures was probably related to the properties of the tribofilms at these temperatures. It is possible that the layers were significantly softened and thus more easily sheared and removed from the sliding surfaces.

5.4 Water-Lubricated Sliding Behaviour

5.4.1 Run-in characteristics

The Syndite and Syndax specimens were run-in according to a similar procedure used for the dry tests and exhibited similar behaviour. For both materials, the surface roughness decreased rapidly from the original lapped finish (~0,3 μm R_a for the pins and ~0,5 μm R_t for the discs) to stabilize at about 0,05 μm R_a. The friction coefficients also decreased during the initial stages of the run-in procedure, whereafter they remained virtually constant at values around 0,05.

In the case of Syndax, a run-in test was also performed using an **untapered** pin. Analogous to the findings during dry sliding, fracture occurred at the pin edges and some of the resultant debris was entrained in the sliding interface. This was associated with an increase in friction coefficient. Wiping the surfaces clean while running resulted in a significant drop in friction

Summary

The study confirmed the hypothesis that the presence of mud constituents such as silica and bentonite in the sliding interface could have a beneficial effect on the friction behaviour of self-mated Syndite. This was mainly related to the removal of the Co-containing tribofilms from the sliding surfaces, by mechanical abrasion and chemical interaction between Co and the drilling fluid constituents (particularly bentonite). The friction coefficient was less sensitive to the presence of barite, probably due to the lower chemical affinity of Co towards this material, but the introduction of haematite into the sliding interface should be avoided, since this resulted in a dramatic increase in friction coefficient and severe surface damage.

These results have clear implications for the design of drilling muds suitable for use with PCD bearings.

5.3.6 Influence of temperature

It was suggested earlier that 'extrusion' of the binder phase under the influence of thermal stresses may have played an important role in the formation of the tribofilms observed on the various sliding couples. The ambient temperature would thus be expected to exert a significant influence on the friction behaviour of self-mated Syndite in particular.

Unlubricated, self-mated Syndite couples were tested at various temperatures under four load conditions. The system was heated by means of two electric tube heaters in the steel carrier disc below the Syndite disc. The test temperature was measured by a thermocouple in contact with the back of the PCD layer on the pin. This thermocouple was also connected to a temperature controller which regulated the heating rate. A maximum temperature of ~160° C for these tests was selected (similar temperatures are typically reached in down-hole drilling applications). At the start of the tests, the sliding couple was allowed to reach equilibrium friction force and temperature conditions when sliding at ambient temperature. The temperature was then increased to ~160° C, at which stage the heating elements were switched off and the system was allowed to cool down.

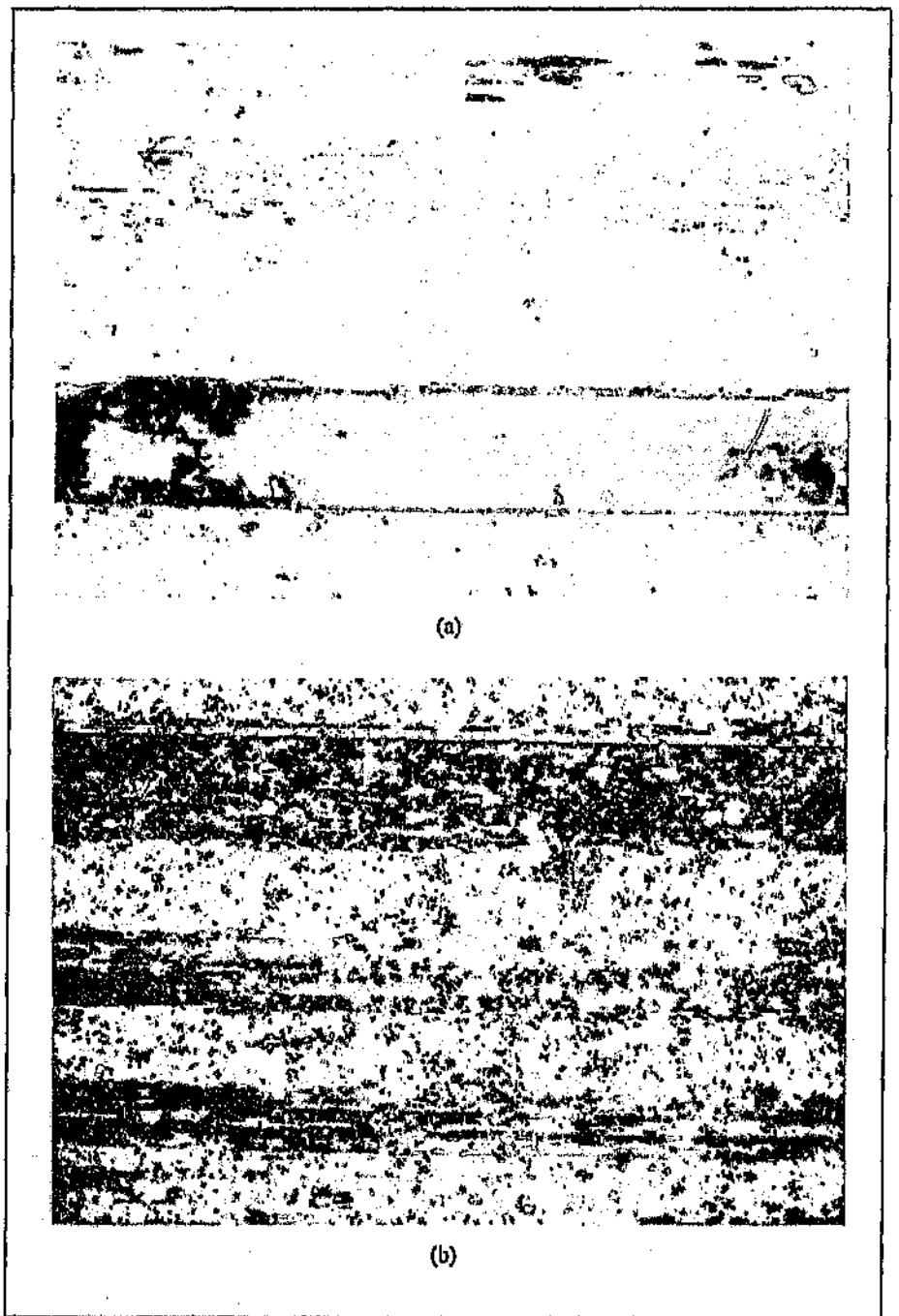

Figure 5.30: Heavy deposits of Co-rich tribofilm, formed on Syndite during a polishing run after the test in the presence of haematite: (a) on pin, 500x; and (b) on disc, 340x mag.

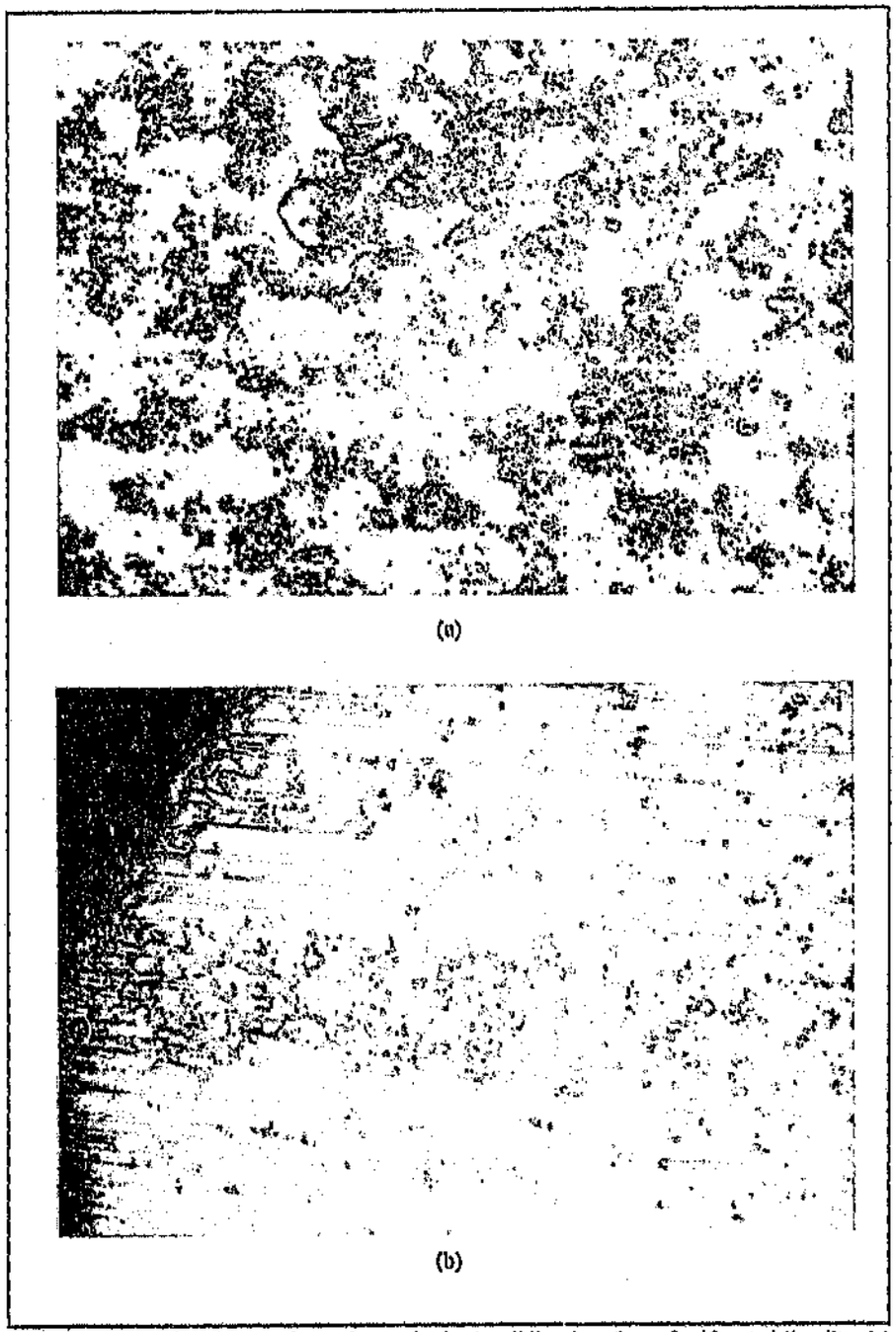

Figure 5.29: Surface damage due to haematite in the sliding interface of self-mated Syndite: (a) 340x mag.; and (b) 140x mag.

Haematite

Dry powdered haematite (hardness 5 - 6 on Mohs' scale) was introduced into the contact area of a polished Syndite couple sliding with a friction coefficient of ~0,2. An instantaneous reaction occurred, the friction coefficient increased rapidly to a value of ~0,6 and this value was maintained for the duration of the test (Figure 5.28).

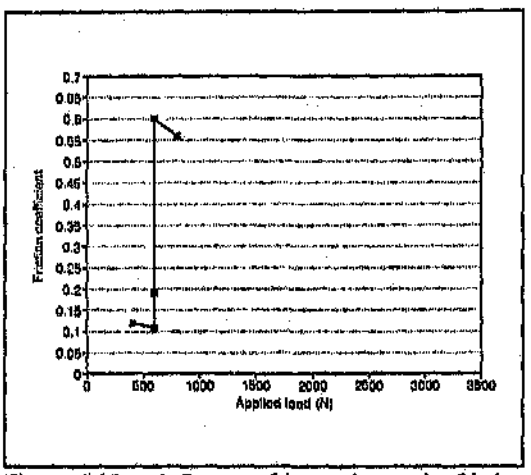

Figure 5.28: Influence of haematite on the friction behaviour of self-mated Syndite.

Examination of the PCD surfaces after the test revealed that severe damage had occurred (Figure 5.29). Severe scratching associated with apparent surface break-up and dislodgement of diamond particles was noted, particularly on the leading part of the pin. Diamond particles broken out of the surface and moving through the sliding contact appeared to have contributed greatly to the surface damage.

As haematite is softer than quartz less severe mechanical damage would have been expected, but in fact the surface damage caused by the haematite was more severe than that from the quartz. However, in contrast to silica, iron is known to act in a similar catalytic fashion to cobalt and promotes the graphitization and degradation of diamond (Section 2.4.4). It is likely, therefore, that the very high friction coefficients encountered and the severe damage sustained during sliding in contact with the haematite were caused by this reaction.

After the test in the presence of haematite, the specimen couple was cleaned with dilute hydrochloric acid and re-run in an attempt at re-polishing the surfaces. This resulted in the development of very heavy deposits of the Co-rich tribofilm on both sliding elements (Figure 5.30). Their formation was probably by the same mechanism as described earlier, but promoted by residual damage on the diamond surfaces caused by the haematite.

After the test no evidence of the presence of the high Co content deposit could be detected on the PCD surfaces. The low friction coefficients could thus be attributable to the absence of the Co containing surface layer, as well as to the lubricating properties of the bentonite (bentonite is soft and is characterized by platelet-like particles, which could be easily sheared in the sliding interface). Slight scratching of the PCD surfaces had occurred, possibly caused by the presence of a small amount of silica present in the bentonite.

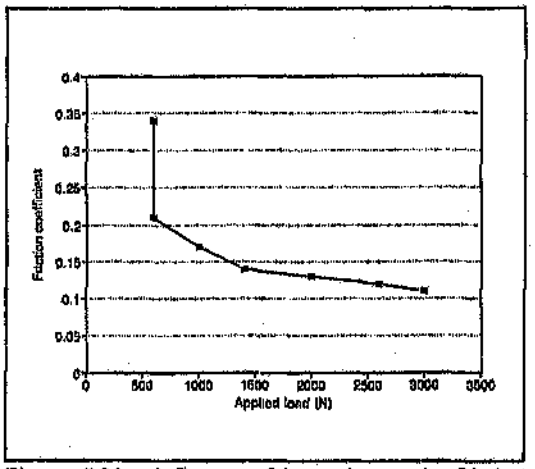

Figure 5.26: Influence of bentonite on the friction behaviour of self-mated Syndite.

Barite

The presence of barite (hardness 3 - 3.5 on Mohs' scale) had a similar, but smaller influence on the Syndite friction coefficient than silica or bentonite (Figure 5.27).

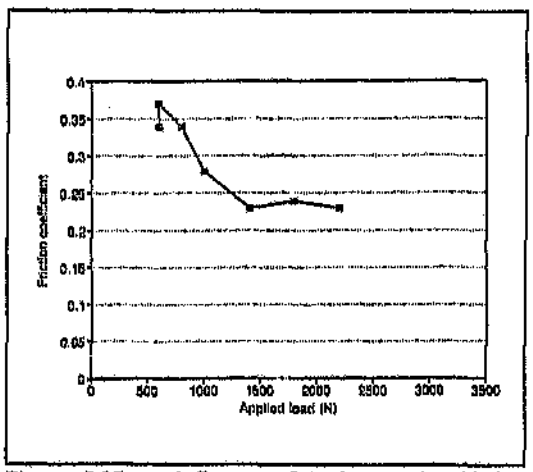

Figure 5.27: Influence of barite on the friction behaviour of self-mated Syndite.

After the test, the Syndite surfaces were well polished and high Co content tribofilms were present on both the pin and the disc. The reason why barite, which is harder than bentonite, did not remove the tribofilms as effectively probably relates to the fact that barite is composed of barium sulphate, towards which Co has little chemical affinity. Bentonite is an aluminium silicate, and it is thus possible that a chemical interaction with the Co occurred, resulting in the preferential removal of Co from the Syndite surface, analogous to mixed Syndite / Syndax sliding couples.

the pin surface, with abrasive wear marks, indications of diamond particle dislodgement and even what appeared to be transverse cracks across some diamond particles. The ring surface showed slight signs of abrasive wear and had a somewhat pitted appearance, possibly due to some diamond particle dislodgement. This damage is attributable to the high hardness of quartz (7 on the Mohs' scale), and the concomitant high point stresses on the Syndite surfaces.

The fact that the friction coefficient of the sliding couple was reduced on the introduction of the sand may have been due to the abrasive action of the quartz on the PCD surfaces, removing all the high Co content deposits, or it may have acted as a solid lubricant.

When precipitated powdered silica was introduced into the contact area of the SD/SD sliding couple the effect on the friction coefficient was the same as with the quartz sand. An immediate drop in friction coefficient was observed on the introduction of the silica powder and this low friction coefficient was maintained over the full load range investigated (Figure 5.25).

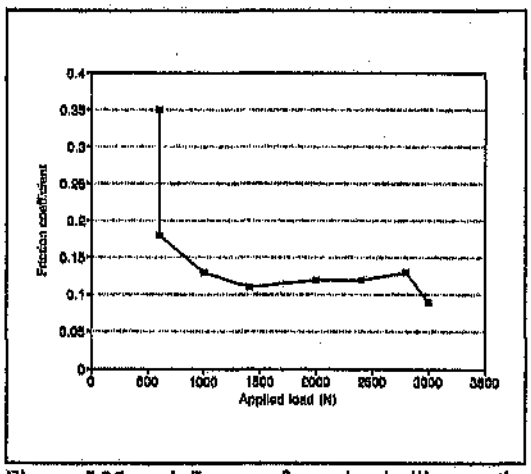

Figure 5.25: Influence of powdered silica on the friction behaviour of self-mated Syndite.

Examination of the PCD surface after the test showed that scratching had occurred, although not as severe as in the case of the sand. There was also no sign of the presence of the high Co content surface layer.

Bentonite

The introduction of dry bentonite into the contact area of a self-mated Syndite couple, caused an immediate decrease in friction coefficient from ~0,3 to 0,2. Under higher loads the friction coefficient was reduced to similar values as obtained in the presence of powdered silica (Figure 5.26). However, the initial decrease was not as sudden as that observed with silica.

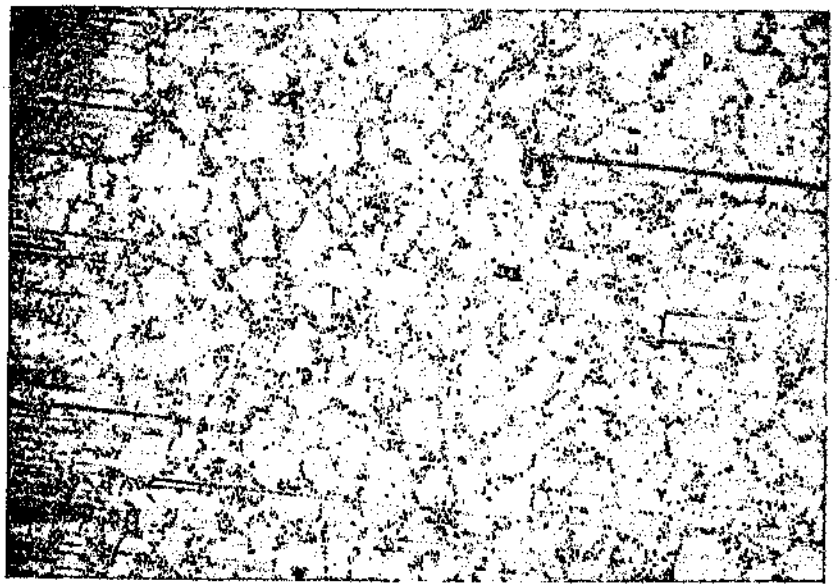

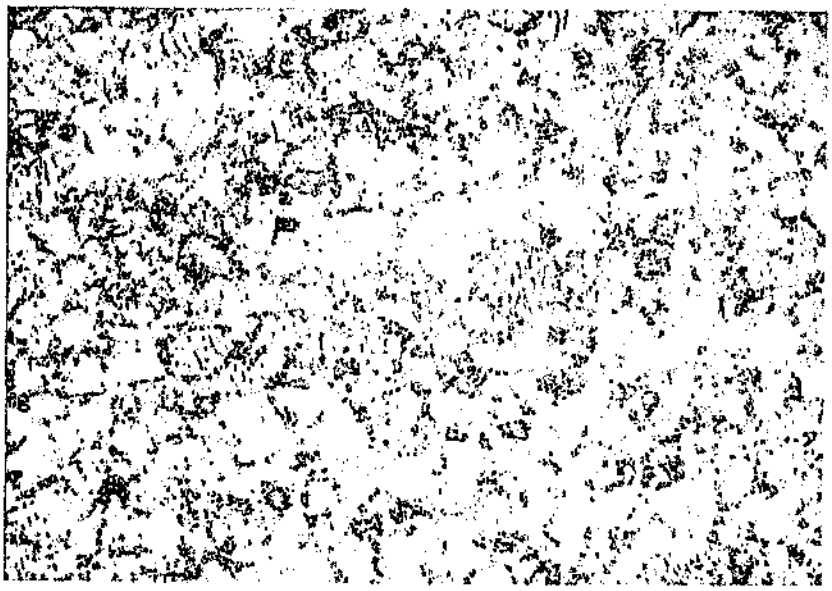

Figure 5.24: Surface appearance of Syndite after sliding in the presence of dry silica, showing abrasive grooving and fracture damage; 500x mag.

usually also contains a small amount of sand, but this is typically limited to 1,5 wt% or less.

Down-hole powerpacks such as positive displacement motors or turbines are driven by the drilling mud. Due to the high mud flowrates (~3500 l/min for a three stage turbine) it is often impractical to seal the powerpack bearing assemblies and, as a result, the radial and thrust bearing assemblies are also exposed to the drilling fluid. One of the perceived advantages of PCD thrust bearings is their ability to operate with fairly agressive drilling mud as lubricant and coolant, while providing superior friction and wear performance compared to traditional elastomer/steel or steel rolling element thrust bearings.

The laboratory investigation described in the previous sections has shown that the performance of self-mated Syndite was limited by the formation of Co-rich tribofilms on the sliding surfaces. Further, the friction coefficient was lowered and the load carrying capacity increased when these films were removed. It was postulated, therefore, that in practical thrust bearing applications the solid drilling mud constituents might be effective as cleaning agents, removing the Co-rich tribofilms from the Syndite surfaces and leading to improved performance. Therefore, the influence of the solid mud constituents silica, bentonite, barite, and haematite on the tribological characteristics of self-mated Syndite was studied under dry sliding conditions. Prior to each test, the Syndite couple was run-in under high load and at a sliding speed of 0,13 m/s to obtain well-developed Co-rich tribofilms on the sliding surfaces. The load was then reduced, the mud constituent under investigation added and the load increased step-wise analogous to the LCC tests.

Silica

Pure quartz sand was introduced into the contact area of a polished, self-mated Syndite couple sliding at 0,13 m/s under a load of 600 N and at a friction coefficient of ~ 0,2. The friction coefficient almost immediately decreased to a value of ~ 0,1 and this low value was maintained when the load was increased to 2 200 N. Examination of the PCD surfaces after the test showed that the Co containing deposit present before the test had been removed and the surfaces scratched. The surface damage, shown in Figure 5.24, was particularly severe on

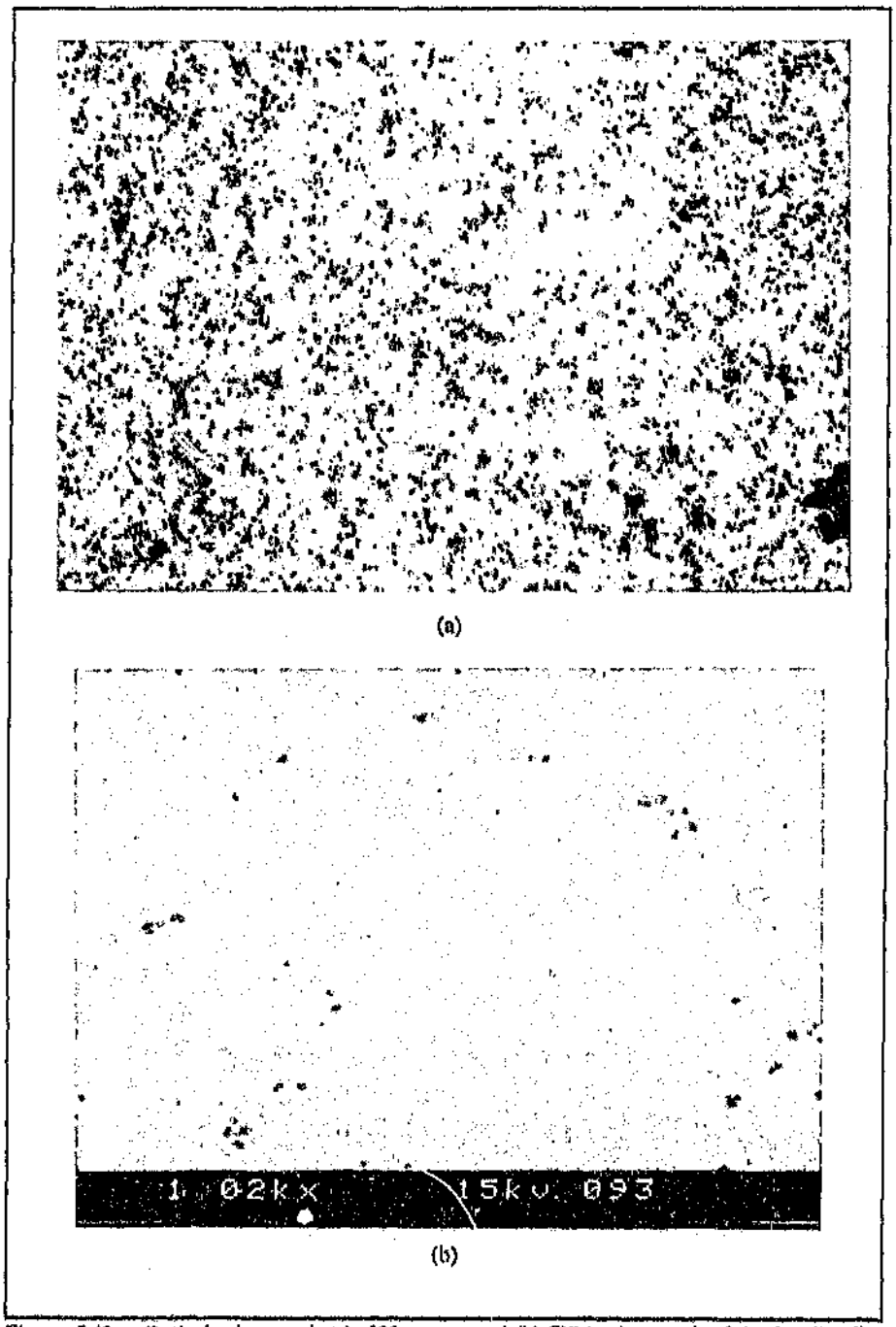

Figure 5.42: Optical micrograph (a), 500x mag., and (b) SEM micrograph of the Syndite disc from the Syndax/Syndite water-lubricated sliding couple.

Syndax (pin) / Syndite (disc)

Close examination of the Syndite disc by optical microscopy techniques revealed that Co-rich tribofilms formed in small patches on the polished diamond surfaces, as well as in the inter-grain areas (Figure 5.42). The films were comparable to those formed on the bulk of the self-mated Syndite surfaces in water-lubricated sliding, but were difficult to see even with optical microscopy, and could not be observed at all under the SEM.

No obvious Si-rich tribofilms were observed on the Syndax pin (Figure 5.43). In contrast to unlubricated sliding of this material couple, the Si-binder phase from the Syndax thus appeared to be unable to 'bind' the Co from the Syndite binder phase in well-developed tribofilms. This could be due to a number of factors, including:

- debris was swept out of the sliding interface by the water and was thus unavailable for tribofilm formation;
- the rate of formation of silicon oxides and hydroxides was probably higher in the presence of water. These could have been easily removed from the surfaces by sliding, and would thus have been unavailable for tribofilm formation;
- less adhesion and material transfer would have occurred in the water-lubricated environment, due to the 'contamination' of the sliding surfaces by oxygen, hydrogen, and water (these molecules rapidly combine with active surfaces created by the sliding process which suppresses adhesion and material transfer);
- comparatively low temperatures also suppressed adhesion and material transfer and reduced the rate of 'thermal migration' of the binder phase from the PCD structure, thus reducing the rate of debris and tribofilm formation (particularly in the case of Syndite).

Analogous to the self-mated Syndite couple in water-lubricated sliding, the Syndax/Syndite couple thus exhibited low friction coefficients (~ 0,1) as a result of the absence of large areas of well-developed Co-rich tribofilms. However, small patches of this tribofilm and the presence of small amounts of wear debris were effective in inducing stick-slip motion which,

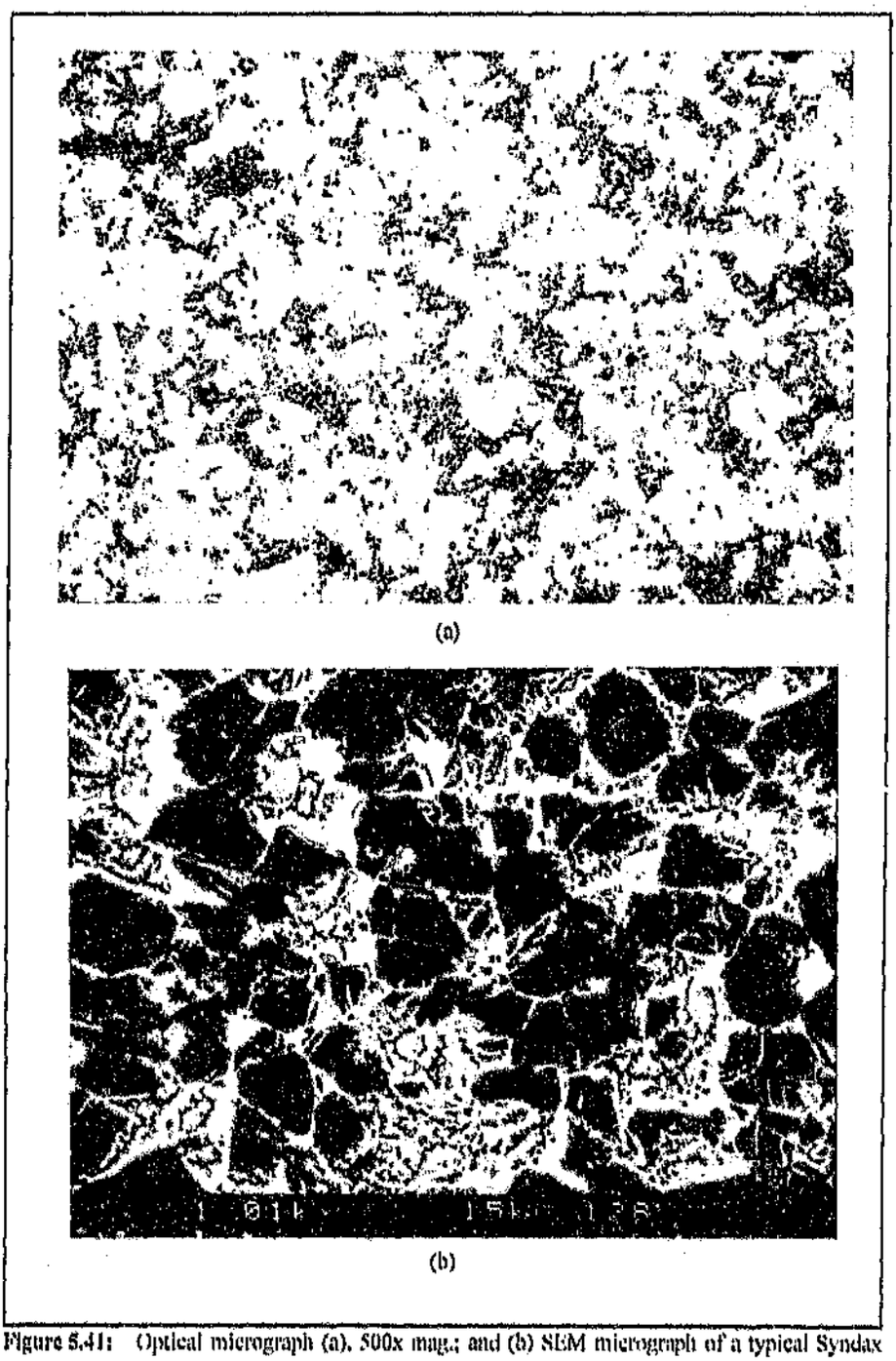

(a)

(b)

Figure 5.41: Optical micrograph (a), 500x mag.; and (b) SEM micrograph of a typical Syndax surface produced in self-mated, water-lubricated sliding.

Self-mated Syndax

The Syndax disc and pin both exhibited highly polished diamond surfaces with somewhat less scoring damage than observed in dry sliding (Figure 5.41). This was confirmed by the fact that the surface roughness of the pin was similar both in and across the sliding directions (0,02 and 0,05 respectively). It thus appears that much of the wear debris was swept out of the contact zone by the water.

Preferential wear of the Si binder phase as well as fragmentation of the edges of the diamond grains in these regions was observed on both sliding elements. The damage appeared to be worse than for dry sliding, which could be related to the fact that Si is susceptible to a chemical wear mechanism in water through the formation of silicon hydroxides. Moreover, much of the loose wear debris was washed away from the contact zone by the water and was thus not allowed to accumulate in the cavities between the diamond grains where it could have protected the underlying Si binder phase. The wear rate of Syndax in a water lubricated environment is thus likely to be higher than in dry sliding.

Detailed microscopic examination revealed no obvious tribofilms on the diamond surfaces. Nevertheless, EDS analyses showed small amounts of Si on the polished surfaces of the diamond grains, which indicated that thin, Si-rich tribofilms were present in these areas. Given the aqueous environment, it is probable that these films would have been largely composed of silicon oxides and hydroxides. These compounds are lubricious and would thus not lead to a significant increase in friction coefficient. Similar observations were made on the unlubricated sliding couple.

The superior friction behaviour of the self-mated Syndax couple was thus attributed to the absence of strongly interacting tribofilms on the diamond surfaces. Preferential wear of the Si binder phase and the absence of large amounts of accummulated debris in the sliding interface left the diamond grains standing proud. Sliding contact was thus dominated by diamond-diamond friction, which is associated with low friction coefficients. Thin, lubricious Si-rich tribofilms may have played a smaller contributory rôle.

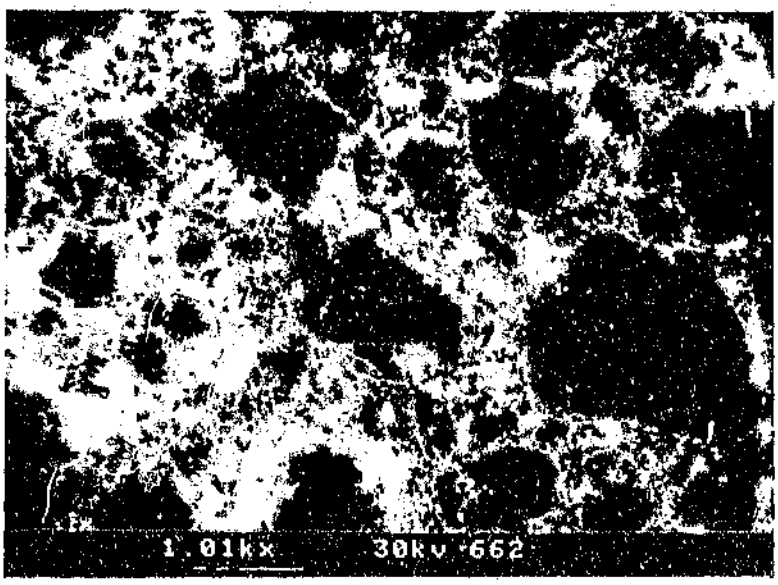

(a)

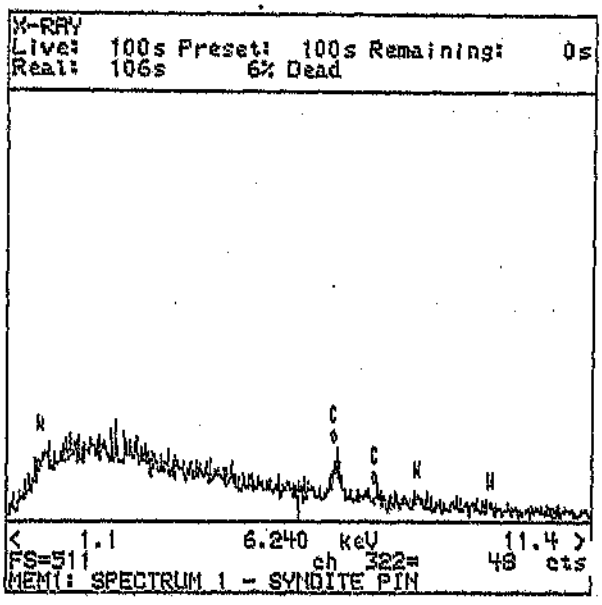

(b)

Figure 5.40: SEM micrograph of a typical Syndite surface produced in self-mated, water-lubricated sliding (a); and (b) EDS spectrum showing small amount of Co on the diamond surfaces.

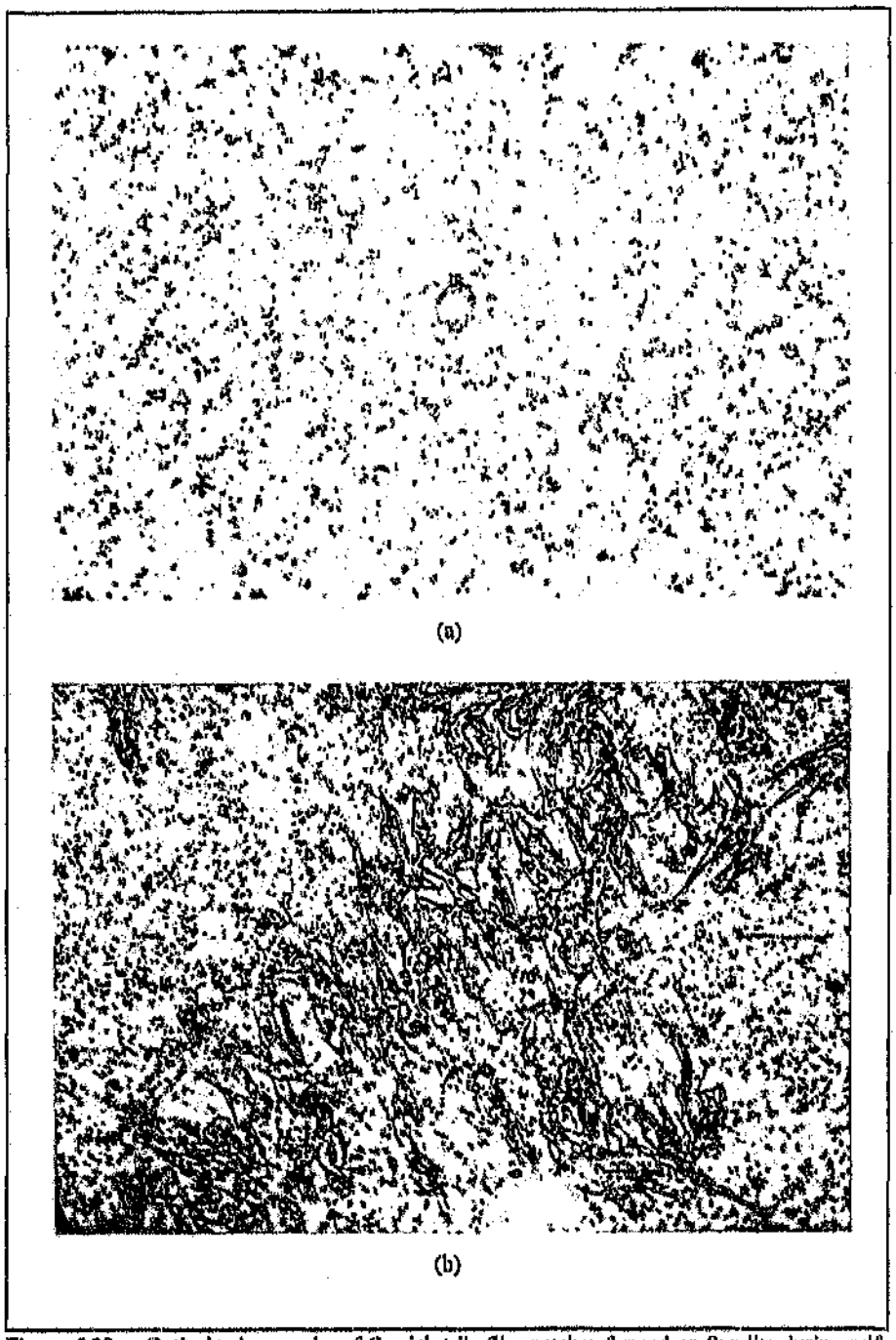

(a)

(b)

Figure 5.39: Optical micrographs of Co-rich triboflim patches formed on Syndite during self-mated, water-lubricated sliding: (a) small patches; and (b) larger patches (500x mag.).

5.4.3 Surface effects and tribofilm formation

Self-mated Syndite

The Syndite surfaces exhibited patchy tribofilms, rich in Co (Figure 5.39). These patches were considerably less well-developed and thinner than those formed during dry sliding, and could not be seen under the SEM (Figure 5.40). Nevertheless, EDS analyses confirmed that small amounts of Co were present on the diamond surfaces.

The low friction coefficients of around 0,1 exhibited by this couple may thus be attributable to the absence of thick, well-developed Co-rich tribofilms, as well as the lubricating and cooling effect of the water. However, the couple appeared to be sensitive to small changes in contact conditions, which resulted in stick-slip motion associated with severe vibrations and noise emission. The LCC was limited to low contact pressures, although the friction coefficient was not affected dramatically.

This behaviour was somewhat different to that shown in dry sliding, where the contact conditions were dominated by well-developed Co-rich tribofilms and relatively high loads could be sustained, albeit at higher coefficients of friction. The temperature of the sliding surfaces may have played a rôle in that a minimum in friction coefficient was found at 160°C in dry sliding (temperature measured at the interface between the PCD layer and the WC-Co support material). This was attributed to the influence of temperature on both the rate of formation and the mechanical properties of the Co-rich tribofilms. In water-lubricated sliding, temperatures were lower and the rate of formation of the tribofilms and associated loose wear debris would have been lower. Furthermore, the small tribofilm patches would not have been softened to the same degree as in dry sliding. It is thus likely that small amounts of loose wear debris and the interaction of the tribofilm patches caused small, localized disruptions in the contact conditions which, in turn, resulted in the observed vibrations and oscillation of the friction coefficient. It is unlikely that graphitization played a major rôle in view of the strong cooling effect of the water and concomitant low contact temperatures.

Syndite (pin) / Syndax (disc)

In contrast to the Syndax (pin) / Syndite (disc) couple, this material couple could sustain a load of 4100 N (contact pressure 64,4 MPa) at a low friction coefficient of 0,1 (Figure 5.38). However, this LCC was not reproducible and was only obtained once out of a total of five tests. In the remaining tests, the couple exhibited much the same behaviour as the Syndax/Syndite couple, i.e. a low LCC of 2800 N, limited by vibration and noise emission.

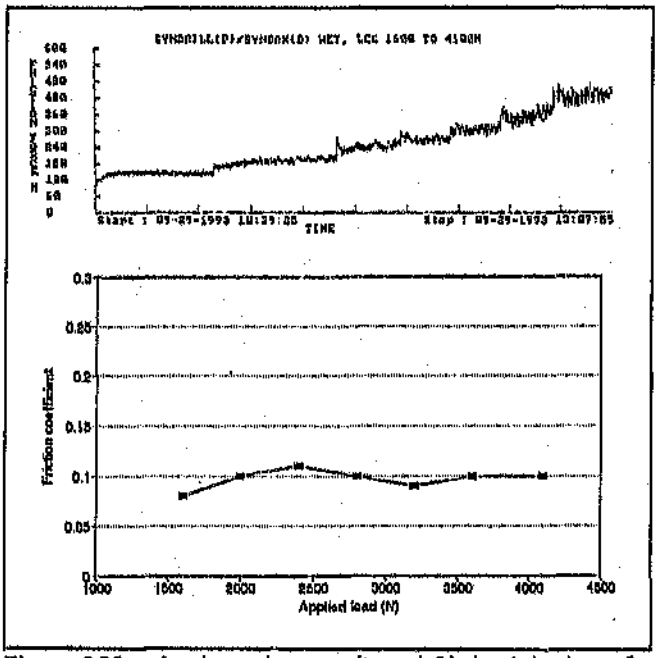

Figure 5.38: Load c. .ying capacity and friction behaviour of a Syndite (pin) / Syndax (disc) couple in water-lubricated sliding.

It was thus concluded that the true LCC of this couple was probably close to 2800 N (contact pressure 44 MPa), although it appeared to be possible under very favourable circumstances to attain a LCC of 4100 N with low friction coefficients.

As for the previous couple, small patches of Co-rich tribofilms were noted on the Syndite surface. Further, analogous to self-mated Syndite in dry sliding, small amounts of loose, Co-rich wear debris were probably present in the contact zone, despite the flushing effect of the water. These factors are thought to be responsible for the unstable friction behaviour at high loads which limits the LCC. No Si-rich tribofilms, which appeared to be effective in binding Co and preventing this phenomenon, were noted on the Syndax surface.

Syndax (pin) / Syndite (disc)

This material couple exhibited a similar trend to the self-mated Syndite couple (Figure 5.37). The friction coefficient increased significantly between 1600 N (contact pressure 25,2 MPa) and 2400 N (contact pressure 37,7 MPa), but still remained at quite a low absolute value of 0,13 maximum. The LCC was limited to 2800 N (contact pressure 44 MPa) by the onset of vibrations and noise emission.

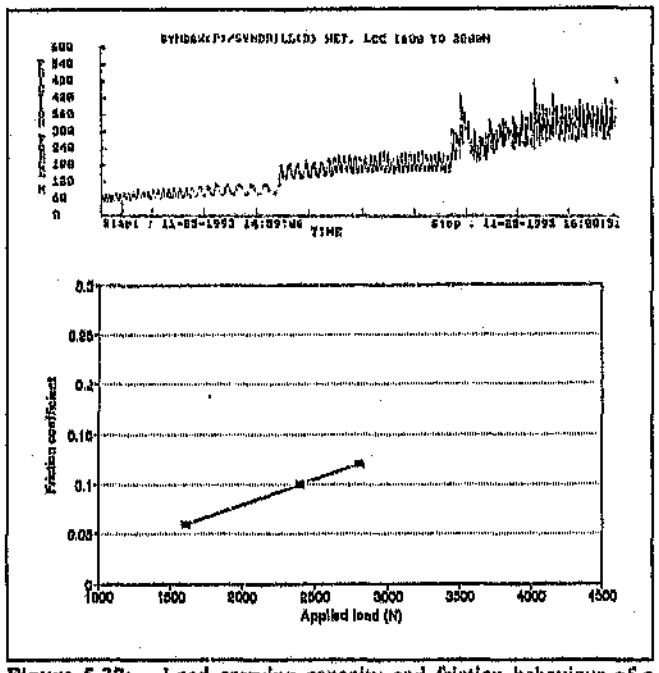

Figure 5.37: Load carrying capacity and friction behaviour of a Syndax (pin) / Syndite (disc) couple in water-lubricated sliding.

In view of the superior performance of this material couple under dry sliding conditions, this behaviour was somewhat unexpected. However, as will be seen in Section 5.4.3, it could be explained in terms of the formation of small patches of the deleterious Co-rich films on the Syndite surface. These were generally not as well-developed as those formed under dry sliding conditions on self-mated Syndite, and thus had little influence on the friction coefficient. However, their presence (and, probably, the presence of some loose, Co-rich wear debris) and interaction was enough to induce stick-slip motion, which limited the load carrying capacity of the couple. Removal of the tribofilms with dilute hydrochloric acid resulted in smoother friction behaviour for a short period of time, until the small tribofilm patches were re-formed. This tended to confirm the above interpretation.

No obvious Si-rich tribofilms were observed on the Syndax surface and this provides an explanation for the presence of the Co-rich tribofilms.

Self-mated Syndax

This couple was able to sustain the maximum load which could be applied with the POD machine, namely 4300 N (contact pressure 70,7 Mpa). As shown in Figure 5.36, the friction coefficient remained virtually constant at very low values (< 0,1) over the entire load range used. The performance of the couple was not influenced significantly by the increase in scatter in friction force which occurred beyond 4000 N. In general, both the LCC and the friction coefficients attained were comparable to those observed under dry sliding conditions. This is a significant finding which suggests that in contrast to self-mated Syndite, self-mated Syndax may be able to run dry for short periods, which has potentially important implications for the robustness of thrust bearings with Syndax sliding surfaces.

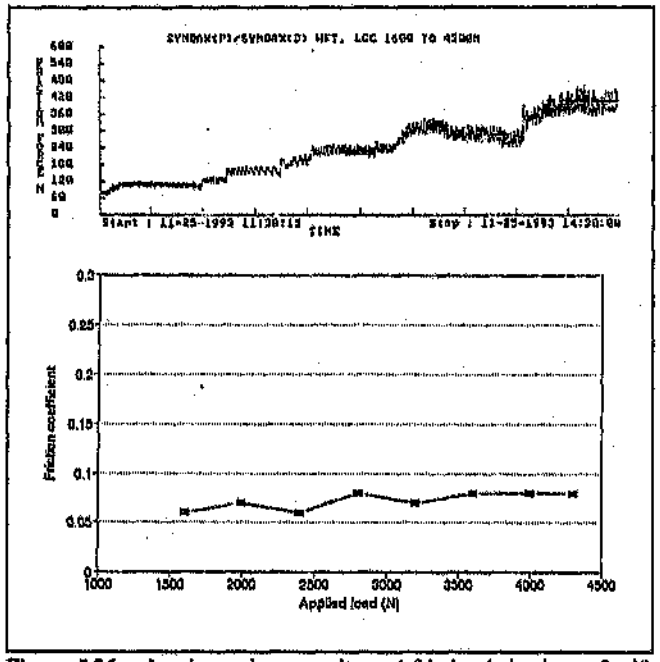

Figure 5.36: Load carrying capacity and friction behaviour of self-mated Syndax in water-lubricated sliding.

No obvious tribofilm formation was noted, although thin Si-rich films were formed on some of the diamond surfaces. These were similar to those observed in dry sliding and were probaly highly oxidized and hydrated due to the presence of water. The surface roughness was increased due to preferential wear of the Si-rich binder phase regions, and so the low coefficients of friction and high LCC were probably not related to hydrodynamic lubrication effects. The superior performance of this material couple was thus attributed to the absence of deleterious Co-rich tribofilms, with thin, lubricious Si-containing tribofilms possibly playing a contributory rôle.

coefficient from ~0,056 to ~0,03. This indicated that the presence of the diamond debris on the sliding surfaces had a detrimental effect on friction behaviour. Nevertheless, the Syndax surfaces exhibited less grooving damage than in dry sliding, probably because much of the loose debris was flushed out of the contact zone by the water.

5.4.2 Influence of load and load carrying capacity (LCC)

Self-Mated Syndite

The results from a LCC test on self-mated Syndite are shown in Figure 5.35. The friction coefficients were extremely low at below 0.1, but increased steadily with increasing load. The LCC was limited by the onset of severe vibrations and noise emission from the sliding couple, which was associated with relatively large fluctuations in friction force. Despite the low friction coefficients which were attained, the maximum LCC of the couple was thus only ~2500 N, which is significantly worse than that attained by the same couple in unlubricated sliding. A possible explanation relates to the extent to which Co-rich tribofilms were formed, the presence of loose wear debris in the contact zone, and influence of temperature on tribofilm formation and friction. (Recall that, in dry sliding, the friction coefficient tended to decrease with temperature and reached an apparent minimum at 160°C). These effects will be discussed in more detail in Section 5.4.3.

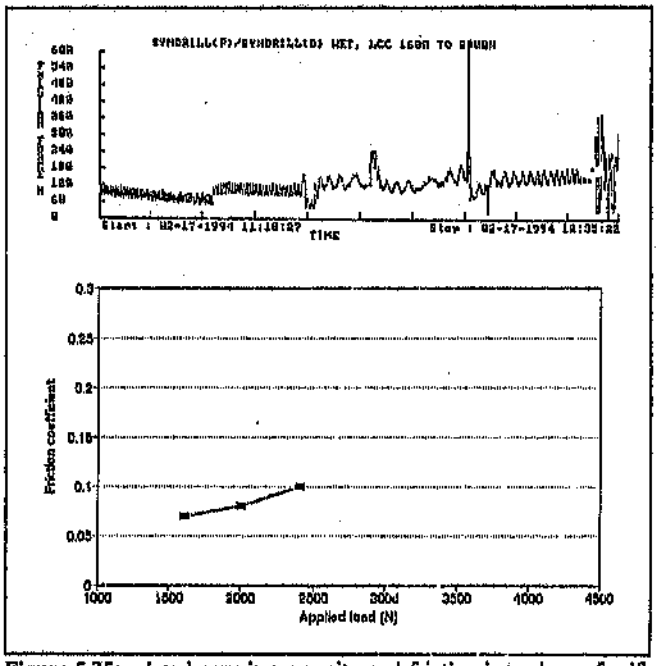

Figure 5.35: Load carrying capacity and friction behaviour of self-mated Syndite in water-lubricated sliding.

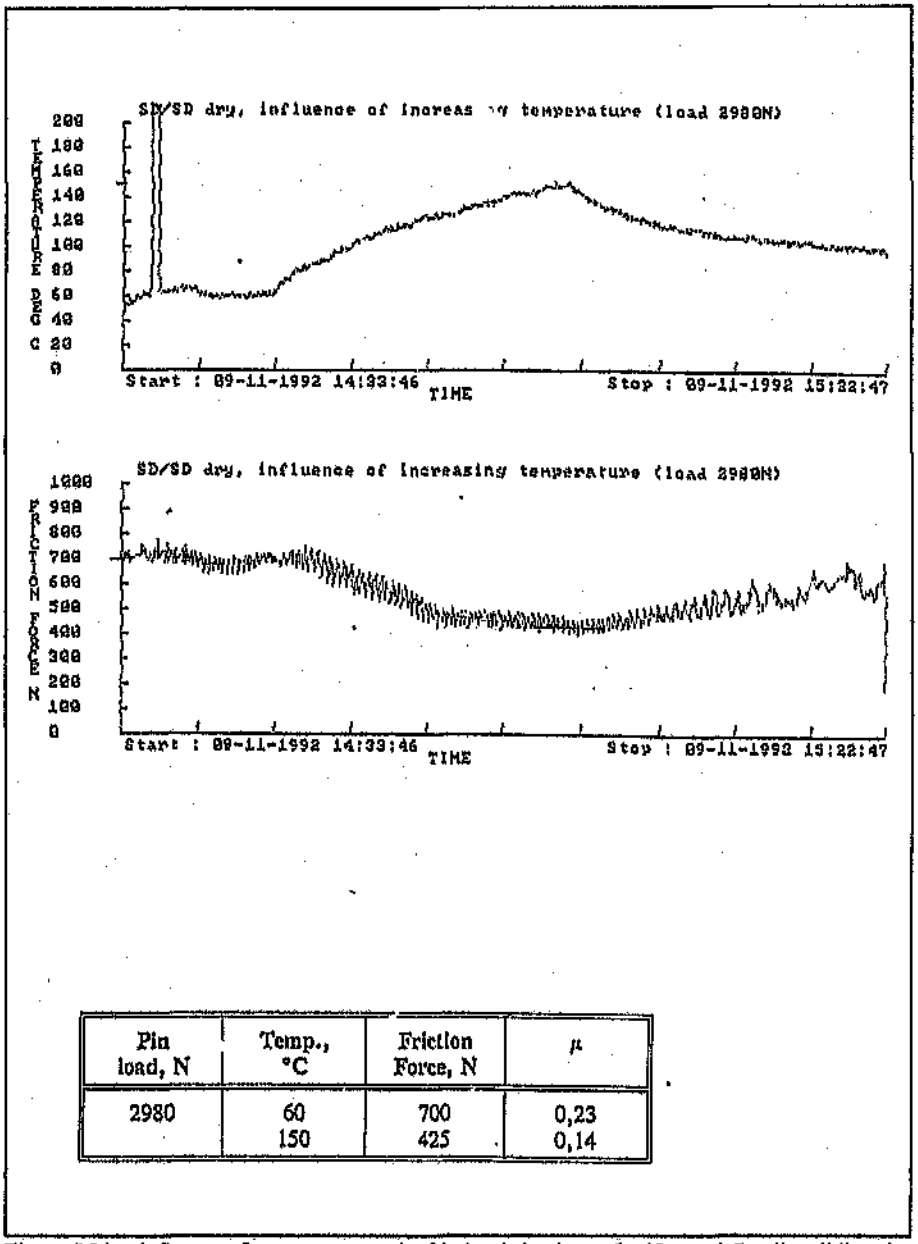

Pin load, N	Temp., °C	Friction Force, N	μ
2980	60	700	0,23
	150	425	0,14

Figure 5.34: Influence of temperature on the friction behaviour of self-mated Syndite sliding dry under a load of 2980 N (contact pressure 46,3 MPa).

haematite was attributed to structural degradation of the diamond surfaces, catalyzed by the iron content of the haematite (iron is known to promote the graphitization of diamond).

The effect of ambient temperature on self-mated Syndite in dry sliding was studied in view of the apparent importance of thermal effects in tribofilm formation. The friction coefficient and associated fluctuations in friction force increased with increasing temperature and reached a maximum a temperature between 60 °C and 100 °C. Beyond this point, both parameters decreased to reach a minimum at about 160 °C. These effects were explained in terms of the influence of temperature on the rate of binder phase migration and tribofilm formation, as well as on the mechanical properties of the tribofilm.

Similar effects were observed under water-lubricated sliding conditions. The load carrying capacity of the self-mated Syndite couple appeared to be limited by the formation of small, Co-rich tribofilm patches, which caused severe stick-slip motion but did not increase the overall friction coefficient dramatically. The self-mated Syndax couple exhibited lower coefficients of friction and much higher LCC, and this was attributed to the absence of such tribofilms. In contrast to dry sliding, the mixed Syndite/Syndax couples showed a similar behaviour to the self-mated Syndite, i.e. limited LCC which was apparently due to the formation of Co-rich tribofilms. In all cases the films were much less well-developed than in dry sliding, and were difficult to observe and analyze. Nevertheless, the observation that the films appeared to promote stick-slip motion, and thus limit the LCC, was confirmed by removing the films with dilute hydrochloric acid, whereupon lower coefficients of friction and smoother friction behaviour were obtained for a short period.

The presence of beneficial Si-rich tribofilms which could bind the Co, analogous to dry sliding, could not be confirmed on the Syndax surfaces. This was probably related to the combined effects of lower temperatures, the presence of water in the contact zone which reduced adhesion and material transfer, and the fact that debris was swept out of the contact area by the water and was thus unavailable for tribofilm formation.

sliding conditions.

Under dry sliding conditions, mixed Syndite/Syndax sliding couples showed lower coefficients of friction and higher LCC than self-mated Syndite. This was related to the formation of Si-rich tribofilms on the Syndax surfaces, which also contained smaller amounts of Co and W from the Syndite binder phase. No deleterious Co-rich tribofilms were present on the Syndite surfaces. It was concluded that Co was preferentially removed from the Syndite surface and transferred to the binder phase regions of the Syndax surface, due to the strong chemical affinity between Co and Si. There was some analytical evidence that a chemical compound rich in Si, Co and O was present in the Si-rich tribofilm. The Co was thus effectively bound in this tribofilm on the Syndax surface, and the potential for the formation and interaction of detrimental Co-rich tribofilms on the Syndite surface was reduced. The determination of the precise nature of the Si-Co-O compound requires a much more detailed, independent XPS study.

The formation of the tribofilms was explained in terms of a thermal binder phase migration mechanism, sustained by diffusion and possibly driven by chemical reactions (oxidation) of the binder phase at the sliding surface. Loose wear debris generated from the binder phase regions probably also played a significant contributory rôle (compaction). Further work, involving for instance model experiments in a controlled atmosphere furnace, coupled with detailed mass spectrometric analyses, is indicated to confirm and describe the proposed binder phase migration and tribofilm formation mechanism in more detail.

The influence of several typical drilling fluid constituents i.e. silica, bentonite, barite and haematite in the contact area of a self-mated Syndite couple was examined under dry sliding conditions. The effects varied from apparently no effect with barite, to reduced friction and no surface damage with bentonite, a reduction in friction accompanied by surface scoring with silica, and increased friction coefficients and severe surface damage with haematite. Beneficial effects were associated with the removal of deleterious Co-rich tribofilms from the sliding surfaces, by a complex mechanism involving both mechanical abrasion and chemical interaction between Co and the drilling fluid constituents. The dramatic negative effect of

capacity of these films appeared to be limited, however, and oscillations in friction coefficient and increased stabilized wear rates were observed at loads of 50 N. The effect was more pronounced for Sialon and was probably related to the different nature of the tribofilms.

All ceramics except alumina developed a characteristic surface finish during sliding, which was essentially independent of the original surface roughness. This has important economic implications since these materials may be thus used in practical applications without prior polishing.

A short study on the influence of water chemistry demonstrated that the presence of significant amounts of chloride and sulphate had a significant and generally beneficial effect on the friction and wear behaviour of alumina and the silicon-based ceramics. Based on available evidence, this was tentatively explained in terms of reduced adhesion and the promotion of iron oxide and hydroxide formation on the steel ball by the presence of sulphate. Adsorption effects may have played a significant contributory rôle, particularly in the case of the silicon-based ceramics. It was suggested that the influence of sulphate may have been more important in this regard than that of chloride. Further work on clarifying the precise mechanisms is indicated in view of the potential importance of these effects in improving the performance of these metal-ceramic sliding couples.

6.3 Polycrystalline Diamond Sliding Couples

The friction behaviour and load carrying capacity (LCC) of various sliding combinations of Syndite and Syndax were studied under dry and water-lubricated conditions. In both cases, the LCC of Syndite was limited by the onset of unstable friction behaviour and increased friction coefficients at higher loads. It was concluded that this was associated with the formation and adhesive interaction of patchy, Co-rich tribofilms on the Syndite surfaces.

Self-mated Syndax exhibited lower coefficients of friction and higher LCC and this was attributed to the absence of Co-rich tribofilms, as a result of the different binder phase composition. The performance of the couple was similar under both dry and water-lubricated

performance limitations and associated friction and wear mechanisms of polycrystalline diamond (PCD), and this was the second focus area of the present work.

To facilitate the work on metal-ceramic sliding couples, a high-speed reciprocating tribometer with computerized data acquisition and control was developed. The main aims of the machine, namely to provide meaningful friction and wear data in a reciprocating mode and over a range of sliding conditions, were satisfactorily achieved. Vibration analyses indicated that reciprocating frequencies between 25 and 35 Hz should be avoided unless further vibration-reducing measures are employed. Some suitable measures were identified. Excellent agreement in measured dynamic friction coefficients was found with a commercially available tribometer, using a standard test arrangement with known friction behaviour.

6.2 Metal-Ceramic Sliding Couples

The friction and wear behaviour of a range of oxide and silicon-based ceramics sliding against AISI 440C stainless steel in deionized water was studied. All the sliding couples exhibited a pronounced two-phase friction and wear behaviour, characterized by a run-in and a steady-state phase. The wear results showed that it is important to quantify not only the total amount of wear, as is commonly done, but also the steady-state wear rate, which is the more important parameter for assessing the long-term operational performance of the sliding couple.

In agreement with published literature, the oxide ceramics generally showed higher friction coefficients and wear rates compared to the silicon-based ceramics. This was explained in terms of different levels of adhesion between the sliding elements and the formation of interfacial metallic transfer films. In the case of zirconia ceramics, increased transformation toughening was found to be related to increased surface fracture damage and metallic transfer film formation. These films were beneficial in that they protected the underlying ceramic surface from further damage and determined the friction and wear behaviour.

The superior friction and wear behaviour of Sialon and Si_3N_4 was related to the formation of lubricious SiO_2-based tribochemical reaction films on these materials. The load carrying

CHAPTER 6

6. CONCLUSIONS

Mining remains one of the most important industry sectors worldwide. Continuing pressure towards reducing unit production costs has driven much research activity in the areas of improved mining systems and more efficient use of engineering materials. In particular, the performance of new mining systems such as hydro-power (the use of water as hydraulic working fluid) in South African gold mines, or down-hole drilling powerpacks in the oil and gas industry, is limited by the tribological performance of sliding material couples. The present study aims to make a contribution in this area by examining the friction and wear characteristics of metal-ceramic and polycrystalline sliding couples for application in reciprocating hydro-power components, and high-load thrust bearings for down-hole powerpacks, respectively.

6.1 General

A study of the existing literature showed that the friction and wear behaviour of ceramics and diamond is governed by a number of complex mechanisms and phenomena. The development of stable tribofilms on the sliding surfaces is of particular importance in this regard, and much work has been performed in an attempt to characterize such layers. Realizing this complexity, several researchers have focused on developing friction and wear maps, which describe the tribological performance of particular material couples over a wide range of operating conditions. The problem remains, however, that few maps are available and much published work is not comparable due to differences in test conditions, materials, and experimental procedures. Studies which are focused on a particular set of applications, like the present one, will thus be required for some time to come.

A fair amount of work has been done on the friction and wear of single crystal diamond and CVD diamond coatings, which has confirmed the very low friction coefficients and wear rates which can be achieved with these materials. However, very little is known about the

influence of temperature on the rate of binder phase extrusion and tribofilm formation, as well as on the mechanical properties of the tribofilm.

Under water-lubricated sliding conditions, similar effects were observed. The load carrying capacity of the self-mated Syndite couple appeared to be limited by the formation of small, Co-rich tribofilm patches. The self-mated Syndax couple exhibited lower coefficients of friction and much higher LCC and this was attributed to the absence of such tribofilms. In contrast to dry sliding, the mixed Syndite/Syndax couples showed a similar behaviour to the self-mated Syndite, i.e. limited LCC which was apparently due to the formation of Co-rich tribofilms. However, in all cases these films were much less well-developed than in dry sliding and were difficult to observe and analyze. Nevertheless, the observation that the films appeared to promote stick-slip motion and thus limit the LCC was confirmed by removing the films with dilute hydrochloric acid, whereupon lower coefficients of friction and smoother friction behaviour was obtained for a short period.

The presence of beneficial Si-rich tribofilms which could bind the Co, analogous to dry sliding, could not be confirmed on the Syndax surfaces. This was probably related to the combined effects of lower temperatures, the presence of water in the contact zone which reduced adhesion and material transfer, and the fact that debris was swept out of the contact area by the water and was thus unavailable for tribofilm formation.

These findings have important commercial implications since they point the way towards the design and selection of improved PCD material couples for thrust bearings used in down-hole drilling applications. Commercial aspects of this work, as embodied in improved thrust bearings, have been protected by three international patent applications.

Under dry sliding conditions, mixed Syndite/Syndax sliding couples also showed lower coefficients of friction and higher LCC than self-mated Syndite. This was related to the formation of Si-rich tribofilms on the Syndax surfaces, which also contained smaller amounts of Co and W from the Syndite binder phase. The absence of deleterious Co-rich tribofilms on the Syndite surfaces led to the suggestion that a strong affinity existed between Si and Co, resulting in the preferential removal of Co from the Syndite surface and transfer to the binder phase regions of the Syndax surface. There was some analytical evidence that a chemical compound rich in Si, Co and O was present in the Si-rich tribofilm. The Co was thus effectively bound in this tribofilm on the Syndax surface, and the potential for the formation and interaction of detrimental Co-rich tribofilms on the Syndite surface was reduced.

The formation of the tribofilms was explained in terms of a thermal binder phase migration mechanism, sustained by diffusion and possibly driven by chemical reactions (oxidation) of the binder phase at the sliding surface. Loose wear debris generated from the binder phase regions probably also played a significant contributory rôle (compaction).

The influence of several typical drilling fluid constituents i.e. silica, bentonite, barite and haematite in the contact area of a self-mated Syndite couple was examined under dry sliding conditions. The effects varied from apparently no effect with barite, to reduced friction and no surface damage with bentonite, a reduction in friction accompanied by surface scoring with silica, and increased friction coefficients and severe surface damage with haematite. Beneficial effects were generally associated with the removal of deleterious Co-rich tribofilms from the sliding surfaces. The dramatic negative effect of haematite was attributed to structural degradation of the diamond surfaces, catalyzed by the iron content of the haematite (iron is known to promote the graphitization of diamond).

The effect of ambient temperature on self-mated Syndite in dry sliding was studied in view of the apparent importance of thermal effects in tribofilm formation. The friction coefficient and associated fluctuations in friction force increased with increasing temperature and reached a maximum a temperature between 60 °C and 100 °C. Beyond this point, both parameters decreased to reach a minimum at about 160 °C. These effects were explained in terms of the

5.5 Commercial Implications

This work has led to the development of an improved PCD thrust bearing for application in conjunction with a down-hole powerpack such as a Moineau motor or turbodrill. Commercially sensitive aspects of this bearing have been protected by two patents [221][222], which have been granted to date in South Africa, the USA, and Australia. Examination of the patents is underway in a number of other countries, including China and Europe. Prototype thrust bearings have been tested successfully both in a full-size test rig as well as in a production oil well in cooperation with the Russian Scientific Drilling Techniques Research Institute (VNIIBT).

The work has also clearly shown that the use of thermally stable PCD, such as Syndax, either as self-mated bearing couples or in conjunction with Syndite, may provide significant improvements in friction behaviour and load carrying capacity. Based on these findings and in view of the potential commercial implications, an international patent application has been submitted for a thrust bearing incorporating such improved PCD sliding couples as bearing surfaces [223].

5.6 Summary

The friction behaviour and load carrying capacity (LCC) of various sliding combinations of Syndite and Syndax were studied under dry and water-lubricated conditions. In both cases, the LCC was limited by the onset of unstable friction behaviour and increased friction coefficients at higher loads. It was concluded that this was associated with the formation and adhesive interaction of patchy, Co-rich tribofilms on the Syndite surfaces.

Self-mated Syndax exhibited lower coefficients of friction and higher LCC and this was attributed to the absence of Co-rich tribofilms, as a result of the different binder phase composition. The performance of the couple was similar under both dry and water-lubricated sliding conditions. It is thus likely that thrust bearings incorporating self-mated Syndax bearing surfaces will exhibit superior performance compared to Syndite bearings.

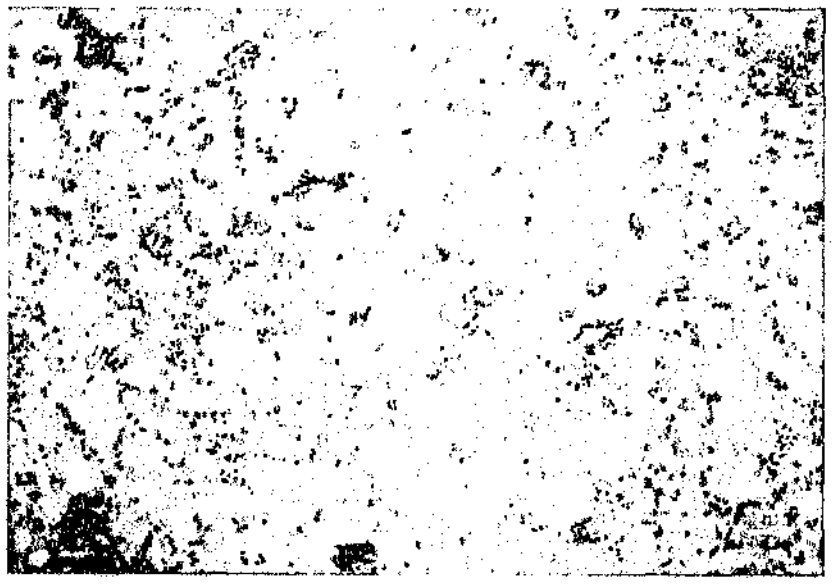

(a)

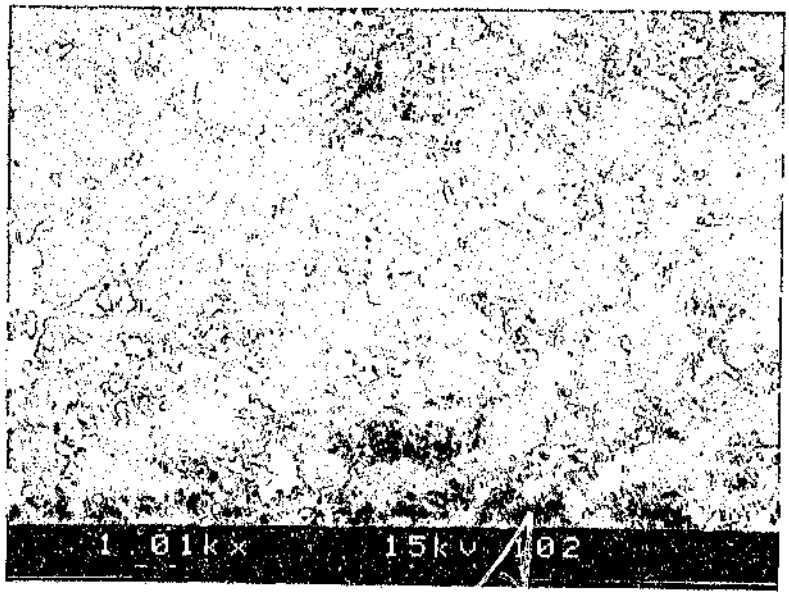

(b)

Figure 5.45: Optical micrograph (a), 500x mag.; and (b) SEM micrograph of the Syndite pin from the Syndite/Syndax water-lubricated sliding couple.

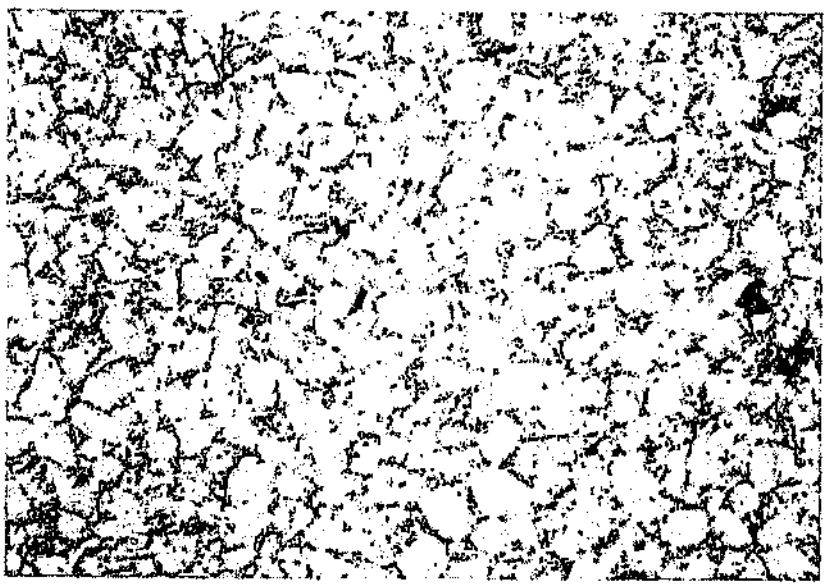

(a)

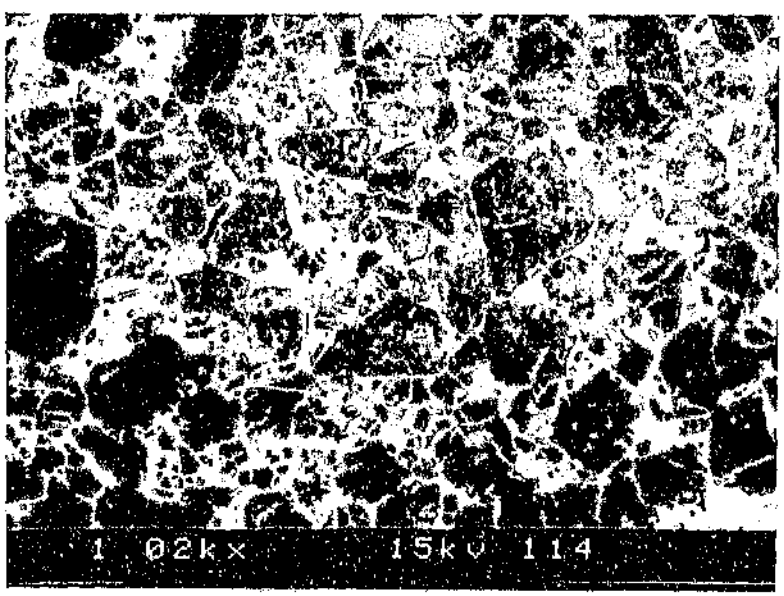

(b)

Figure 5.44: Optical micrograph (a), 500x; and (b) SEM micrograph of the Syndax disc from the Syndite/Syndax water-lubricated sliding couple.

in turn, caused severe vibrations and limited the LCC.

Although the presence of Co-rich wear debris and tribofilm patches was not easily observed microscopically or confirmed analytically, their effect on friction and LCC was confirmed by removing the tribofilm patches with dilute hydrochloric acid and re-running the test at a load close to the LCC. It was found that the couple initially ran very smoothly and with low coefficients of friction, but stick-slip sliding accompanied by vibrations and noise commenced with increasing test duration.

Syndite (pin) / Syndax (disc)

The behaviour of this couple appeared to be very similar to that of the Syndax/Syndite couple. The Syndax disc showed some preferential wear of the Si binder phase, but no well-developed Si- or Co-rich tribofilms were detected (Figure 5.44).

The Syndite pin exhibited highly polished diamond surfaces with small patches of Co-rich tribofilms at the grain boundaries (Figure 5.45).

The fundamental mechanism which dominated the friction behaviour and LCC in water-lubricated sliding thus seemed to be similar for the two mixed Syndite/Syndax couples. In both couples, the absence of large areas of well-developed Co-rich tribofilms resulted in low friction coefficients. Of course, the lubricating effect of the water, as well as the presence of thin and lubricious, Si-rich tribofilms on the Syndax surfaces may also have contributed to the low friction coefficients. For various reasons which were presented in the previous paragraphs, Si-rich tribofilms which were effective in 'binding' the Co in dry sliding did not form. Therefore, small patches of Co-rich tribofilms were developed on the Syndite surfaces and these induced stick-slip motion, vibrations, and noise emission which, in turn, limited the LCC to low loads.



(a)



(b)

Figure 5.43: Optical micrograph (a), 500x mag.; and (b) SEM micrograph of the Syndax pin from the Syndax/Syndite water-lubricated sliding couple.

118. Nakamura Y and Hiriyama S: Effect of Liquid Lubrications on the Wear of Grey Cast Iron Against Si-Al-O-N Ceramic; Wear, Vol. 137, pp. 91 - 97, 1990.

119. Gee M G: Some Observations of Ceramic-Metal Sliding Wear; Br. Ceram. Proc., Vol. 39, Issue - Eng. Ceram. 2, pp. 141 - 153, 1987.

120. Kapsa P, Maurin-Perrier P and Pijard B: Frictional Properties of Silicon Carbide Against Steel and Sapphire in Dry Conditions; Ref. No. C182/87, IMechE, pp. 687 - 694, 1987.

121. Van den Berg P H J and De With G: Wear and Strength of Mg-PSZ, Worn on Hardened Steel, Journal of the European Ceramic Society, Vol. 8, no. 2, pp. 123 - 133, 1991.

122. Holmberg K, Andersson P and Valli J, Proc. Leeds-Lyon Symp. on Tribology Int. Dyn., 1987.

123. Sullivan S I. and Athwal S S: The Mild Wear of a Low-alloy Steel at Temperatures up to 500°C; Tribology International, Vol. 16, pp. 123, 1983.

124. Quinn T F J, Rowson D M and Sullivan J L: The Application of the Oxidational Theory of Mild Wear to the Sliding Wear of Low-alloy Steel; Wear, Vol. 65, pp. 1 - 20, 1980.

125. Quinn T F J, Sullivan J L and Rowdson D M: Wear, Vol. 94, pp. 175 - 191, 1984.

126. Vardavoulias M, Jouanny-Fresy C and Jeandin M: Wear, Vol. 165, pp. 141 - 149, 1993.

127. Vardavoulias M: Wear, Vol. 173, pp. 105 - 114, 1994.

128. Suh N P, Abrahamson E P, Jahanmir S and Collins D A: Failure by Delamination During Wear; Proceedings of the Workshop on Failure Analysis and the SEM, ITT Research Institute, Chicago, Illinois, 1974.

129. Suh N P: Wear, Vol. 25, pp. 111, 1973.

130. Suh N P, Saka N and Jahanmir S: Wear, Vol. 44, pp. 127, 1977.

131. Suh N P: Update on the Delamination Theory of Wear, Paper presented at the 1980 ASM Materials Science Seminar, Pittsburgh, Pennsylvania, 1980.

106. Gee M G: The Formation of Glass in the Wear of reaction-Bonded Silicon Nitride: J. Phys. D: Appl. Phys., Vol. 25, pp. A182 -A188, 1992.

107. Gee M G and Butterfield D: The Combined Effect of Speed and Humidity on the Wear and Friction of Silicon Nitride: Wear, Vol. 162 - 164, pp. 234 - 245, 1993.

108. McHenry K D, Yonushonis T and Tressler R E: Low-Temperatures Subcritical Crack Growth in SiC and Si_3N_4: J. Amer. Ceram. Soc., Vol. 59, pp. 272, 1976.

109. Takadoum J, Zsigo Z and Roques-Carmes C: Short Communication: Wear Mechanism of Silicon Nitride: New Observations: Wear, Vol. 174, pp. 239 - 242, 1994.

110. Yamamoto Y and Ura A: Influence of Interposed Wear Particles on the Wear and Friction of Silicon Carbide in Different Dry Atmospheres: Wear, Vol. 154, pp. 141 - 150, 1992.

111. Ishigaki H, Nagata R and Iwasa M: Effect of Adsorbed Water on Friction of Hot-Pressed Silicon Nitride and Silicon Carbide at Slow Speed Sliding: Wear, Vol. 121, pp. 107 - 116, 1988.

112. Andersson P and Blomberg A: Instability in the Tribochemical Wear of Silicon Carbide in Unlubricated Sliding Contacts: Wear, Vol. 174, pp. 1 - 7, 1994.

113. Yang C and Bahadur S: Friction and Wear Behaviour of Alumina-Based Ceramics in Dry and Lubricated Sliding against Tool Steel: Wear, Vol. 157, pp. 263 - 277, 1992.

114. Libsch T A, Becker P C and Rhee S K: Dry Friction and Wear of Toughened Zirconias and Toughened Aluminas Against Steel: Wear, Vol. 110, pp. 263 - 283, 1986.

115. Zhou L, Gao Y-M, Zhou J-E and Zhou Q-D: Unlubricated Sliding Wear Mechanism of Fine Ceramics Al_2O_3 and ZrO_2 Against High Chromium Cast Iron: Wear, Vol. 176, pp. 39 - 48, 1994.

116. Feller H-G and Wienstroth U: Gleitverschleiß bei oszillierender Belastung an Metall/Keramik Systemen: Z. Metallkunde, Vol. 80, No. 5, pp. 352 - 358, 1989.

117. Osipova I I and Kovaltchenko A M: Studies of Friction Pair Si_3N_4-Steel Wear Mechanisms: Key Engineering Materials, Vol. 89 - 91, pp. 731 - 736, 1994.

94. Michaelske T A, Bunker B C and Freiman S W: J. American Ceram. soc., Vol. 69, pp. 721 - 724, 1986.

95. Jahanmir S and Dong X: Mechanism of Mild to Severe Wear Transition in Alpha-Alumina: Journal of Tribology, Vol. 114, pp. 403 - 411, 1992.

96. Gee M G: Modification to the Surface Layers of Alumina in Sliding Wear: British Ceram. Proceedings, Vol. 48, pp. 11 - 24, 1991.

97. Gee M G: The Formation of Aluminium Hydroxide in the Sliding Wear of Alumina: Wear, Vol. 153, pp. 201 - 227, 1992.

98. Fischer T E: Chemical Effects in Friction: NATO ASI Series, Series E, Vol. 220, pp. 299 - 312, 1992.

99. Lancaster J K, Mashal Y A-H and Atkins A G: The Role of Water in the Wear of Ceramics: J. Phys. D: Appl. Phys., Vol. 25, pp. A205 - A211, 1992.

100. Hibi Y and Enomoto Y: Tribochemical Wear of Silicon Nitride in Water, n-Alcohols and their Mixtures: Wear, Vol. 133, pp. 133 - 145, 1989.

101. Cranmer D C: Wear Surface Analysis of Silicon Nitride: Lubrication Engineering, Vol. 44, No. 12, pp. 975 - 980, 1988.

102. Imada Y, Kamamura K, Honda F and Nakajima K: The Tribological Reaction Accompanying Friction and Wear of Silicon Nitride Containing Titanium Nitride: Journal of Tribology, Vol. 114, pp. 230 - 235, 1992.

103. Skopp A, Woydt M and Habig K-H: Unlubricated Sliding Friction and Wear of Various Si_3N_4 Pairs Between 22° and 100 °C: Tribology International, Vol. 23, No. 3, pp. 189 - 199, 1990.

104. Page R A, Blanchard-Ardid C R and Wei W: Effect of Particulate Additions on the Contact Damage Resistance of Hot-Pressed Si_3N_4: Journal of Materials Science, Vol. 23, pp 946 - 957, 1988.

105. Woydt M, Skopp A and Habig K-H: Dry Friction and Wear of Self-Mated Sliding Couples of SiC-TiC and Si_3N_4-TiN: Wear, Vol. 148, pp. 377 - 394, 1991.

82. Berthier Y: Experimental Evidence for Friction and Wear Modelling; Wear, Vol. 139, pp. 77 - 92, 1990.

83. Sasaki S: The Effects of Surrounding Atmosphere on the Friction and Wear of Alumina, Zirconia, Silicon Carbide and Silicon Nitride; Wear of Materials 1989, vol. 7, No. 1, pp. 409 - 417, 1989.

84. Gates R S, Hsu S M and Klaus E E: Ceramic Tribology: Methodology and Mechanisms of Alumina Wear; NIST Special Publication, Vol. 758, 229 pages, 1988.

85. Perez-Unzueta A J, Beynon J H and Gee M G: Effects of Surrounding Atmosphere on the Wear of Sintered Alumina; Wear, Vol. 146, pp. 179 - 196, 1991.

86. Takadoum J: Tribological Behaviour of Alumina Sliding on Several Kinds of Materials; Wear, Vol. 170, pp. 285 - 290, 1993.

87. Kapelski G: Etudes des Propriétés Tribologiques de Céramiques thermo-mécaniques en Fonction de la Température et pour Différents Environements; Thesis, University of Limoges, 1989.

88. Lancaster J K: A Review of the Influence of Environmental Humidity and Water on Friction, Lubrication and Wear; Tribology International, Vol. 23, No. 6, pp. 371 - 389, 1990.

89. Jeng M-C and Yan L-Y: Environmental Effects on Wear Behaviour of Alumina; Wear, Vol. 161, pp. 111 - 119, 1993.

90. Ishigaki H, Kawaguchi I, Iwasa M and Toibana Y: Friction and Wear of Hot-Pressed Silicon Nitride and Other Ceramics; Journal of tribology, Vol. 108, pp. 514 - 521, 1986.

91. Klaffke D and Habig K-H: Fretting Wear Tests of Silicon Carbide; Wear of Materials 1987, ASME, pp. 361 - 370, 1987.

92. Klaffke D: Tribological Surface Layers in the Fretting of Ceramics; Proc. 14th Leeds-Lyon Symposium on Interface Dynamics; Elsevier, pp. 237 - 244, 1988.

93. Denape J: Wear Debris Action in Sliding Friction of Ceramics; Wear Particles, Dowson *et al* (editors), Elsevier, pp. 453 - 462, 1992.

69. Tucci A and Esposito L: Microstructure and Tribological Properties of ZrO$_2$ Ceramics: Wear, vol. 172, pp. 111 - 119, 1994.

70. Blomberg A, Hogmark S and Lu J: An Electron Microscopy Study of Worn Ceramic Surfaces: Tribology International, Vol. 26, No. 6, pp. 369 - 381, 1993.

71. Andersson P and Blomberg A: Alumina in Unlubricated Sliding Point, Line and Plane Contacts: Wear, Vol. 170, pp. 191 - 198, 1993.

72. Hogmark S, Olsson M and Blomberg A: Wear Mechanisms of Advanced Ceramic Materials: Journal of Hard Materials, Vol. 3, No. 2, pp. 153 - 167, 1992.

73. Ajayi O O and Ludema K C: Mechanism of Transfer Film Formation during Repeat Pass Sliding of Ceramic Materials: Wear, Vol. 140, pp. 191 - 206, 1990.

74. Woydt M and Habig K H: High temperature Tribology of Ceramics: Tribology International, Vol. 22, No. 2, pp. 75 - 88, 1989.

75. Gee M G and Mutharu C S: The Measurement of Sliding Friction and Wear at High Temperature: Int. J. High Technology Ceramics, Vol. 4, pp. 319 - 331, 1988.

76. Nickel K G, Danzer R, Schneider G and Petzow G: Corrosion and Oxidation of Advanced Ceramics: Powder Metallurgy International, Vol. 21, No. 3, pp. 29 - 33, 1989.

77. Yeomans J A and Arbabi H: A Microstructural Investigation of Cylindrical Wear Debris: British Ceramic Transactions J. Vol. 89, No. 4, pp. 144 - 145, 1990.

78. Arbabi H, Watts J F and Briggs J: A Chemical Study of Wear Particles and Other Features Associated with the Wear of Ceramics: Tribology International, Vol. 23, No. 4, pp. 235 - 243, 1990.

79. Denape J and Lamon J: Sliding Friction of Ceramics: Mechanical Action of the Wear Debris: Journal of Materials Science, Vol. 25, pp. 3592 - 3604, 1990.

80. Hawthorne H M: On the Role of Interfacial Debris Morphology in a Conforming Contact Tribosystem: Wear, Vol. 149, pp. 169 - 185, 1991.

81. Alexeyev N M: On the Motion of Material in the Border Layer in Solid State Friction: Wear, Vol. 139, pp. 33 - 48, 1990.

58. Wang Y S, Hsu S M and Munro R G: Ceramics Wear Maps: Alumina: Lubrication Engineering, Vol. 47, No. 1, pp. 63 - 69, 1991.

59. Lim D S, Park S K and Moon H: Wear Diagram for Sliding of Silicon Nitrides: in Wear testing of Advanced Materials, Divakar R and Blau P J (eds), ASTM, pp. 151 - 160, 1992.

60. Dong X and Jahanmir S: Wear Transition Diagram for Silicon Nitride: Wear, Vol. 165, pp. 169 - 180, 1993.

61. Konvopoulos K and Li H: The Effect of Tribofilm Formation and Humidity on the Friction and Wear Properties of Ceramic Materials: J. of Tribology, Vol. 114, pp. 131 - 140, 1992.

62. Blomberg A, Olsson M and Hogmark S: Wear Mechanisms and Tribo Mapping of Al_2O_3 and SiC in Dry Sliding: Wear, Vol. 171, pp. 77 - 89, 1994.

63. Bauer M, Kapsa Ph, Loubet J L, Ramos S M M, Canut B, Gea L and Thevenard P: Tribological Properties of Niobium Implanted Alumina: Tribology International, Vol. 25, No. 5, pp. 319 - 327, 1992.

64. Wallbridge N, Dowson D and Roberts E W: The Wear Characteristics of Sliding Pairs of High Density Polycrystalline Aluminium Oxide under both Dry and Wet Conditions: Wear of Materials 1983, Ludema K C (ed), ASME, New York, pp. 202 - 211, 1983.

65. Stachowiak G W and Stachowiak G B: Unlubricated Wear and Friction of Toughened Zirconia Ceramics at Elevated Temperatures: Wear, Vol. 143, pp. 277 - 295, 1991.

66. Bondschuh W and Zum Gahr K H: Einfluß der Korngröße auf Reibung und Gleitverschleiß von TZP-ZrO_2-Keramik bei Festkörper- und Mischreibung: Mat.-wiss. u. Werkstofftechn., Vol. 24, pp. 12 - 19, 1993.

67. Andersson P and Holmberg K: Limitations on the Use of Ceramics in Unlubricated Sliding Applications due to Transfer Layer Formation: Wear, Vol. 175, pp. 1 - 8, 1994.

68. Stachowiak G W and Stachowiak G B: Unlubricated Friction and Wear Behaviour of Toughened Zirconia Ceramics: Wear, Vol. 132, pp. 151 - 171, 1989.

46. Chen C P and Knapp W J: Delayed fracture of an alumina ceramic: J. Amer. Ceram. Soc., Vol. 60, pp. 87, 1976.

47. Fischer T E, Anderson M P, Jahanmir S and Salher R: Friction and Wear of Tough and Brittle Zirconia in Nitrogen, Air, Water, Hexadecane and Hexadecane Containing Stearic Acid: Wear, Vol. 124, pp. 133 - 148, 1988.

48. Scott H G: Friction and Wear of Zirconia at Very Low Sliding Speeds: Wear of Materials 1985, ASME, pp. 8 - 12, 1985.

49. Stachowiak G W and Stachowiak G B: Environmental Effects on Wear and Friction of Toughened Zirconia Ceramics: Wear, Vol. 160, pp. 153 - 162, 1993.

50. Lancaster J K: Material-Specific Wear Mechanisms: relevance to Wear Modelling: Wear, Vol. 141, pp. 159 - 183, 1990.

51. Rabinowicz E: New Coefficients Predict Wear of Metal Parts: Product Engineering, Vol. 19, pp. 71 - 73, 1958.

52. Rabinowicz E: The Wear Coefficient: Magnitude, Scatter, Uses: ASME Journ. of Lubr. Tech., Vol. 103, pp. 188 - 194, 1981.

53. Tabor D: Status and Direction of Tribology as a Science in the 80's: Understanding and Prediction: Proc. Int. Conf. on Tribology in the 80's, NASA CP 2300, vo. 1, NASA, 1984.

54. Munro R G and Hsu S M: Advanced Ceramics: A Critical Assessment of Wear and Lubrication: NISTIR 88-3722, National Technical Information Service, Springfield, VA, 1988.

55. Hsu S M, Lim D S, Wang Y S and Munro R G: Ceramics Wear Maps: Concept and Method Development: Lubrication Engineering, Vol. 47, No. 1, pp. 49 - 54, 1991.

56. Woydt M, Klaffke D, Habig K-H and Czichos H: Tribological Transition Phenomena of Ceramic Materials: Wear, Vol. 136, pp. 373 - 381, 1990.

57. Hsu S M, Wang Y S and Munro R G: Quantitative Wear Maps as a Visualization of Wear Mechanism Transitions in Ceramic Materials: Wear, Vol. 134, pp. 1 - 11, 1989.

36. Hannink R H J, Murray M J and Scott H G: Friction and Wear of Partially Stabilized Zirconia: Basic Science and Practical Applications; Wear, Vol. 100, pp. 355 - 366, 1984.

37. Fischer T E, Anderson M P and Jahanmir S: Influence of Fracture toughness on the Wear Resistance of Yttria-Doped Zirconium Oxide; J. Am. Ceram. Soc., Vol. 72, No. 2, pp. 252 - 257, 1989.

38. Stachowiak G W and Stachowiak G B: Wear and Friction Characteristics of PSZand TZP Ceramics; Key Engineering Materials, Vol. 53 - 55, pp. 778 - 784, 1991.

39. Bundschuh W and Zum Gahr K H: Effect of Temperature on Friction and Oscillating Sliding Wear of Dense and Porous 3Y-TZP Zirconia Ceramics; Tribology International, Vol. 27, No. 2, pp. 97 - 103, 1994.

40. Birkby I, Harrison P and Stevens R: The Effect of Surface Transformation on the Wear Behaviour of Zirconia TZP Ceramics; Journal of the European Ceramic Society, Vol. 5, pp. 37 - 45, 1989.

41. Ishigaki J, Nagata R and Iwasa M: Friction and Wear of Partially Stabilized Zirconia; Proc. Conf. on Tribology: Friction, Lubrication and Wear, 50 Years On; Vol. 2, IMechE, pp. 609 - 614, 1987.

42. Woydt M, Kadoori J, Habig K-H and Hausner H: Unlubricated Sliding Behaviour of Various Zirconia-Based Ceramics; Journal of the European Ceramic Society, Vol. 7, pp. 135 - 145, 1991.

43. Chen Y M, Rigaut B and Armanet F: Wear Behaviour of Partially Stabilized Zirconia at High Sliding Speed; Journal of the European Ceramic Society, Vol. 6, pp. 383 - 390, 1990.

44. Chen Y M, Rigaut B, Pavy J C and Armanet F: Wear Particles Forming by Phase Transformation in PSZ Ceramics During High Speed Sliding; Wear Particles, Dowson D *et al* (editors), Elsevier Science Publishers, pp. 115 - 120, 1992.

45. Zum Gahr K H: Sliding Wear of Ceramic-Ceramic, Ceramic-Steel and Steel-Steel Pairs in Lubricated and Unlubricated Contact; Wear, Vol. 133, pp. 1 - 22, 1989.

24. Vaughan D A J and Guiu F: Cyclic fatigue of Advanced Ceramics by Repeated Indentation; British Ceramic Proc., Vol. 39, Issue - Eng. Ceram. 2, pp. 101 - 107, 1987.

25. Brookes C A and Parry A R: Some Fundamental Aspects of the Mechanical Wear of Hard Ceramic Crystals due to Sliding; Materials Science and Engineering A; Vol. A 105 - 106, pp. 143 - 150, 1988.

26. Fischer T E and Tomizawa H: Interaction of Tribochemistry and Microfracture in the Friction and Wear of Silicon Nitride; Wear, Vol. 105, pp. 29 - 45, 1985.

27. Tomizawa H and Fischer T E: Friction and Wear of Silicon Nitride and Silicon Carbide in Water: Hydrodynamic Lubrication at Low Sliding Speed Obtained by Tribochemical Wear; ASLE Trans., Vol. 30, pp. 41 - 46, 1986.

28. Glaeser W A: Friction and Wear of Ceramics; ASM Handbook, Vol 18., pp. 812 - 815, 1992.

29. Winer W O and Ting B Y: Development of a Theory of Wear of Ceramics; available as Report No. ORNL/Sub-84-7802/1, Order No. DE88015327, NTIS, 1988.

30. Ajayi O O and Ludema K C: Surface Damage of Structural Ceramics: Implications for Wear Modeling; Wear, Vol. 124, pp. 237-257, 1988.

31. Ajayi O O and Ludema K C: The Effect of Microstructure on Wear Modes of Ceramic Materials; Wear, Vol. 154, pp. 371 - 385, 1992.

32. Zum Gahr K H, Bundschuh W and Zimmerlin B: Effect of Grain Size on Friction and Sliding Wear of Oxide Ceramics; Wear Vol. 162 - 164, pp. 269 - 279, 1993.

33. Gritzner G, Konrad R, Puchner C and Kladnig W: Mechanical Properties of Pressureless Sintered Tetragonal Y_2O_3-Stabilized ZrO : ,Powder Metallurgy International, Vol. 23, No. 1, pp. 26 - 30, 1991.

34. Lewis C F: Zirconia: The Tough Contender; Materials engineering, pp. 43 - 45, May 1989.

35. Evans A G: High Toughness Ceramics; Materials Science and Engineering, Vol. A 105/106, pp. 65 - 75, 1988.

13. Tabor D: Friction and a Dissipative Process: in Fundamentals of Friction: Macroscopic and Microscopic Processes, Singer I L and Pollock H M (eds), NATO ASI Ser., Ser. E, Vol. 220, pp. 3 - 24, 1992.

14. Godet M: The Third-Body Approach: A Mechanical View of Wear: Wear, Vol. 100, pp. 437 - 452, 1984.

15. Hutchings I M: Tribology: Friction and Wear of Engineering Materials: Edward Arnold, London, pp. 44 - 48, 1992.

16. Lancaster J K, Mashal Y A and Atkins A G: Particle Detachment Processes in the Dry and Lubricated Wear of Ceramics: Wear Particles, Tribology Series, Vol. 21, pp. 237 - 246, 1992.

17. Evans A G and Marshall D B: Wear Mechanisms in Ceramics: Fundamentals of Friction and Wear of Materials, ASM, pp 439 - 452, 1980.

18. Marshall D B, Lawn B R and Evans A G: Elastic/Plastic Indentation Damage in Ceramics: The Lateral Crack System: J. Amer. Cer. Soc., Vol. 65, pp. 561 - 566, 1982.

19. Lawn B R, Evans A G and Marshall D B: Elastic/Plastic Indentation Damage in Ceramics: The Median/Radial Crack System: J. Amer. Cer. Soc., Vol. 63, pp. 574 - 581, 1980.

20. Lawn B R and Evans A G: A Model for Crack Initiation in Elastic/Plastic Indentation Fields: J. Mat. Sci. Vol. 12, pp. 2195 - 2199, 1977.

21. Sliney H E: The Effects of Ion-Plated Silver and Sliding Friction on Tensile Stress-Induced Cracking in Aluminium Oxide: Lubrication Engineering, Vol. 19, pp. 153 - 159, 1993.

22. Rosenfield A R: A Model of Sliding Wear of Ceramics: J. Mater. Eng., Vol. 12, pp. 295 - 298, 1990.

23. Braza J F, Cheng H S, Fine M E, Gangopadhyay A K, Keer L M and Worden R E: Mechanical Failure Mechanisms in Ceramic Sliding and Rolling Contacts: STLE Tribology Trans., Vol. 32, No. 1, pp. 1 - 8, 1989.

REFERENCES

1. Greil P: Opportunities and Limits in Engineering Ceramics: Powder Metallurgy International, Vol. 21, No. 2, pp. 40 - 46, 1989.

2. Steijn R P: On the Wear of Sapphire: J. Appl. Phys., Vol. 32, No. 10, pp. 1951 - 1958, 1961.

3. Miyoshi K and Buckley D H: Friction, Deformation and Fracture of Single-Crystal Silicon Carbide: ASLE Trans., Vo. 22, No. 1, pp. 79 - 90, 1979.

4. Lawn B R and Swain M V: Microfracture beneath Point Indentations in Brittle Solids: J. Mater. Sci., Vol. 10, pp. 113 - 122, 1975.

5. Lawn B R: Hertzian Fracture in Single Crystals with the Diamond Structure: J. Appl. Phys., Vol. 39, No. 10, pp. 4828 - 4836, 1968.

6. Frank F C and Lawn B R: On the Theory of Hertzian Fracture: Proc. R. Soc. London, Ser. A, Vol. 299, pp. 291 - 306, 1967.

7. Buckley D H and Miyoshi K: Friction and Wear of Ceramics: Wear, Vol. 100, pp. 333 - 353, 1984.

8. Cranmer D C: Ceramic Tribology - Needs and Opportunities: Tribol. Trans., Vol. 31, No. 2, pp. 164 - 173, 1988.

9. Buckley D H and Miyoshi K: Tribological Properties of Structural Ceramics: Treatise on Materials Science and Technology, Vol. 29, pp. 293 - 365, 1989.

10. Larsen-Basse J: Basic Theory of Solid Friction: ASM Handbook, Vol. 8, pp. 27 - 38, 1992.

11. Czichos H, Becker S and Lexow J: Multilaboratory Tribotesting: Results from the Versailles Advanced Materials and Standards Programme on Wear Test Methods: Wear, Vol. 114, pp. 109 - 130, 1987.

12. Czichos H, Becker S and Lexow J: International Multilaboratory Sliding Wear Tests with Ceramics and Steel: Wear, Vol. 135, pp. 171 - 191, 1989.

6.4 Hydro-Power Mining Systems

Metal-ceramic couples suitable for application in reciprocating components in hydro-powered stoping equipment need to exhibit a low friction coefficient and steady friction behaviour, coupled with an acceptable steady-state wear rate, in order to ensure satisfactory component operation and lifetimes. In view of these requirements, this work has demonstrated that the silicon-based ceramics were generally superior to the oxide ceramics. In deionized water, preference should be given to Si_3N_4 because of the apparent higher load carrying capacity and lower wear rate compared to Sialon. In mine waters which exhibit a similar composition to the synthetic Unisel mine water solution and which are typically used as the hydro-power working fluid, both Sialon and Si_3N_4 are considered to be equally suitable. In this case, even the AISI 440C-alumina couple would be suitable as a result of the beneficial influence of the mine water constituents on friction and wear, provided the poor fracture toughness of the alumina ceramic can be tolerated.

6.5 PCD Thrust Bearings

It was confirmed that self-mated Syndite shows promise for application in high-load thrust bearings lubricated by water-based drilling fluid. However, thrust bearings incorporating self-mated Syndax bearing surfaces will exhibit superior LCC and more stable friction behaviour. Similarly, mixed Syndite/Syndax sliding couples provide superior bearing performance under dry sliding conditions, but show little advantage over self-mated Syndite under water-lubricated conditions. It was also concluded that the addition of bentonite, silica, and barite to the drilling fluid can improve the friction behaviour and LCC of self-mated Syndite. Haematite additions must be avoided since they cause rapid seizure and severe damage of the bearing surfaces.

Most of these findings have been confirmed by laboratory and field tests of prototype PCD thrust bearings. Commercially sensitive aspects of this work have been protected by three international patent applications.

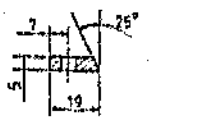

SECTION A-A

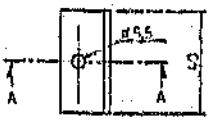

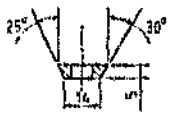

SECTION A-A

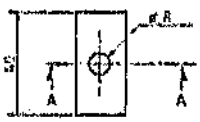

CLAMPING FIXTURE

DATE	27-10-1987	
DRAWN	G.F.R.A. DAMM	DRG. NO. 5
SCALE	1:1	

SECTION A-A

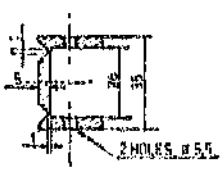



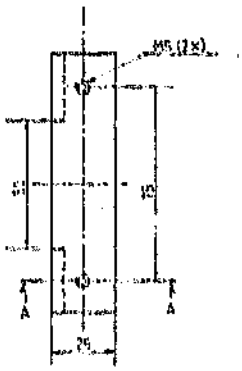

FLEXURES

DATE	13-10-1987	
DRAWN	G.F.R.A. DAMM	DRG. NO. 6
SCALE	1:1	

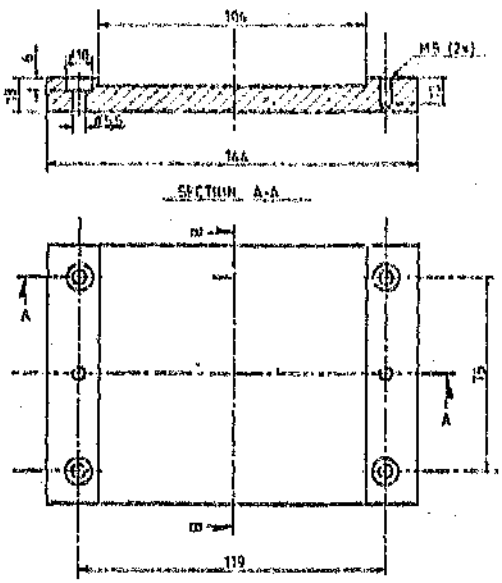
SECTION A-A
SECTION B-B
SPECIMEN STAGE SUPPORT
DRG NO. 3

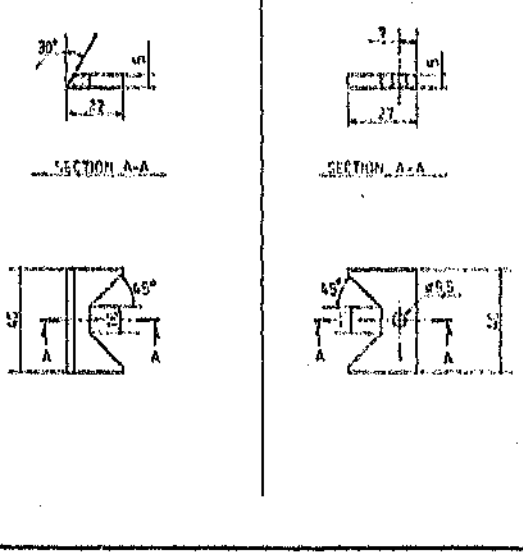
SECTION A-A
SECTION A-A
CLAMPING FIXTURE
DRG NO. 4

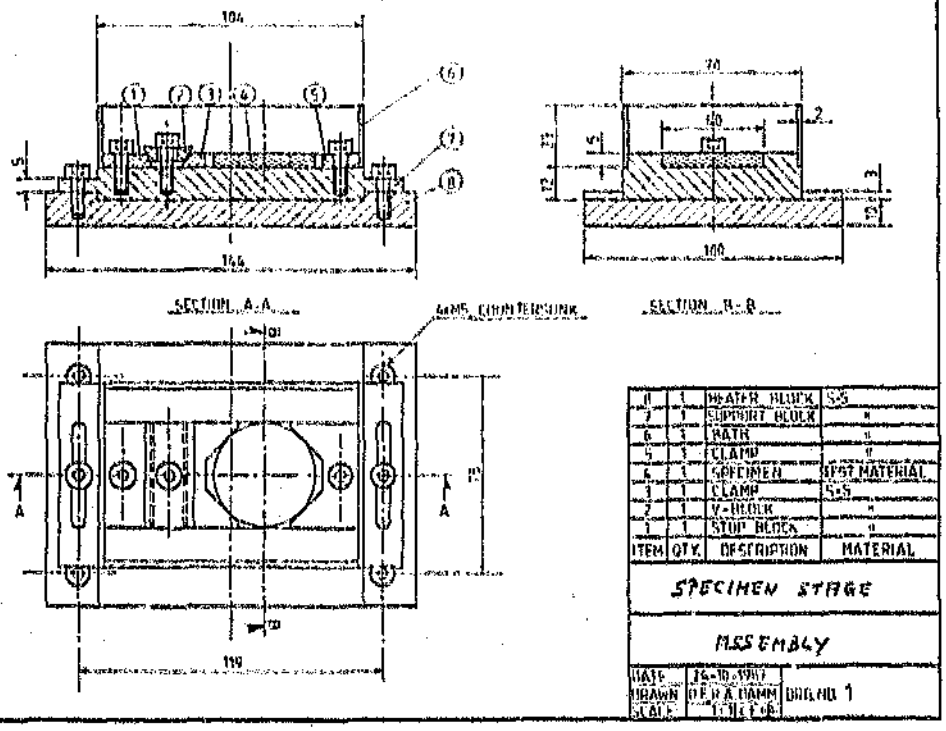

ITEM	QTY.	DESCRIPTION	MATERIAL
8	1	HEATER BLOCK	S-S
7	1	SUPPORT BLOCK	"
6	1	PATH	"
5	1	CLAMP	"
4	1	SPECIMEN	TEST MATERIAL
3	1	CLAMP	S-S
2	1	V-BLOCK	"
1	1	STOP BLOCK	"

SPECIMEN STAGE

ASSEMBLY

DATE	26-10-1987	
DRAWN	DERA DAMM	DRG NO 1
SCALE	1:1	

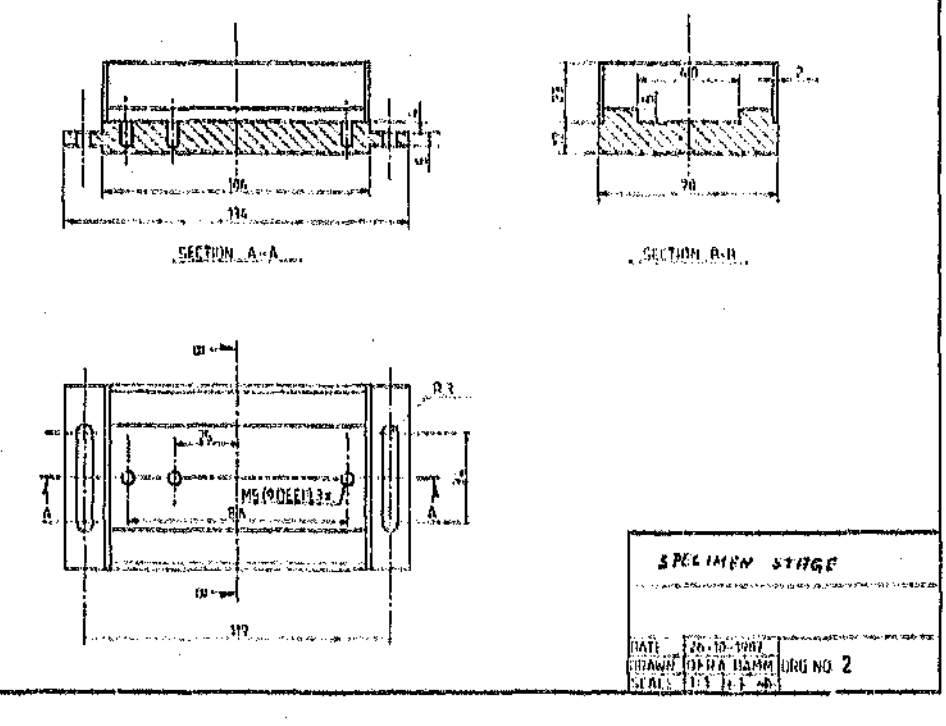

SPECIMEN STAGE

DATE	26-10-1987	
DRAWN	DERA DAMM	DRG NO 2
SCALE	1:1	

APPENDIX A

Reciprocating sliding tribometer design drawings

(Note: These drawings have been photo-reduced and are not to scale).

217. Pipkin N J and Tank K. Private Communication. De Beers Diamond Research Laboratory, Johannesburg, 1993.

218. Binary Alloy Phase Diagrams, Vol 1, Editor-in-Chief T B Massalski, ASM, 1986.

219. Moulder J F, Stickle W F, Sobol P E and Bomben K D: Handbook of X-ray Photoelectron Spectroscopy: Ed. J Chastain, Perkin-Elmer Corporation, USA, 1992.

220. Almond E A, Lay L A and Gee M G: Comparison of Sliding and Abrasive Wear Mechanisms in Ceramics and Cemented Carbides; Inst. Phys. Conf. Ser. No. 75, Chapter 9, Paper presented at 2nd Int. Conf. Science Hard Mater., Rhodes, pp. 919 - 948, 1986.

221. Damm O F R A and Tank K: Diamond Bearing Assembly; South African Patent No. 93/7866, 1994.

222. Damm O F R A and Tank K: Diamond Bearing Assembly; South African Patent No. 93/7867, 1994.

223. Damm O F R A, Tank K and Tomlinson P N: Bearing Assembly; South African Patent Application No. 93/2167, 1993.

205. Guillou M-O, Henshall J L and Hooper R M: Repeated Point Contact Loading on Ce-TZP: Wear, Vol. 170, pp. 247 - 253, 1993.

206. Becker P C, Libsch T A and Rhee S K: Wear Mechanisms of Toughened Zirconias. Ceram. Eng. Sci. Proc., Vol. 6, No. 7 - 8, pp. 1040 - 1058, 1985.

207. Jahanmir S and Fischer T E: Friction and Wear of Silicon Nitride Lubricated by Humid Air, Water, Hexadecane and Hexadecane + 0,5 % Stearic Acid: Tribology Trans., STLE, Vol.31, pp. 32 - 43, 1988.

208. Sasaki S: Effects of pH Value and Fatty Acid Sodium on Friction and Wear of Alumina Under Lubrication With Water: Proc. Japanese Congr. Mater. Res., Vol. 33, pp. 205 - 211, 1990.

209. Löffelbein B, Woydt M and Habig K-H: Sliding Friction and Wear of Ceramics in Neutral, Acid and Basic Aqueous Solutions: Wear, Vol. 162 - 164, pp. 220 - 228, 1993.

210. Wei D and Spikes H A: The Lubricity of Diesel Fuels: Wear, Vol. 111, pp. 217 - 235, 1986.

211. Bugarcic H: The Influence of Contamination on Metallic Friction: Wear, Vol. 113, pp. 21 - 35, 1986.

212. Kotvis P V and Tysoe W T: The Surface Chemistry of Chlorinated Hydrocarbon Lubrication Additives: Applied Surface Science, Vol. 40, pp. 213 - 221, 1989.

213. Tanita Y, Honda F and Nakajima K: Surface Reactions of Extreme Pressure Additive on Steel Surface in Ceramics-Steel Couples: J. of Tribology, Vol. 110, pp. 394 - 401, 1988.

214. Gates R S and Hsu S M: Effect of Selected Chemical Compounds on the Lubrication of Silicon Nitride: Tribology Trans., Vol. 34, No. 3, pp. 417 - 425, 1991.

215. Fayeks S: Private Communication, University of the Witwatersrand, 1995.

216. Pipkin N J: Private Communication: De Beers Diamond Research Laboratory, Johannesburg, 1995.

193. Paton R and Howarth D: Corrosion Properties of New Development Steels for the Gold Mining Industry; Proc. 5th Int. Conf. Appl. Corr. Tech., SACI, Johannesburg, South Africa, Aug. 1990.

194. Bowden F P and Tabor D: The Friction and Lubrication of Solids; Oxford University Press, 1950.

195. Fischer T E and Mullins W M: Relation Between Surface Chemistry and Tribology of Ceramics; J. Materials Eng., Vol. 6, pp. 51 - 60, 1994.

196. Denape j, Marzinotto A and Petit J A: Roughness Effect of Silicon Nitride Sliding on Steel under Boundary Lubrication; Wear, Vol. 159, pp. 173 - 184, 1992.

197. Gee M G; Wear Mechanisms for Ceramics; Br. Ceram. Proc. [BCPREL], Vol. 46 (Adv. Eng. Ceram.), pp. 287 - 296, 1990.

198. Handbook of Chemistry and Physics, 65th Edition, eds. Weast R C, Astle M J and Beyer W H, CRC Press, Boca Raton, Florida, 1984.

199. Bhushan B and Gupta B K; Handbook of Tribology: Materials, Coatings and Surface Treatments; McGraw-Hill, New York, 1991.

200. Levi E M, Robbins C R and McMurdie H F; Phase Diagrams for Ceramists, 1969 Supplement, ed. Reser M K, The American Ceramic Society, Columbus, Ohio, 1969.

201. Hannink R H J, Murray M J and Marmach M; Magnesia Partially Stabilized Zirconias (Mg-PSZ) as Wear Resistant Materials; Wear of Materials 1983, ASMeehE, p. 181, 1983.

202. Sasaki S; Effects of Environment on Friction and Wear of Ceramics; Bulletin of Mechanical Engineering Laboratory, Japan, ISSN 0374-2725, 1992.

203. Rainforth W M and Stevens R; A Transmission Electron Microscopy Study of Wear of Magnesia Partially Stabilized Zirconia; Wear, Vol. 162 - 164, pp. 322 - 331, 1993.

204. Woydt M, Kadoorit J, Hausner H and Habig K H; Development of Engineering Ceramics According to Tribological Considerations; cfi/Ber., DKG, Vol. 67, pp.123 - 130, 1990.

179. Wilks J and Wilks E M: Wear and Polishing of Diamond: In J E Field (ed.). The Properties of Natural and Synthetic Diamond, Academic Press, London, pp 573 - 604, 1992.

180. Wilks E M and Wilks J: The Resistance of Diamond to Abrasion: J. Phys. D: Appl. Phys., Vol. 5, pp. 1902 - 1919, 1972.

181. Hayward L P: Surf. Coatings Technology, Vol. 49, pp 554, 1991.

182. Grill A: Review of the Tribology of Diamond-Like Carbon: Wear, Vol. 168, pp. 143 - 153, 1993.

183. Crompton D, Hirst W and Howse M G W: The Wear of Diamond: Proc. Royal Soc. London A, Vol. 333, pp. 435 - 454, 1973.

184. Hitchiner M P, Wilks E M and Wilks J: The Polishing of Diamond and Diamond Composite Materials: Wear, Vol. 94, pp. 103 - 120, 1984.

185. Miller D and Ball A: The Wear of Diamonds in Impregnated Diamond Bit Drilling: Wear, Vol. 141, pp. 311 - 320, 1991.

186. Lin T-P, Hood M, Cooper G A and Li X: Wear and Failure Mechanisms of Polycrystalline Diamond Compact Bits: Wear, Vol. 156, pp. 133 - 150, 1992.

187. Appl F C, Wilson C C and Lakshman I: Measurement of Forces, Temperatures and Wear of PDC Cutters in Rock Cutting: Wear, Vol. 169, pp. 9 - 24, 1993.

188. Glowka D A and Stone C M: Thermal Response of Polycrystalline Diamond Compact Cutters under Simulated Downhole Conditions: Society of Petroleum Engineers Journal, pp. 143 - 156, April 1985.

189. Harper G: Personal Communication, Chamber of Mines Research Organization, 1990.

190. Stevens R: Zirconia and Zirconia Ceramics: Magnesium Elektron Ltd., 1986.

191. Yin-Quian C, Xiang-Dong D, Fu-Xing W, Qi-Gong C and Zhang-Xiao Z: On Wear Mechanisms of Sialon and Metal in Dry Sliding, Wear, Vol. 137, pp. 175 - 186, 1990.

192. Guillou M-O, Henshall J L and Hooper R M: Repeated Point Contact Loading on Ce-TZP: Wear, Vol. 170, pp. 247 - 253, 1993.

165. Hayward I P: Friction and Wear Properties of Diamonds and Diamond Coatings: Surface and Coatings Technology, Vol. 49, pp. 554 - 559, 1991.

166. Enomoto Y and Tabor D: Proc. Royal Soc. London, A373, pp. 405 - 417, 1981.

167. Casey M and Wilks J: The Friction of Diamond Sliding on Polished Cube Faces of Diamond: J. Phys. D: App. Phys., Vol. 6, pp. 1772 - 1781, 1973.

168. Samuels B and Wilks J: The Friction of Diamond Sliding on Diamond: J. Of Materials Science, Vol. 23, pp. 2846 - 2864, 1988.

169. Feng Z: PhD Dissertation, University of Cambridge, Cambridge, UK, 1991.

170. Feng Z and Field J E: Friction of Diamond on Diamond and Chemical Vapour Deposition Diamond Coatings: Surface and Coatings Technology, Vol 47, pp. 631 - 645, 1991.

171. Feng Z and Field J E: The Friction and Wear of Diamond Sliding on Diamond: J. Phys. D: Appl. Phys.: Vol. 25, pp. A33 - A39, 1992.

172. Gardos M N and Soriano B L: The Effect of Environment on the Tribological Properties of Polycrystalline Diamond Films: J. Mater. Res., Vol. 5, No. 11, pp. 2599 - 2609, 1990.

173. Jahanmir S, Deckman D E, Ives L K, Feldman A and Farabaugh E: Tribological Characteristics of Synthesized Diamond Films on Silicon Carbide: Wear of Materials, Vol. 7, No. 1, pp. 375 - 379, 1989.

174. Plano L. S, Hayward I and Wegand J: CVD Diamond Films for Tribological Applications: Report D8REP4, Crystallume, Menlo Park, USA, 1990.

175. Hayward I P and Singer I L: The Tribological Behaviour of Diamond Coatings: New Diamond Science and Technology, Proc. Int. Conf., pp. 785 - 789, 1990.

176. Hayward I P, Singer I L and Seitzman L E: Effect of Roughness of the Friction of Diamond on CVD Diamond Coatings: Wear, Vol. 157, pp. 215 - 227, 1992.

177. Bull S J and Matthews A: Diamond for Wear and Corrosion Applications: Diamond and Related Materials, Vol. 1, pp. 1049 - 1064, 1992.

178. Field J E and Freeman C J: J. Mater. Sci., Vol. 24, pp. 1069 - 1072, 1989.

1993.

155. Tomlinson P N: Applications of Diamond Grits and Composites: In J E Field (ed.). The Properties of Natural and Synthetic Diamond. Academic Press, London, pp. 637 - 666, 1992.

156. Burns R C and Davies G J: Growth of Synthetic Diamond: In J E Field (ed.). The Properties of Natural and Synthetic Diamond. Academic Press. London, pp. 395 - 422, 1992.

157. Sato Y and Kamo M: Synthesis of Diamond from the Vapour Phase: In J E Field (ed.). The Properties of Natural and Synthetic Diamond. Academic Press. London, pp. 423 - 470, 1992.

158. Pehrsson P E, Celii F G and Butler J E: Chemical Mechanisms of Diamond CVD: In R F Davis (ed.). Diamond Films and Coatings. Noyes Publications. New Jersey, USA, pp. 68 - 146, 1993.

159. Koba R J: Technology of Vapour Phase Growth of Diamond Films: In R F Davis (ed.). Diamond Films and Coatings. Noyes Publications. New Jersey, USA, pp. 147 - 182, 1993.

160. Lux B and Haubner R: Diamond as a Wear-Resistant Coating: In R F Davis (ed.). Diamond Films and Coatings. Noyes Publications. New Jersey, USA, pp. 183 - 243, 1993.

161. Sneddon M V and Hall D R: Polycrystalline Diamond: Manufacture, Wear Mechanisms, and Implications for Bit Design: J. Of Petroleum Technology, pp. 1593 - 1601, December 1988.

162. Henjered A, Hellsing M, Andren H-O, and Norden H: The Presence of Cobalt at WC/WC Interfaces: Inst. Phys. Conf. Ser. No. 75: Chapter 4, ed. Almond E A Brookes C A and Warren R, pp. 303 - 309, 1986.

163. Tank K: Private Communication: De Beers Diamond Research Laboratory, Johannesburg, 1995.

164. Tabor D and Field J E: Friction of Diamond: In J E Field (ed.). The Properties of Natural and Synthetic Diamond. Academic Press. London, pp. 547 - 572, 1992.

1989.

144. Demizu K, Ishigaki H and Wadabayashi R: Dry Friction of Silicon Carbide and Silicon Nitride Against Metals: The Effect of Humidity and Oxide Films: J. of Tribology, Vol. 111, pp. 401 - 405, 1989.

145. Papaphilippou C, Vardavoulias M and Jeandin M: The Influence of Humidity and the Rôle of Debris in the Unlubricated Wear of Ductile Cast Iron Against Alumina: Wear, Vol. 177, pp. 151 - 157, 1994.

146. Holzhauer W, Johnson R L and Murray S F: Wear Characteristics of Water-Lubricated Al_2O_3-Metal Sliding Couples: Wear of Materials 1981, ASME, pp. 676 - 684, 1981.

147. Salonen P, Andersson P and Lintula P: Oil Lubricated and Water Lubricated Pin-On-Disc Wear Tests with Engineering Ceramics: Publication No. C228, Helsinki University of Technology, 1990.

148. Andersson P: Water-Lubricated Pin-On-Disc Tests with Ceramics: Wear, Vol. 154, pp. 37 - 47, 1992.

149. Ravikiran A and Pramila Bai B N: Water-Lubricated Sliding of Al_2O_3 Against Steel: Wear, Vol. 171, pp. 33 - 39, 1993.

150. He Y J, Winnubst A J A, Schipper D J, Bakker P M V, Burggraaf A J and Verweij H: Friction and Wear Behaviour of Ceramic-Hardened Steel Couples Under Reciprocating Sliding Motion: Wear, Vol. 184, pp. 33 - 43, 1995.

151. Yang C and Bahadur S: Friction and Wear Behaviour of Alumina-Based Ceramics in Dry and Lubricated Sliding Against Tool Steel: Wear of Materials 1991, ASME, pp. 383 - 391, 1991.

152. Brookes C A: Indentation Hardness, Plasticity and Creep of Diamond: In J E Field (ed.), The Properties of Natural and Synthetic Diamond, Academic Press, London, pp. 515 - 546, 1992.

153. Yoder M N: Diamond Properties and Applications: In R F Davis (ed.), Diamond Films and Coatings, Noyes Publications, New Jersey, USA, pp. 1 - 30, 1993.

154. Nassau K: Synthesis of Bulk Diamond: History and Present Status: In R F Davis (ed.), Diamond Films and Coatings, Noyes Publications, New Jersey, USA, pp. 31 - 67,

132. Lim S C and Ashby M F: Wear Mechanism Maps; Acta Metall., Vol. 35, p. 1, 1987.

133. Gautier P and Kato K: Wear Mechanisms of Silicon Nitride, Partially Stabilized Zirconia and Alumina in Unlubricated Sliding Against Steel; Wear, vol. 162 - 164, pp. 305 - 313, 1993.

134. Klaffke D: Fretting Wear of Ceramics; Tribology International, Vol. 22, No. 2, pp. 89 - 101, 1989.

135. Aronov V and Mesyef T: Wear in Ceramic/Ceramic and Ceramic/Metal Reciprocating Sliding Contact: Part 1; J. Tribol., Vol. 108, pp. 16 - 21, 1986.

136. Miyoshi K and Buckley D H: Tribological Properties and Surface Chemistry of Silicon Carbide at Temperatures to 1500°C; ASLE Trans. Vol. 26, No. 1, pp. 53 - 63, 1987.

137. Stachowiak G W, Stachowiak G B and Batchelor A W: Metallic Film Transfer During Metal-Ceramic Unlubricated Sliding; Wear, Vol. 132, pp. 361 - 381, 1989.

138. Fang L, Gao Y, Zhou L and Li P: Unlubricated Sliding Wear of Ceramics Against Graphitized Cast Irons; Wear, Vol. 171, pp. 129 - 134, 1994.

139. Ravikiran A and Pramila Bai B N: High Speed Sliding of Al_2O_3 Pins Against an EN24 Steel Disc; Wear, Vol. 162 - 164, pp. 296 - 304, 1993.

140. Holmberg K, Andersson P and Valli J: Three-Body Interaction in Metal-Ceramic and Ceramic-Ceramic Contacts; in: Interface Dynamics, Proc. 14th Leeds-Lyon Symposium on Tribology; Dowson D, Taylor D M, Godet M and Berthe D (eds.); Elsevier Science Publishers B V; pp. 227 - 235, 1988.

141. Takadoum J and Roques-Carmes C: Influence of the Oxidation Activity of Metals on Friction and Wear of Ceramic-Metal Systems; Surface and Coatings Technology, Vol. 52, pp. 153 - 158, 1992.

142. Takadoum J and Zsiga Z: Effect of Water Vapour in Air on Friction and Wear of Al_2O_3, Si_3N_4 and Partially Stabilized Zirconia Sliding on Various Metals; J. Mater. Sci. Letters, Vol. 12, No. 11, pp. 791 - 793, 1993.

143. Denizu K, Wadabayashi R and Ishigaki H: Dry Friction of Oxide Ceramics Against Metals: The Effect of Humidity; Tribology Trans., Vol. 33, No. 4, pp. 505 - 510,

PSZ, GROUND SURFACES

Applied loads 20, 30 and 50 N (from top to bottom)

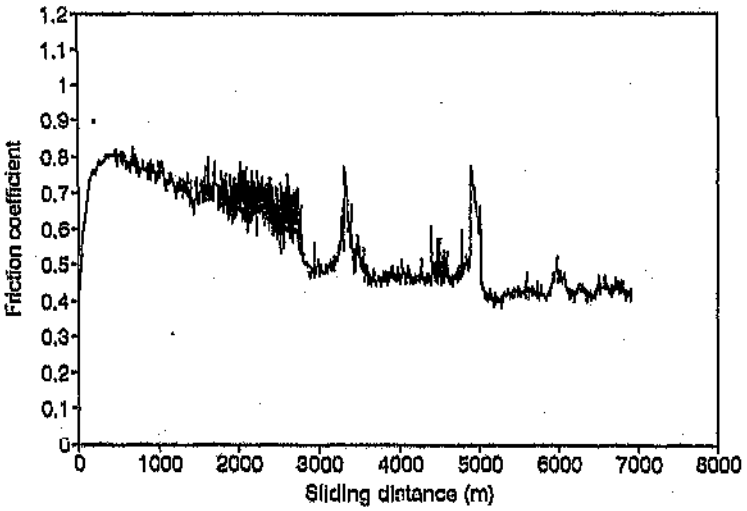

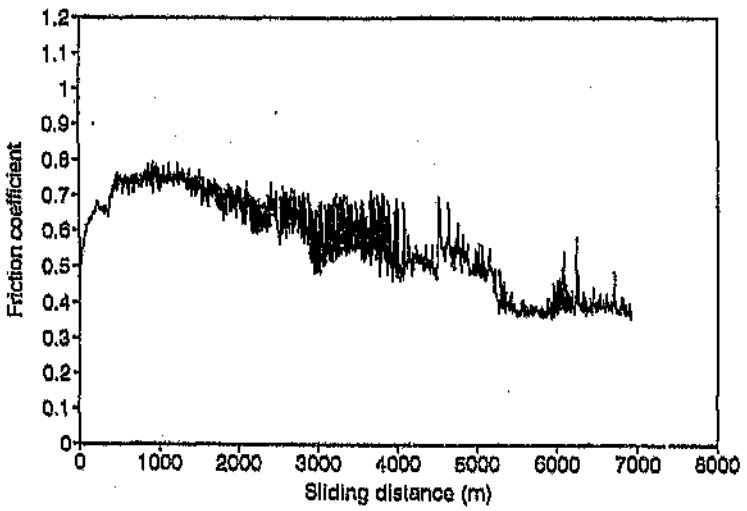

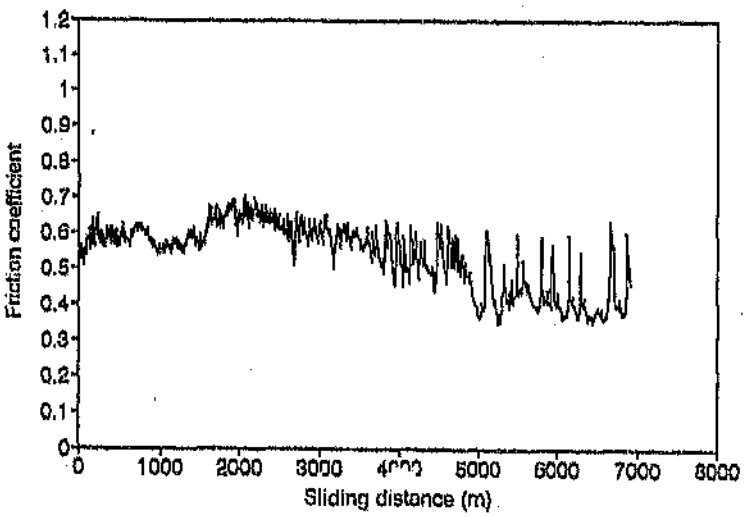

ALUMINA, POLISHED SURFACES

Applied loads 20, 30 and 50 N (from top to bottom)

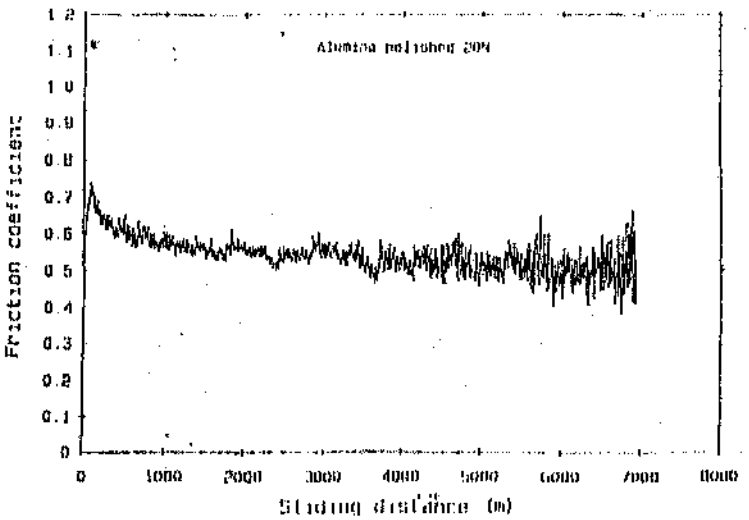

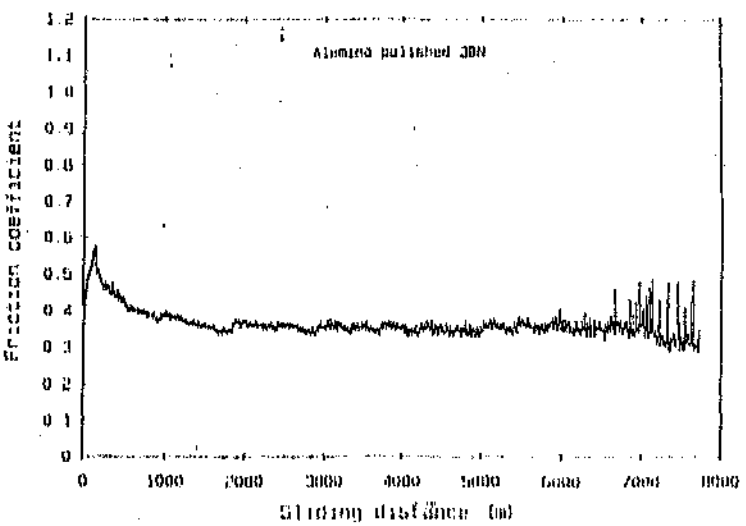

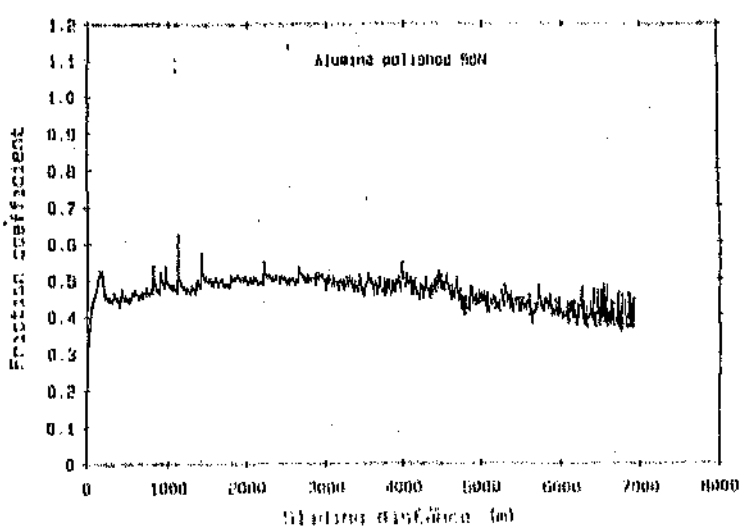

ALUMINA, GROUND SURFACES

Applied loads 20, 30 and 50 N (from top to bottom)

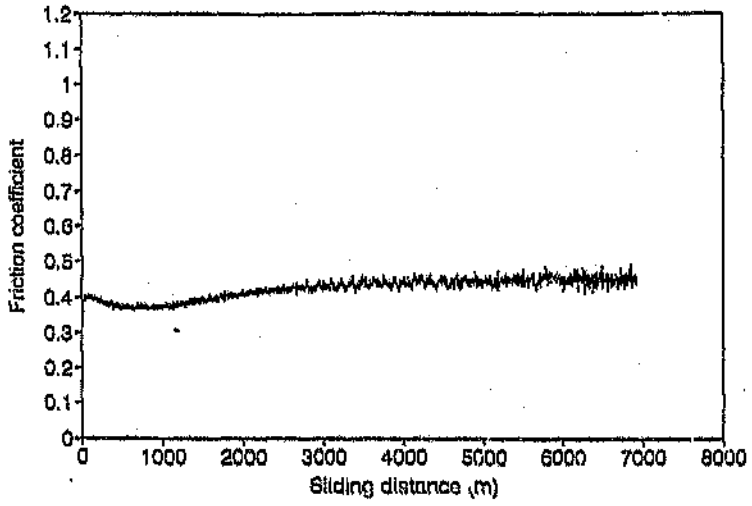

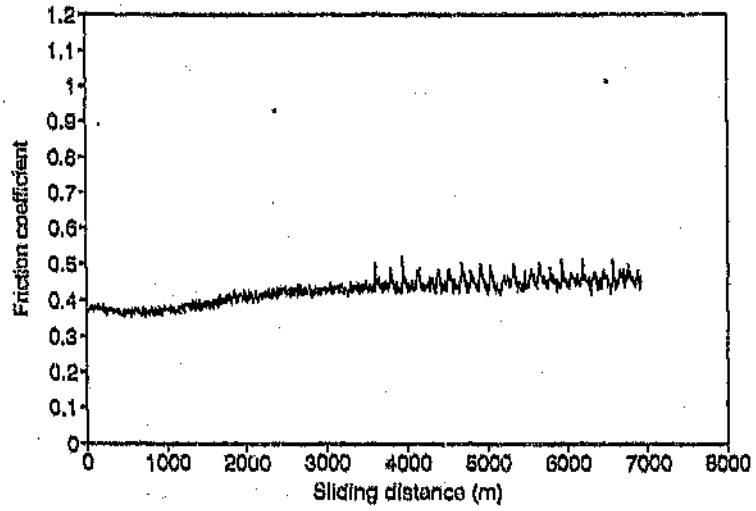

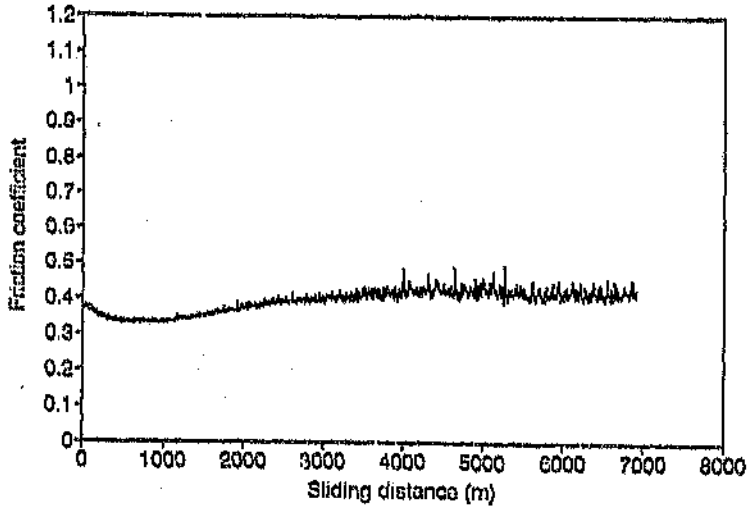

APPENDIX B

Friction coefficient curves for metal-ceramic sliding couples

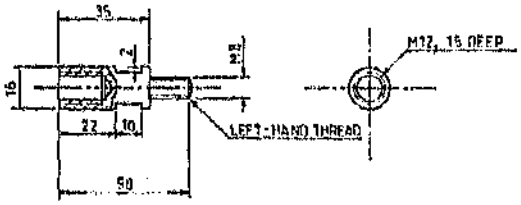

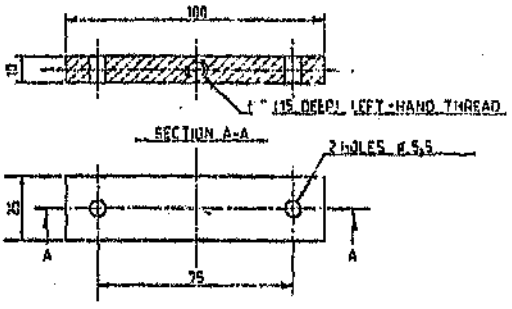

2 off, one without M8 thread

FRICTION FORCE TRANSDUCER

CONNECTING BOLT + PLATE

DATE	07-01-1988
DRAWN	OFRA DAMM
SCALE	1:1

DRG NO 21

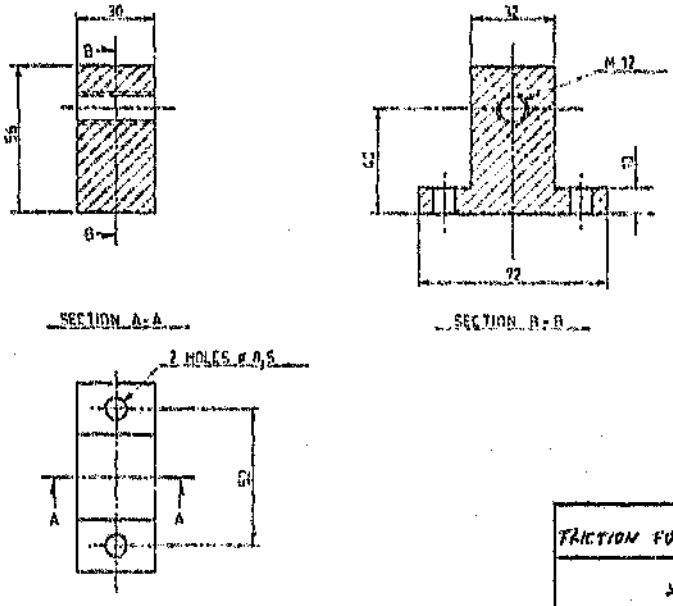

FRICTION FORCE TRANSDUCER

SUPPORT

DATE	07-01-1988
DRAWN	OFRA DAMM
SCALE	1:1

DRG NO 22

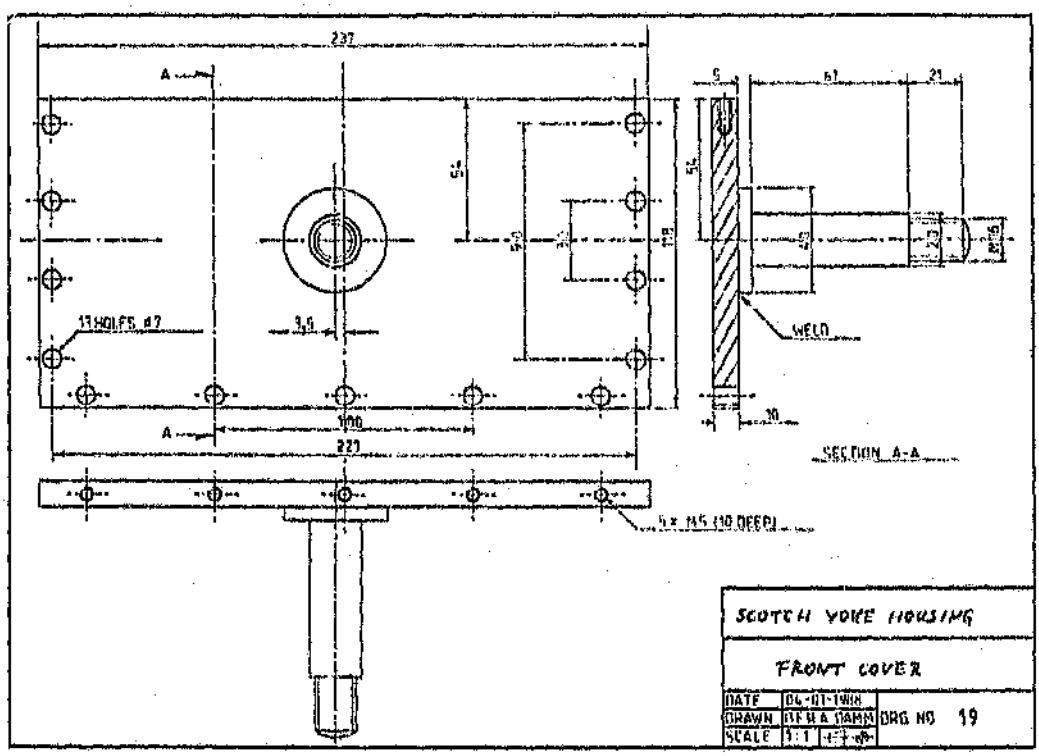
237
A
54
13 HOLES ø7
3,5
100
221
5
61
21
WELD
10
SECTION A-A
5 x M5 (10 DEEP)
SCOTCH YOKE HOUSING
FRONT COVER
DATE 04-01-1988
DRAWN BERA DAMM
SCALE 1:1
DRG NO 19

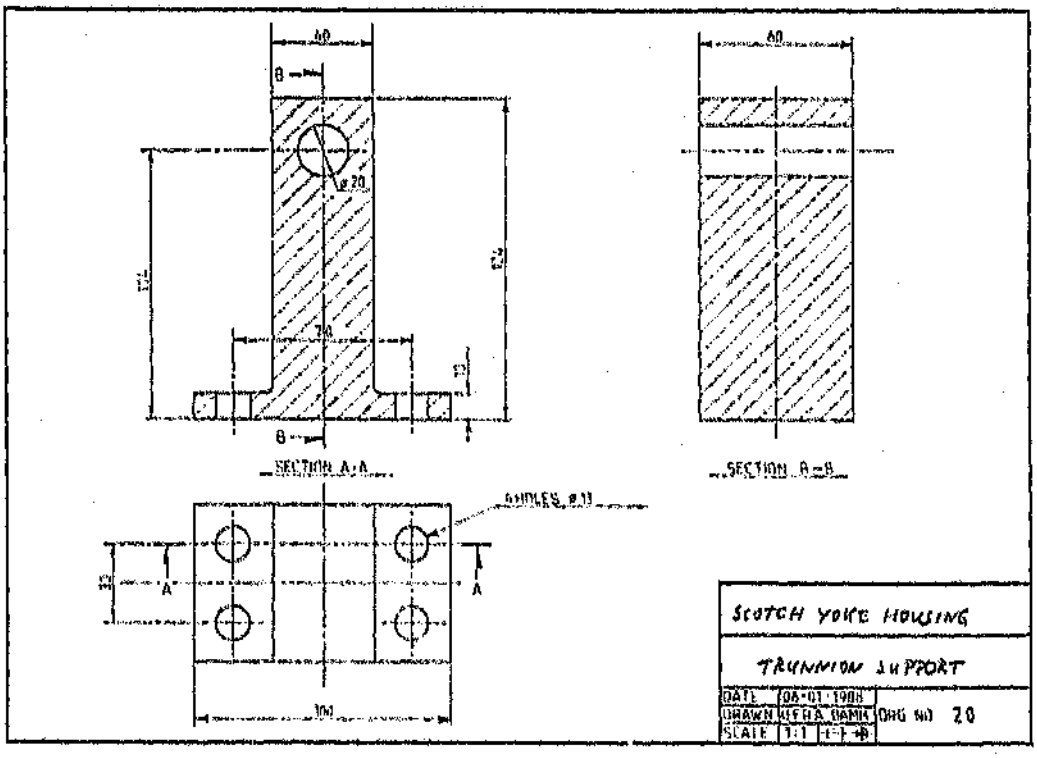
60
B
ø20
124
70
SECTION A-A
SECTION B-B
4 HOLES ø13
A
100
SCOTCH YOKE HOUSING
TRUNNION SUPPORT
DATE 08-01-1988
DRAWN BERA DAMM
SCALE 1:1
DRG NO 20

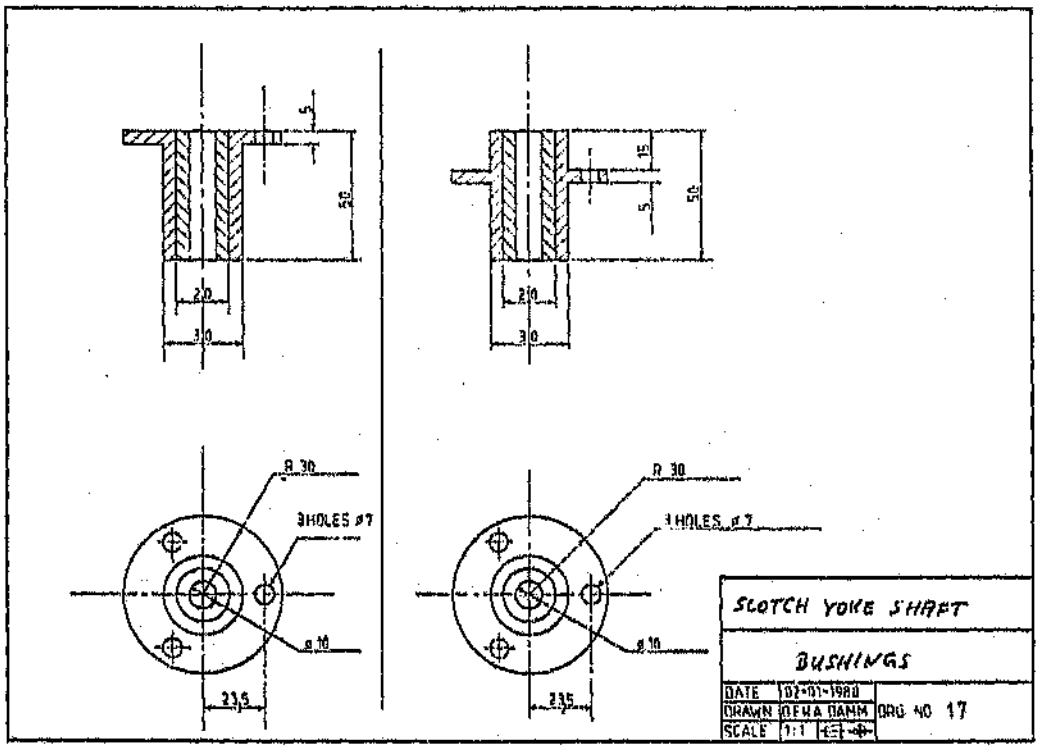

SCOTCH YOKE SHAFT BUSHINGS	
DATE	02-01-1988
DRAWN	DEWA DAMM
SCALE	1:1
DRG NO	17

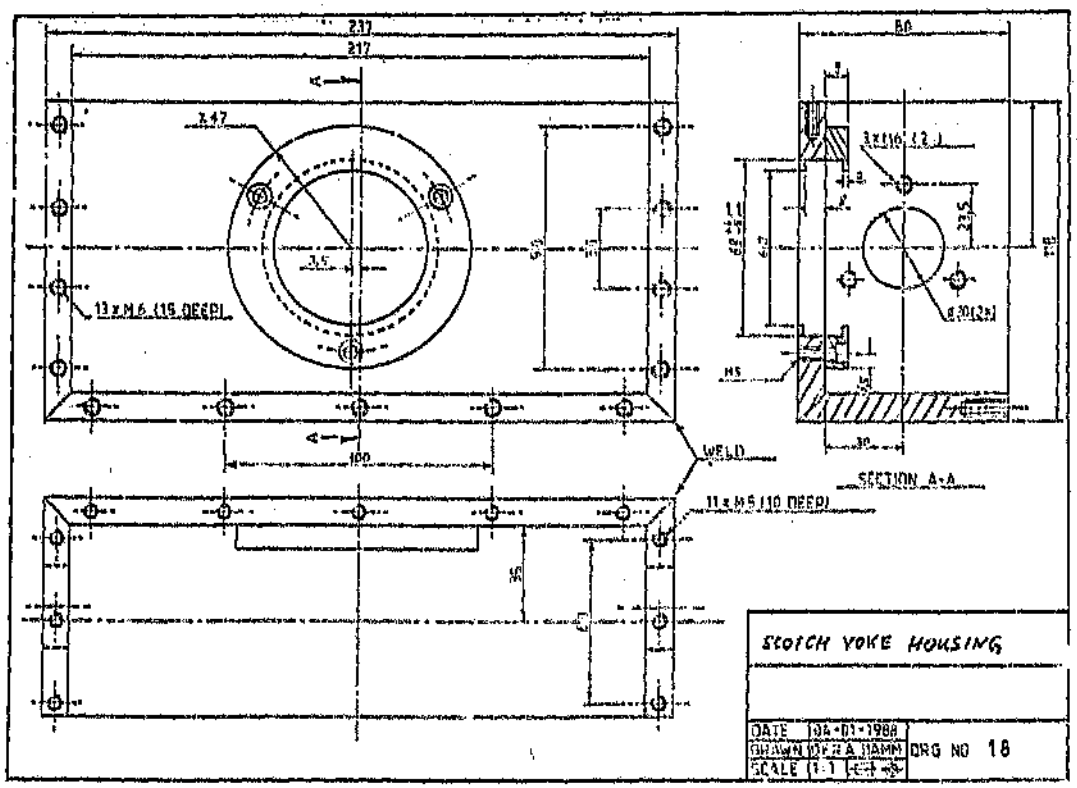

SCOTCH YOKE HOUSING	
DATE	04-01-1988
DRAWN	DEWA DAMM
SCALE	1:1
DRG NO	18

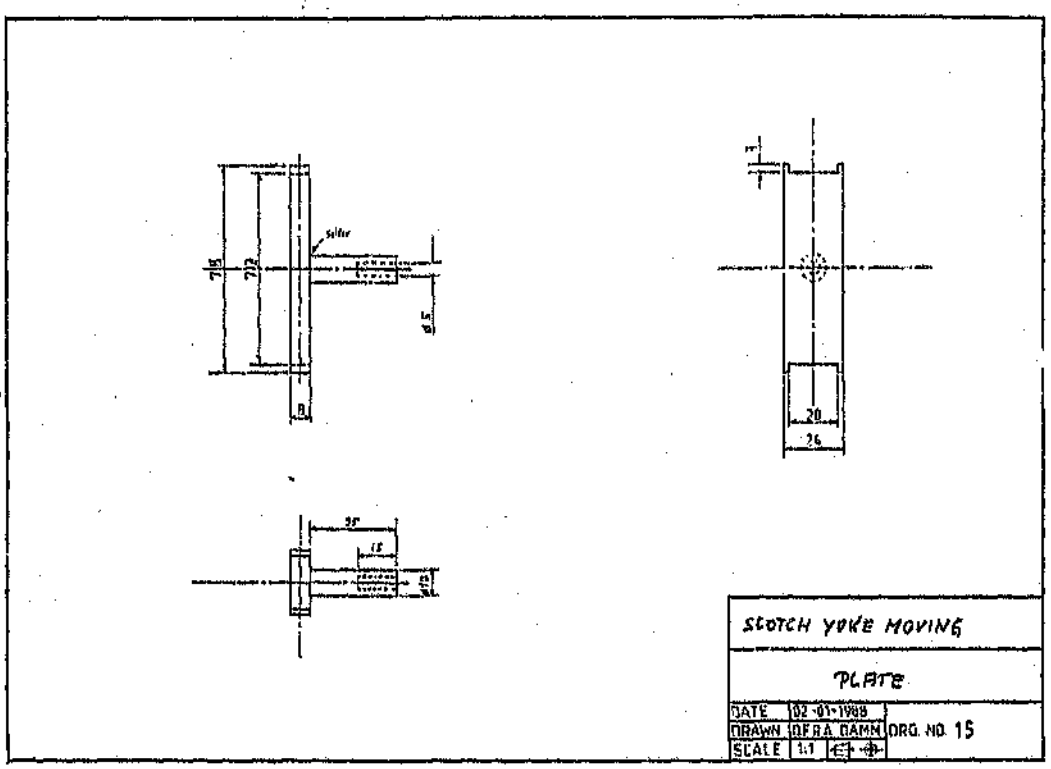

SCOTCH YOKE MOVING PLATE	
DATE	02-01-1988
DRAWN	DERA DAMM
SCALE	1:1
DRG. NO. 15	

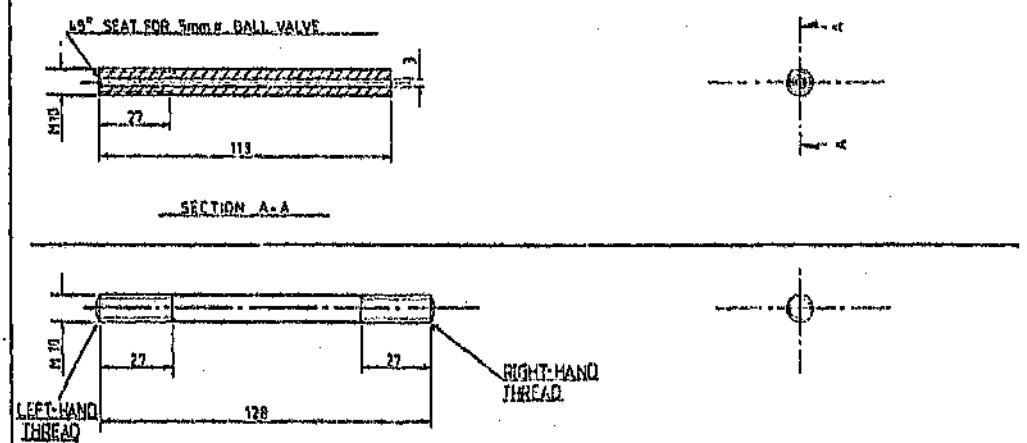

SCOTCH YOKE SHAFT	
DATE	02-01-1988
DRAWN	DERA DAMM
SCALE	1:1
DRG NO 16	

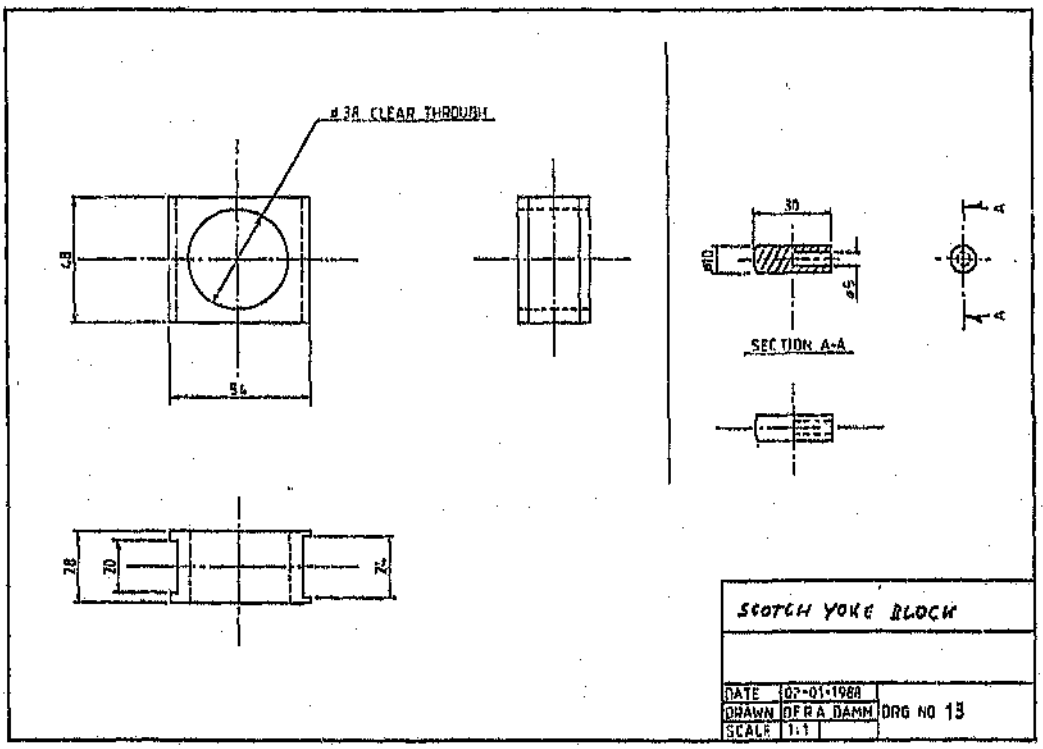

SCOTCH YOKE BLOCK

DATE	02-01-1988
DRAWN	DERA DAMM
SCALE	1:1

DRG NO 13

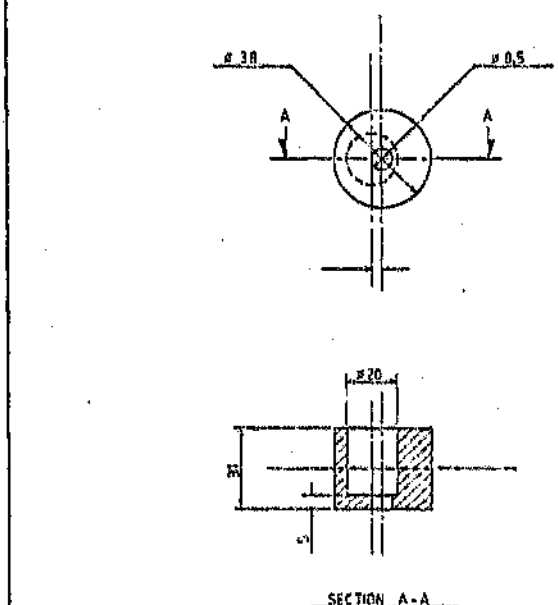

SCOTCH YOKE CAM

DATE	02-01-1988
DRAWN	DERA DAMM
SCALE	1:1

DRG NO 14

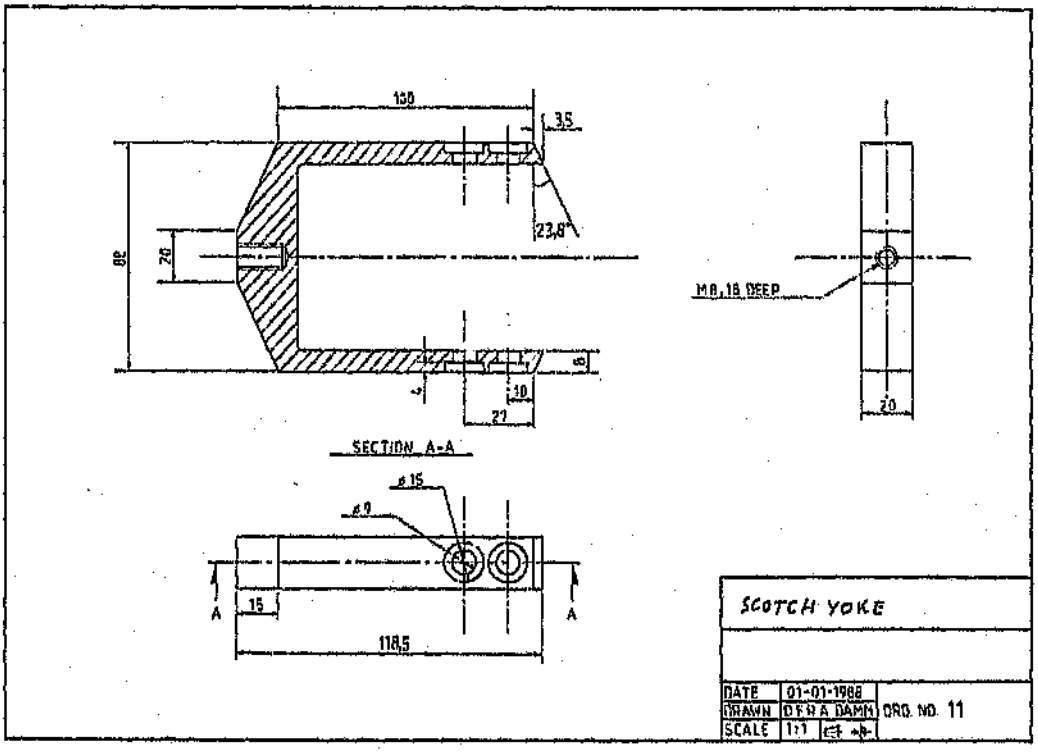
130
35
23,8°
80
28
M8,18 DEEP
20
10
22
SECTION A-A
ø15
ø9
A
15
A
118,5
SCOTCH YOKE
DATE 01-01-1988
DRAWN DERA DAMM
ORD NO. 11
SCALE 1:1

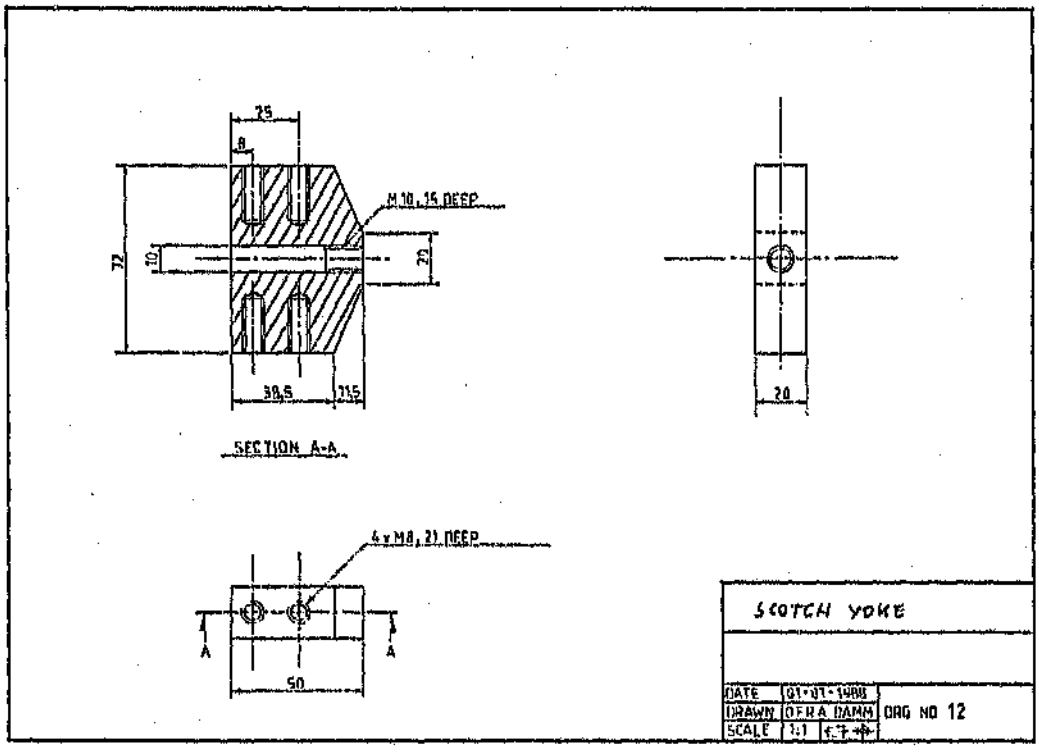
25
8
M10,15 DEEP
72
10
20
38,6
31,5
20
SECTION A-A
4 x M8, 21 DEEP
A
A
50
SCOTCH YOKE
DATE 01-01-1988
DRAWN DERA DAMM
ORD NO 12
SCALE 1:1

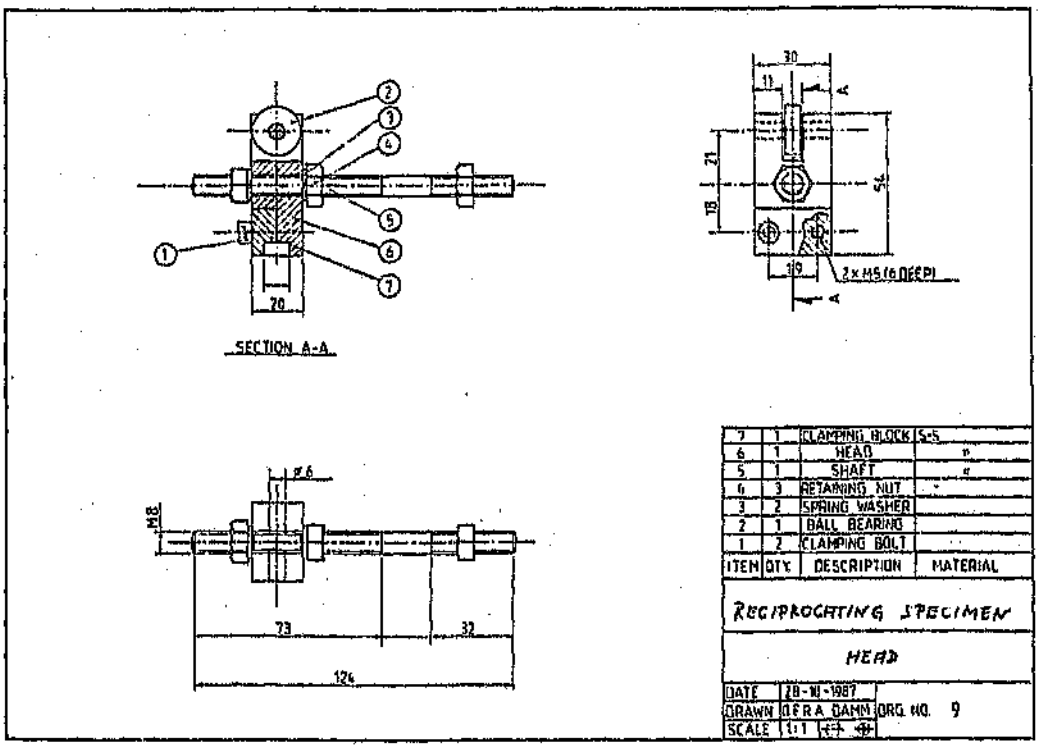

ITEM	QTY	DESCRIPTION	MATERIAL
7	1	CLAMPING BLOCK	S-S
6	1	HEAD	"
5	1	SHAFT	"
4	3	RETAINING NUT	"
3	2	SPRING WASHER	
2	1	BALL BEARING	
1	2	CLAMPING BOLT	

RECIPROCATING SPECIMEN

HEAD

DATE	28-10-1987
DRAWN	O.E.R.A. DAMM
SCALE	1:1

ORG. NO. 9

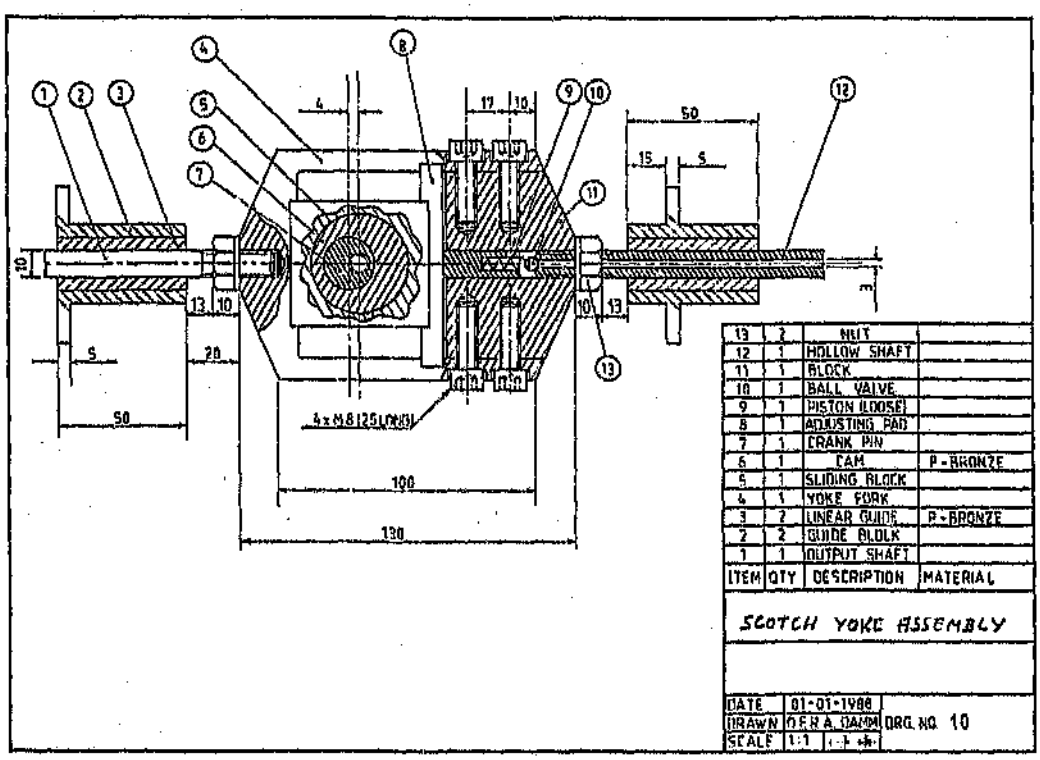

ITEM	QTY	DESCRIPTION	MATERIAL
13	2	NUT	
12	1	HOLLOW SHAFT	
11	1	BLOCK	
10	1	BALL VALVE	
9	1	PISTON (LOOSE)	
8	1	ADJUSTING PAD	
7	1	CRANK PIN	
6	1	CAM	P-BRONZE
5	1	SLIDING BLOCK	
4	1	YOKE FORK	
3	2	LINEAR GUIDE	P-BRONZE
2	2	GUIDE BLOCK	
1	1	OUTPUT SHAFT	

SCOTCH YOKE ASSEMBLY

DATE	01-01-1988
DRAWN	O.E.R.A. DAMM
SCALE	1:1

ORG. NO. 10

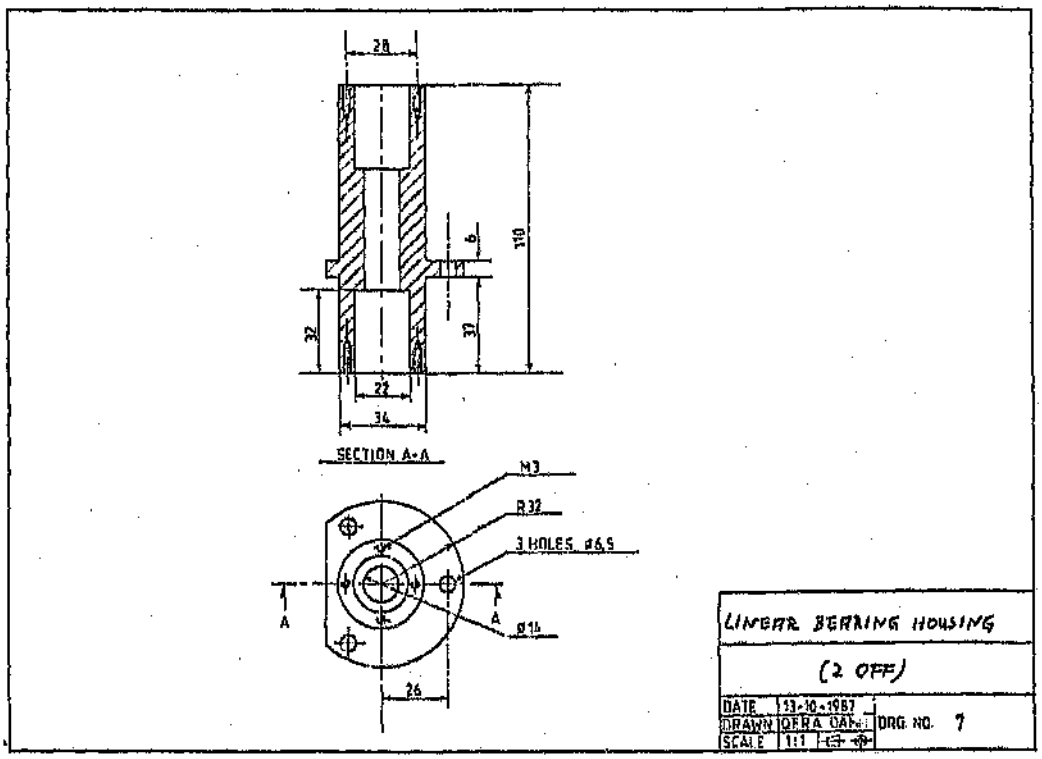

LINEAR BEARING HOUSING

(2 OFF)

DATE	13-10-1987
DRAWN	OFRA OAMM
SCALE	1:1

DRG NO. 7

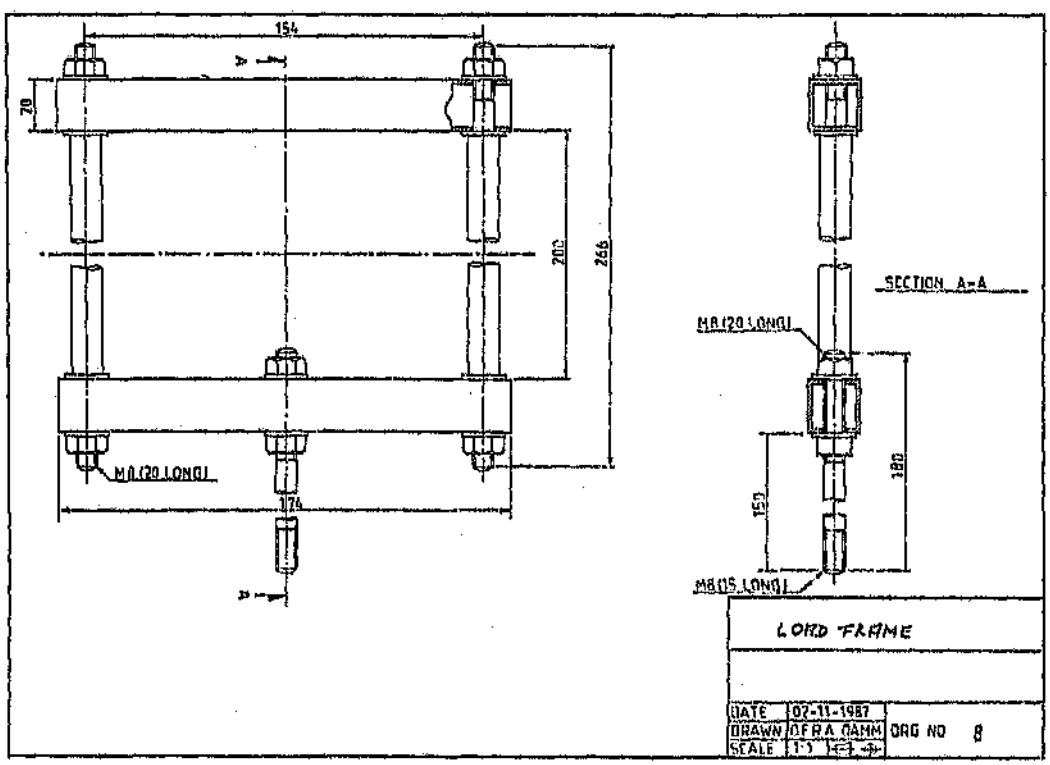

LORD FRAME

DATE	07-11-1987
DRAWN	OFRA OAMM
SCALE	1:1

DRG NO 8

SILICON NITRIDE, POLISHED SURFACES

Applied loads 20, 30 and 50 N (from top to bottom)

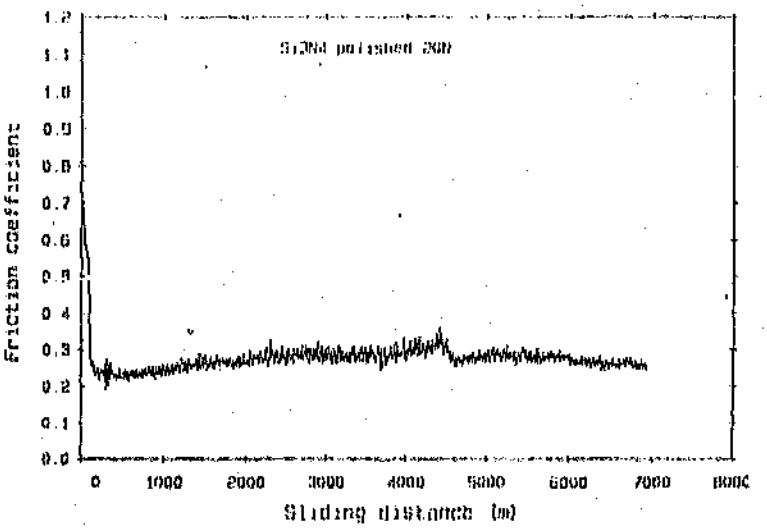

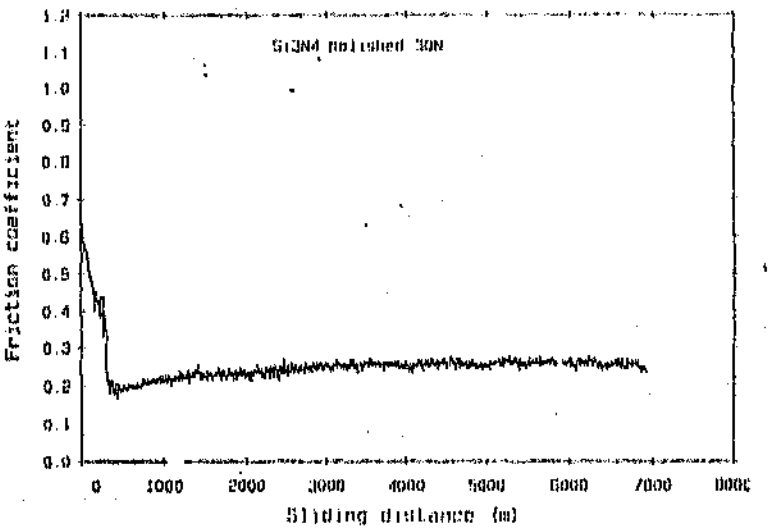

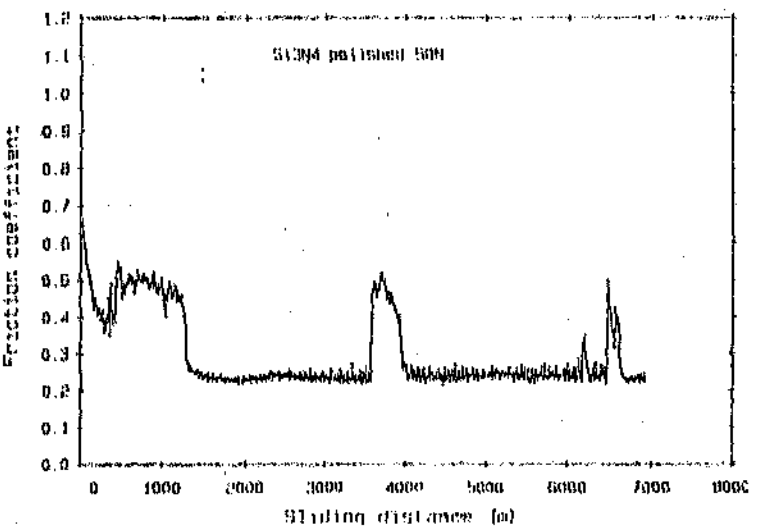

SILICON NITRIDE, GROUND SURFACES

Applied loads 20, 30 and 50 N (from top to bottom)

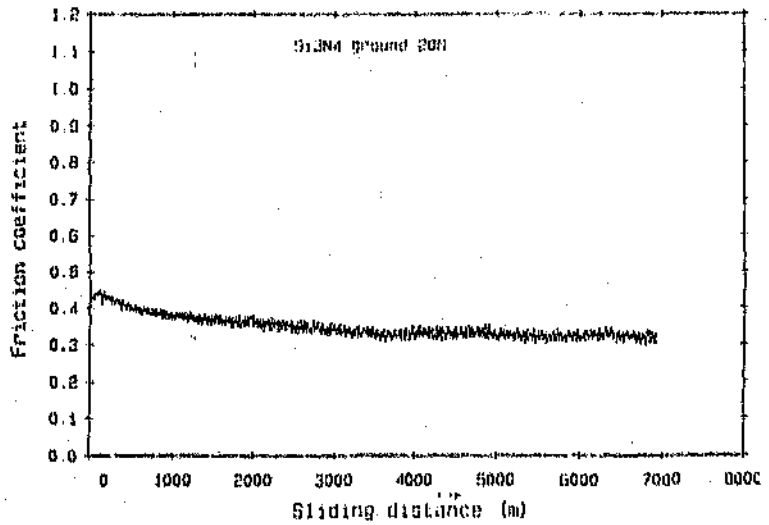

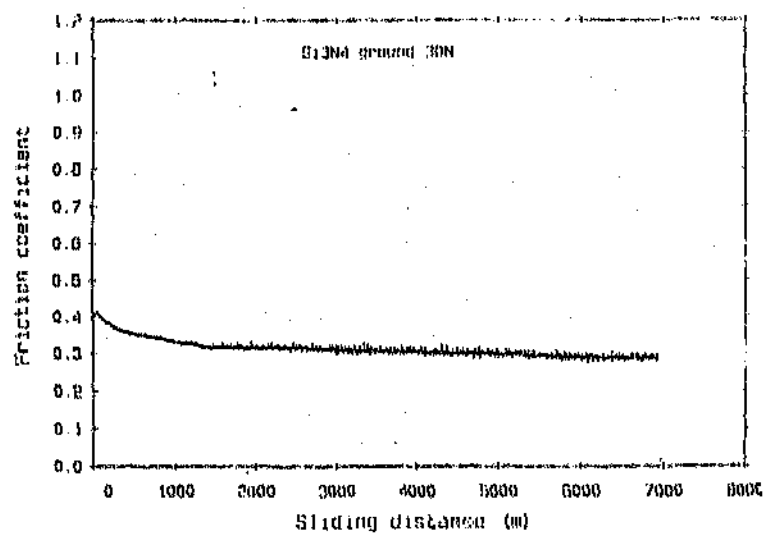

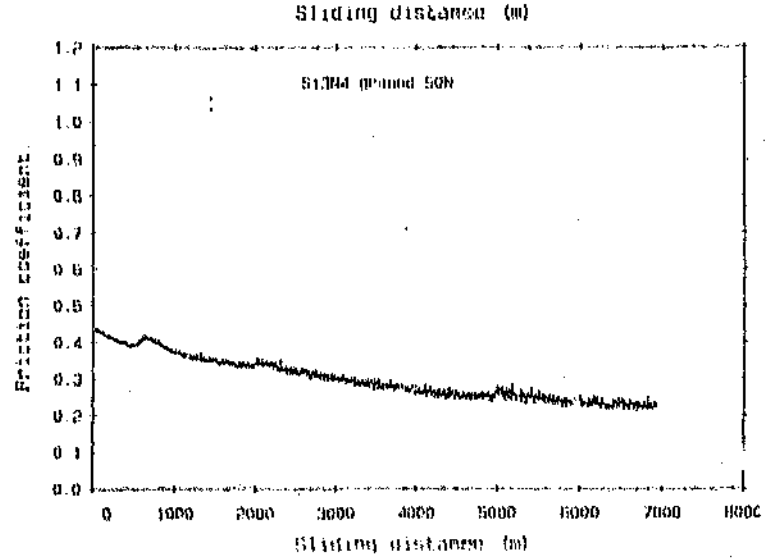

SIALON 101, POLISHED SURFACES

Applied loads 20, 30 and 50 N (from top to bottom)

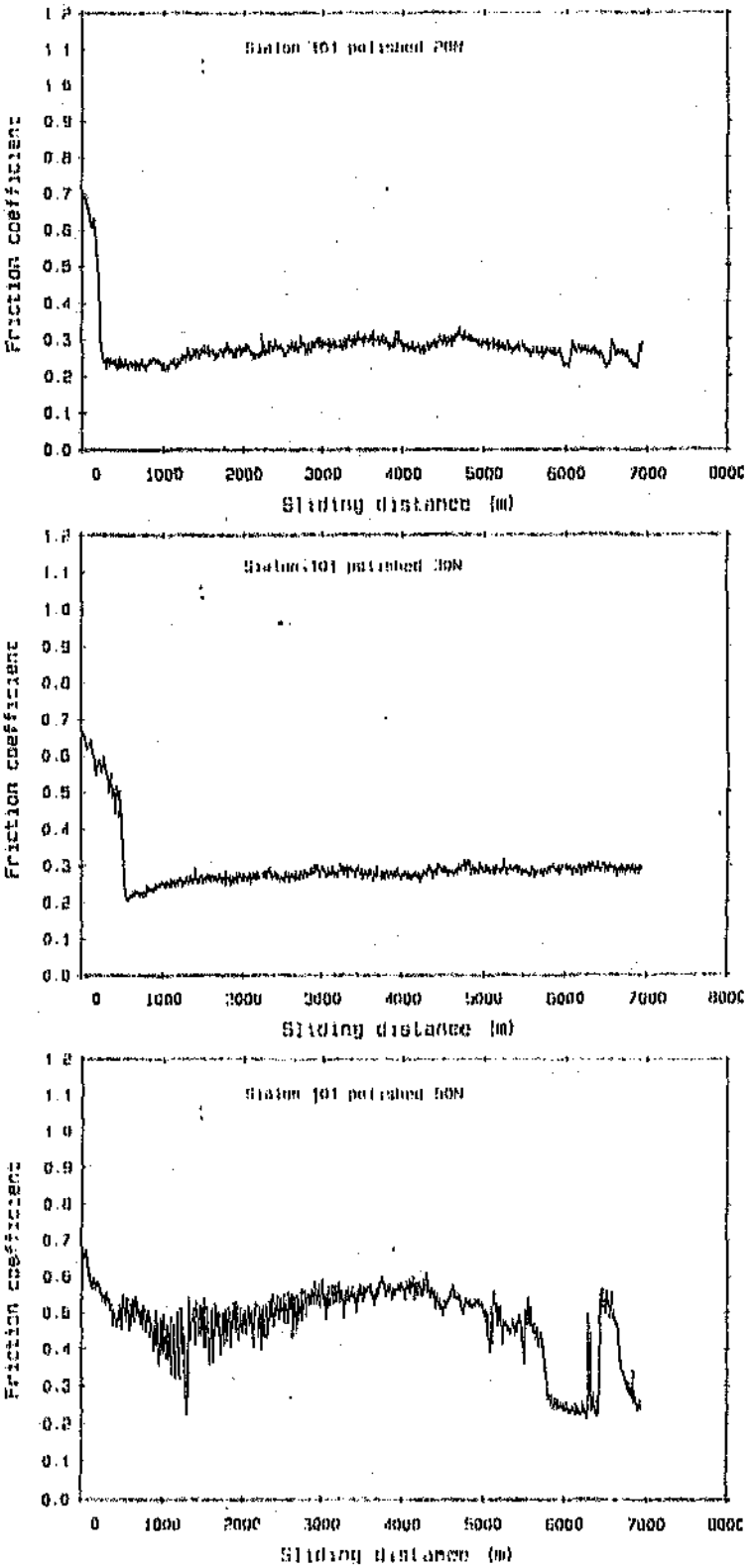

SIALON 101, GROUND SURFACES

Applied loads 20, 30 and 50 N (from top to bottom)

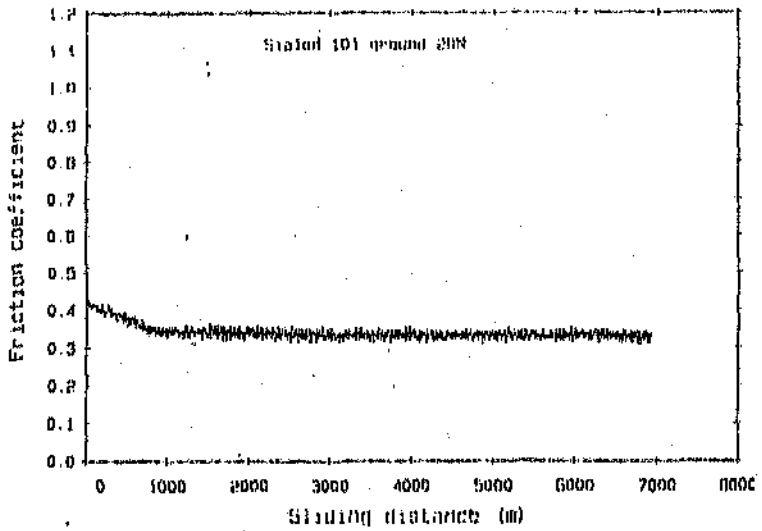

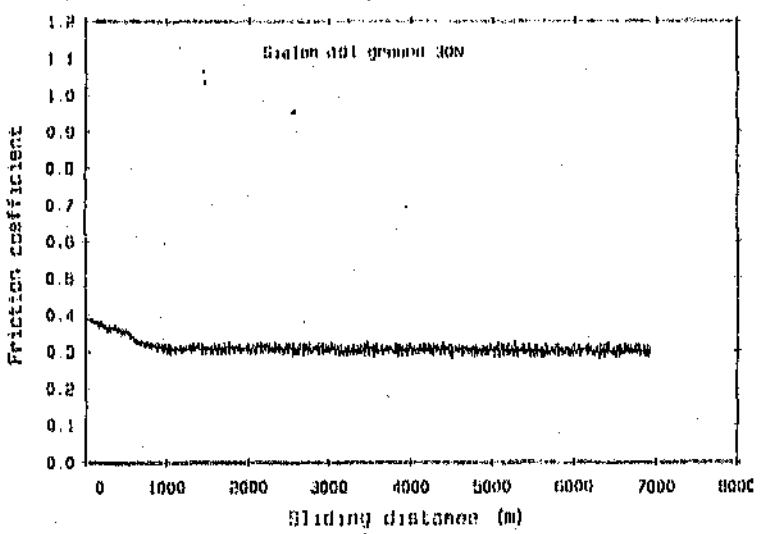

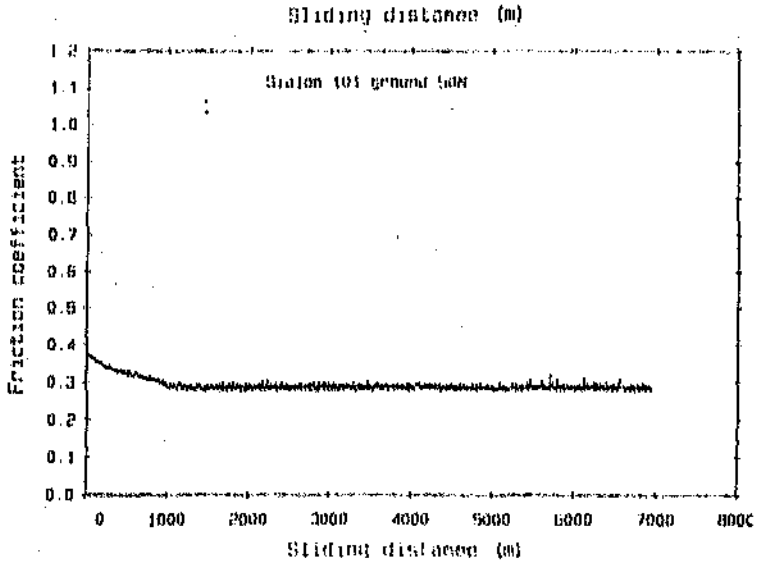

Ce-TZP, POLISHED SURFACES

Applied loads 20, 30 and 50 N (from top to bottom)

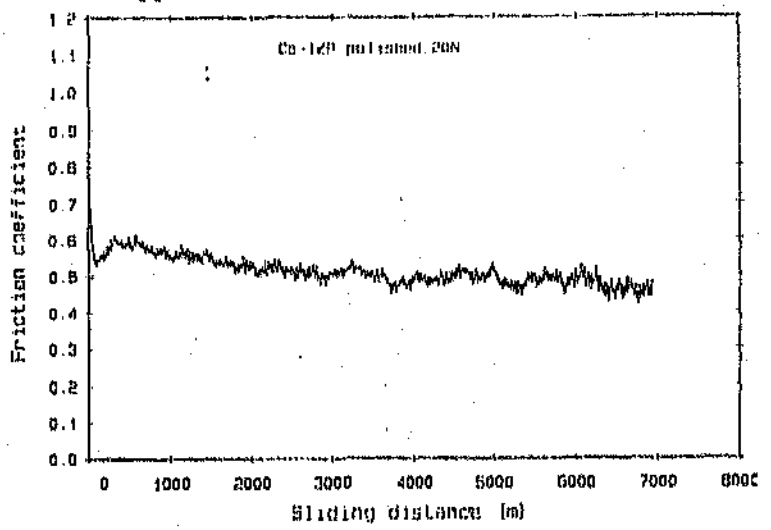

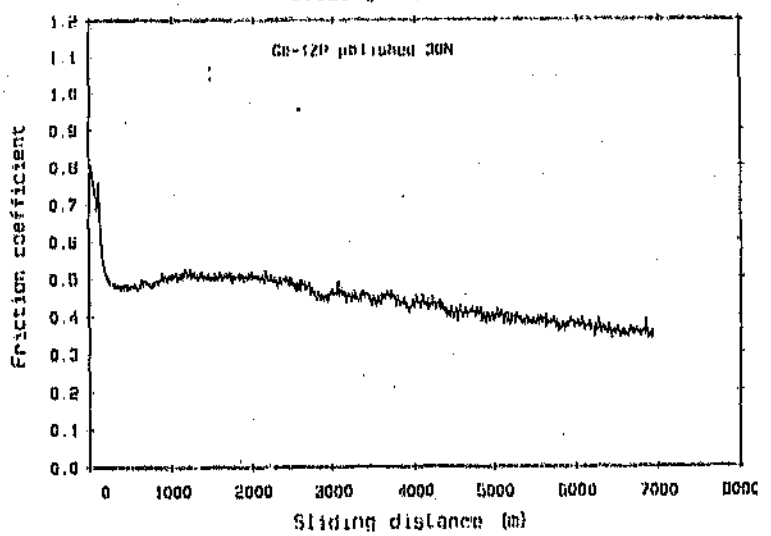

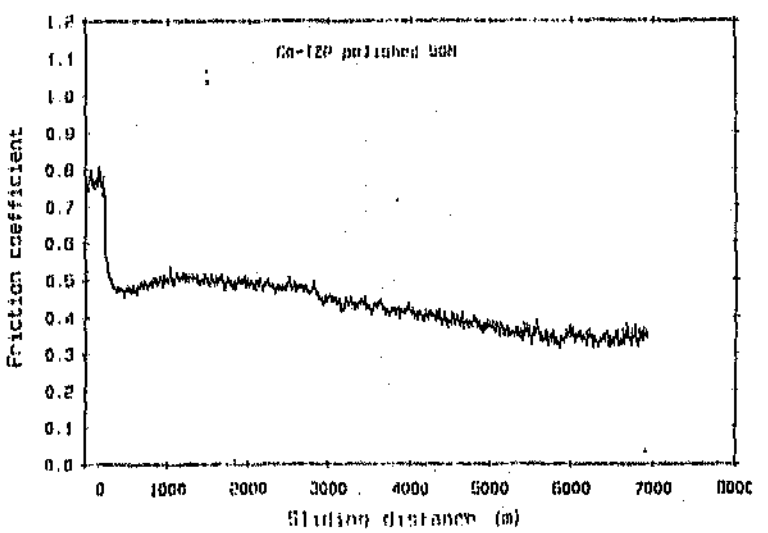

Ce-TZP, GROUND SURFACES

Applied loads 20, 30 and 50 N (from top to bottom)

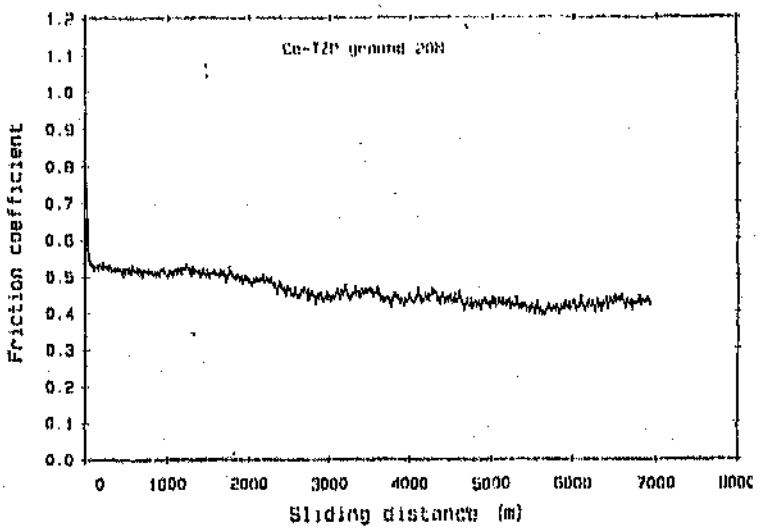

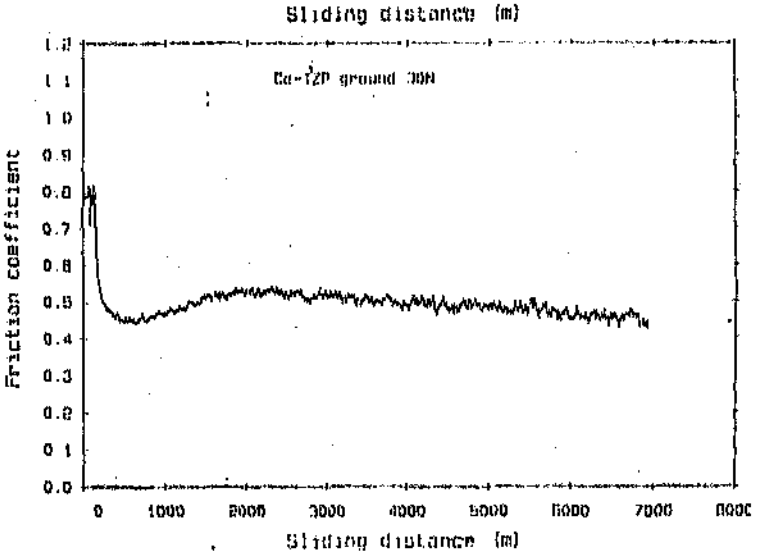

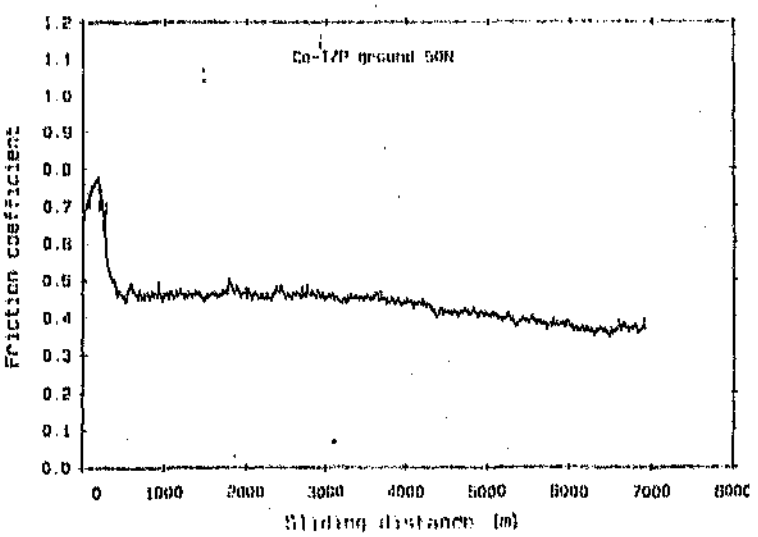

3Y-TZP, POLISHED SURFACES

Applied loads 20, 30 and 50 N (from top to bottom)

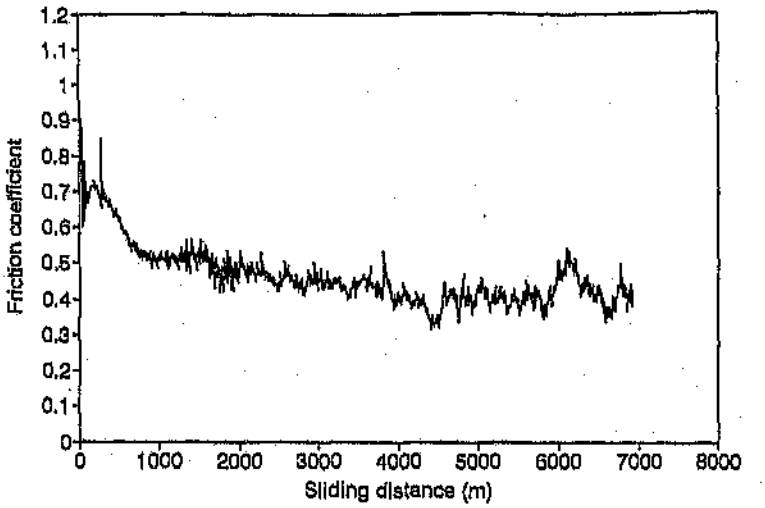

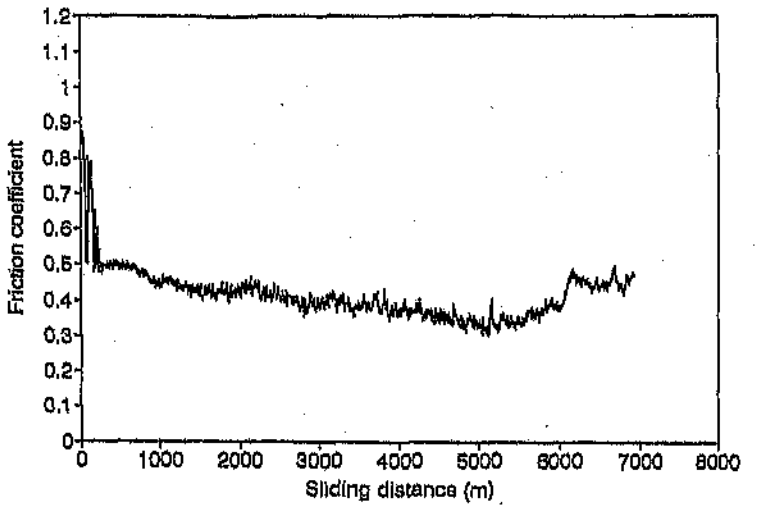

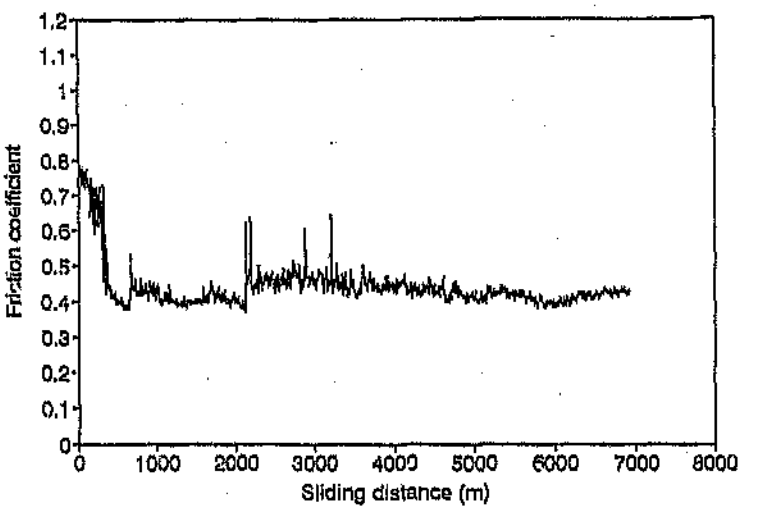

3Y-TZP, GROUND SURFACES

Applied loads 20, 30 and 50 N (from top to bottom)

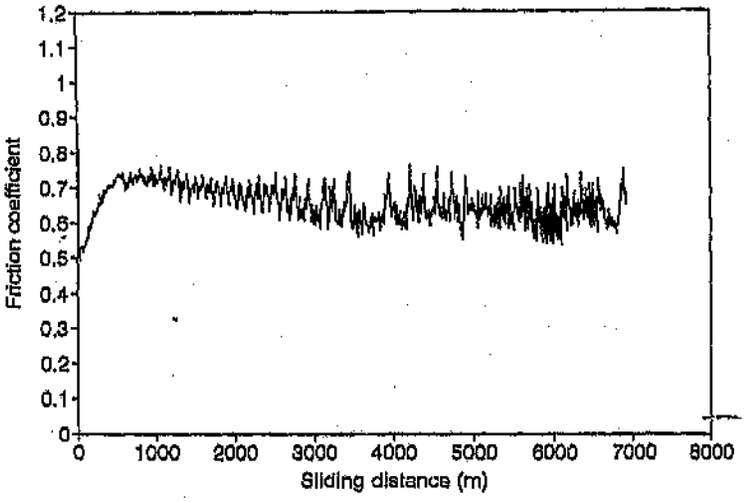

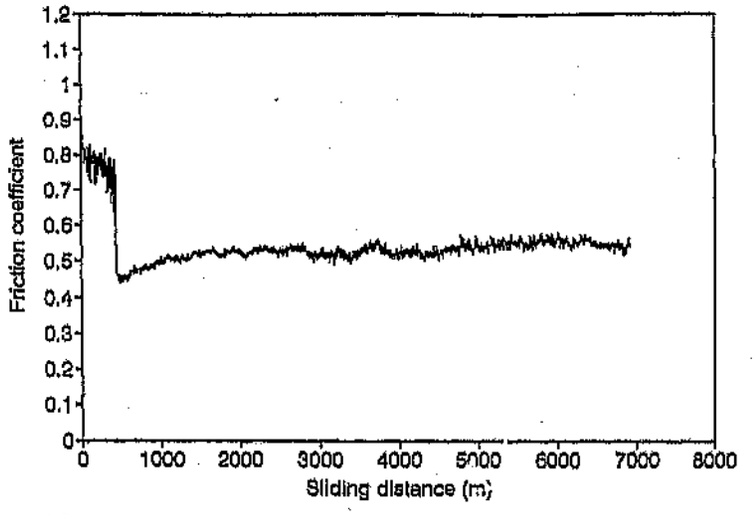

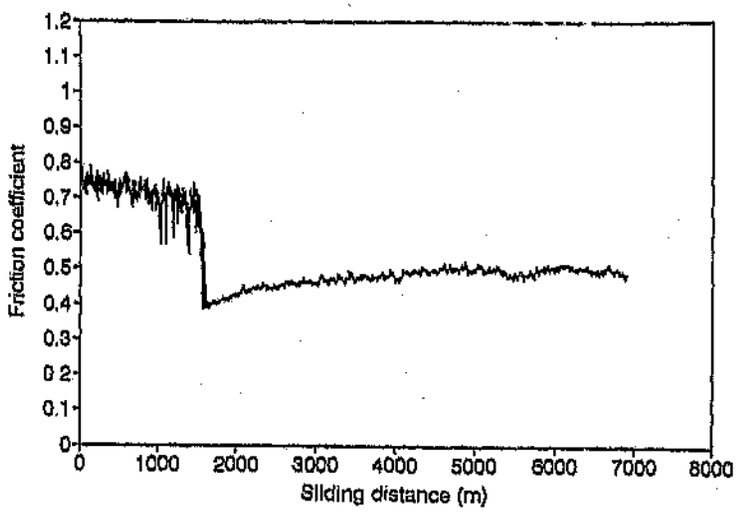

PSZ, POLISHED SURFACES

Applied loads 20, 30 and 50 N (from top to bottom)

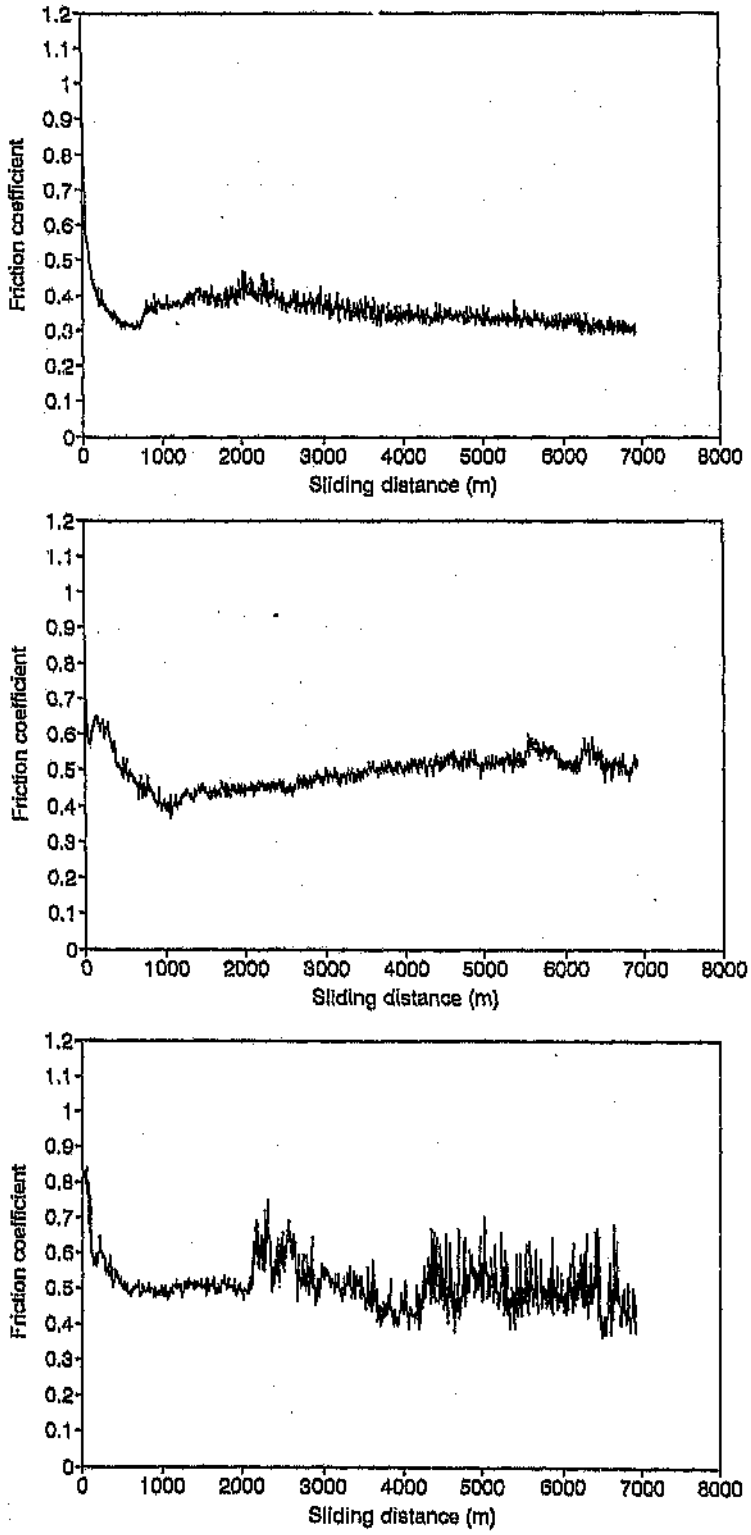

Author: Damm Oliver Frank Rudolf August.
Name of thesis: Friction and wear of selected metal-ceramic and polycrystalline diamond sliding couples.

PUBLISHER:
University of the Witwatersrand, Johannesburg
©2015

LEGALNOTICES:

Copyright Notice: All materials on the University of the Witwatersrand, Johannesburg Library website are protected by South African copyright law and may not be distributed, transmitted, displayed or otherwise published in any format, without the prior written permission of the copyright owner.

Disclaimer and Terms of Use: Provided that you maintain all copyright and other notices contained therein, you may download material (one machine readable copy and one print copy per page)for your personal and/or educational non-commercial use only.

The University of the Witwatersrand, Johannesburg, is not responsible for any errors or omissions and excludes any and all liability for any errors in or omissions from the information on the Library website.